FLOODING ON CORAL REEF-LINED COASTS: CURRENT STATE OF KNOWLEDGE AND FUTURE CHALLENGES

EDITED BY: Curt D. Storlazzi, William J. Skirving, John J. Marra, Robert Timothy McCall and Andrew W. M. Pomeroy

PUBLISHED IN: Frontiers in Marine Science

frontiers Research Topics

frontiers

Frontiers eBook Copyright Statement

The copyright in the text of individual articles in this eBook is the property of their respective authors or their respective institutions or funders. The copyright in graphics and images within each article may be subject to copyright of other parties. In both cases this is subject to a license granted to Frontiers.

The compilation of articles constituting this eBook is the property of Frontiers.

Each article within this eBook, and the eBook itself, are published under the most recent version of the Creative Commons CC-BY licence. The version current at the date of publication of this eBook is CC-BY 4.0. If the CC-BY licence is updated, the licence granted by Frontiers is automatically updated to the new version.

When exercising any right under the CC-BY licence, Frontiers must be attributed as the original publisher of the article or eBook, as applicable.

Authors have the responsibility of ensuring that any graphics or other materials which are the property of others may be included in the CC-BY licence, but this should be checked before relying on the CC-BY licence to reproduce those materials. Any copyright notices relating to those materials must be complied with.

Copyright and source acknowledgement notices may not be removed and must be displayed in any copy, derivative work or partial copy which includes the elements in question.

All copyright, and all rights therein, are protected by national and international copyright laws. The above represents a summary only. For further information please read Frontiers' Conditions for Website Use and Copyright Statement, and the applicable CC-BY licence.

ISSN 1664-8714
ISBN 978-2-88966-478-8
DOI 10.3389/978-2-88966-478-8

About Frontiers

Frontiers is more than just an open-access publisher of scholarly articles: it is a pioneering approach to the world of academia, radically improving the way scholarly research is managed. The grand vision of Frontiers is a world where all people have an equal opportunity to seek, share and generate knowledge. Frontiers provides immediate and permanent online open access to all its publications, but this alone is not enough to realize our grand goals.

Frontiers Journal Series

The Frontiers Journal Series is a multi-tier and interdisciplinary set of open-access, online journals, promising a paradigm shift from the current review, selection and dissemination processes in academic publishing. All Frontiers journals are driven by researchers for researchers; therefore, they constitute a service to the scholarly community. At the same time, the Frontiers Journal Series operates on a revolutionary invention, the tiered publishing system, initially addressing specific communities of scholars, and gradually climbing up to broader public understanding, thus serving the interests of the lay society, too.

Dedication to Quality

Each Frontiers article is a landmark of the highest quality, thanks to genuinely collaborative interactions between authors and review editors, who include some of the world's best academicians. Research must be certified by peers before entering a stream of knowledge that may eventually reach the public - and shape society; therefore, Frontiers only applies the most rigorous and unbiased reviews.
Frontiers revolutionizes research publishing by freely delivering the most outstanding research, evaluated with no bias from both the academic and social point of view. By applying the most advanced information technologies, Frontiers is catapulting scholarly publishing into a new generation.

What are Frontiers Research Topics?

Frontiers Research Topics are very popular trademarks of the Frontiers Journals Series: they are collections of at least ten articles, all centered on a particular subject. With their unique mix of varied contributions from Original Research to Review Articles, Frontiers Research Topics unify the most influential researchers, the latest key findings and historical advances in a hot research area! Find out more on how to host your own Frontiers Research Topic or contribute to one as an author by contacting the Frontiers Editorial Office: frontiersin.org/about/contact

FLOODING ON CORAL REEF-LINED COASTS: CURRENT STATE OF KNOWLEDGE AND FUTURE CHALLENGES

Topic Editors:
Curt D. Storlazzi, United States Geological Survey (USGS), United States
William J. Skirving, National Oceanic and Atmospheric Administration (NOAA), United States
John J. Marra, National Centers for Environmental Information, National Oceanic and Atmospheric Administration, United States
Robert Timothy McCall, Deltares (Netherlands), Netherlands
Andrew W.M. Pomeroy, University of Western Australia, Australia

Citation: Storlazzi, C. D., Skirving, W. J., Marra, J. J., McCall, R. T., Pomeroy, A. W. M., eds. (2021). Flooding on Coral Reef-lined Coasts: Current State of Knowledge and Future Challenges. Lausanne: Frontiers Media SA. doi: 10.3389/978-2-88966-478-8

Table of Contents

frontiers in Marine Science

EDITORIAL
published: 07 January 2021
doi: 10.3389/fmars.2020.635240

Editorial: Flooding on Coral Reef-Lined Coasts: Current State of Knowledge and Future Challenges

William Skirving[1,2], *Andrew Pomeroy*[3,4], *Robert McCall*[5], *John Marra*[6] *and Curt Storlazzi*[7]*

[1] Coral Reef Watch, National Oceanic and Atmospheric Administration, College Park, MD, United States, [2] ReefSense Pty Ltd., Cranbrook, QLD, Australia, [3] Oceans Institute, University of Western Australia, Perth, WA, Australia, [4] Australian Institute of Marine Science, Perth, WA, Australia, [5] Unit of Marine and Coastal Systems, Deltares, Delft, Netherlands, [6] National Environmental Satellite, Data and Information Service (NESDIS) National Centers for Environmental Information, National Oceanic and Atmospheric Administration, Honolulu, HI, United States, [7] Pacific Coastal and Marine Science Center, U.S. Geological Survey, Santa Cruz, CA, United States

Keywords: sea level, waves, beaches, sediment transport, runup, flood, inundation, coastal resilience

Editorial on the Research Topic

Flooding on Coral Reef-Lined Coasts: Current State of Knowledge and Future Challenges

Many low-lying, tropical, coral reef-lined coasts and islands are experiencing wave-driven flood events that currently strike with little to no warning. These events are a result of a combination of sea surface elevation and wave height, and can cause severe flooding even on windless, sunny days. With rising sea levels, over the coming decades, coastal flooding in all its forms will have significantly increased impacts. Increasing the resilience of coastal communities while decreasing the risk to lives and livelihood is critical in these locations.

Understanding and predicting coastal flooding is therefore a challenging and urgent problem. Although this issue is global in scale, understanding and predicting flooding along tropical, coral reef-lined shorelines presents unique challenges owing to the complexity of these shorelines, which have been little studied and for which there are few data.

To address the urgent need for coastal flooding early warning system (EWS) and future scenario modeling tools, the UFORIC (Understanding Flooding on Reef-lined Island Coasts; https://geoblueplanet.org/blue-planet-activities/uforic/) working group was established in 2018. This group has committed to meet regularly to advance and update work plans. The ultimate goal of this working group is to develop the tools and research that aid disaster risk management and climate change adaptation in coral reef-lined coasts. Such developments require a multi-disciplinary research effort, and thus the UFORIC working group includes leading coastal engineers, physical oceanographers, geologists, geographers, ecologists, remote-sensing specialists, and climate-change scientists.

The first UFORIC workshop was held in Hawaii during February 2018. Apart from an improved level of cooperation and collaboration within the community, a number of outcomes have been realized since the workshop, including but not limited to: A workshop report, published in EOS (Storlazzi, 2018); a paper that summarizes the "Steps to Develop Early Warning Systems and Future Scenarios of Storm Wave-driven Flooding Along Coral Reef-lined Coasts" (published in this Research Topic: Winter et al.), the formation of the Wave-driven Flood-forecasting on Reef-lined Coasts Early warning system (WaveFoRCE) project (https://geoblueplanet.org/waveforce/), and the creation of this Frontiers in Marine Science Research Topic.

This Research Topic has 8 papers that address a number of the key aspects of the UFORIC goals, which if realized, will lead to the development of tools to accurately predict wave-driven flooding on

OPEN ACCESS

Edited and reviewed by:
Marta Marcos, University of the Balearic Islands, Spain

***Correspondence:**
Curt Storlazzi
cstorlazzi@usgs.gov

Specialty section:
This article was submitted to Coastal Ocean Processes, a section of the journal Frontiers in Marine Science

Received: *30 November 2020*
Accepted: *07 December 2020*
Published: *07 January 2021*

Citation:
Skirving W, Pomeroy A, McCall R, Marra J and Storlazzi C (2021) Editorial: Flooding on Coral Reef-Lined Coasts: Current State of Knowledge and Future Challenges. Front. Mar. Sci. 7:635240. doi: 10.3389/fmars.2020.635240

the order of days, and the development of scenario methodologies, leading to long-term projections of wave-driven flooding on the order of decades.

These key aspects are described in Winter et al. and include an improved understanding of (1) sea level (tidal and non-tidal residuals); (2) offshore wave conditions; (3) nearshore waves and wave-driven water levels; (4) reef accretion, sediment production and reef-to-shore transport; and (5) the development of sedimentary coasts. While 1, 2, and 3 are key for the development of coastal flooding in a short-term forecast, an understanding of all 5 aspects are necessary for the development of future scenarios.

The importance of points 1–3 above are highlighted by Hoeke et al., who compare and contrast flooding events on Tuvalu and Kiribati to identify contributions of regional sea level variations and wave-driven processes to reef-island flooding. Cheriton et al. further our understanding of nearshore waves on reef-lined coasts by studying the occurrence and characteristics of infragravity and very-low frequency waves at seven sites in the Pacific, representing a range of reef geometries. Lastly, Wandres et al. investigate the potential of existing numerical, statistical and empirical models to reproduce wave-driven nearshore hydrodynamics observed on Fiji's Coral Coast. All three papers have implications for the way in which EWS should be set up, as well as for the assessment of the effects of climate change on future flood risk.

Processes that contribute to, shape and influence shallow water bathymetry and beach profiles are discussed by Rosenberger et al., who describe a hydrodynamics and sediment transport study on a fringing reef/lagoon complex in Western Australia. Risandi et al. investigate the influence of reefs on hydrodynamics and how this shapes and modifies the shoreline as offshore waves and water levels vary, by studying a pocket beach in southwestern Australia. David and Schlurmann continue this line of research by investigating the influence of hydrodynamic drivers and their role in the changing sediment volumes of reefs, by studying the sand spit Thoondu, located on Fuvahmulah, Maldives.

The studies described above highlight the variation in coral reef morphology and the role reef morphology has on nearshore hydrodynamics and coastal flooding. Structuring coral reef variability into information that is useful for coastal flooding modeling and EWS is the topic of the contribution of Scott et al. to the Research Topic. In this paper, they describe how they have simplified a large dataset of measured coral reef topobathymetric cross-shore profiles (>30,000) using machine learning and numerical modeling, to develop a set of representative cluster profiles that can accurately be used to describe hydrodynamics (e.g., wave runup) at the shoreline. This technique lends itself to use in global EWS systems such as that being developed by the WaveFoRCE team.

Although only a subset of the knowledge necessary for short term forecasting of wave-driven flood events on coral reef-lined coasts, and the development of accurate long term scenarios, the papers in this Research Topic contribute valuable knowledge to this field. They also provide an insight into the highly complex science behind successful prediction of wave-driven flooding on coral reef-lined coasts throughout the world.

AUTHOR CONTRIBUTIONS

All authors listed have made a substantial, direct and intellectual contribution to the work, and approved it for publication.

FUNDING

This work was partially supported by the U.S. Geological Survey's Coastal and Marine Hazards and Resources Program, NOAA grant NA19NES4320002 (Cooperative Institute for Satellite Earth System Studies) at the University of Maryland/ESSIC, and the U.S. Department of Defense's Strategic Environmental Research and Development Program. The scientific results and conclusions, as well as any views or opinions expressed herein, are those of the author(s) and do not necessarily reflect the views of NOAA or the Department of Commerce.

ACKNOWLEDGMENTS

We thank all authors, reviewers, and editors who have contributed to this Research Topic.

REFERENCES

Storlazzi, C. D. (2018). Challenges of forecasting flooding on coral reef-lined coasts. *Eos* 99. doi: 10.1029/2018EO098517

Conflict of Interest: WS is employed by ReefSense Pty Ltd, and RM is employed by Deltares.

The remaining authors declare that the research was conducted in the absence of any commercial or financial relationships that could be construed as a potential conflict of interest.

Copyright © 2021 Skirving, Pomeroy, McCall, Marra and Storlazzi. This is an open-access article distributed under the terms of the Creative Commons Attribution License (CC BY). The use, distribution or reproduction in other forums is permitted, provided the original author(s) and the copyright owner(s) are credited and that the original publication in this journal is cited, in accordance with accepted academic practice. No use, distribution or reproduction is permitted which does not comply with these terms.

frontiers in Marine Science

PERSPECTIVE
published: 31 March 2020
doi: 10.3389/fmars.2020.00199

Steps to Develop Early Warning Systems and Future Scenarios of Storm Wave-Driven Flooding Along Coral Reef-Lined Coasts

Gundula Winter[1], Curt Storlazzi[2], Sean Vitousek[2], Ap van Dongeren[1], Robert McCall[1], Ron Hoeke[3], William Skirving[4], John Marra[5], Johan Reyns[1], Jerome Aucan[6], Matthew Widlansky[7], Janet Becker[8], Chris Perry[9], Gerd Masselink[10], Ryan Lowe[11], Murray Ford[12], Andrew Pomeroy[11], Fernando Mendez[13], Ana Rueda[13] and Moritz Wandres[14]*

[1] Unit of Marine and Coastal Systems, Deltares, Delft, Netherlands, [2] Pacific Coastal and Marine Science Center, U.S. Geological Survey, Santa Cruz, CA, United States, [3] Sea Level, Waves and Coastal Extremes Group, Commonwealth Scientific and Industrial Research Organisation, Melbourne, VIC, Australia, [4] NESDIS, Center for Satellite Applications and Research, National Oceanic and Atmospheric Administration, Cranbrook, QLD, Australia, [5] NESDIS, National Centers for Environmental Information, National Oceanic and Atmospheric Administration, Honolulu, HI, United States, [6] Laboratory for Studies in Geophysics and Spatial Oceanography, Research Institute for Development, Noumea, New Caledonia, [7] International Pacific Research Center, University of Hawai'i, Honolulu, HI, United States, [8] Department of Mechanical and Aerospace Engineering, University of California, San Diego, San Diego, CA, United States, [9] Department of Geography, University of Exeter, Exeter, United Kingdom, [10] School of Biological and Marine Sciences, University of Plymouth, Plymouth, United Kingdom, [11] UWA Oceans Institute and Oceans Graduate School, The University of Western Australia, Perth, WA, Australia, [12] School of Environment, The University of Auckland, Auckland, New Zealand, [13] Department of Sciences and Techniques in Water and Environment, University of Cantabria, Santander, Spain, [14] Geoscience, Energy and Maritime Division, Pacific Community (SPC), Suva, Fiji

OPEN ACCESS

Edited by:
Juan Jose Munoz-Perez, University of Cádiz, Spain

Reviewed by:
Jennifer M. Brown, National Oceanography Centre, United Kingdom
Yann Balouin, Bureau de Recherches Géologiques et Minières, France

***Correspondence:**
Curt Storlazzi
cstorlazzi@usgs.gov

Specialty section:
This article was submitted to Coastal Ocean Processes, a section of the journal Frontiers in Marine Science

Received: 11 October 2019
Accepted: 13 March 2020
Published: 31 March 2020

Citation:
Winter G, Storlazzi C, Vitousek S, van Dongeren A, McCall R, Hoeke R, Skirving W, Marra J, Reyns J, Aucan J, Widlansky M, Becker J, Perry C, Masselink G, Lowe R, Ford M, Pomeroy A, Mendez F, Rueda A and Wandres M (2020) Steps to Develop Early Warning Systems and Future Scenarios of Storm Wave-Driven Flooding Along Coral Reef-Lined Coasts. Front. Mar. Sci. 7:199. doi: 10.3389/fmars.2020.00199

Tropical coral reef-lined coasts are exposed to storm wave-driven flooding. In the future, flood events during storms are expected to occur more frequently and to be more severe due to sea-level rise, changes in wind and weather patterns, and the deterioration of coral reefs. Hence, disaster managers and coastal planners are in urgent need of decision-support tools. In the short-term, these tools can be applied in Early Warning Systems (EWS) that can help to prepare for and respond to impending storm-driven flood events. In the long-term, future scenarios of flooding events enable coastal communities and managers to plan and implement adequate risk-reduction strategies. Modeling tools that are used in currently available coastal flood EWS and future scenarios have been developed for open-coast sandy shorelines, which have only limited applicability for coral reef-lined shorelines. The tools need to be able to predict local sea levels, offshore waves, as well as their nearshore transformation over the reefs, and translate this information to onshore flood levels. In addition, future scenarios require long-term projections of coral reef growth, reef composition, and shoreline change. To address these challenges, we have formed the UFORiC (Understanding Flooding of Reef-lined Coasts) working group that outlines its perspectives on data and model

requirements to develop EWS for storms and scenarios specific to coral reef-lined coastlines. It reviews the state-of-the-art methods that can currently be incorporated in such systems and provides an outlook on future improvements as new data sources and enhanced methods become available.

Keywords: coral reef, coast, flooding, sea level, waves, Early Warning System, climate-change scenarios

INTRODUCTION

Tropical coral reef-lined coasts are becoming increasingly at risk of local and remotely generated wave-driven flooding. The frequency and severity of these flood events differ regionally depending on local variability and trends in the hydrodynamic forcing such as mean sea level, storm occurrence, and wave climate (e.g., Vitousek et al., 2017a; Reguero et al., 2019). While these challenges are universal for all types of coastlines, communities of reef-lined coasts are facing additional challenges. Firstly, coral reefs are living bio-geomorphic systems whose structure and function highly depend on their health. Globally, reef health is under threat from local stressors, ocean acidification, and global warming (Hoegh-Guldberg et al., 2017; Hughes et al., 2017). The deteriorating state of reefs reduces their natural coastal protection function (Sheppard et al., 2005; Ferrario et al., 2014; Beck et al., 2018) because reefs with reduced structure attenuate less waves (Harris et al., 2018) and because effective reef depth increases through a combination of sea-level rise, slowing rates of vertical reef accretion (Perry et al., 2018), and dredging of reefs for building material as practiced in some island nations. Secondly, when human dwellings and critical infrastructure are located within low-lying coastal plains or atoll rims (e.g., Kumar and Taylor, 2015; Owen et al., 2016), islands are highly vulnerable to flooding events (Beetham and Kench, 2018) with limited options for retreat to higher grounds. Reef-lined coasts can be exposed to highly energetic locally generated wind-sea when they are located within the area of influence of tropical cyclones but also to remotely generated ocean swell (Hoeke et al., 2013). For reef-lined islands exposed to tropical storms (particularly, those situated on a shallow continental shelf), flood levels are further aggravated by high storm-surge levels.

Recent events such as Typhoon Haiyan (Roeber and Bricker, 2015) and widespread flooding of islands due to remotely generated swell in the western Pacific (Hoeke et al., 2013) highlight the need to warn the public of impending coastal flooding events. Short-term forecasts (typically up to 7 days) produced by an Early Warning System (EWS) allow local authorities to issue timely warnings and to coordinate preparedness and evacuation measures, which ultimately reduces risk to lives and assets. Such systems have been implemented in sandy coast environments (e.g., Kleermaeker et al., 2012), but reef-lined coasts demand different modeling approaches due to: (1) the relatively larger importance of infragravity waves (see Bertin et al., 2018 for a recent review on infragravity waves), (2) increased setup over the reef due to its structure (Buckley et al., 2016), and not yet well understood (3) wave breaking on the forereef and (4) reef development, sediment production, and reef-to-shore transport, and (5) the development of the (sedimentary) coastline.

In the next decades, the frequency and severity of extreme sea-level events is predicted to increase, particularly along low-latitude coastlines (Wahl et al., 2017; Vousdoukas et al., 2018). Extreme events may damage both natural and built infrastructure immediately, while less severe but frequent marine flooding may cause salt water contamination of the fresh water lenses, leaving them unusable for human consumption and agriculture. Without adaptation the lack of water and food security is anticipated to be a primary driver that renders many coral reef-lined coasts uninhabitable (Storlazzi et al., 2018). Where coastal adaptation is not feasible, communities will be forced to migrate landward or to relocate elsewhere, potentially causing significant cultural and societal impacts. Building resilience into natural, built, and socio-economic systems requires adequate time for planning and implementation. Understanding future changes in waves and extreme sea levels and resultant flood hazards are key to inform effective coastal adaptation in the long-term (several decades). Hazard scenarios need to provide projections of sea level rise and coral reef state that are long enough to detect trends amongst the annual and decadal variations that will dominate regional sea levels over the next two decades (Wahl et al., 2017).

The development of accurate EWS to forecast short-term coastal hazards and scenario modeling capabilities to project long-term impacts of climate change is critical to support local managers and planners with adequate decision support tools to reduce the current and emerging risk of coastal flooding. At present, numerous factors hinder the development of EWS and long-term modeling tools: Reef-lined coasts remain under-represented in terms of *in situ* data collection and there is a lack of fundamental data on reef morphology, island topography, local sea level, and nearshore wave climate (particular under extreme conditions); and islands are often below the resolution of global models, with little to no higher-resolution regional models available in most of the world. Here, we outline approaches to construct these modeling tools with currently available methods and data and we provide an outlook on potential improvements to these tools as new data and methods become available and point out key research gaps to address.

BACKGROUND: APPROACHES TO STORM-DRIVEN COASTAL FLOOD MODELING FOR REEF-LINED COASTS

The processes to consider for coastal flooding in a short-term forecast (1–3) and a future scenario (1–5) include: (1) sea level

(tidal and non-tidal residuals); (2) offshore wave conditions; (3) nearshore waves and wave-driven water levels; (4) reef accretion, sediment production and reef-to-shore transport; and (5) the development of sedimentary coasts (**Figure 1**).

Modeling Requirements and Available Tools

In the following, we first outline the steps required to build an EWS suited to predict flooding on short-time scales and then we describe the requirements to model projections of future flooding for different climate-change, socio-demographic and coastal management scenarios.

EWS Methodology (Short-Term Predictions, on the Order of Days)

Most of the individual components required to develop a simple prototype EWS for coastal flooding along reef-lined coasts are already available. An EWS needs to link four of the five modules illustrated in **Figure 2** that forecast: (1) sea level (tidal and non-tidal residuals); (2) offshore wave conditions; (3) nearshore waves and wave-driven water levels; (5) coastal flooding; and in more sophisticated models (4) event-driven sediment transport. We next outline the individual modules and the data requirements that are essential to build an EWS.

The local tidal levels for a prototype EWS can presently be predicted through harmonic analysis using tidal constituents derived from tide gauges. For remote locations without tide gauges, tidal water levels are extracted from global tide models that typically integrate satellite altimetry such as FES2014 (Carrere et al., 2015) or TPXO (Egbert and Erofeeva, 2002). More accurate sea-level forecasts need to incorporate sea-level anomalies due to ocean circulations, which are provided operationally on a global and regional scale by an increasing number of institutions (Tonani et al., 2015). Recent developments in the modeling of sea-level anomalies allow even seasonal outlooks (McIntosh et al., 2015) with better skill when results from multiple forecast models are combined (Widlansky et al., 2017). In the long term, technological advances in satellite technology, such as Sentinel-3 (ESA, 2019), ICESat-2 (NASA, 2019b) and the SWOT satellite mission that is to be launched in 2021 (NASA, 2019b), will eventually be able to provide sea-level observations at high spatial resolution and in real-time to be used for data assimilation in operational systems as, for example, currently employed in Lellouche et al. (2018).

Offshore wave heights can currently be provided by operational global wave models such as WaveWatch-III (WW3; Tolman, 2009). Local effects including wave refraction, diffraction, and locally generated wind-sea (e.g., due to tropical cyclones) can be accounted for through regionally downscaled models that make use of numerical techniques such as SWAN (Booij et al., 1999), analytical functions based on linear wave theory, or empirical methods. All downscaling techniques require accurate bathymetry and validation data. More so than in other environments, phasing and directional spectral information of the wave field are important because they influence wave generation in the infragravity (IG) and very low frequency (VLF) bands, which can excite resonance over reef platforms and cause flooding (Péquignet et al., 2009; Roeber and Bricker, 2015). The spectral information to accurately estimate IG and VLF motions may be available from satellites in the future when data from improved satellite altimeters (e.g., SWOT) can be combined with directional spectral data derived from Synthetic-Aperture Radar (SAR) satellite observations (Le Traon et al., 2015). This would improve wave observations currently limited to significant wave heights (e.g., from Sentinel-3).

The output of the offshore wave module is fed into the nearshore module to estimate extreme water levels at the shoreline, for example using the parameterization by Merrifield et al. (2014). As coastal flooding can also be related to wave run-up and overtopping rather than only mean water levels at the shoreline, an improved nearshore wave module would predict wave run-up levels from offshore wave data (e.g., from WW3), for example, using probabilistic or deterministic models such as BEWARE (Pearson et al., 2017) or HyCReWW (Rueda et al., 2019). These models of run-up are parameter-based and require most importantly characteristic reef dimensions such as reef width, depth, slope, and hydrodynamic roughness (reef complexity and/or coral cover) that can be extracted from satellite imagery or automated remote sensing algorithms (e.g., Dekker et al., 2011; Chirayath and Earle, 2016). In the long-term, increasing computational capacity will enable the use of dynamic process-based transect (1D), two-dimensional (2D-horizontal) or fully 3D models in the nearshore module that can also include event-driven sediment and coral rubble transport and resultant morphological updates (Vila-Concejo and Kench, 2017).

In the flood module, the water levels and wave run-up levels from the nearshore module will need to be translated into a meaningful site-specific measure of flooding. Local topographic surveys (e.g., LIDAR) are not available or not in a standardized elevation datum for most reef-island locations. Without these data, water and wave run-up levels can be referenced to the highest high-water level or other benchmark so that end-users can judge the severity of a flood event based on experience. This local knowledge can be systematically surveyed and used in combination with a hindcast of key past events to forecast the likely extent and inundation height of a future flooding event. Globally available topographic data sets such as SRTM (NASA, 2019a) and derived products that improve vertical accuracy (e.g., Kulp and Strauss, 2018) still have insufficient spatial resolution (3 arcseconds) to resolve pathways for flood waters (e.g., channels and small-scale depressions). In the future, improved remote sensing techniques from such satellites as ICESat-2 will provide higher resolution and more accurate topographic and nearshore bathymetric data for detailed flood mapping.

Scenario Methodology (Long-Term Projections, on the Order of Decades)

In order to evaluate different future scenarios of waves and sea-level extremes, modeling capabilities need to be developed to make projections of expected flood levels for the coming decades under these scenarios. These should be key inputs for sustainable coastal adaptation planning that reduce expected sea-level rise impacts. The projection modeling suite will require information from the four modules essential for an EWS (sea

1. Sea level	2. Offshore wave conditions	3. Nearshore waves and water levels	4. Sediment prod. and transport	5. Coastline development
Global Mean Sea Level (GMSL) • Ice melt (mass change) • Steric expansion (volume change) Regional Sea Level (RSL) • GIA/ice sheet melt fingerprints • Inter-decadal variability, e.g. Pacific Decadal Oscillation (PDO) • Inter-annual variability, e.g. El Niño-Southern Oscillation (ENSO) • Seasonal variability • Daily to monthly variability: Ocean weather (barotropic pressure, meso-scale eddies, currents) • Daily to annual variability: Astronomic Tides Regional and Local vertical land motion (VLM) • Gradual and episodic	Wind Sea • Direct hits from tropical cyclones • Trade winds • Local winds Long-period swell • Far-field from extra-tropical and tropical cyclones • Trade winds (Tsunamis • Not subject of this manuscript)	Incident waves (2-25s period) • Refraction around islands • Diffraction • Sheltering • Shoaling • Breaking • Frictional dissipation • Wave setup • Wind waves generated inside the lagoon • Swell waves penetrating into lagoons Infragravity waves (25-250s) • Phasing with incident wave groups • Asymmetry (important for sediment transport and overtopping) Very-low frequency waves (>250s) • Importance for specific range of reefs, 200-400m • Seiching and resonance Storm surge • Duration and height Wave run-up	Bathymetry • Reef width • Reef depth • Forereef steepness • Lagoon width • Number and width of reef channels Coral and coralline algae • Reef development, accretion and erosion • Reef structure, dependent on species assemblage and cover Carbonate sediment • Sediment production • Sediment budget Event-driven sediment transport	Topography • Slope, height, width • Natural and built infrastructure • Erosion, accretion (vertical and horizontal)

FIGURE 1 | Processes relevant to wave-driven coastal flooding, from offshore to onshore: 1. Sea level. 2. Offshore wave conditions. 3. Nearshore waves and wave-driven water levels. 4. Reef development, sediment production, and reef-to-shore transport. 5. Coastline development. The table lists the key drivers of flooding for each of component.

level, wave climate, nearshore wave transformation, and water level over future reef structures). In addition to these data, future projections need to account for the state of reef health, carbonate sediment production and lagged transport to the coastline ("4" in **Figure 2**). Coral reefs exhibit natural variation but ocean warming (Hughes et al., 2017) and local stressors such as land-based sources of pollution, over fishing and disease (e.g., Ban et al., 2014) change reef morphology due to mortality, species selection, and modified growth rates. Thus, projections will need to evaluate different scenarios of climate change (related to ocean warming and rainfall) and socio-economic developments to account for differences in species assemblage, coral cover (and physical roughness), carbonate sediment production, and vertical reef accretion rates that combined with sea level projections determine future reef depths and consequently the coastal protection function of reefs (e.g., Ferrario et al., 2014; Quataert et al., 2015).

Global and regionally downscaled sea-level projections have already been developed (e.g., Kopp et al., 2017), but need to be further downscaled to account for local trends where regional sea-level trends are incoherent as, for example, in the Caribbean (Torres and Tsimplis, 2013). Improved downscaling techniques must include both gradual and episodic vertical land motions, ice-melt fingerprints, and other physical processes (e.g., Kopp et al., 2014). Likewise, global and regional wave-climate projections are already available (e.g., Hemer et al., 2013), but also need to be statistically or dynamically downscaled to a local level. The offshore water level and wave climate can be used in parametric models to transform waves to the nearshore and to calculate water level and wave run-up at the shoreline.

	Availa -bility	Sea Level (SL)	Offshore Waves (OW)	Nearshore Waves and Water Levels (NW)	Sediment Production and Transport (SP)	Flooding/ Coastline Development (CD)
Early Warning System (EWS) components	Now	• Astronomic tide prediction (harmonic analysis)	• Operational global ocean wave models	• Empirical/analytic wave setup and runup formulations for reefs	• Not needed	• Thresholds referenced to highest high tides
	Near future (~5 years)	• Global ocean models with tides and sea surface height anomalies	• Satellite wave height, period, and direction data • Ensemble forecasting	• Probabilistic or deterministic wave transformation models • Wave generation inside lagoons • Swell penetrating into lagoons (high resolution models)	• Not needed	• Threshold system referenced to event thresholds from local knowledge • Measurements of run-up • Database of threshold statistics • Compound flooding
	Mid future (~10 years)	• Integration of observational (satellite and in situ) and model data	• Machine-learned downscaling function for swell • Surface winds from satellite • Directional wave spectra from satellite	• Process-based transect models • Process-based 2D model of nearshore transformations	• Not needed	• Local event thresholds
Scenario components	Now	• Sea surface height projections based on statistical projections	• Wave climate projections	• Empirical/analytic wave setup and runup formulations for reefs	• Sediment production	• Shorelines morphostatic + Bruun (1962) rule
	Near future (~5 years)	• Sea surface height projections from dynamic climate change models	• Statistical or dynamic downscaling wave climate projections	• Probabilistic or deterministic wave transformation models • Wave generation inside lagoons	• Sediment budget and pathways based on coral reef ecosystem projections	• Conceptual shoreline models • Compound flooding
	Mid future (~10 years)	• Add land motions (gradual and episodic) • Add ice melt fingerprints • Include more physics in downscaling model	• Dynamic wave projections	• Process-based transect models • Process-based 2D model of nearshore transformations • Spatially varying reef evolution (depth and roughness)	• Sediment source, transport, and sink evolution based on coral reef ecosystem projections	• Island geomorphic evolution • Projections of future engineering structures

Data requirements

NW: Basic reef morphology data and local winds

CD: Past events from local knowledge/ records to define local event thresholds

All: Higher temporal and spatial resolution satellite data for sea level, waves and beach morphology

OW: Wave buoy data

CD: Historic shoreline change and Sediment layering

SL: Deployment of additional tide gauges with co-located GPS

OW: Intermediate water (30-100 m) bathymetry

NW: Shallow-water (0-30 m) bathymetry and reef rugosity from satellites.

FIGURE 2 | Modules required to develop **(top)** a coastal flood Early Warning System (EWS) and **(bottom)** a scenario modeling tool, which can be implemented immediately (now), in the near-term, and in the long term. Blue boxes on the right describe key data gaps that need to be filled to develop the next generation of EWS or scenario modeling tool.

These parametric models can produce a large set of scenarios to address uncertainties in sea-level and wave-climate projections and to identify key scenarios that can be evaluated with dynamic two-dimensional models. More sophisticated nearshore models need to include local wave growth and hence require wind fields downscaled from global projections. Future scenarios also need to account for changes and uncertainties in coral-reef morphology and species assemblages, which determine wave dynamics on reefs (Baldock et al., 2014) and ultimately nearshore water levels and wave run-up (Quataert et al., 2015).

Simple projections of future flooding often apply a "morphostatic" approach that neglects future shoreline adjustments in response to altered reef states. Application of the simple Bruun (1962) rule to predict beach profile changes in response to sea-level rise are hardly valid because the concept of a "closure depth" developed for open sandy coastlines is not relevant for reef-lined coastlines (Cowell and Kench, 2001). More sophisticated predictive models that account for sediment production and sinks specific to reef-lined coasts will require data on historic shorelines, as well as sediment coring and dating to understand trends in sediment production and accumulation through time (Perry et al., 2018), especially over the past few decades where the impact of recent sea-level rise in many portions of the tropical Pacific Ocean (Becker et al., 2012) can be used to better project future changes. Such models also need to include anthropogenic interventions such as engineering structures that impact upon future shoreline development. Recently, long-term shoreline evolution models have been developed for open-coast sandy beaches with simple configurations (e.g., Vitousek et al., 2017b; Robinet et al., 2018; Antolínez et al., 2019), yet, few studies (e.g., de Alegria-Arzaburu et al., 2013) exist for coral reef-lined beaches, especially at longer time scales. While existing studies of wave-driven evolution of perched beaches might represent a suitable proxy for reef-lined coasts either the dimensions of the submerged barriers are not consistent with coral reefs (e.g., González et al., 1999), the potential effect of infragravity waves has not been considered and/or they provide only conceptual models (e.g., Gallop et al., 2012).

Finally, for such a projection modeling suite to be of value to coastal planners and decision-makers, a selection of relevant scenarios of climate change, sea-level rise, and (local)

socio-economic development is essential to assess different management options.

Overall, future advances in EWS and scenario modeling capabilities may mainly follow from (1) enhanced computational capacity resulting in the use of models that incorporate more physical processes, (2) better parameterization of small-scale processes in these models, (3) improved topographic-bathymetric data, and (4) the integration of more observational data, which may be sourced through remote sensing, low-cost monitoring or citizen science. Detailed data requirements for these future advances are:

- Better spatial coverage with tide gauges, particularly with co-located GPS receivers that identify local land subsidence or uplift at the shoreline;
- Better coverage with wave buoys, especially in the southern hemisphere;
- Nearshore bathymetry between the 100 and 10 m isobaths for downscaling of wave data;
- Direct observations of wave run-up to improve our understanding of the physical processes relevant to run-up onshore of coral reefs and to calibrate and validate models, particularly during extreme events;
- High (approximately 2 m horizontal) spatial resolution bathymetry and topography between 10 m depths and 10 m land elevations; as well as habitat maps for wave modeling and forecasting of absolute flood levels and extents; and
- Historical analysis of flood events and impacts to validate EWS.

To develop more accurate forecasts tools, research needs to address the following knowledge gaps:

- Improved downscaling techniques for offshore waves, possibly through development of machine-learning algorithms, to downscale global wave projections (not unique to reef-lined coasts);
- Better estimates of vertical reef growth rates under different ecological states of the reef to project future water depth on the reef with sea-level rise, which is a governing parameter for wave dissipation over the reef and wave run-up at the shoreline;
- Quantification of carbonate sediment production and transport, which is still little researched but important for projections of shoreline configurations.
- Physically based roughness parameterization from coral cover and reef benthic complexity in dynamic models because current models simply scale friction formulations developed for sandy beds and do not account for energy dissipation within the coral canopy;
- Better understanding of wave breaking over reefs, which has been little researched due to the difficult instrumentation of the surf zone on reefs but which controls wave setup, VLF and IG motions, residual sea-swell wave heights onshore of the reef, and wave run-up;
- Better understanding of the importance of infragravity, very-low frequency waves, and seiching to flooding along reef-lined coasts, which has been documented for selected extreme events (e.g., Péquignet et al., 2009; Roeber and Bricker, 2015) to inform the selection of an appropriate nearshore wave model;
- Better understanding of the importance of two-dimensional wave processes that can drive alongshore variability in wave run-up in coral reef-lined coastlines to evaluate the need for a fully two-dimensional nearshore model.

WAY FORWARD

To address the urgent need for coastal flooding EWS and future scenario modeling tools, the UFORiC (Understanding Flooding Of Reef-lined Coasts) working group has been established. This group has committed to meet regularly to advance and update work plans. The ultimate goal of this working group is to develop the tools and research that aid disaster risk management and climate change adaptation in coral reef-lined coasts. A priority of UFORiC is to establish links with national meteorological services and emergency managers, as well as other stakeholders such as development banks and insurance companies. The development of EWS and scenario modeling tools requires a multi-disciplinary research effort, and thus the UFORiC working group includes leading coastal engineers, physical oceanographers, geologists, geographers, ecologists, remote-sensing specialists, and climate-change scientists. The effective implementation of these tools would be aided by training on data acquisition, management and interpretation (e.g., Cambers and Diamond, 2010).

AUTHOR CONTRIBUTIONS

CS, AD, RM, RH, WS, and JM contributed to the conception and design of the study. GW, CS, and SV wrote the first draft of the manuscript. All authors contributed to manuscript revision, read, and approved the submitted version.

FUNDING

This research is a product of the UFORiC working group, which was supported by the National Oceanic and Atmospheric Administration (NOAA), the U.S. Geological Survey (USGS), Deltares, and the Commonwealth Scientific and Industrial Research Organisation (CSIRO), and under the auspices of the Group on Earth Observations (GEO) Blue Planet initiative. The scientific results and conclusions, as well as any views or opinions expressed herein, are those of the author(s) and do not necessarily reflect the views of NOAA or the Department of Commerce. Use of trademark names does not imply US Government endorsement of products.

REFERENCES

Antolínez, J. A. A., Méndez, F. J., Anderson, D., Ruggiero, P., and Kaminsky, G. M. (2019). Predicting climate-driven coastlines with a simple and efficient multiscale model. *J. Geophys. Res. Earth Surf.* 124, 1596–1624. doi: 10.1029/2018jf004790

Baldock, T. E., Golshani, A., Callaghan, D. P., Saunders, M. I., and Mumby, P. J. (2014). Impact of sea-level rise and coral mortality on the wave dynamics and wave forces on barrier reefs. *Mar. Pollut. Bull.* 83, 155–164. doi: 10.1016/j.marpolbul.2014.03.058

Ban, S. S., Graham, N. A. J., and Connolly, S. R. (2014). Evidence for multiple stressor interactions and effects on coral reefs. *Glob. Chang. Biol.* 20, 681–697. doi: 10.1111/gcb.12453

Beck, M. W., Losada, I. J., Menéndez, P., Reguero, B. G., Díaz-Simal, P., and Fernández, F. (2018). The global flood protection savings provided by coral reefs. *Nat. Commun.* 9:2186. doi: 10.1038/s41467-018-04568-z

Becker, M., Meyssignac, B., Letetrel, C., Llovel, W., Cazenave, A., and Delcroix, T. (2012). Sea level variations at tropical Pacific islands since 1950. *Glob. Planet. Change* 8, 85–98. doi: 10.1016/j.gloplacha.2011.09.004

Beetham, E., and Kench, P. S. (2018). Predicting wave overtopping thresholds on coral reef-island shorelines with future sea-level rise. *Nat. Commun.* 9:3997. doi: 10.1038/s41467-018-06550-1

Bertin, X., Bakker, A. D., Dongeren, A. V., Coco, G., André, G., Ardhuin, F., et al. (2018). Infragravity waves: from driving mechanisms to impacts. *Earth Sci. Rev.* 177, 774–799. doi: 10.1016/j.earscirev.2018.01.002

Booij, N., Ris, R., and Holthuijsen, L. H. (1999). A third-generation wave model for coastal regions: 1. Model description and validation. *J. Geophys. Res. Oceans* 104, 7649–7666. doi: 10.1029/98JC02622

Bruun, P. (1962). Sea-level rise as a cause of shore erosion. *J. Waterways Harb. Div.* 88, 117–132.

Buckley, M. L., Lowe, R. J., Hansen, J. E., and Van Dongeren, A. R. (2016). Wave setup over a fringing reef with large bottom roughness. *J. Phys. Oceanogr.* 46, 2317–2333. doi: 10.1175/JPO-D-15-0148.1

Cambers, G., and Diamond, P. (2010). *Sandwatch: Adapting to Climate Change and Educating for Sustainable Development*. Paris: UNESCO.

Carrere, L., Lyard, F., Cancet, M., and Guillot, A. (2015). "FES 2014, a new tidal model on the global ocean with enhanced accuracy in shallow seas and in the Arctic region," in *Proceedings EGU General Assembly Conference Abstracts* (Vienna: EGU General Assembly).

Chirayath, V., and Earle, S. A. (2016). Drones that see through waves–preliminary results from airborne fluid lensing for centimetre-scale aquatic conservation. *Aquat. Conserv.* 26, 237–250. doi: 10.1002/aqc.2654

Cowell, P. J., and Kench, P. S. (2001). The morphological response of atoll islands to sea-level rise. Part 1: modifications to the shoreface translation model. *J. Coast. Res. Spec. Issue* 34, 633–644.

de Alegria-Arzaburu, A. R., Mariño-Tapia, I., Enriquez, C., Silva, R., and González-Leija, M. (2013). The role of fringing coral reefs on beach morphodynamics. *Geomorphology* 198, 69–83. doi: 10.1016/j.geomorph.2013.05.013

Dekker, A. G., Phinn, S. R., Anstee, J., Bissett, P., Brando, V. E., Casey, B., et al. (2011). Intercomparison of shallow water bathymetry, hydro-optics, and benthos mapping techniques in Australian and Caribbean coastal environments. *Limnol. Oceanogr. Methods* 9, 396–425. doi: 10.4319/lom.2011.9.396

ESA (2019). *European Space Agency: Sentinel-3 Mission Overview*. Available online at: https://sentinel.esa.int/web/sentinel/missions/sentinel-3 (accessed March 15, 2019).

Egbert, G. D., and Erofeeva, S. Y. (2002). Efficient inverse modeling of Barotropic ocean tides. *J. Atmos. Ocean. Technol.* 19, 183–204. doi: 10.1175/1520-0426(2002)019<0183:eimobo>2.0.co;2

Ferrario, F., Beck, M. W., Storlazzi, C. D., Micheli, F., Shepard, C. C., and Airoldi, L. (2014). The effectiveness of coral reefs for coastal hazard risk reduction and adaptation. *Nat. Commun.* 5:3794. doi: 10.1038/ncomms4794

Gallop, S. L., Bosserelle, C., Eliot, I., and Pattiaratchi, C. B. (2012). The influence of limestone reefs on storm erosion and recovery of a perched beach. *Cont. Shelf Res.* 47, 16–27. doi: 10.1016/j.csr.2012.08.001

González, M., Medina, R., and Losada, M. A. (1999). Equilibrium beach profile model for perched beaches. *Coast. Eng.* 36, 343–357. doi: 10.1016/S0378-3839(99)00018-6

Harris, D. L., Rovere, A., Casella, E., Power, H., Canavesio, R., Collin, A., et al. (2018). Coral reef structural complexity provides important coastal protection from waves under rising sea levels. *Sci. Adv.* 4:eaao4350. doi: 10.1126/sciadv.aao4350

Hemer, M. A., Fan, Y., Mori, N., Semedo, A., and Wang, X. L. (2013). Projected changes in wave climate from a multi-model ensemble. *Nat. Clim. Chang.* 3, 471–476. doi: 10.1038/nclimate1791

Hoegh-Guldberg, O., Poloczanska, E. S., Skirving, W., and Dove, S. (2017). Coral reef ecosystems under climate change and ocean acidification. *Front. Mar. Sci.* 4:158. doi: 10.3389/fmars.2017.00158

Hoeke, R. K., McInnes, K. L., Kruger, J. C., McNaught, R. J., Hunter, J. R., and Smithers, S. G. (2013). Widespread inundation of Pacific islands triggered by distant-source wind-waves. *Glob. Planet. Change* 108, 128–138. doi: 10.1016/j.gloplacha.2013.06.006

Hughes, T. P., Barnes, M. L., Bellwood, D. R., Cinner, J. E., Cumming, G. S., Jackson, J. B. C., et al. (2017). Coral reefs in the Anthropocene. *Nature* 546, 82–90. doi: 10.1038/nature22901

Kleermaeker, S., Verlaan, M., Kroos, J., and Zijl, F. (2012). "A new coastal flood forecasting system for the Netherlands," in *Proceedings of the Hydro12 - Taking Care of the Sea* (Heeg: Hydrographic Society Benelux).

Kopp, R. E., DeConto, R. M., Bader, D. A., Hay, C. C., Horton, R. M., Kulp, S., et al. (2017). Evolving understanding of Antarctic ice-sheet physics and ambiguity in probabilistic sea-level projections. *Earths Future* 5, 1217–1233. doi: 10.1002/2017ef000663

Kopp, R. E., Horton, R. M., Little, C. M., Mitrovica, J. X., Oppenheimer, M., Rasmussen, D. J., et al. (2014). Probabilistic 21st and 22nd century sea-level projections at a global network of tide-gauge sites. *Earths Future* 2, 383–406. doi: 10.1002/2014EF000239

Kulp, S. A., and Strauss, B. H. (2018). CoastalDEM: A global coastal digital elevation model improved from SRTM using a neural network. *Remote Sens. Environ.* 206, 231–239. doi: 10.1016/j.rse.2017.12.026

Kumar, L., and Taylor, S. (2015). Exposure of coastal built assets in the South Pacific to climate risks. *Nat. Clim. Chang.* 5:992. doi: 10.1038/nclimate2702

Le Traon, P. Y., Antoine, D., Bentamy, A., Bonekamp, H., Breivik, L. A., Chapron, B., et al. (2015). Use of satellite observations for operational oceanography: recent achievements and future prospects. *J. Oper. Oceanogr.* 8, s12–s27. doi: 10.1080/1755876X.2015.1022050

Lellouche, J. M., Greiner, E., Le Galloudec, O., Garric, G., Regnier, C., Drevillon, M., et al. (2018). Recent updates to the Copernicus Marine Service global ocean monitoring and forecasting real-time 1/12° high-resolution system. *Ocean Sci.* 14, 1093–1126. doi: 10.5194/os-14-1093-2018

McIntosh, P. C., Church, J. A., Miles, E. R., Ridgway, K., and Spillman, C. M. (2015). Seasonal coastal sea level prediction using a dynamical model. *Geophys. Res. Lett.* 42, 6747–6753. doi: 10.1002/2015GL065091

Merrifield, M. A., Becker, J. M., Ford, M., and Yao, Y. (2014). Observations and estimates of wave-driven water level extremes at the Marshall Islands. *Geophys. Res. Lett.* 41, 7245–7253. doi: 10.1002/2014GL061005

NASA (2019a). *Jet Propulsion Laboratory: Shuttle Radar Topography Mission*. Available online at: https://www2.jpl.nasa.gov/srtm/ (accessed March 15, 2019).

NASA (2019b). *Jet Propulsion Laboratory: Surface Water and Ocean Topography Mission*. Available online at: https://swot.jpl.nasa.gov/ (accessed March 15, 2019).

Owen, S. D., Kench, P. S., and Ford, M. (2016). Improving understanding of the spatial dimensions of biophysical change in atoll island countries and implications for island communities: a Marshall Islands' case study. *Appl. Geogr.* 72, 55–64. doi: 10.1016/j.apgeog.2016.05.004

Pearson, S. G., Storlazzi, C. D., van Dongeren, A. R., Tissier, M. F. S., and Reniers, A. J. H. M. (2017). A bayesian-based system to assess wave-driven flooding hazards on coral reef-lined coasts. *J. Geophys. Res. Oceans* 122, 10099–10117. doi: 10.1002/2017JC013204

Péquignet, A. C. N., Becker, J. M., Merrifield, M. A., and Aucan, J. (2009). Forcing of resonant modes on a fringing reef during tropical storm Man-Yi. *Geophys. Res. Lett.* 36:L03607. doi: 10.1029/2008GL036259

Perry, C. T., Alvarez-Filip, L., Graham, N. A. J., Mumby, P. J., Wilson, S. K., Kench, P. S., et al. (2018). Loss of coral reef growth capacity to track future increases in sea level. *Nature* 558, 396–400. doi: 10.1038/s41586-018-0194-z

Quataert, E., Storlazzi, C., van Rooijen, A., Cheriton, O., and van Dongeren, A. C. G. L. (2015). The influence of coral reefs and climate change on wave-driven flooding of tropical coastlines. *Geophys. Res. Lett.* 42, 6407–6415. doi: 10.1002/2015gl064861

Reguero, B. G., Losada, I. J., and Méndez, F. J. (2019). A recent increase in global wave power as a consequence of oceanic warming. *Nat. Commun.* 10:205. doi: 10.1038/s41467-018-08066-0

Robinet, A., Idier, D., Castelle, B., and Marieu, V. (2018). A reduced-complexity shoreline change model combining longshore and cross-shore processes: the LX-Shore model. *Environ. Model. Softw.* 109, 1–16. doi: 10.1016/j.envsoft.2018.08.010

Roeber, V., and Bricker, J. D. (2015). Destructive tsunami-like wave generated by surf beat over a coral reef during Typhoon Haiyan. *Nat. Commun.* 6:7854. doi: 10.1038/ncomms8854

Rueda, A., Cagigal, L., Pearson, S. G., Antolinez, J. A. A., Storlazzi, C. D., van Dongeren, A., et al. (2019). HyCReWW: a hybrid coral reef waves and water level metamodel. *Comput. Geosci.* 127, 85–90. doi: 10.1016/j.cageo.2019.03.004

Sheppard, C., Dixon, D. J., Gourlay, M., Sheppard, A., and Payet, R. (2005). Coral mortality increases wave energy reaching shores protected by reef flats: examples from the Seychelles. *Estuar. Coast. Shelf Sci.* 64, 223–234. doi: 10.1016/j.ecss.2005.02.016

Storlazzi, C. D., Gingerich, S. B., van Dongeren, A., Cheriton, O. M., Swarzenski, P. W., Quataert, E., et al. (2018). Most atolls will be uninhabitable by the mid-21st century because of sea-level rise exacerbating wave-driven flooding. *Sci. Adv.* 4:eaap9741. doi: 10.1126/sciadv.aap9741

Tolman, H. L. (2009). *User manual and system documentation of WAVEWATCH III TM version 3.14*. Silver Spring, MD: NOAA.

Tonani, M., Balmaseda, M., Bertino, L., Blockley, E., Brassington, G., Davidson, F., et al. (2015). Status and future of global and regional ocean prediction systems. *J. Oper. Oceanogr.* 8, s201–s220. doi: 10.1080/1755876X.2015.1049892

Torres, R. R., and Tsimplis, M. N. (2013). Sea-level trends and interannual variability in the Caribbean Sea. *J. Geophys. Res. Oceans* 118, 2934–2947. doi: 10.1002/jgrc.20229

Vila-Concejo, A., and Kench, P. (2017). Storms in coral reefs. *Coast. Storms Process. Impacts* 127–149. doi: 10.1002/9781118937099.ch7

Vitousek, S., Barnard, P. L., Fletcher, C. H., Frazer, N., Erikson, L., and Storlazzi, C. D. (2017a). Doubling of coastal flooding frequency within decades due to sea-level rise. *Sci. Rep.* 7:1399. doi: 10.1038/s41598-017-01362-7

Vitousek, S., Barnard, P. L., Limber, P., Erikson, L., and Cole, B. (2017b). A model integrating longshore and cross-shore processes for predicting long-term shoreline response to climate change. *J. Geophys. Res. Earth Surf.* 122, 782–806. doi: 10.1002/2016JF004065

Vousdoukas, M. I., Mentaschi, L., Voukouvalas, E., Verlaan, M., Jevrejeva, S., Jackson, L. P., et al. (2018). Global probabilistic projections of extreme sea levels show intensification of coastal flood hazard. *Nat. Commun.* 9:2360. doi: 10.1038/s41467-018-04692-w

Wahl, T., Haigh, I. D., Nicholls, R. J., Arns, A., Dangendorf, S., Hinkel, J., et al. (2017). Understanding extreme sea levels for broad-scale coastal impact and adaptation analysis. *Nat. Commun.* 8:16075. doi: 10.1038/ncomms16075

Widlansky, M. J., Marra, J. J., Chowdhury, M. R., Stephens, S. A., Miles, E. R., Fauchereau, N., et al. (2017). Multimodel ensemble sea level forecasts for tropical pacific islands. *J. Appl. Meteorol. Climatol.* 56, 849–862. doi: 10.1175/JAMC-D-16-0284.1

Conflict of Interest: The authors declare that the research was conducted in the absence of any commercial or financial relationships that could be construed as a potential conflict of interest.

Copyright © 2020 Winter, Storlazzi, Vitousek, van Dongeren, McCall, Hoeke, Skirving, Marra, Reyns, Aucan, Widlansky, Becker, Perry, Masselink, Lowe, Ford, Pomeroy, Mendez, Rueda and Wandres. This is an open-access article distributed under the terms of the Creative Commons Attribution License (CC BY). The use, distribution or reproduction in other forums is permitted, provided the original author(s) and the copyright owner(s) are credited and that the original publication in this journal is cited, in accordance with accepted academic practice. No use, distribution or reproduction is permitted which does not comply with these terms.

frontiers in Marine Science

ORIGINAL RESEARCH
published: 25 May 2020
doi: 10.3389/fmars.2020.00361

Hydro-Morphological Characterization of Coral Reefs for Wave Runup Prediction

Fred Scott[1,2]*, *Jose A. A. Antolinez*[1], *Robert McCall*[1], *Curt Storlazzi*[3], *Ad Reniers*[4] and *Stuart Pearson*[4,1]

[1] Unit Marine and Coastal Systems, Deltares, Delft, Netherlands, [2] W.F. Baird & Associates, Oakville, ON, Canada, [3] U.S. Geological Survey, Santa Cruz, CA, United States, [4] Department of Hydraulic Engineering, Faculty of Civil Engineering and Geosciences, Delft University of Technology, Delft, Netherlands

Many coral reef-lined coasts are low-lying with elevations <4 m above mean sea level. Climate-change-driven sea-level rise, coral reef degradation, and changes in storm wave climate will lead to greater occurrence and impacts of wave-driven flooding. This poses a significant threat to their coastal communities. While greatly at risk, the complex hydrodynamics and bathymetry of reef-lined coasts make flood risk assessment and prediction costly and difficult. Here we use a large (>30,000) dataset of measured coral reef topobathymetric cross-shore profiles, statistics, machine learning, and numerical modeling to develop a set of representative cluster profiles (RCPs) that can be used to accurately represent the shoreline hydrodynamics of a large variety of coral reef-lined coasts around the globe. In two stages, the large dataset is reduced by clustering cross-shore profiles based on morphology and hydrodynamic response to typical wind and swell wave conditions. By representing a large variety of coral reef morphologies with a reduced number of RCPs, a computationally feasible number of numerical model simulations can be done to obtain wave runup estimates, including setup at the shoreline and swash separated into infragravity and sea-swell components, of the entire dataset. The predictive capability of the RCPs is tested against 5,000 profiles from the dataset. The wave runup is predicted with a mean error of 9.7–13.1%, depending on the number of cluster profiles used, ranging from 312 to 50. The RCPs identified here can be combined with probabilistic tools that can provide an enhanced prediction given a multivariate wave and water level climate and reef ecology state. Such a tool can be used for climate change impact assessments and studying the effectiveness of reef restoration projects, as well as for the provision of coastal flood predictions in a simplified (global) early warning system.

Keywords: data mining, cluster analysis, K-means, coral reefs, wave runup, XBeach

OPEN ACCESS

Edited by:
Juan Jose Munoz-Perez, University of Cádiz, Spain

Reviewed by:
Rodolfo Silva, National Autonomous University of Mexico, Mexico
Pushpa Dissanayake, University of Kiel, Germany

***Correspondence:**
Fred Scott
fredscott10@gmail.com

Specialty section:
This article was submitted to Coastal Ocean Processes, a section of the journal Frontiers in Marine Science

Received: *31 January 2020*
Accepted: *28 April 2020*
Published: *25 May 2020*

Citation:
Scott F, Antolinez JAA, McCall R, Storlazzi C, Reniers A and Pearson S (2020) Hydro-Morphological Characterization of Coral Reefs for Wave Runup Prediction. Front. Mar. Sci. 7:361. doi: 10.3389/fmars.2020.00361

1. INTRODUCTION

Flooding of coral reef-lined coasts affects thousands of vulnerable communities around the world, and climate change induced sea level rise (SLR) and coral degradation are going to continue to intensify the magnitude and frequency of hazardous flooding events (Ferrario et al., 2014; Quataert et al., 2015; Storlazzi et al., 2015; Vitousek et al., 2017).

The low elevations of most coral reef-lined coasts increase the relative influence of the incoming swell waves and therefore make them extremely susceptible to flooding, especially during tropical

cyclones or "blue-sky" events. "Blue-sky" events refer to the idea that large waves and potential flooding can occur even when the weather seems calm due to the arrival of remotely generated swell waves (Hoeke et al., 2013). Swell results in wave setup (Longuet-Higgins and Stewart, 1964) and typically generates infragravity waves (Pomeroy et al., 2012), amplifying wave runup at the shoreline and potentially causing flooding.

In addition, the impact of flooding is growing due to socioeconomic development within flood-prone zones, where unplanned urbanization is leading to a higher likelihood of flood-related deaths (Chilunga et al., 2017). The increase in exposure and vulnerability requires that inhabitants have sufficient warning in order to increase preparedness and implement flood mitigation measures. Unfortunately, for millions of people living in areas at risk of coastal flooding (UNFPA, 2014), the vast majority have no early warning system (EWS) in place due to high cost and/or the required technology. This problem has gained worldwide attention, and as a result the United Nations-endorsed Sendai Framework for Disaster Risk Reduction has called for the improved access to early warning systems and disaster risk assessments by 2030 (UNISDR, 2015). A simple, globally applicable tool to better understand and forecast wave runup will enhance access to early warnings of flood events and will, in turn, increase coastal resilience for numerous communities around the globe.

Wave-driven flooding can be forecast based on the expected wave runup at the beach. Wave runup is the discrete water-level elevation maxima, measured in the foreshore, with respect to still water level (Hunt, 1959). If the wave runup is greater than the beach crest elevation, overtopping will occur (**Figure 1A**), which if sustained poses a threat of flooding for the area behind the beach. A common measure of wave runup used in engineering applications is the 2% exceedence value ($R_{2\%}$) (Holman, 1986). This value is widely used for scaling the impacts of, for example, severe storms on sandy beaches (Sallenger, 2000; Stockdon et al., 2006). Wave runup is mainly dependent on the morphology (relative to the surge level) and offshore wave conditions.

Field measurements have quantified wave dynamics and wave-driven water levels on fringing coral reefs (Hardy and Young, 1996; Cheriton et al., 2016) and shown the complexity of the hydrodynamics in these systems (Storlazzi et al., 2004). The complex interaction between the reef morphology and the hydrodynamics on the reef has so far hampered the development of reliable parametric estimates of wave runup on reef-lined coasts.

In view of this complexity, numerical models are typically used to obtain estimates of wave runup at the shoreline. Numerical models can account for these hydrodynamic interactions, and can be applied to estimate extreme conditions that have never been measured, but are likely to happen or expected in a plausible future scenario (e.g., Anderson et al., 2019). Coral reef hydrodynamics have been modeled extensively (Storlazzi et al., 2011; van Dongeren et al., 2013; Buckley et al., 2014; Bosserelle et al., 2015; Lashley et al., 2018) with good predictive skill.

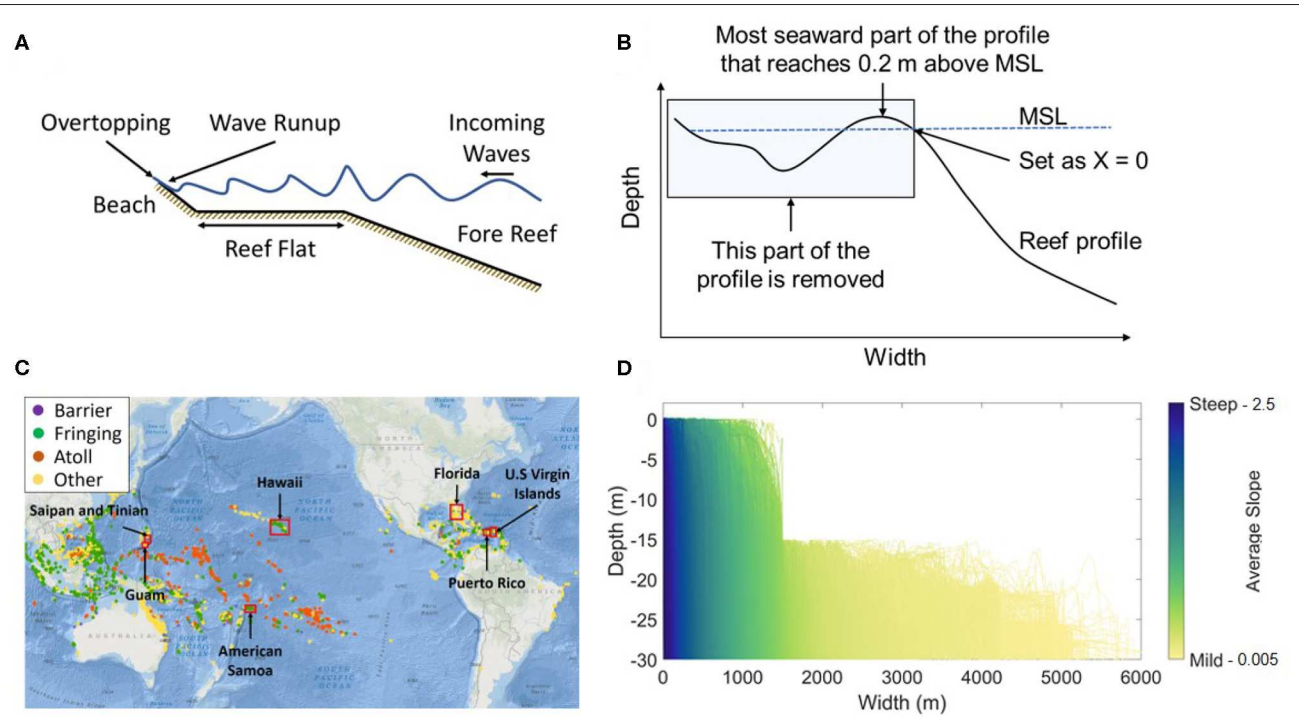

FIGURE 1 | Coral reef profile dataset information including **(A)** a schematic of a typical fringing reef demonstrating wave runup and overtopping from incoming waves, **(B)** an example of how the reference point (X = 0) was set at MSL for aligning the cross-shore profiles, **(C)** a map of the locations where the coral reef topobathymetric cross-shore profiles in the dataset have been collected (ReefBase, 2019; Storlazzi et al., 2019), and **(D)** the selected cross-shore profiles for the study plotted and colored based on their average slope which range from 0.005 to 2.5.

However, each simulation of a deterministic process-based model provides only the results for the specific bathymetry included in the simulation. Coral reefs have a wide range of morphologies (**Figure 1D**), and each are exposed to variable hydrodynamic conditions. Therefore, the results from a single model simulation are highly location-specific, and far from being universally-applicable. Modeling each and every morphology individually, however, would be computationally extremely impractical and unnecessary since two reef profiles similar in shape would be expected to have similar hydrodynamic responses under the same hydrodynamic conditions (e.g., water level, wave, and wind characteristics), forming a set of redundant model runs. In that case, one of the reef profiles could be simulated in a model and used as an estimate of wave runup for the other.

To increase the applicability of numerical model wave runup predictions, Pearson et al. (2017) developed the "Bayesian Estimator for Wave Attack in Reef Environments" (BEWARE). BEWARE makes use of parameterized fringing coral reef profiles (beach slope, reef flat width, and fore reef slope) and hydrodynamic conditions (water depth, wave height, and wave period) to generate a synthetic database of wave runup. The database includes the results of the thousands of combinations of values for each profile parameter and offshore forcing conditions. After training the Bayesian Network (BN) with the synthetic database, it acts as an emulator or surrogate for the numerical model and provides a probabilistic estimate of wave runup for real-world coral reef profiles based on the similarity of morphology and wave conditions to that stored in the database. The database has been useful for other reanalysis studies (Pearson et al., 2018; Rueda et al., 2019b), but there are limitations that come with it. Only simplified cross-shore profiles characteristic of a fringing reef can be used (e.g., **Figure 1A**), and it is not representative of the global diversity of reef morphology.

This paper attempts to build upon the work of Pearson et al. (2017) by providing a methodology to account for the global variety in coral reef morphology, and their characteristic hydrodynamic response (wave runup) to offshore forcing conditions which can be used instead of the simplified cross-shore profiles in improved versions of the BEWARE model. We combine machine learning, statistics, and simulated swash dynamics using the XBeach Non Hydrostatic (XBNH) numerical model (Smit et al., 2010; McCall et al., 2014) to reduce the high diversity of coral reef topo-bathymetric profiles (>30,000) into a set of 50–312 representative cluster profiles (RCPs). We also propose a simplified approach to characterize the hydrodynamic response for any real-world coral reef cross-shore profile in terms of the simulated response of the RCPs. The methodology developed in this paper is designed to be transferable to other coastal environments, providing numerous opportunities and applications in large-scale wave runup simulation and EWSs.

Section 2 of this manuscript introduces the coral reef dataset. Section 3 describes the methodology to classify the RCPs and how to use them as a forecasting tool. Section 4 presents the results of each methodological step and of an application test case. Section 5 includes a discussion on the sensitivities of the machine learning, statistical, and numerical tools used for the development of this research, as well as the implications of the results obtained in further applications such as EWS and climate change assessment studies. Finally, we summarize the main conclusions of this research in section 6.

TABLE 1 | Spatial distribution of coral reef topobathymetric cross-shore profiles included in the initial dataset, as well as the number of profiles from each location included in the study.

Location	Profiles	Percent of total profiles (%)	Profiles omitted in Step 0	Profiles used in Steps 1–4
American Samoa	1,198	4.0	21	1,177
Saipan and Tinian	1,035	3.4	126	909
Guam	1,295	4.3	50	1,245
USVI	1,664	5.5	532	1,132
Hawaii	13,404	44.4	1,395	12,009
Puerto Rico	5,531	18.3	2,604	2,927
Florida	6,039	20.0	4,984	1,055
Total	30,166	–	9,712	20,454

2. CORAL REEF DATASET

The data used for this study consists of 30,166 measured coral reef topobathymetric cross-shore profiles (Storlazzi et al., 2019) from seven regions distributed through the Pacific Ocean, Atlantic Ocean, and Caribbean Sea (**Figure 1C**), measured between 2001 and 2016. The geographical distribution of the reef profiles is provided in **Table 1**.

The profiles are aligned by taking the 0 m elevation contour with respect to mean sea level (MSL) as the shoreline reference point. Measured data points were homogenized in an uniform one-dimensional grid spaced 2 m going seaward from the shoreline. A summary of the profile dataset focusing on nearshore averaged slope geometry (computed between shoreline and 30 m depth) is presented in **Figure 1D**. This dataset was then filtered using procedures explained in section 3.1.

3. DEVELOPMENT OF REPRESENTATIVE CLUSTER PROFILES (RCPS) FOR CORAL REEFS

To create the set of representative profiles, unsupervised cluster analysis techniques were used with the coral reef morphology and results from XBNH as inputs. The representative profiles were then tested to determine their predictive skill. The steps of the methodology are detailed in this section and are illustrated in **Figure 2**.

3.1. Step 0: Data Pre-processing and Filtering

The profiles included in the analysis were carefully selected to ensure that they resembled a reef in front of habitable land, and were not too wide so that they could accurately be modeled with XBNH. These criteria are explained in greater detail below.

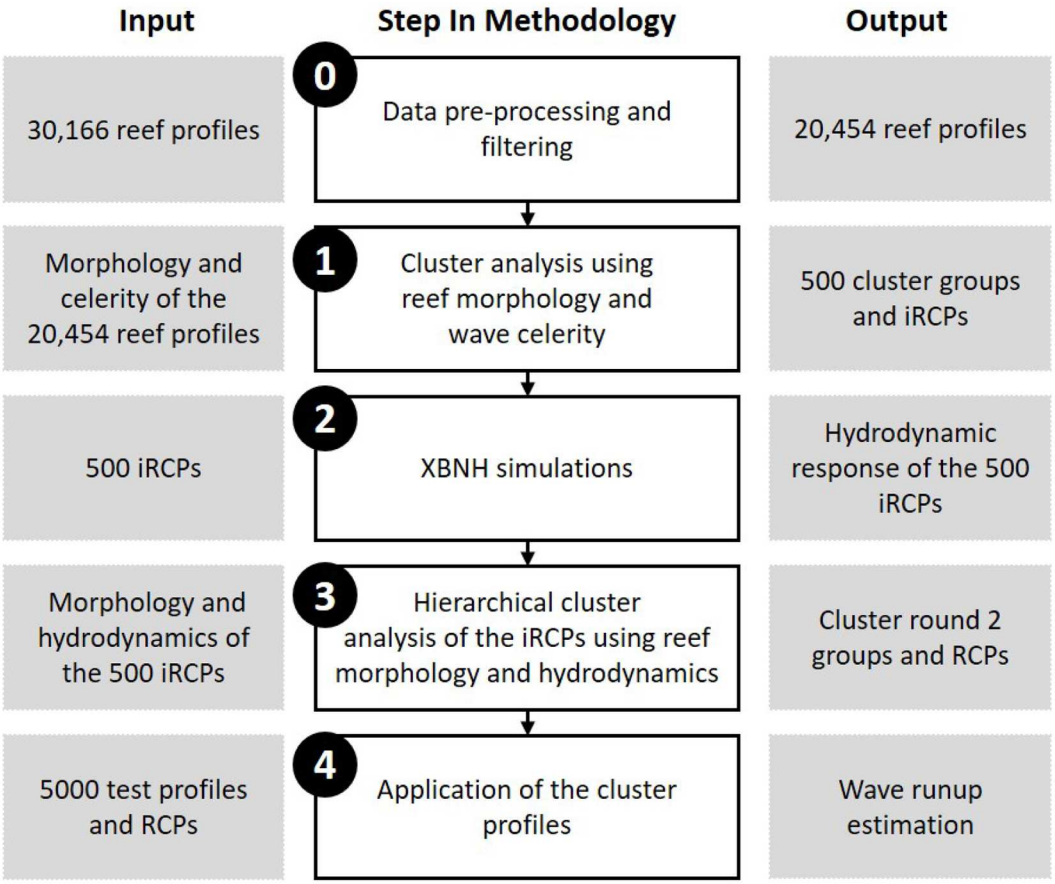

FIGURE 2 | The methodology used to reduce the initial dataset of coral reef topobathymetric cross-shore profiles to the representative cluster profiles (RCPs). Steps 0 and 1 highlight the first data reduction step to create the 500 initial representative cluster profiles (iRCPs), Steps 2 and 3 are used to further cluster the profiles and to form the final RCPs, and Step 4 includes using the RCPs for wave runup prediction.

Firstly, land was classified as the most seaward part of the profile with an elevation greater than or equal to 0.2 m above MSL, as detailed in **Figure 1B**. Low-lying coral islands have mean elevations around 2 m above present sea level (Storlazzi et al., 2018), so a value of 0.2 m is relatively low. However, if a greater threshold was used, multiple cross-shore profiles included an offshore protruding segment that was deemed unrealistic. These would have a major impact on the wave transformation over the reef and so for the purpose of this study a lower threshold of 0.2 m was used.

Secondly, the width limitation was set to ensure that all profiles included in the analysis could be accurately modeled using a one-dimensional XBNH model. Any profiles which reach -15 m depth at widths greater than 1.5 km (i.e., 10–20 wave lengths from the shoreline) were deemed too wide to accurately model, as one-dimensional XBNH models do not account for wind input, or large-scale topographic refraction. These 9,712 profiles, mostly from Florida (**Table 1**), were therefore removed from the dataset, resulting in 20,454 profiles to be used in Steps 1–4 of this study. The selected profiles for Steps 1–4 are shown in **Figure 1D**, colored based on their average slope.

3.2. Step 1: Data Reduction Using Reef Morphology and Wave Celerity

3.2.1. Cluster Analysis

To group the similar coral reef profiles and identify dominant RCPs, unsupervised machine learning was applied on the reef topobathymetric cross-shore profiles resulting from Step 0. In particular, we applied cluster analysis which is used to group a collection of objects into smaller subsets or clusters. The goal is to have the objects within each group more closely related to one another than to objects assigned to different clusters (Friedman et al., 2001). Machine learning techniques have been successfully applied for identifying patterns in different fields and processes including: waves (Antolínez et al., 2016), ocean currents (Chiri et al., 2019), sediment transport (Antolínez et al., 2018), sediment distribution (Antolínez et al., 2019), profile morphodynamics (de Queiroz et al., 2019), and atmospheric conditions (Rueda et al., 2019a).

In this study, we use the K-means algorithm (Hartigan, 1975; Hartigan and Wong, 1979) with an initialization using K-means++ (Arthur and Vassilvitskii, 2006). After exploring several different distance metrics (squared euclidean and cityblock) and

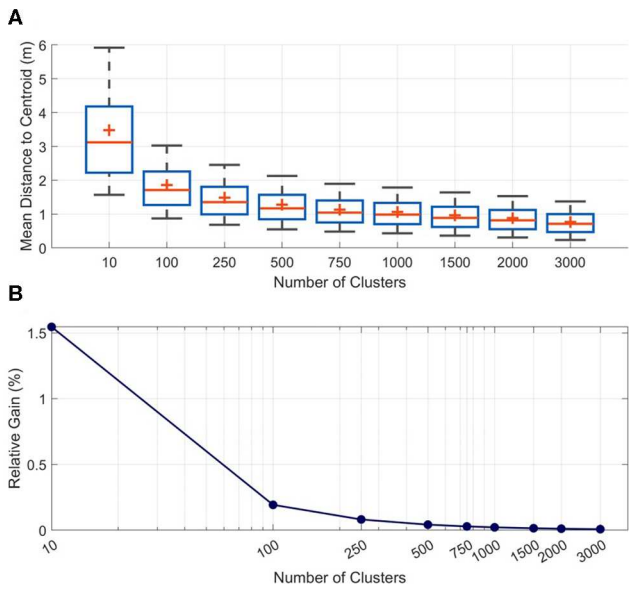

FIGURE 3 | (A) The distribution of the mean distance between a profile and its assigned centroid (iRCP) using K-medians for the varying number of tested cluster groups. **(B)** The relative gain in morphologic similarity of grouped profiles compared to the required XBeach Non-Hydrostatic (XBNH) model runs. This comparison is made to a reference case of all profiles being part of one cluster group, requiring 4 XBNH model runs. The relative gain is measured as the reduction in the mean distance between profiles and their centroid, divided by the additional required XBNH model runs, normalized to provide the result as a percentage.

statistical techniques (K-medoids, Gaussian mixture modeling, Principal Component Analysis, and Maximum Dissimilarity) (Friedman et al., 2001) the K-means clustering algorithm with the cityblock distance metric resulted in the most accurate grouping due to the profile prealignment done in Step 0. The cityblock distance metric computes the distances between observations as the sum of absolute differences, and results in each centroid being formed as the component-wise median of the observations in that cluster; therefore the method is referred to as "K-medians."

A range (10–3,000) of initial RCPs (iRCPs) were formed using this technique to determine what may be the optimal number. This was assessed by comparing the morphological similarity of grouped topobathymetric cross-shore profiles and the required number of XBNH model runs needed for Step 2 in the methodology (**Figure 3**). The mean difference in morphology between a profile and its assigned centroid (iRCP) decreases significantly moving from 10 to 500 cluster groups, however beyond 500 cluster groups the gain in morphologic similarity reduces (**Figure 3A**) as does the added value of morphological similarity in comparison to the required number of XBNH model runs (**Figure 3B**), referred to here as the relative gain.

The relative gain is calculated as:

$$Gain = \frac{X_0 - \overline{D}}{XB_{runs}} \quad (1)$$

$$Relative\ Gain\ (\%) = \frac{Gain}{X_0} \times 100\% \quad (2)$$

Where X_0 is the mean distance between all profiles and their centroid for the case of all profiles being placed in one cluster group [units (m)], $\overline{D}$ is the mean distance between all profiles and their respective centroid [units (m)], and XB_{runs} is the number of required XBNH model runs [units (-)]. The *Relative Gain* (%) is then a measure of how well the clustering has increased the morphologic similarity of the grouped profiles, weighted against the number of required XBNH model runs. Using these two metrics, 500 iRCPs was determined to be the ideal combination of intra-cluster similarity and high data reduction.

3.2.2. Cluster Analysis Inputs

The initial cluster analysis was performed using the water depth and computed wave celerity as inputs (**Figure 4**). Whereas, water depth has previously been used to define cross-shore profile clusters (Cohn and Ruggiero, 2016; Costa et al., 2016; Duce et al., 2016), wave celerity was included in this study to provide greater specificity between profiles in shallower depths. Wave celerity is more sensitive to changes in water depth in shallow water than in deep water, so its inverse was used as a non-linear weighting component in the clustering algorithm, with higher weight given to depth similarity in shallow areas (**Figure 4C**).

Using a wave period of 8 s, the celerity was computed using linear wave theory at each cross-shore position in order to obtain an equivalent dataset to the cross-shore depths. An 8 s period was used as a representative value for waves reaching coral reef lined coasts, although the specific value is not crucial for this application. This is because in shallow water the celerity for all realistic wave periods tends to $\sqrt{gh}$, providing the desired effect.

A value of infinity is reached for the inverse celerity at depths of 0 or above MSL. For these points, the inverse celerity was set to 0. The goal is that profiles with similar characteristics are grouped together; assigning the same value for these instances guides profiles with similar characteristics to be grouped in the cluster analysis. The depths and inverse celebrities were then combined into one matrix to be used for the cluster analysis by normalizing the values using max-min scaling. The morphology and inverse celerity received equal weighting (**Figure 4A**).

3.3. Step 2: XBNH Simulations

XBNH is a process-based numerical wave and water level model. It includes a non-hydrostatic pressure correction term that allows wave-by-wave modeling of the surface elevation and depth-averaged flow (McCall et al., 2014). This model has similar accuracy to that of lower order Boussinesq models and has commonly been used since its development for wave modeling over coral reefs (Quataert et al., 2015; Pearson et al., 2017; Lashley et al., 2018; Klaver et al., 2019; Rueda et al., 2019b).

We applied four wave conditions to each of the 500 iRCPs using XBNH. The objective was to obtain hydrodynamic responses for each profile to be used as a proxy for a further data reduction. The wave conditions used for the simulations are shown in **Table 2**. Two wave heights and wave steepnesses were selected with constant water level, reef friction, and beach slope to generate the four conditions. The wave height and

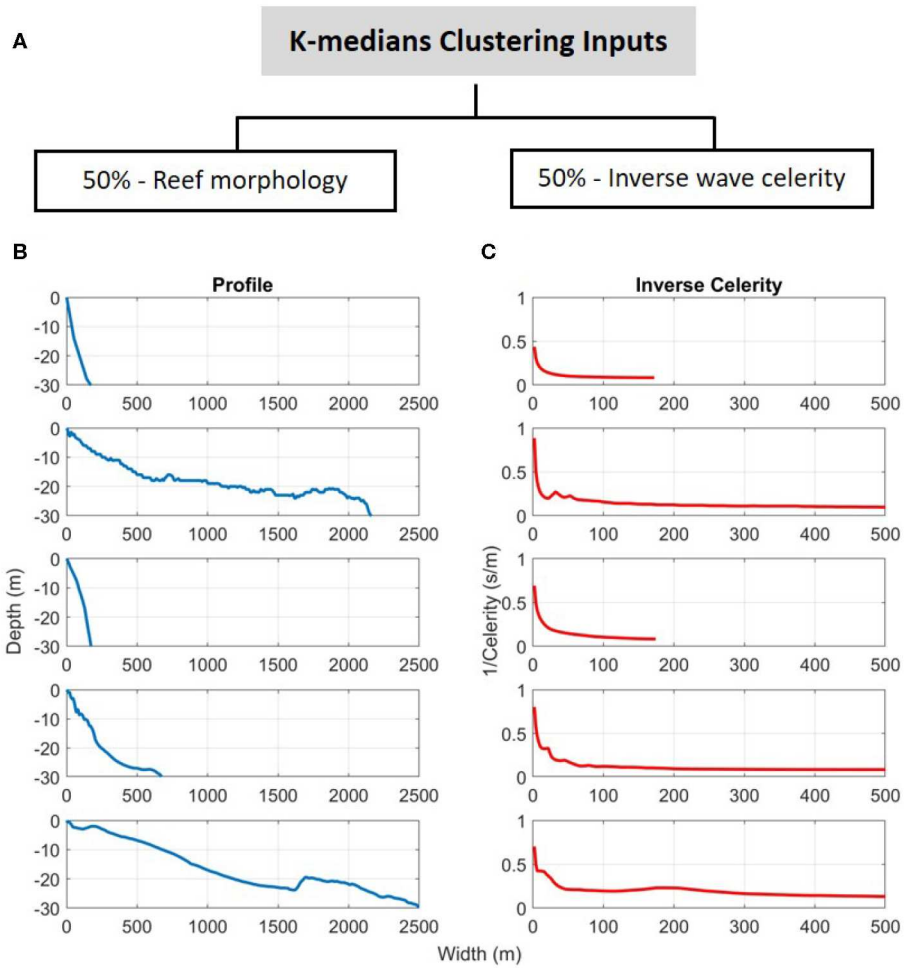

FIGURE 4 | The inputs used for the K-medians algorithm, **(A)** highlighting the weighting assigned to the two inputs; reef morphology and inverse wave celerity. **(B,C)** Examples of these two inputs for 5 topobathymetric cross-shore profiles.

TABLE 2 | XBeach model wave loading conditions and additional reef profile parameters.

			Wave loading condition			
Symbol	**Parameter**	**Units**	**1**	**2**	**3**	**4**
H_0	Wave height	m	3	3	7	7
$\frac{H_0}{L_0}$	Wave steepness	–	0.05	0.01	0.05	0.01
T	Wave period	s	6.2	13.9	9.5	21.2
n_0	Offshore water level	m + MSL	1	1	1	1
c_f	Coefficient of friction (Reef, Beach)	–	0.05, 0.01	0.05, 0.01	0.05, 0.01	0.05, 0.01
B_{beach}	Beach slope	–	1/10	1/10	1/10	1/10

steepness values were selected to represent typical wind wave and swell events that any of these regions could experience and could cause flooding. They were also chosen to vary considerably to ensure profiles are grouped which experience similar hydrodynamics from a wide range of conditions, not just one event. A dimensionless coefficient of friction (c_f) of 0.05 was used for the reef profile below MSL per Pearson et al. (2017), and a coefficient of friction of 0.01 was used for the beach (above MSL). To compute the wave runup potential, a semi-infinite beach slope was required. This was implemented using a beach slope of 1/10 from the shoreline position, reaching an elevation of 30 m above MSL.

XBNH was applied in one-dimensional mode which does not account for some of the dynamics that occur on natural reefs.

However, the dataset consists of one-dimensional profiles, and extrapolating them to an unknown two-dimensional bathymetry would involve many unwarranted assumptions, as well as a steep increase in computational time. One-dimensional analysis on coral reefs has been done for many applications, and the choice for our methods builds on existing observations along 1D transects in the field (Péquignet et al., 2011; Becker et al., 2014; Cheriton et al., 2016) and laboratory environments (Massel and Gourlay, 2000; Nwogu and Demirbilek, 2010; Buckley et al., 2016), as well as many 1D numerical modeling studies (Yao et al., 2012; Quataert et al., 2015; Pearson et al., 2017; Beetham and Kench, 2018). Furthermore, the one-dimensional modeling will represent a conservative estimate for wave runup, as the forcing is shore-normal (Guza and Feddersen, 2012; Quataert et al., 2015).

3.4. Step 3: Data Reduction Using Hydrodynamic Response

In an effort to further reduce the dataset, the 500 iRCPs were grouped based on their hydrodynamic response in the XBNH simulations. Since the objective of the RCPs is to forecast wave run-up, if there are two or more profiles of the 500 iRCPs which experience very similar wave run-up characteristics for all wave conditions, they essentially form a redundant group and can all be represented by one of the profiles. Agglomerative hierarchical clustering (Day and Edelsbrunner, 1984) was used to find which of the 500 iRCPs should be grouped together.

3.4.1. Cluster Analysis Inputs

The variables used for this stage of data reduction include both the reef morphology and hydrodynamic response; each with 50% weighting (**Figure 5A**). Morphology is included again to account for the fact that only four wave conditions were tested in XBNH. These are insufficient data to guarantee similar wave runup results across the full range of potential hydrodynamic conditions. Including morphology reduces this uncertainty. The hydrodynamics include the $R_{2\%}$, setup at the shoreline, and swash separated into infragravity and sea-swell components. The $R_{2\%}$ was calculated by isolating all wave runup events and distinguishing the 2% exceedance value. The setup was calculated as the mean water level at the shoreline over the duration of the XBNH model run. Lastly, the swash was calculated by first generating the spectrum of the water level timeseries at the shoreline. The spectrum was then split into infragravity and sea-swell components at a frequency of 0.05 Hz (period = 20 s) (Herbers et al., 1995) and the two swash values were calculated from the spectral energy using trapezoidal numerical integration (Stockdon et al., 2006). The 50% weighting is divided equally among the three hydrodynamic components.

3.4.2. Agglomerative Hierarchical Clustering

Agglomerative hierarchical clustering builds a hierarchy from the individual observations (in this case, iRCPs) by progressively merging clusters which have the smallest inter-group dissimilarity (Madhulatha, 2012). A dendrogram is typically used to visualize hierarchical clustering (**Figure 5B**). The lowest level of the hierarchy includes all of the iRCPs treated as individual clusters, and at the highest level all iRCPs are grouped together into one cluster. This method stops grouping when a threshold of dissimilarity is reached. Therefore, varying thresholds and measures of dissimilarity will result in different final numbers of RCPs. For this study, the inconsistency coefficient was used as the measure of dissimilarity (Zahn, 1971; Jain and Dubes, 1988) which compares the height of each link with the average height of other links at the same level. Using values of 0.68, 0.72, 1.1, 1.14, and 1.54, final groups of 312, 201, 149, 109, and 50 RCPs of varying sizes were generated and compared for this study.

One of the iRCPs from each group formed during the hierarchical clustering process was selected to be the representative cluster profile (RCP). This profile was the closest to the mean in terms of $R_{2\%}$. If there are two iRCPs in the final group, they would both be equal distance from the mean; in that case the iRCP which represents the greater number of profiles from the first round of cluster analysis was selected as the RCP.

3.5. Step 4: Application of Representative Cluster Profiles

The prediction of the RCPs can be evaluated by comparing the wave runup estimate generated from the RCPs to the modeled wave runup from a set of test topobathymetric cross-shore profiles. To do so, 5000 test profiles were randomly taken from the post-Step 0 dataset after sorting them by average slope to ensure that the shapes of the test profiles were sufficiently varied. Each of these profiles were simulated in XBNH under the same four wave loading conditions that were used for the iRCPs in Step 2.

3.5.1. Matching Test Profiles to Representative Cluster Profiles

Two methods were used to match the test profiles to their corresponding RCPs: a direct match to the RCPs, and a probabilistic matching technique. For both cases, test profiles are first matched to the 500 iRCPs of Step 1, and the relationship is followed between iRCP to RCP (Step 3) to determine the appropriate RCP match. This is done because the match is based on the profile morphology and inverse celerity, and therefore the match must be made to the iRCPs that were formed based on those same parameters.

The direct match is simply done by calculating the pairwise distance between the test profile and 500 iRCPs. The distance is a sum of the distance between the normalized depths and celerity; the same variables used in the first cluster analysis. The match is made to the iRCP with the smallest distance and then to the corresponding RCP.

The probabilistic matching method revolves around the softmax function which is a method used in neural networks to predict the probabilities associated with a multinoulli distribution (Goodfellow et al., 2016). It maps a vector of inputs to a posterior probability distribution (Goodfellow et al., 2016). Once the distances have been calculated between a test profile and all iRCPs, if the distances are input into the softmax function, each distance is attributed a probability ranging between 0 and 1.

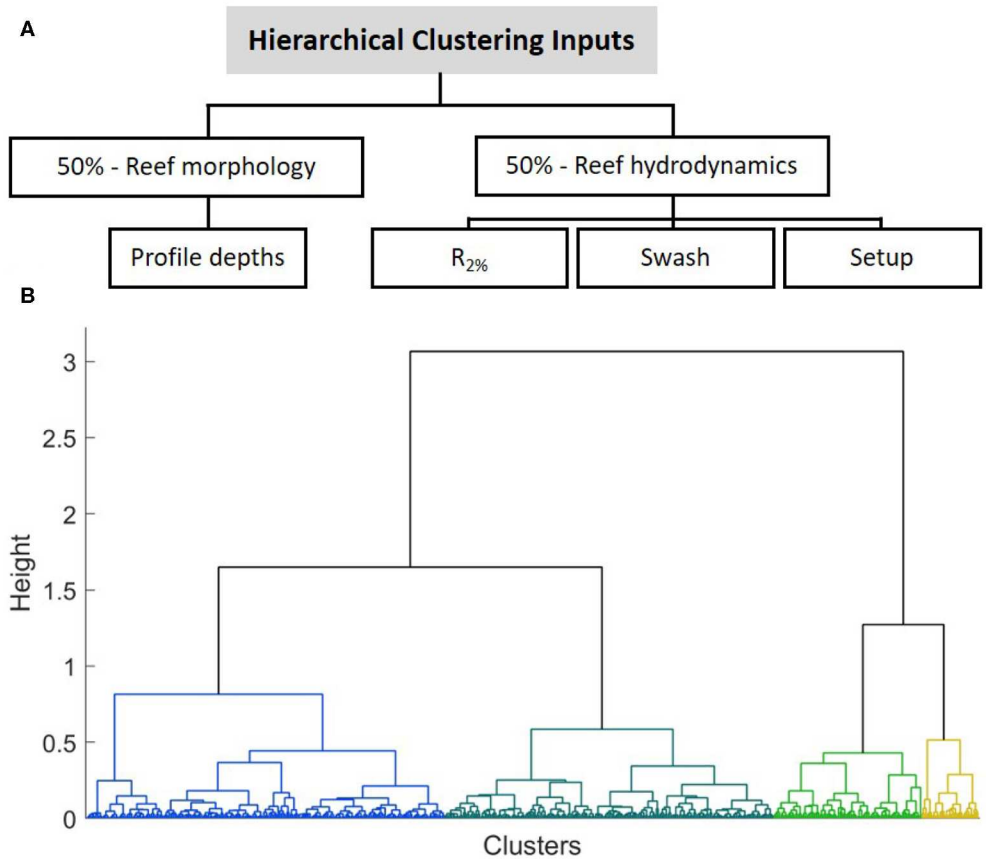

FIGURE 5 | The inputs used for the hierarchical clustering algorithm, **(A)** highlighting the weighting assigned to the inputs; morphology and hydrodynamics separated into $R_{2\%}$, setup and swash. **(B)** The dendrogram used to visualize the hierarchical clustering results of the 500 initial representative cluster profiles (iRCPs). The coloring represents an example of the grouping of the 500 iRCPs if a height cutoff value of 1 is used, forming four clusters.

The softmax function is defined as:

$$S(x)_i = \frac{exp(-B * x_i)}{\sum_{j=1}^{n} exp(-B * x_j)} \quad (3)$$

where $S(x)$ is the probability of matching to iRCP i, x_i is the distance between the test profile and iRCP i, x_j is the distance between the test profile and iRCP j, B is the stiffness parameter, and n is the number of iRCPs.

The B value essentially acts as an inverse variance, such that larger values of B will cause the distribution to be narrower so that probabilities associated to large distances between profiles will become small. Multiple B values were tested to compare the effect on the accuracy of the $R_{2\%}$ estimate.

The steps of the probabilistic matching technique are listed below:

1. Calculate the distance between the test profile and the 500 iRCPs.
2. Use the softmax function to transform the distances into probabilities. A lesser distance will lead to a greater match probability.
3. Determine the match probability to the RCPs by summing the probabilities of the grouped iRCPs.
4. Use the probabilities as weights and generate the estimate of the wave runup as an ensemble average.

3.5.2. Performance Metrics

The accuracy of the RCP prediction of $R_{2\%}$ was assessed using common performance metrics including the root mean square error ($RMSE$), coefficient of determination (R^2), bias, skill and scatter index (SI). RMSE is a measure of how concentrated the data is around the line of best fit. If all data points lie on the line of best fit, the RMSE is 0. R^2 is a measure of the variance in the dependent variable (modeled value) that is predictable from the independent variable (RCP estimation). Bias is the tendency of the RCP estimate to either over or underestimate the modeled value. The skill score (Murphy, 1988) is a measure of accuracy of prediction, where a value of 1 indicates a perfect prediction. The scatter index is the RMSE normalized by the mean observed value, which provides insights on the variance of the errors.

These metrics are defined as:

$$RMSE = \sqrt{\frac{1}{n}\Sigma_{i=1}^{n}(R_{2\%TP_i} - R_{2\%RCP_i})^2} \quad (4)$$

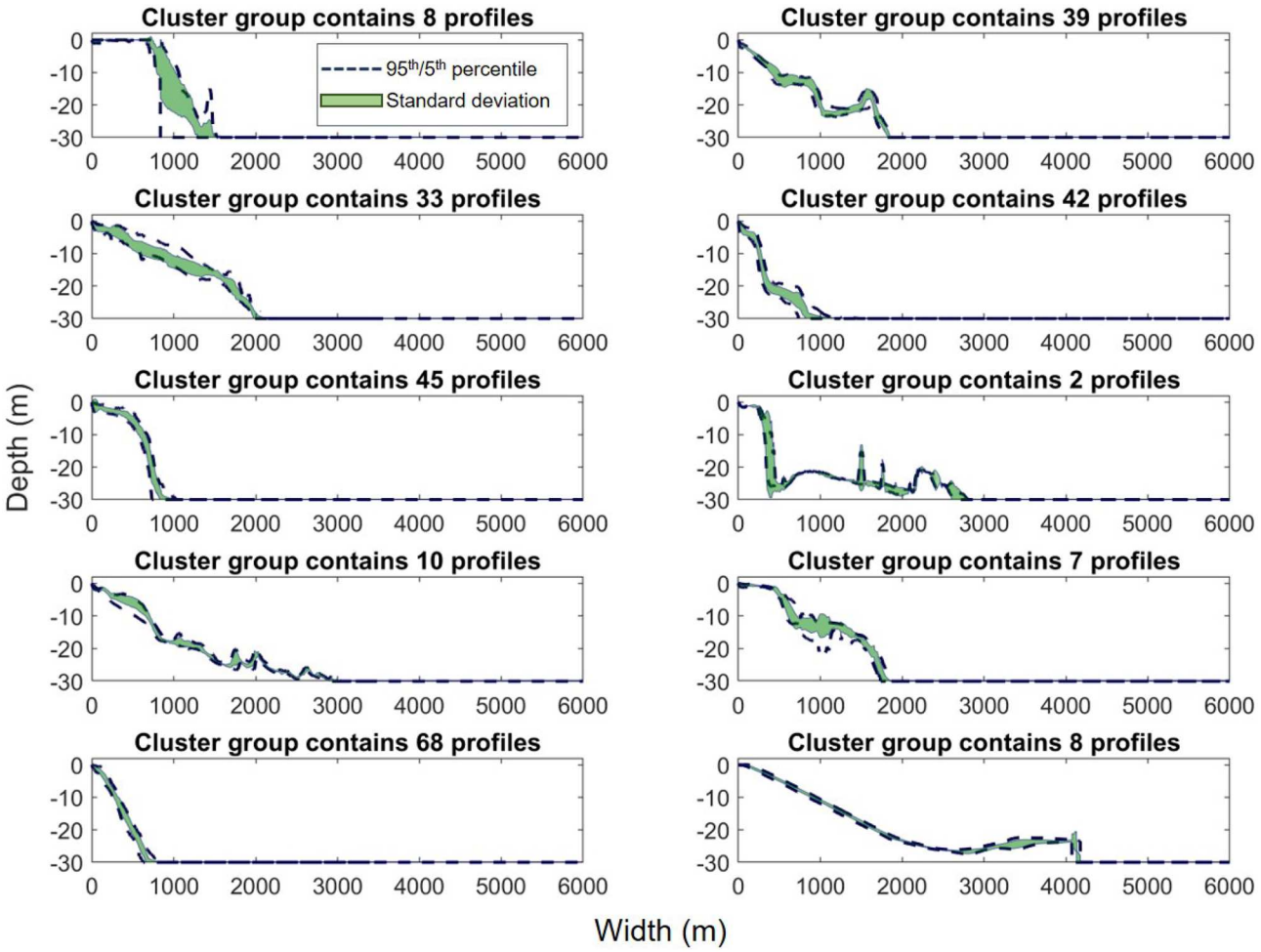

FIGURE 6 | Example of 10 cluster groups used to form the initial representative cluster profiles (iRCPs). The x-axis represents the cross-shore width and the y-axis the elevation. The green area defines the standard deviation within the cluster and the blue dashed lines the 5th and 95th percentiles. The number of reef topobathymetric cross-shore profiles within the cluster is shown in the title of each subplot.

$$Bias = \overline{R_{2\%RCP}} - \overline{R_{2\%TP}} \tag{5}$$

$$R^2 = \frac{1}{n}\sum_{i=1}^{n}(R_{2\%RCP_i} - R_{2\%TP_i})^2 \tag{6}$$

$$Skill = 1 - \frac{RMSE^2}{\sigma^2_{R_{2\%TP}}} \tag{7}$$

$$SI = \frac{RMSE}{\overline{R_{2\%TP}}} \tag{8}$$

where $R_{2\%RCP}$ is the forecasted $R_{2\%}$ from the RCPs, $R_{2\%TP}$ is the modeled $R_{2\%}$ of the test profile, $\sigma_{R_{2\%TP}}$ is the standard deviation of the modeled $R_{2\%}$ of the test profiles and n is the number of test profiles.

4. RESULTS

4.1. Step 1: Cluster Round 1

The first cluster analysis organized the 20,454 profiles resulting from Step 0 into 500 groups. The median of each group is used as the representative profile and is known as the iRCP. The 500 iRCPs are shown in **Figure S1**. An example of ten cluster groups is shown in **Figure 6**, illustrating the range in morphologies within the groups using the 95th and 5th percentile as bounds, and the standard deviation. The cluster analysis groups profiles with similar shape and with lesser variance in shallower depths.

4.2. Step 2: XBNH Simulations

The XBNH simulations with the 500 iRCPs were mainly used to generate input for the data reduction in Step 3, however it is also interesting to analyze the range of hydrodynamic results across such a variety of coral reef morphologies.

In general, there is a greater variance in the hydrodynamics for the 500 iRCPs under the more severe loading conditions (**Figure 7**). Loading condition 4, which includes a 7 m significant wave height and 21 s period, has the greatest range of $R_{2\%}$ and setup, whereas loading condition 1 with a 3 m significant wave height and 6 s period has the narrowest range of results for these parameters (**Figures 7A,B**). Both the infragravity and sea-swell

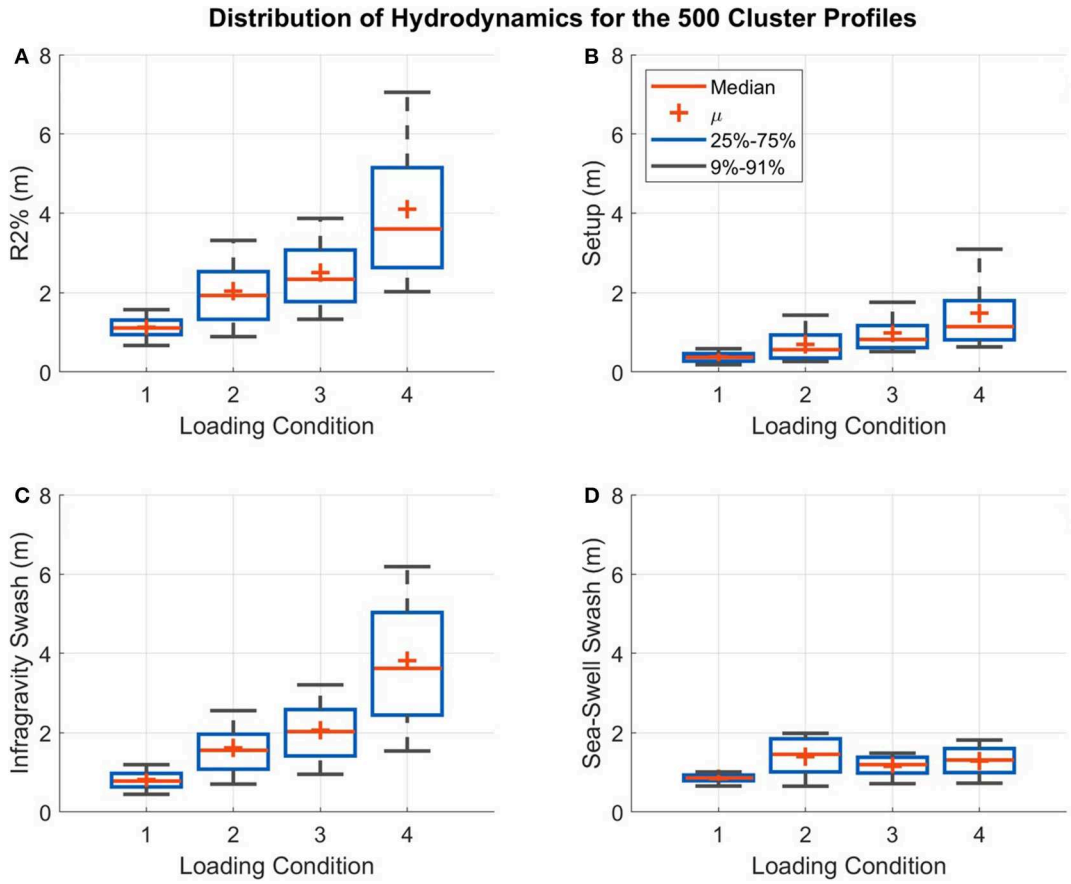

FIGURE 7 | Distributions of the results of the XBeach Non-Hydrostatic (XBNH) runs for the 500 initial representative cluster profiles (iRCPs), including the $R_{2\%}$ **(A)**, setup at the shoreline **(B)**, infragravity **(C)**, and sea-swell swash **(D)**. The loading condition numbers along the x-axis correspond to the numbering in **Table 2**.

swash are typically greater for the wave conditions with the higher period (lesser steepness) (**Figures 7C,D**).

4.3. Step 3: Cluster Round 2

The second round of data reduction grouped the 500 iRCPs by morphology and hydrodynamics. Five different thresholds were used to limit the dissimilarity of joined observations, as explained in section 3.4.2, resulting in different numbers of final RCPs. The five thresholds resulted in 312, 201, 149, 109, and 50 RCPs.

To assess the success of Step 3, the intra-cluster similarity of the XBNH results was compared. This was done by measuring the relative difference of the relevant hydrodynamic parameters between grouped iRCPs. XBNH results are only available for the 500 iRCPs and so the analysis was done with these results, however the 500 iRCPs represent the original 20,454 profiles included in the study, and therefore this step provides a measure of how similar the hydrodynamics are for all the profiles grouped through the two cluster analyses. The $R_{2\%}$, setup at the shoreline, and swash separated into infragravity and sea-swell components were compared. As expected, the relative difference increases when there are fewer cluster groups because more profiles with varying hydrodynamic results are being grouped together (**Figure 8A**). This leads to the conclusion that the accuracy of the hydrodynamic prediction using the RCPs will be greater when more RCPs are included.

The general relationship, which matches previous research (Storlazzi et al., 2011; Quataert et al., 2015; Pearson et al., 2017), is that reefs with wide flats, shallow average depths and mild fore-reef slopes result in the lowest wave runup, whereas reefs with very narrow reef flats, greater average depths, and steeper foreshores result in the highest wave runup (**Figure 8B**). This supports the inverse celerity weighting to decipher between the different profiles.

4.4. Step 4: Application of the Representative Cluster Profiles

The forecast of the RCPs was tested with 5000 profiles from the dataset. As mentioned in section 3.5.1, two methods to match the test profiles to the cluster profiles were assessed.

4.4.1. Probabilistic Match

Using the probabilistic matching method, the most accurate estimate of $R_{2\%}$ was obtained with the highest B value (**Figure 9A**). When comparing the estimated $R_{2\%}$ from the RCPs to the model results, a B of 1,200 resulted in a mean relative difference between 9.7 and 13.1% depending on the

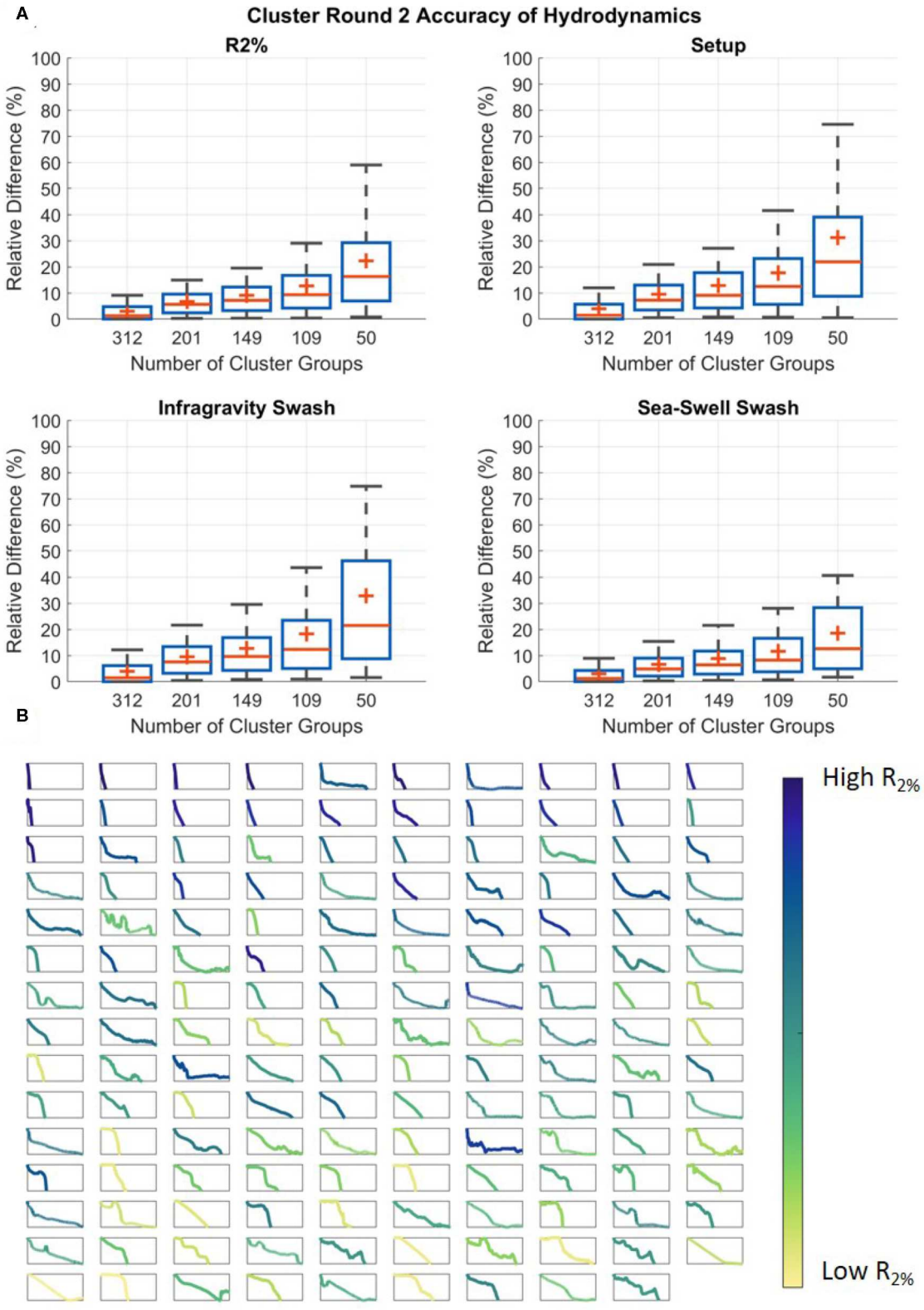

FIGURE 8 | (A) The similarity of the $R_{2\%}$ (top left), setup at the shoreline (top right), infragravity (bottom left), and sea-swell swash (bottom right) of the grouped initial representative cluster profiles (iRCPs) from the hierarchical cluster analysis (Step 3). The x-axis contains the number of representative cluster profiles (RCPs), and the

(Continued)

FIGURE 8 | y-axis is the relative difference in the XBeach Non-Hydrostatic (XBNH) model results between all grouped profiles and their representative profiles. The grouped profiles are the iRCPs from Step 1, and the representative profiles are the RCPs formed in Step 3. **(B)** The RCPs for the case of 149 cluster groups, colored based on their relative wave runup rank, and sorted based on their average slope from 0 to 15 m depth. The x-axis is the profile width set at a constant range of 0 to 3,068 m, and the y-axis is the profile depth from MSL set at a constant range of −30 to 0 m.

number of RCPs, ranging from 312 to 50. In contrast, a B value of 100 results in the mean relative difference always being greater than 20%. Referring to the example test profile in **Figure 9B**, when B = 100, no RCP is given a match probability greater than 10% and many are given a probability above 0.1%, whereas when B = 1,200, two RCPs are assigned the majority of the probability at about 40% each and few others carry any probability at all. The general trend is that as B increases the association to the closest RCP increases and the estimate becomes more accurate (**Figures 9A,B**), although this is not the case for all profiles.

The B value was capped at 1,200 since this was deemed to be the upper limit for the softmax function to operate properly with the current inputs. There is not an optimized value of B for the softmax function applied in this study since the range of applicable B values is dependent on the input x_i and x_j from Equation (3). For the values used in this study, it was found that B values >1,200 resulted in function errors.

4.4.2. Probabilistic vs. Direct Match

While using the probabilistic method, the estimation is most accurate when the association to one RCP is greatest. However, a direct match to the single most similar RCP generally does not result in a greater accuracy. The comparison of the probabilistic matching method using the high B value of 1,200 compared to the direct matching method is shown in **Figure 10A**. For the 5,000 test profiles, the direct matching technique results in slightly greater error in the $R_{2\%}$ estimates.

The results from the two matching techniques differ the most at the lowest number of RCPs (50). Here, the probabilistic method offers the greatest benefit. If a profile is not very similar to any RCPs, which is more common when there are fewer RCPs to match to, the probabilistic method is able to draw an estimate as an average of the most similar RCPs, most likely combining over and under estimated values. Conversely, for the direct match method the best estimate is one of the over or under estimated values. An example of this is shown in **Figure 10B** where the test profile does not match well to any RCP and the direct matching method therefore provides inaccurate $R_{2\%}$ estimates. The estimates increase in accuracy under the probabilistic matching method where the $R_{2\%}$ value is derived from multiple RCPs instead.

An added benefit of the probabilistic method is that confidence bands can be added to the $R_{2\%}$ estimate (**Figure 10B**). To cover the full range of potential outcomes, all RCPs with a match above 1% can be used to create a confidence band to aid the prediction, which when matching to a single RCP cannot be provided.

4.4.3. Cluster Profiles Predictive Skill

The predictive skill of the RCPs while using the probabilistic matching method for the 5,000 test profiles is shown in **Figure 11**. There is a strong linear relationship for the case of 312 RCPs, meaning that the majority of the data points have <10% deviation between predicted and modeled values, which gradually reduces moving toward 50 RCPs. For all RCP values, the majority of instances when the error is >10% occur at lower $R_{2\%}$ values, meaning that the estimate is typically more accurate for predicting flood scenarios (high $R_{2\%}$) compared to more mild conditions.

All performance metrics, explained in section 3.5.2, lead to similar findings. The *RMSE* continuously decreases for greater numbers of RCPs, meaning that the data is most concentrated around the line of best fit with more RCPs. The increasing R^2 and skill, as well as the decreasing *SI* all suggest that the predictability is enhanced as more RCPs are used. Finally, the bias switches between positive and negative suggesting either over or underestimating, however in all cases it is relatively low.

These results suggest that the RCPs are highly effective in predicting the $R_{2\%}$ for the 5,000 test profiles considered for this study. When using 312 RCPs the accuracy is greatest, forecasting the $R_{2\%}$ with a mean relative difference of 9.7%. Fewer RCPs can be used, however, increased data reduction comes at the expense of higher predictive error. Using 50 RCPs (fewest tested) results in a mean relative difference of 13.1%. These error values are within the same range as the empirical equation developed by Stockdon et al. (2006) to calculate $R_{2\%}$ for natural beaches, used by engineers around the world.

5. DISCUSSION

The presented methods and techniques have not been widely used for applications in coastal engineering. This section provides the main sensitivities and potential future applications of this work.

5.1. Cluster Analysis

Two cluster analyses were performed to develop the RCPs of the dataset. The techniques to generate these RCPs can vary significantly, and although the presented methods were selected in order to create the optimal RCPs, modifications could be made which would alter the outcome. The key sensitivities of the cluster analysis include the cluster method, the variables, and the weighting of the variables.

Many cluster analysis techniques are applicable for this type of study, and each has pros and cons (Friedman et al., 2001; Rai and Singh, 2010). Other methods have also been applied and compared in other coastal engineering applications (Camus et al., 2011). For this dataset, K-medians was determined to result in the

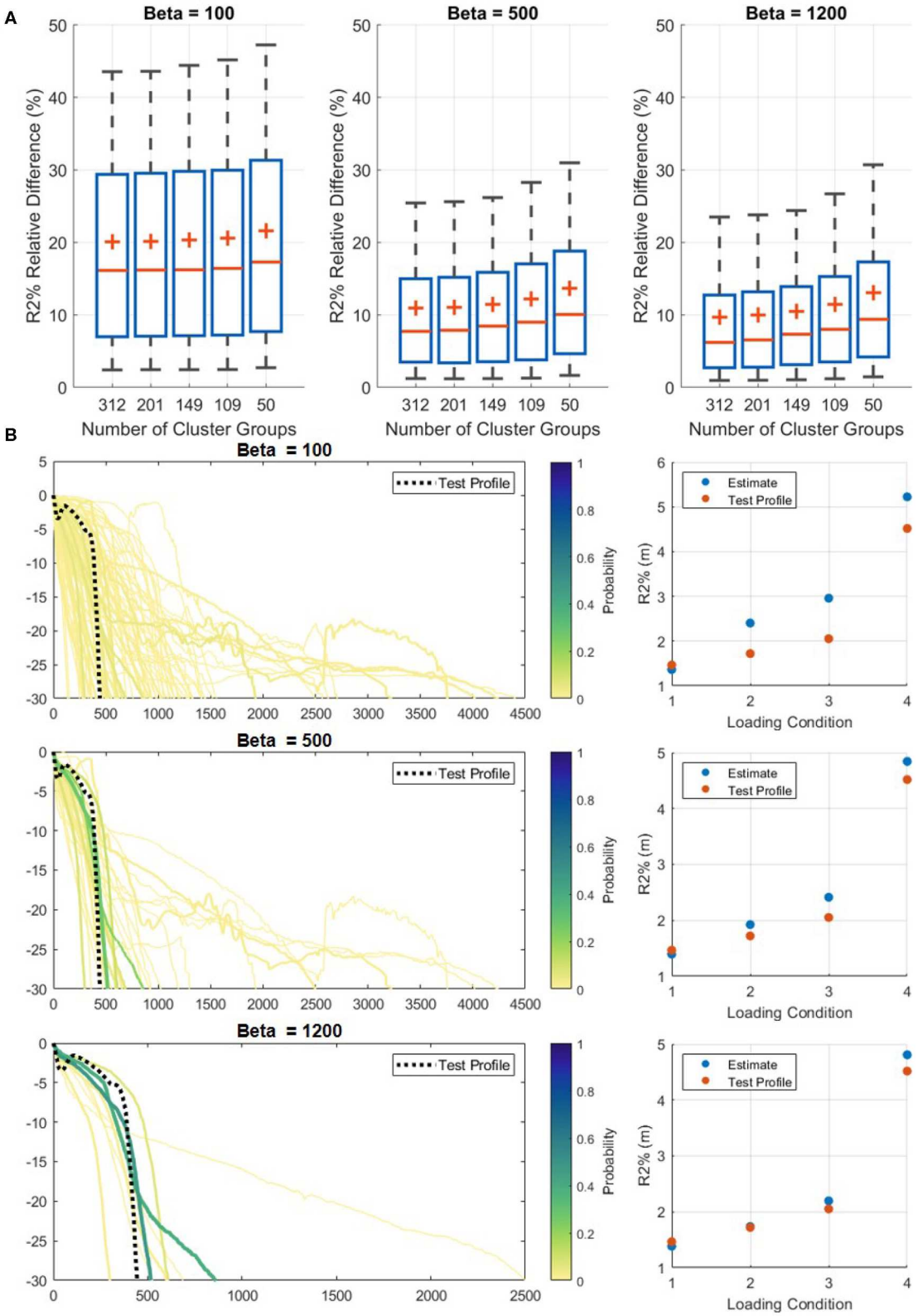

FIGURE 9 | Results of the influence of the *B* value in the probabilistic matching method. **(A)** For increasing values of *B* and representative cluster profiles (RCPs), the accuracy of the $R_{2\%}$ estimation increases. **(B)** An example of matching the RCPs with one real-world test profile for varying values of *B*. As *B* increases, the match to the most similar RCP increases and fewer RCPs are given any match probability. RCPs are only plotted if they have a match probability above 0.1%. The scatter plots provide the modeled value and estimate of $R_{2\%}$ for the four loading conditions (**Table 2**).

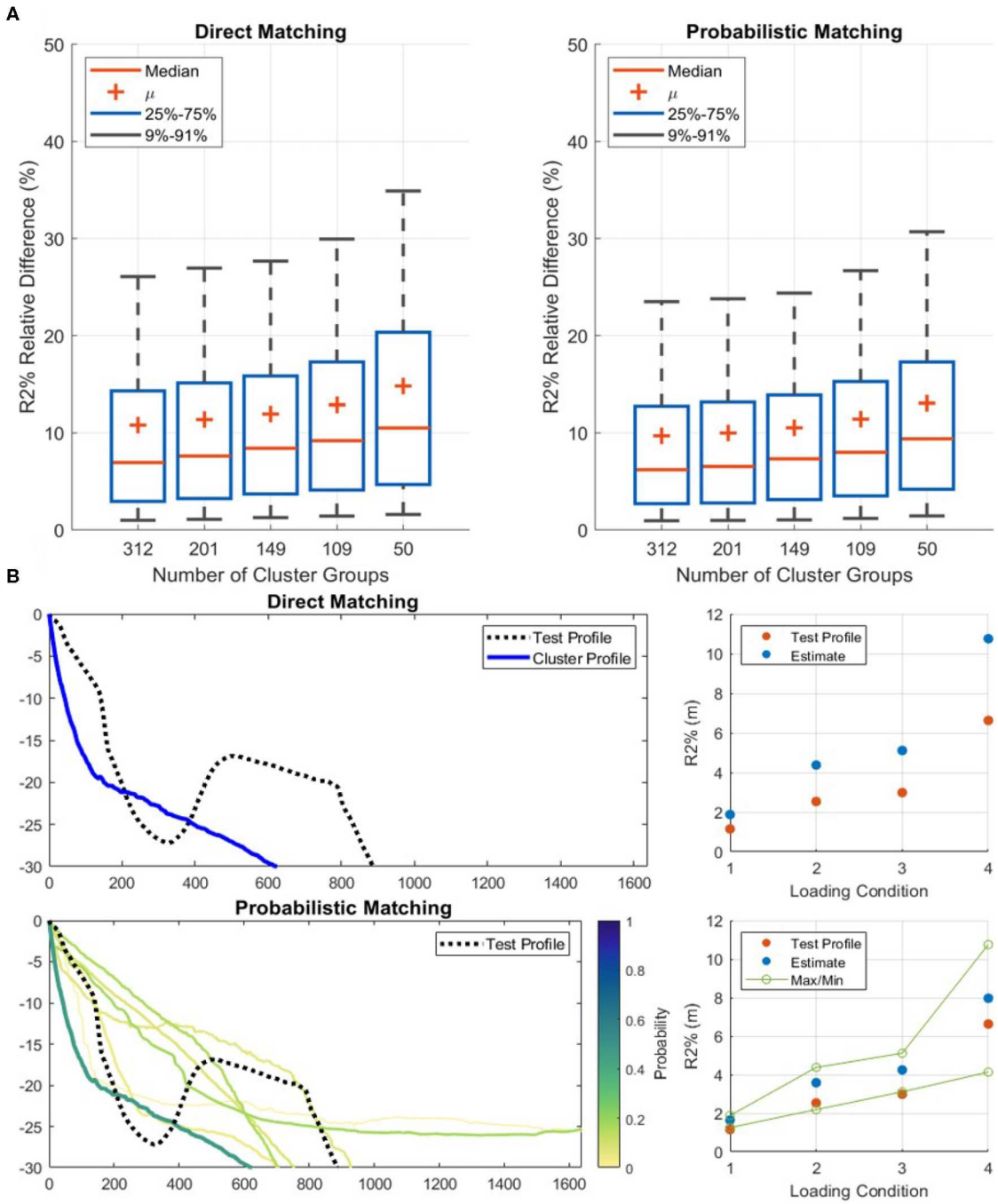

FIGURE 10 | Results of the direct and probabilistic matching method. **(A)** The probabilistic technique has a slightly greater accuracy in $R_{2\%}$ estimation. For both cases, the accuracy decreases as the number of representative cluster profiles (RCPs) decrease. **(B)** An example of the two matching techniques when using 50 RCPs with one of the unique test profiles. The scatter plots provide the modeled value and estimate of $R_{2\%}$ for the four loading conditions (**Table 2**). The test profile does not match well to any of the RCPs, and therefore the $R_{2\%}$ estimation from the direct matching technique suffers. The estimation from the probabilistic technique is influenced from multiple RCPs and is more accurate for all four loading conditions. The green values in the scatter plot represent the confidence bands that can be determined while using the probabilistic technique.

least intra-cluster variance of morphology compared to K-means, K-medoids, Maximum Dissimilarity, and Principal Component Analysis. However, other benefits may come from using one of the other methods which has not been explored. Hierarchical clustering was selected for the second cluster analysis because it works well with varying attribute types or large datasets, and

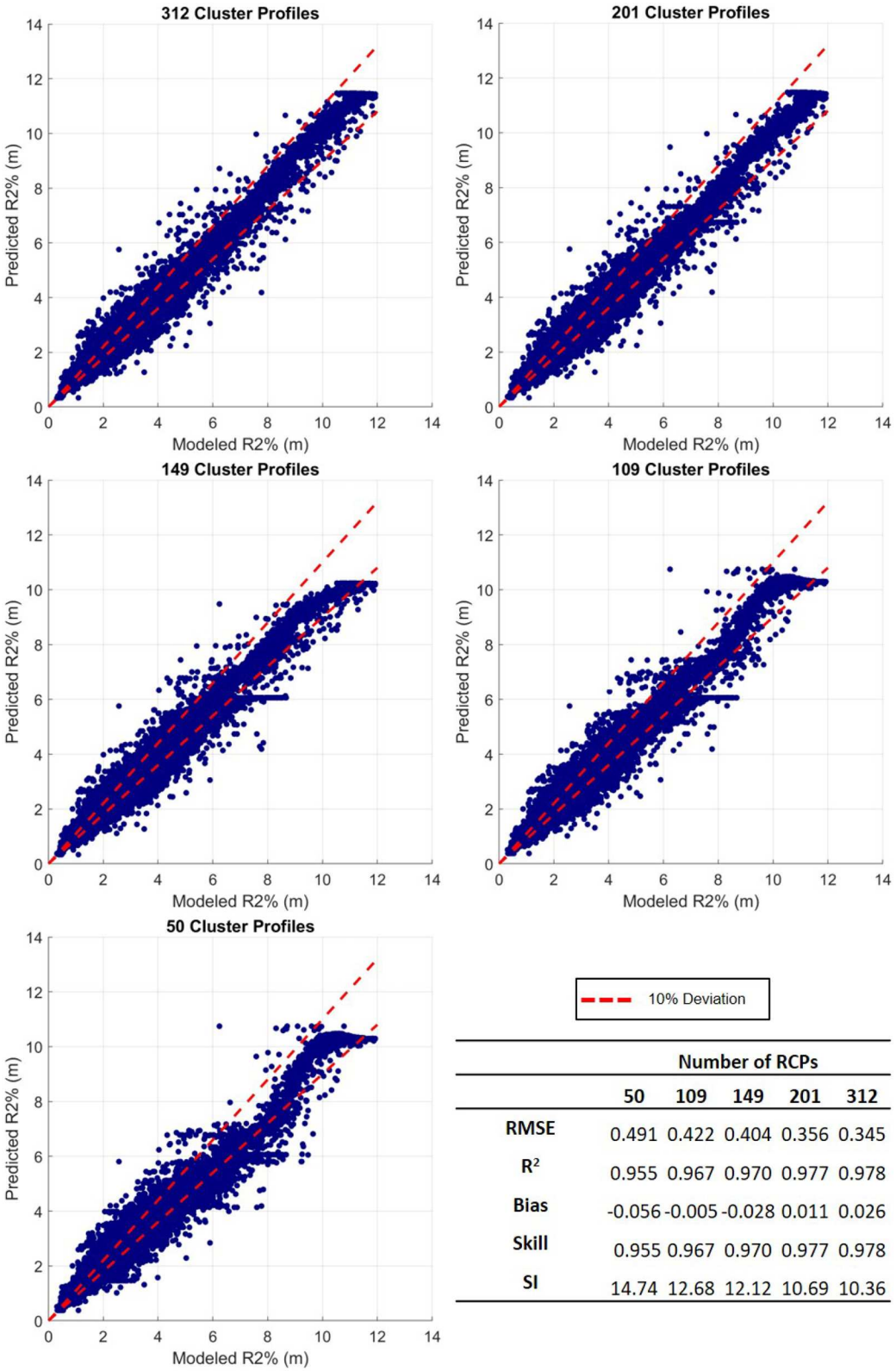

	Number of RCPs				
	50	109	149	201	312
RMSE	0.491	0.422	0.404	0.356	0.345
R^2	0.955	0.967	0.970	0.977	0.978
Bias	-0.056	-0.005	-0.028	0.011	0.026
Skill	0.955	0.967	0.970	0.977	0.978
SI	14.74	12.68	12.12	10.69	10.36

FIGURE 11 | Modeled vs. estimated $R_{2\%}$ for the five different numbers of representative cluster profiles (RCPs), ranging from 312 (top left) to 50 (bottom left). The table in the bottom right provides data comparison statistics, explained in section 3.5.2.

a threshold can be set to limit the intra-cluster dissimilarity (Madhulatha, 2012).

Apart from the clustering technique itself, the input into the algorithm is equally important. In the first cluster analysis, the normalized bathymetric profile depths and inverse wave celerity were used (**Figure 4**) to group similarly shaped profiles with an emphasis on the shallower part of the profile. This selection is appropriate for the goal of this study, however other parameters could be used as well. The celerity does not account for the impact of the slope of the fore reef, which is known to impact the infragravity components of the incoming waves (Storlazzi et al., 2011; Quataert et al., 2015; Pearson et al., 2017). Using celerity therefore excludes a potentially key aspect of successful grouping. In the second cluster analysis, the topobathymetric cross-shore profile was combined with the hydrodynamic response at the shoreline determined from the XBNH simulations for the input into the clustering algorithm. These were selected to group profiles with the most similar flooding characteristics, but again, other parameters may be used. For example, the infragravity and sea-swell components of the wave height at a certain distance offshore may be beneficial to add as an input, however by using the $R_{2\%}$, setup, and swash separated into infragravity and sea-swell components, most of the important information is already included.

Lastly, the weighting of the inputs can be modified to vary the relative importance of certain inputs. In the first cluster analysis, the inverse wave celerity was included as a weighting function. This is because the wide variety of coral reef morphologies makes it difficult to apply a simple weighting function that can be used across all topobathymetric cross-shore profiles. Since the required weighting is proportionate to the depths (values), not the cross-shore position (variables), the weight for the same variable (cross-shore position) would not be consistent across all profiles. Therefore, the inverse wave celerity was selected which includes the influence of the shallow depths of the profile. For both the first and second cluster analysis, 50% weighting was applied to the morphology and 50% to the celerity or hydrodynamics. An equal balance was selected because the relative contribution of the inputs to the successful clustering based on wave runup is not certain. It would be interesting to compare the RCPs with different weighting assigned to the morphology and hydrodynamics, for example if 100% weighting was assigned to the hydrodynamics. Most likely the results would not be influenced heavily because the morphology also characterizes the hydrodynamic response.

5.2. Wave Conditions

The results from the XBNH simulations are a driving factor for the final grouping of the iRCPs. In this study, four wave conditions were used (**Table 2**) that ranged in period from 6 to 21 s, and in height from 3 to 7 m. Although they were chosen strategically to cover a wide range of potential flooding conditions and different types of ocean waves, if two profiles have similar wave runup over these four conditions, it does not necessarily mean that they always will for higher or lower energy conditions. The cluster analysis and accuracy of RCP's prediction are therefore limited by the variety of tested wave conditions.

5.3. Estimating Wave Runup

Two methods for using the RCPs to estimate the wave runup were developed. The probabilistic approach has proven to typically have a greater accuracy in the $R_{2\%}$ prediction compared to the direct matching method and comes with the added benefit of a confidence band associated with the estimate (**Figure 10**). Other matching techniques could be developed and tested, however the idea of using probabilities associated with the prediction is beneficial if considering implementing the RCPs with a Bayesian Network (BN) or other probabilistic tool. BNs are probabilistic models that have been successfully used to make predictions of hydrodynamics and morphology in numerous coastal applications (Gutierrez et al., 2011, 2015; Plant and Holland, 2011; Poelhekke et al., 2016). After being trained with sufficient data, they rely on Bayesian probability to make predictions of desired output. In this case, the input would be the profile and offshore wave conditions, and the output would be the wave runup and other hydrodynamic results. The results of the probabilistic matching could also be fed into the network to aid the prediction.

To further validate the results, the RCPs should be used to estimate the wave runup of coral reef profiles that were not included in the initial dataset. Since the 5,000 test profiles were included in the generation of the RCPs, at least one of the RCPs should be similar in shape and wave runup to each of the test profiles. For other cross-shore profiles with morphology within the range of the profiles included in this study, the accuracy of the wave runup estimation should not vary significantly.

To include a new batch of coral reef profiles, the methodology would have to be repeated. This would require going back to Step 0 to filter and align the profiles before performing the first cluster analysis. An update would only be beneficial if the new profiles are significantly different to any of the 500 iRCPs presented in this study; only then would a new cluster group be created. Otherwise, the new profiles would join one of the existing cluster groups and the outcome would not have a significant change.

5.4. Application of the Methodology

The presented methodology has been demonstrated with many coral reef properties set as constant. It is well-established that changes in the roughness and friction (Lowe et al., 2005; Pomeroy et al., 2012; Monismith et al., 2015; Buckley et al., 2016; Rogers et al., 2017, 2018; Osorio-Cano et al., 2019; Reguero et al., 2019), porosity (Lowe et al., 2008; Asher et al., 2016; Asher and Shavit, 2019; Zhu et al., 2019), and storm surge (Hoeke et al., 2013; Smithers and Hoeke, 2014; Tajima et al., 2016) will affect the hydrodynamics over a coral reef, and in turn the resulting wave runup at the shoreline. Therefore, the RCPs as they are currently do provide a means to estimate wave runup based on reef morphology, although the estimate is limited to coral reefs with similar properties used in this study. The effects of the reef properties were excluded from the scope of this study because the information for this dataset is not available. Although the properties are not included, we were able to distinguish the representative profile shapes which can be used to form the foundation for an effective tool that does encompass

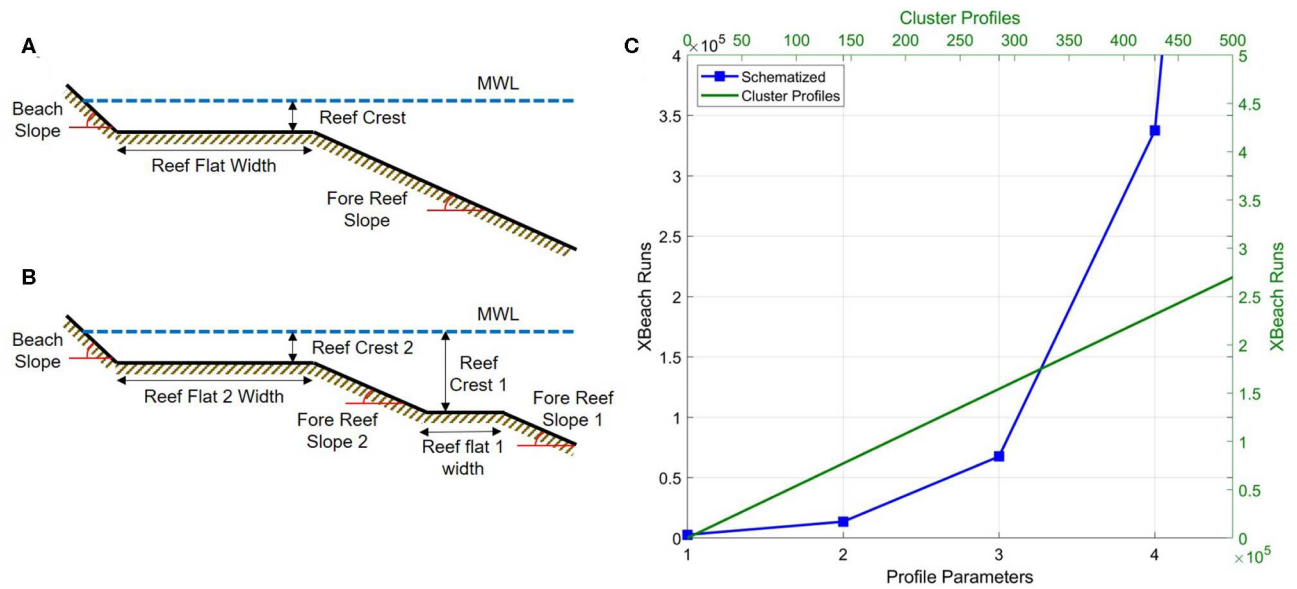

FIGURE 12 | The required number of XBeach Non-Hydrostatic (XBNH) runs **(C)** for different numbers of representative cluster profiles (RCPs) (top and right axis) or a schematized profile (bottom and left axis) such as that of BEWARE, assuming 540 XBNH runs are needed per profile (Pearson et al., 2017). **(A)** An example of a schematized profile with four parameters and **(B)** how three more parameters are required to be added to the schematized profile in order to represent a second reef flat, corresponding to the x-axis in **(C)**.

the full range of effects that physical reef properties have on the hydrodynamics.

As mentioned in section 1, this study was conducted to continue the work of Pearson et al. (2017), and the intended use of the RCPs is to replace the simplified profiles used in developing a predictive model such as BEWARE. Combining the RCPs with such a model would be a step toward the development of a global flood EWS for coral-reef lined coasts. To do so, similar steps done by Pearson et al. (2017) would have to be followed, including training the model with XBNH results that incorporate the variation in reef properties, such as performing multiple simulations for the same reef profile but with varying values of friction. Each of these combinations is then also required to be simulated under a range of wave conditions. This way, the model includes the combination of the full range of reef morphologies, physical properties, and offshore forcing conditions, which also allows the user to estimate wave runup based on these specifics.

One of the benefits of using the RCPs compared to a simplified reef profile (e.g., Pearson et al., 2017) is that when a greater variety of reef morphologies are included (more cluster profiles), the number of required XBNH runs increases linearly. For a simplified reef profile defined by parameters (e.g., fore reef slope, reef flat width, reef crest height), additional parameters must be included to expand the variety in morphology that they can represent (e.g., **Figures 12A,B** where an irregularity along the reef flat is added). Each additional parameter exponentially increases the number of combinations of profile shapes, and in turn exponentially increases the number of required XBNH runs, as shown in **Figure 12**. Therefore, the RCPs heavily reduce the computational time required to create a probabilistic model.

Apart from wave runup estimation, another use for the RCPs within a probabilistic model is estimating future impacts based on climate change scenarios. Since the model is a quick and accurate tool, many different loading conditions with varying offshore water levels and wave parameters could be analyzed to estimate the associated flooding impacts that they would cause. Since the RCPs encapsulate such a wide variety of real-world topobathymetric profiles, large-scale climate change estimates could be made to assess the effects of different rates of SLR on multiple different coral reef profiles, providing valuable information about the types of coastlines and their associated communities and infrastructure that are most at risk.

A comparison between the estimated wave runup from the RCPs and BEWARE with measured wave runup has not been done. It is difficult to source valid field measurements of wave runup, and they are typically recorded at time intervals much greater than what is modeled, as well as at varying vertical levels which make the comparison challenging. The assumption is that the RCPs would enhance the predictive accuracy, especially for the obscure reef profiles, most dissimilar to the schematic fringing reef used in BEWARE.

6. CONCLUSIONS

Data mining techniques were used to reduce an extensive dataset of coral reef topobathymetric cross-shore profiles to a subset of RCPs. We carried out two stages of cluster analysis that grouped the profiles based on morphology, inverse wave celerity, and hydrodynamic response to typical storm wave conditions.

Techniques developed here can be used to effectively match real-world coral reef cross-shore profiles to the RCPs in order to generate an estimate of wave runup.

The RCPs have demonstrated a high predictive skill for the $R_{2\%}$, used to indicate extreme wave runup and potential flooding. The accuracy of projections is in the same range as the empirical equation of $R_{2\%}$ for natural beaches (Stockdon et al., 2006) that is used by engineers around the world. A useful next step would be to incorporate the RCPs into a BN or other probabilistic model, developed to also accommodate the ranges in physical reef properties such as friction which have been omitted from this study. Such a model would be able to provide accurate estimates of wave runup for an extensive array of coral reefs and offshore wave conditions, and could form the basis of an EWS and scenario assessment tool for reef-lined coasts.

DATA AVAILABILITY STATEMENT

All coral reef profiles used in this study, as well as the XBNH results for the 500 iRCPs is available as a NetCDF (*.nc) file at the following location: https://doi.org/10.5066/P9C39WNE.

AUTHOR'S NOTE

Any use of trade, firm, or product names is for descriptive purposes only and does not imply endorsement by the U.S. Government.

AUTHOR CONTRIBUTIONS

FS has been the main author of this research, first working on this topic during his thesis at Deltares/TU Delft, and continuing while working at Baird & Associates. RM and JA were the daily supervisors, offering guidance and ideas throughout the entire process. AR, CS, and SP were also all supervisors, involved in monthly meetings to provide insights and guidance. The work largely built off of previous work done by SP, and many of the coding applications can be attributed to him.

FUNDING

This material was based upon work supported by the U.S. Geological Survey under Grant/Cooperative Agreement No. G20AC00009. Funding was made available through the Deltares Quantifying flood hazards and impacts (11203750) Strategic Research Program.

ACKNOWLEDGMENTS

For **Figure 1C**, information/data/maps provided by ReefBase (http://www.reefbase.org). Coral reefs provided by UNEP-WCMC. We thank the two reviewers for their constructive feedback which has greatly improved the quality of our manuscript.

SUPPLEMENTARY MATERIAL

The Supplementary Material for this article can be found online at: https://www.frontiersin.org/articles/10.3389/fmars.2020.00361/full#supplementary-material

Figure S1 | The 500 initial representative cluster profiles (iRCPs) organized by width. The x-axis corresponds to width and is set from 0 to 7 km and the y-axis corresponds to depth and is set from −30 to 2 m.

REFERENCES

Anderson, D., Rueda, A., Cagigal, L., Antolinez, J. A. A., Mendez, F. J., and Ruggiero, P. (2019). Time-varying emulator for short and long-term analysis of coastal flood hazard potential. *J. Geophys. Res.* 124, 9209–9234. doi: 10.1029/2019JC015312

Antolínez, J. A. A., Méndez, F. J., Anderson, D., Ruggiero, P., and Kaminsky, G. M. (2019). Predicting climate-driven coastlines with a simple and efficient multiscale model. *J. Geophys. Res.* 124, 1596–1624. doi: 10.1029/2018JF004790

Antolínez, J. A. A., Méndez, F. J., Camus, P., Vitousek, S., González, E. M., Ruggiero, P., et al. (2016). A multiscale climate emulator for long–term morphodynamics (MUSCLE–morpho). *J. Geophys. Res.* 121, 775–791. doi: 10.1002/2015JC011107

Antolínez, J. A. A., Murray, A. B., Méndez, F. J., Moore, L. J., Farley, G., and Wood, J. (2018). Downscaling changing coastlines in a changing climate: the hybrid approach. *J. Geophys. Res.* 123, 229–251. doi: 10.1002/2017JF004367

Arthur, D., and Vassilvitskii, S. (2006). *k-means++: The advantages of careful seeding.* Technical Report. Stanford, CA. Available online at: http://ilpubs.stanford.edu:8090/778/

Asher, S., Niewerth, S., Koll, K., and Shavit, U. (2016). Vertical variations of coral reef drag forces. *J. Geophys. Res.* 121, 3549–3563. doi: 10.1002/2015JC011428

Asher, S., and Shavit, U. (2019). The effect of water depth and internal geometry on the turbulent flow inside a coral reef. *J. Geophys. Res.* 124, 3508–3522. doi: 10.1029/2018JC014331

Becker, J. M., Merrifield, M. A., and Ford, M. (2014). Water level effects on breaking wave setup for Pacific Island fringing reefs. *J. Geophys. Res.* 119, 914–932. doi: 10.1002/2013JC009373

Beetham, E., and Kench, P. S. (2018). Predicting wave overtopping thresholds on coral reef-island shorelines with future sea-level rise. *Nat. Commun.* 9:3997. doi: 10.1038/s41467-018-06550-1

Bosserelle, C., Kruger, J., Movono, M., and Reddy, S. (2015). *Wave Inundation on the Coral Coast of Fiji*. Technical report, Engineers Australia and IPENZ.

Buckley, M., Lowe, R., and Hansen, J. (2014). Evaluation of nearshore wave models in steep reef environments. *Ocean Dyn.* 64, 847–862. doi: 10.1007/s10236-014-0713-x

Buckley, M. L., Lowe, R. J., Hansen, J. E., and Van Dongeren, A. R. (2016). Wave setup over a fringing reef with large bottom roughness. *J. Phys. Oceanogr.* 46, 2317–2333. doi: 10.1175/JPO-D-15-0148.1

Camus, P., Mendez, F. J., Medina, R., and Cofi no, A. S. (2011). Analysis of clustering and selection algorithms for the study of multivariate wave climate. *Coast. Eng.* 58, 453–462. doi: 10.1016/j.coastaleng.2011.02.003

Cheriton, O. M., Storlazzi, C. D., and Rosenberger, K. J. (2016). Observations of wave transformation over a fringing coral reef and the importance of low–frequency waves and offshore water levels to runup, overwash, and coastal flooding. *J. Geophys. Res.* 121, 3121–3140. doi: 10.1002/2015JC011231

Chilunga, F. P., Rodriguez-Llanes, J. M., and Guha-Sapir, D. (2017). Rapid urbanization is linked to flood lethality in the small island developing states (SIDS): a modeling study. *Prehosp. Disast. Med.* 32, S190–S190. doi: 10.1017/S1049023X17005015

Chiri, H., Abascal, A. J., Castanedo, S., Antolínez, J. A. A., Liu, Y., Weisberg, R. H., et al. (2019). Statistical simulation of ocean current patterns using autoregressive logistic regression models: a case study in the Gulf of Mexico. *Ocean Model*. 136, 1–12. doi: 10.1016/j.ocemod.2019.02.010

Cohn, N., and Ruggiero, P. (2016). The influence of seasonal to interannual nearshore profile variability on extreme water levels: modeling wave runup on dissipative beaches. *Coast. Eng.* 115, 79–92. doi: 10.1016/j.coastaleng.2016.01.006

Costa, M. B. S. F., Araújo, M., Araújo, T. C. M., and Siegle, E. (2016). Influence of reef geometry on wave attenuation on a Brazilian coral reef. *Geomorphology* 253, 318–327. doi: 10.1016/j.geomorph.2015.11.001

Day, W. H. E., and Edelsbrunner, H. (1984). Efficient algorithms for agglomerative hierarchical clustering methods. *J. Classif.* 1, 7–24. doi: 10.1007/BF01890115

de Queiroz, B., Scheel, F., Caires, S., Walstra, D.-J., Olij, D., Yoo, J., et al. (2019). Performance evaluation of wave input reduction techniques for modeling inter-annual sandbar dynamics. *J. Mar. Sci. Eng.* 7:148. doi: 10.3390/jmse7050148

Duce, S., Vila-Concejo, A., Hamylton, S. M., Webster, J. M., Bruce, E., and Beaman, R. J. (2016). A morphometric assessment and classification of coral reef spur and groove morphology. *Geomorphology* 265, 68–83. doi: 10.1016/j.geomorph.2016.04.018

Ferrario, F., Beck, M. W., Storlazzi, C. D., Micheli, F., Shepard, C. C., and Airoldi, L. (2014). The effectiveness of coral reefs for coastal hazard risk reduction and adaptation. *Nat. Commun.* 5:3794. doi: 10.1038/ncomms4794

Friedman, J., Hastie, T., and Tibshirani, R. (2001). *The Elements of Statistical Learning, Vol. 1*. New York, NY: Springer series in statistics. doi: 10.1007/978-0-387-21606-5_1

Goodfellow, I., Bengio, Y., and Courville, A. (2016). *Deep Learning*. Cambridge, MA: MIT Press.

Gutierrez, B. T., Plant, N. G., and Thieler, E. R. (2011). A Bayesian network to predict coastal vulnerability to sea level rise. *J. Geophys. Res.* 116. doi: 10.1029/2010JF001891

Gutierrez, B. T., Plant, N. G., Thieler, E. R., and Turecek, A. (2015). Using a Bayesian network to predict barrier island geomorphologic characteristics. *J. Geophys. Res.* 120, 2452–2475. doi: 10.1002/2015JF003671

Guza, R. T., and Feddersen, F. (2012). Effect of wave frequency and directional spread on shoreline runup. *Geophys. Res. Lett.* 39:11607. doi: 10.1029/2012GL051959

Hardy, T. A., and Young, I. R. (1996). Field study of wave attenuation on an offshore coral reef. *J. Geophys. Res.* 101, 14311–14326. doi: 10.1029/96JC00202

Hartigan, J. A. (1975). *Clustering Algorithms*. New York, NY: John Wiley & Sons.

Hartigan, J. A., and Wong, M. A. (1979). Algorithm AS 136: a K-means clustering algorithm. *Appl. Stat.* 28:100. doi: 10.2307/2346830

Herbers, T. H. C., Elgar, S., Guza, R. T., and O'Reilly, W. C. (1995). Infragravity-frequency (0.005–0.05 Hz) motions on the shelf. Part II: Free waves. *J. Phys. Oceanogr.* 25, 1063–1079. doi: 10.1175/1520-0485(1995)025<1063:IFHMOT>2.0.CO;2

Hoeke, R. K., McInnes, K. L., Kruger, J. C., McNaught, R. J., Hunter, J. R., and Smithers, S. G. (2013). Widespread inundation of Pacific islands triggered by distant-source wind-waves. *Glob. Planet. Change* 108, 128–138. doi: 10.1016/j.gloplacha.2013.06.006

Holman, R. A. (1986). Extreme value statistics for wave run-up on a natural beach. *Coast. Eng.* 9, 527–544. doi: 10.1016/0378-3839(86)90002-5

Hunt, I. (1959). Design of seawalls and breakwaters. *J. Waterw. Harb. Div.* 85, 123–152.

Jain, A. K., and Dubes, R. C. (1988). *Algorithms for Clustering Data*. Englewood Cliffs: Prentice Hall.

Klaver, S., Nederhoff, C. M., Giardino, A., Tissier, M. F. S., van Dongeren, A. R., and van der Spek, A. J. F. (2019). Impact of coral reef mining pits on nearshore hydrodynamics and wave runup during extreme wave events. *J. Geophys. Res.* 124, 2824–2841. doi: 10.1029/2018JC014165

Lashley, C. H., Roelvink, D., van Dongeren, A., Buckley, M. L., and Lowe, R. J. (2018). Nonhydrostatic and surfbeat model predictions of extreme wave run-up in fringing reef environments. *Coast. Eng.* 137, 11–27. doi: 10.1016/j.coastaleng.2018.03.007

Longuet-Higgins, M. S., and Stewart, R. W. (1964). Radiation stresses in water waves; a physical discussion, with applications. *Deep Sea Res. Oceanogr. Abstracts* 11, 529–562. doi: 10.1016/0011-7471(64)90001-4

Lowe, R. J., Falter, J. L., Bandet, M. D., Pawlak, G., Atkinson, M. J., Monismith, S. G., et al. (2005). Spectral wave dissipation over a barrier reef. *J. Geophys. Res.* 110. doi: 10.1029/2004JC002711

Lowe, R. J., Shavit, U., Falter, J. L., Koseff, J. R., and Monismith, S. G. (2008). Modeling flow in coral communities with and without waves: a synthesis of porous media and canopy flow approaches. *Limnol. Oceanogr.* 53, 2668–2680. doi: 10.4319/lo.2008.53.6.2668

Madhulatha, T. S. (2012). An overview on clustering methods. *IOSR J. Eng.* 2, 719–725. doi: 10.9790/3021-0204719725

Massel, S. R., and Gourlay, M. R. (2000). On the modelling of wave breaking and set-up on coral reefs. *Coast. Eng.* 39, 1–27. doi: 10.1016/S0378-3839(99)00052-6

McCall, R. T., Masselink, G., Poate, T. G., Roelvink, J. A., Almeida, L. P., Davidson, M., et al. (2014). Modelling storm hydrodynamics on gravel beaches with XBeach-G. *Coast. Eng.* 91, 231–250. doi: 10.1016/j.coastaleng.2014.06.007

Monismith, S. G., Rogers, J. S., Koweek, D., and Dunbar, R. B. (2015). Frictional wave dissipation on a remarkably rough reef. *Geophys. Res. Lett.* 42, 4063–4071. doi: 10.1002/2015GL063804

Murphy, A. H. (1988). Skill scores based on the mean square error and their relationships to the correlation coefficient. *Month. Weather Rev.* 116, 2417–2424. doi: 10.1175/1520-0493(1988)116<2417:SSBOTM>2.0.CO;2

Nwogu, O., and Demirbilek, Z. (2010). Infragravity wave motions and runup over shallow fringing reefs. *J. Waterway Port Coast. Ocean Eng.* 136, 295–305. doi: 10.1061/(ASCE)WW.1943-5460.0000050

Osorio-Cano, J. D., Alcérreca-Huerta, J. C., Mari no-Tapia, I., Osorio, A. F., Acevedo-Ramírez, C., Enriquez, C., et al. (2019). Effects of roughness loss on reef hydrodynamics and coastal protection: approaches in Latin America. *Estuar. Coasts* 42, 1742–1760. doi: 10.1007/s12237-019-00584-4

Pearson, S. G., Storlazzi, C. D., van Dongeren, A. R., Tissier, M. F. S., and Reniers, A. (2017). A Bayesian-based system to assess wave-driven flooding hazards on coral reef-lined coasts. *J. Geophys. Res.* 122, 10099–10117. doi: 10.1002/2017JC013204

Pearson, S. G., van der Lugt, M., van Dongeren, A., Hagenaars, G., and Burzel, A. (2018). *Quick-Scan Runup Reduction Through Coral Reef Restoration in the Seychelles*. Technical report, Deltares.

Péquignet, A., Becker, J. M., Merrifield, M. A., and Boc, S. J. (2011). The dissipation of wind wave energy across a fringing reef at Ipan, Guam. *Coral Reefs* 30, 71–82. doi: 10.1007/s00338-011-0719-5

Plant, N. G., and Holland, K. T. (2011). Prediction and assimilation of surf-zone processes using a Bayesian network: Part I: Forward models. *Coast. Eng.* 58, 119–130. doi: 10.1016/j.coastaleng.2010.09.003

Poelhekke, L., Jäger, W. S., Van Dongeren, A., Plomaritis, T. A., McCall, R., and Ferreira, Ó. (2016). Predicting coastal hazards for sandy coasts with a Bayesian Network. *Coast. Eng.* 118, 21–34. doi: 10.1016/j.coastaleng.2016.08.011

Pomeroy, A., Lowe, R., Symonds, G., van Dongeren, A., and Moore, C. (2012). The dynamics of infragravity wave transformation over a fringing reef. *J. Geophys. Res.* 117. doi: 10.1029/2012JC008310

Quataert, E., Storlazzi, C., Van Rooijen, A., Cheriton, O., and Van Dongeren, A. (2015). The influence of coral reefs and climate change on wave-driven flooding of tropical coastlines. *Geophys. Res. Lett.* 42, 6407–6415. doi: 10.1002/2015GL064861

Rai, P., and Singh, S. (2010). A survey of clustering techniques. *Int. J. Comput. Appl.* 7, 1–5. doi: 10.5120/1326-1808

ReefBase (2019). *A Global Information System for Coral Reefs*. Available online at: http://www.reefbase.org

Reguero, B. G., Secaira, F., Toimil, A., Escudero, M., Díaz-Simal, P., Beck, M. W., et al. (2019). The risk reduction benefits of the Mesoamerican Reef in Mexico. *Front. Earth Sci.* 7:125. doi: 10.3389/feart.2019.00125

Rogers, J. S., Maticka, S. A., Woodson, C. B., Alonso, J. J., and Monismith, S. G. (2018). Connecting flow over complex terrain to hydrodynamic roughness on a coral reef. *J. Phys. Oceanogr.* 48, 1567–1587. doi: 10.1175/JPO-D-18-0013.1

Rogers, J. S., Monismith, S. G., Fringer, O. B., Koweek, D. A., and Dunbar, R. B. (2017). A coupled wave-hydrodynamic model of an atoll with high friction: mechanisms for flow, connectivity, and ecological implications. *Ocean Modell.* 110, 66–82. doi: 10.1016/j.ocemod.2016.12.012

Rueda, A., Cagigal, L., Antolínez, J. A. A., Albuquerque, J. C., Castanedo, S., Coco, G., et al. (2019a). Marine climate variability based on weather patterns for a complicated island setting: the New Zealand case. *Int. J. Climatol.* 39, 1777–1786. doi: 10.1002/joc.5912

Rueda, A., Cagigal, L., Pearson, S., Antolínez, J. A. A., Storlazzi, C., van Dongeren, A., et al. (2019b). HyCReWW: a hybrid coral reef wave and water level metamodel. *Comput. Geosci.* 127, 85–90. doi: 10.1016/j.cageo.2019.03.004

Sallenger, A. H. Jr. (2000). Storm impact scale for barrier islands. *J. Coast. Res.* 16, 890–895. Available online at: www.jstor.org/stable/4300099

Smit, P. B., Stelling, G. S., Roelvink, D., van Thiel de Vries, J., McCall, R., van Dongeren, A., et al. (2010). *XBeach: Non-Hydrostatic Model*. Delft: Delft University of Technology and Deltares.

Smithers, S. G., and Hoeke, R. K. (2014). Geomorphological impacts of high-latitude storm waves on low-latitude reef islands–Observations of the December 2008 event on Nukutoa, Takuu, Papua New Guinea. *Geomorphology* 222, 106–121. doi: 10.1016/j.geomorph.2014.03.042

Stockdon, H. F., Holman, R. A., Howd, P. A., and Sallenger, A. H. (2006). Empirical parameterization of setup, swash, and runup. *Coast. Eng.* 53, 573–588. doi: 10.1016/j.coastaleng.2005.12.005

Storlazzi, C. D., Elias, E., Field, M. E., and Presto, M. K. (2011). Numerical modeling of the impact of sea-level rise on fringing coral reef hydrodynamics and sediment transport. *Coral Reefs* 30, 83–96. doi: 10.1007/s00338-011-0723-9

Storlazzi, C. D., Elias, E. P. L., and Berkowitz, P. (2015). Many atolls may be uninhabitable within decades due to climate change. *Sci. Rep.* 5:14546. doi: 10.1038/srep14546

Storlazzi, C. D., Gingerich, S. B., van Dongeren, A., Cheriton, O. M., Swarzenski, P. W., Quataert, E., et al. (2018). Most atolls will be uninhabitable by the mid-21st century because of sea-level rise exacerbating wave-driven flooding. *Sci. Adv.* 4:eaap9741. doi: 10.1126/sciadv.aap9741

Storlazzi, C. D., Ogston, A. S., Bothner, M. H., Field, M. E., and Presto, M. K. (2004). Wave- and tidally-driven flow and sediment flux across a fringing coral reef: Southern Molokai, Hawaii. *Continent. Shelf Res.* 24, 1397–1419. doi: 10.1016/j.csr.2004.02.010

Storlazzi, C. D., Reguero, B. G., Cole, A. D., Lowe, E., Shope, J. B., Gibbs, A. E., et al. (2019). *Rigorously Valuing the Role of U.S. Coral Reefs in Coastal Hazard Risk Reduction*. Technical report, US Geological Survey. doi: 10.3133/ofr20191027

Tajima, Y., Shimozono, T., Gunasekara, K. H., and Cruz, E. C. (2016). Study on locally varying inundation characteristics induced by Super Typhoon Haiyan. Part 2: Deformation of storm waves on the beach with fringing reef along the East Coast of Eastern Samar. *Coast. Eng. J.* 58:1640003. doi: 10.1142/S0578563416400039

UNFPA (2014). *Population and Development Profiles: Pacific Island Countries*. Technical report, United Nations Population Fund.

UNISDR (2015). *Sendai Framework for Disaster Risk Reduction 2015 - 2030*. Technical report, United Nations Office for Disaster Risk Reduction.

van Dongeren, A., Lowe, R., Pomeroy, A., Trang, D. M., Roelvink, D., Symonds, G., et al. (2013). Numerical modeling of low-frequency wave dynamics over a fringing coral reef. *Coast. Eng.* 73, 178–190. doi: 10.1016/j.coastaleng.2012.11.004

Vitousek, S., Barnard, P. L., Fletcher, C. H., Frazer, N., Erikson, L., and Storlazzi, C. D. (2017). Doubling of coastal flooding frequency within decades due to sea-level rise. *Nature* 7:1399. doi: 10.1038/s41598-017-01362-7

Yao, Y., Huang, Z., Monismith, S. G., and Lo, E. Y. M. (2012). 1DH Boussinesq modeling of wave transformation over fringing reefs. *Ocean Eng.* 47, 30–42. doi: 10.1016/j.oceaneng.2012.03.010

Zahn, C. T. (1971). Graph-theoretical methods for detecting and describing gestalt clusters. *IEEE Trans. Comput.* 100, 68–86. doi: 10.1109/T-C.1971.223083

Zhu, G., Ren, B., Wang, Y., and Wang, C. (2019). "Experimental research of wave transformation on porous coral reef," in *International Conference on Offshore Mechanics and Arctic Engineering, Vol. 58769* (Glasgow: American Society of Mechanical Engineers), V001T01A031. doi: 10.1115/OMAE2019-96582

Conflict of Interest: The authors declare that the research was conducted in the absence of any commercial or financial relationships that could be construed as a potential conflict of interest.

Copyright © 2020 Scott, Antolinez, McCall, Storlazzi, Reniers and Pearson. This is an open-access article distributed under the terms of the Creative Commons Attribution License (CC BY). The use, distribution or reproduction in other forums is permitted, provided the original author(s) and the copyright owner(s) are credited and that the original publication in this journal is cited, in accordance with accepted academic practice. No use, distribution or reproduction is permitted which does not comply with these terms.

frontiers in Marine Science

ORIGINAL RESEARCH
published: 03 June 2020
doi: 10.3389/fmars.2020.00351

In situ Observations of Wave Transformation and Infragravity Bore Development Across Reef Flats of Varying Geomorphology

Olivia M. Cheriton, Curt D. Storlazzi and Kurt J. Rosenberger*

Pacific Coastal and Marine Science Center, U.S. Geological Survey, Santa Cruz, CA, United States

The character and energetics of infragravity ("IG," 25 s < period < 250 s) and very-low frequency ("VLF," period > 250 s) waves over coral reef flats can enhance shoreline erosion or accretion, and also govern extreme shoreline events such as runup, overwash, and flooding on coral reef-lined coasts. Here we use *in situ* wave measurements collected along cross-reef transects at 7 sites on Pacific islands with varying reef geomorphologies to examine under what conditions IG waves occur and what factors enhance their irregularity. In general, a greater fraction of total wave energy was transferred to the IG band on reefs with steeper fore reef slopes and shallower reef flats. The IG wave amplitudes scaled with increasing water levels, but it was primarily at lower water levels when these waves became pitched onshore (negatively asymmetrical) and peaked (positively skewed). However, our results also highlight the importance of reef-flat width and slope as important morphological controls on IG waves, as the most asymmetric, bore-like, IG waves occurred on the wider reef flats, and the most skewed IG waves at the site with the steepest reef-flat. On the wider reef flats, IG wave-wave capture was observed during periods of large offshore wave forcing and enhanced VLF wave energy. Because similar IG wave motions over plane beaches enhance sea-swell ("SS," period < 25 s) bore-merging in the surf zone, we posit that VLF waves over reef flats may facilitate IG bore merging, and this may lead to larger, more pitched-onshore bores at the shoreline. In addition, greater IG wave heights appear to support the transmission of larger secondary short-period waves over the reef flat, independent of overall water levels. As irregular IG waves may be strong drivers of cross-reef sediment transport as well as runup, understanding the conditions and reef geomorphologies that lead to low-frequency, energetic bores on reef flats is critical to forecasting how coral reef-lined coasts will respond to sea-level rise and climate change.

Keywords: reef flat, infragravity waves, wave asymmetry, wave skewness, bore merging, water levels

OPEN ACCESS

Edited by:
Hajime Kayanne,
The University of Tokyo, Japan

Reviewed by:
Charles Alan Jacoby,
St. Johns River Water Management District, United States
Anne-Christine Pequignet,
Met Office, United Kingdom

****Correspondence:***
Olivia M. Cheriton
ocheriton@usgs.gov

Specialty section:
This article was submitted to Coral Reef Research, a section of the journal Frontiers in Marine Science

Received: *18 November 2019*
Accepted: *27 April 2020*
Published: *03 June 2020*

Citation:
Cheriton OM, Storlazzi CD and Rosenberger KJ (2020) In situ Observations of Wave Transformation and Infragravity Bore Development Across Reef Flats of Varying Geomorphology. Front. Mar. Sci. 7:351. doi: 10.3389/fmars.2020.00351

INTRODUCTION

The quality and degree of irregularity in surface gravity waves are considered important factors in sediment transport in shallow coastal environments. A purely symmetrical wave produces symmetric underlying water velocities, such that the positive phase onshore flow is balanced by the negative phase offshore flow and the net transport by the wave is effectively zero. Conversely, non-linear or irregular waves have corresponding asymmetric velocities and accelerations that can lead to a non-zero net transport. But predicting this transport under irregular surface waves is not straightforward, not only because of the non-linear interactions between the different types of fluid motions (e.g., orbital motions, currents, and small-scale turbulence), but also phase-lag effects with bed shear stress, sediment entrainment and settling rates, which all vary with sediment types and seafloor morphology. For example, finer sediment may have opposing net transport to coarser sediment simply owing to the varying time each grain size spends in suspension (i.e., different settling velocities).

The degree of irregularity in surface waves is often evaluated by quantifying the skewness (peaked-ness) and asymmetry (forward or backward pitch) of the waves. As incident, short-period waves approach a shoreline, the shoaling seafloor causes the waves to become peaked (skewed) and pitched forward (asymmetric). Skewed waves have strong onshore velocities associated with the crest and weaker offshore velocities under the troughs. Enhanced bed shear stresses from the strong onshore velocities mobilize sediment from the bed, and the velocity imbalance creates a net transport of the suspended material, that can be either onshore (e.g., Hoefel and Elgar, 2003; Silva et al., 2011) or offshore (Ruessink et al., 2009), depending on the sediment type and background flow. Waves that have no skewness, but are asymmetric are thought to have relatively negligible net transport because, although velocities increase faster (greater acceleration) during the positive phase, this is counteracted by the longer duration of the negative phase tail of the wave. However waves in shallow water typically exhibit both skewness and asymmetry. Skewed, asymmetric waves have been studied for plane beaches, using flume studies (Grasso et al., 2011), field observations (Elgar et al., 2001), and models (Ruessink et al., 2009). These studies found that, due to phase-lag effects, waves dominated by velocity skewness lead to offshore net transport, but with sufficiently large wave asymmetry, this effect diminishes and net transport can be onshore.

Research into irregular waves on coasts fronted by coral reefs is still a relatively emergent field of research. Findings from plane beach investigations are not necessarily transferable to fringing reef-lined coasts for several reasons. First, the bathymetric profiles of reef-lined coasts are starkly different from those of gently sloping beaches; the fore reef slopes tend to be steep, with an abrupt shift at the reef crest to shallow, gentle-sloping reef flat platforms and/or lagoons. Secondly, coral reefs can have much greater bed roughness, as well as greater variations in bed roughness across their profiles, varying between the extremes of relatively smooth "pavement" reefs with little coral coverage to rough regimes with high coral coverage or/and bedrock rugosity. As a result of the high heterogeneity in bathymetric slope and bed roughness, the propagation and transformation of waves from offshore to onshore across reefs differs from that of plane beaches. As offshore sea-swell ("SS," periods $T < 25$ s) waves approach a reef-lined coast, a relatively steep fore reef leads to a shallow reef crest, where the waves break and the majority of the sea-swell wave energy is dissipated (Lowe et al., 2005). Through this breakpoint-forced momentum flux (Pomeroy A. et al., 2012) and non-linear wave-wave interactions (Nwogu and Demirbilek, 2010), the waves reform into a mixture of short- and long-period waves that propagate shoreward across the reef, typically leading to the characteristic biomodal wave spectrum over the reef flat (e.g., Lowe et al., 2005; van Dongeren et al., 2013). On certain reefs, these longer-period infragravity ($25 \text{ s} < T < 250$ s) and very-low frequency ("VLF," $T > 250$ s) waves dominate (Péquignet et al., 2009; Cheriton et al., 2016). In addition, the shallow reef platforms can engender both standing and resonant wave behavior (Péquignet et al., 2009; Nwogu and Demirbilek, 2010; Pomeroy A. W. M. et al., 2012; Gawehn et al., 2016; Buckley et al., 2018).

It is known that waves driven by extreme events such as storms (Stoddart, 1971; Bayliss-Smith, 1988; Scoffin, 1993; Etienne and Terry, 2012) and tsunamis (Kench et al., 2008) can either erode or accrete shorelines of coral reef-lined coasts, but the degree to which chronic exposure to skewed, asymmetrical waves drives sediment transport across reefs remains unclear. A flume study by Pomeroy et al. (2015) found that, compared to bedload and the mean Eulerian flow, IG wave skewness and asymmetry were the strongest drivers of cross-shore sediment transport over the simulated reef flat. Additional laboratory and modeling studies have investigated how different reef morphologies control the resulting IG wave motions and irregularity over reefs. The slope of the fore reef is now understood to be a primary control on infragravity wave generation over reefs, with the most energetic IG motions associated with slopes > 1/6 (Masselink et al., 2019). Although steeper fore reefs may generate larger IG waves, steeper fore-reef slopes may also act to reduce the asymmetry of the reef flat IG waves (Chen et al., 2019). Reef-flat bed roughness also has a small effect, whereby smoother beds lead to more asymmetrical waves, due to decreased dissipation from turbulence and bottom friction (Quiroga and Cheung, 2013; Chen et al., 2019). Interestingly, these factors – the fore-reef steepness and bed roughness – were found to have negligible effects on wave skewness (Chen et al., 2019).

MATERIALS AND METHODS

Reef Locations

We collected wave observations from 7 cross-shore transects over fringing reefs on the islands of Kwajalein and Roi-Namur in the Republic of the Marshall Islands, as well as the U.S. Hawaiian Islands of Maui and Molokai (**Table 1** and **Figures 1A,D,G,J**). Roi-Namur and Kwajalein are islands at

TABLE 1 | List of our 7 study sites, providing locations, latitudes and longitudes, as well as reef characteristics.

Site name	Island	Latitude, longitude	Deployment period	Forereef slope	Reef flat width (m)	Reef flat slope	Reef flat water depth (m)
Kwaj-W	Kwajalein, RMI	8.72°N, 167.74°E	4 months (Nov 2014 – Feb 2015)	1:15–1:12*	90	1:80	0.0–1.1
Kwaj-E	Kwajalein RMI	8.72°N, 167.74°E	4 months (Nov 2014 – Feb 2015)	1:11–1:9*	105	1:200	0.0–1.5
Roi-W	Roi-Namur, RMI	9.40°N, 167.46°E	4 month (Nov 2014 – Feb 2015)	1:8	250	1:900	0.0–1.7
Roi-E	Roi-Namur, RMI	9.40°N, 167.46°E	4 months (Nov 2014 – Feb 2015)	1:6	300	1:550	0.0–1.5
Lahaina	Maui, USA	20.86°N, 156.68°W	3 months (Jul – Sep 2017)	1:18	200	1:330	0.5–1.5
Ukumehame	Maui, USA	20.79°N, 156.58°W	2 months (Jul – Aug 2017)	1:14	270	1:500	0.7–1.6
Waiakane	Molokai, USA	21.08°N, 157.15°W	4 months (Jun – Sep 2018)	1:12	750	1:1300	0.6–1.6

*Reef flat width is approximate (± 20 m) distance from the foot of the beach berm to the reef crest. *Kwajalein fore reef slopes are estimates; see section Materials and Methods.*

the northern and southern portions of Kwajalein Atoll, located in the Equatorial Pacific. The transects were on the ocean-side perimeter of both islands, which are lined by a relatively horizontal reef flat that is often fully exposed at low tide. At the reef crest, the reef platform abruptly steepens to the fore reef that has higher morphological relief and greater coral coverage. The Lahaina and Ukumehame transects were on the western side of Maui, Hawaii, United States. These reefs have less steep fore reefs, and deeper reef flats, with variable relief. The final transect of Waiakane was on the southwestern coast of Molokai, Hawaii, United States. This site has a broad reef flat characterized by high-relief coral on the fore reef and outer reef flat, transitioning to relatively smooth, muddy substrate by the inner reef flat.

For all sites except Kwajalein, the fore-reef steepness was determined by the slope between the fore-reef seabed at 20 and 5 m depth. For Kwajalein, since we lack bathymetry for the fore reef, the fore-reef steepness was estimated from the slope of the fore-reef pressure sensor location to the reef crest, using two different reef crest depths: the depth of the outer reef-flat sensor (steeper slope) and the depth given by linear interpolation between the outer reef-flat and the fore-reef pressure sensors (less-steep slope). The resulting fore-reef slope ranges are in accordance with the divers' visual observations of this site compared to the others. The reef-flat bed slope was determined using the distance and change in bed elevation between the outer and inner reef-flat sites.

Wave Measurements

Each shore-normal transect consisted of 4–5 RBR pressure gages (solo Dwave sensors for Kwajalein W and Roi-Namur W, and Virtuoso Dwave sensors for the other sites), with one or two placed on the fore reef, and three across the reef flat, from the outer reef flat just onshore of the reef crest to the shoreline (**Table 1** and **Figures 1A,D,G,J**). At all sites except for Waiakane, pressure measurements were collected at 2 Hz over a 34 min burst (4,096 samples). At Waiakane, the sensors sampled continuously at 4 Hz; for processing, these records were partitioned into hourly segments (14,400 samples). At Roi-Namur E, the fore-reef pressure sensor was fouled for a portion of the deployment; for these missing data, we used the pressure bursts from a Nortek Acoustic Wave and Current (AWAC) profiler that was deeper on the fore reef at 20 m depth, and ∼670 m to the west off the Roi-Namur E transect line. The AWAC pressure was collected at 1 Hz over a 34 min burst (2,048 samples), but these bursts started 5 min after the RBR pressure gages.

The following method for calculating bulk wave statistics was applied across all pressure sensors. First, each pressure record was corrected for atmospheric pressure using hourly measurements obtained from nearby weather stations: the Kwajalein Bucholz Army Airfield weather station for the Kwajalein and Roi-Namur sites; the National Oceanic and Atmospheric Administration's (NOAA) Kahului Harbor station (KLIH1)[1] for the Lahaina and Ukumehame sites; and, for the Waiakane site, a weather station we installed near the Kaunakakai Harbor, approximately 13 km east of the study site. After subtracting the atmospheric pressure, the resultant sea pressure values were used to find the one-dimensional energy spectra, *S(f)*, using the Welch's averaged modified periodogram method, which utilizes a Hamming window (length of 1/2 the number of burst samples) with 50% overlap. Pressure response factor corrections were applied to the spectra, which were then partitioned along SS, IG, and VLF frequency bands. Significant wave height was determined as $H_s = 4\sqrt{\int_{f_2}^{f_1} S(f)\,df}$, and the root-mean-squared wave height was computed as $H_{rms} = \sqrt{8\int_{f_2}^{f_1} S(f)\,df}$, where f_1 and f_2 are the lower and upper frequency limits for each wave band, and *S(f)* is the one-dimensional energy spectra, as stated above. The peak period, T_p, was identified as the frequency associated with the peak energy in each band, and the total energy associated with each frequency band was determined as $E = 0.5(H_{rms}/2)^2$.

The wave envelope for a given fore-reef water level burst record, η, was found using $A_t = \sqrt{\mathcal{H}^* i\mathcal{H}}$, where $\mathcal{H}$ is the Hilbert transform of the high-pass filtered η (SS frequencies), and iH represents the complex conjugate. Resonance periods for the reefs were determined using the open basin approximation for the fundamental mode: $T_0 = 4L/\sqrt{gh}$, where L is the width of the reef flat, g is gravitational acceleration, and h is the mean water depth across the reef flat.

[1] www.ndbc.noaa.gov

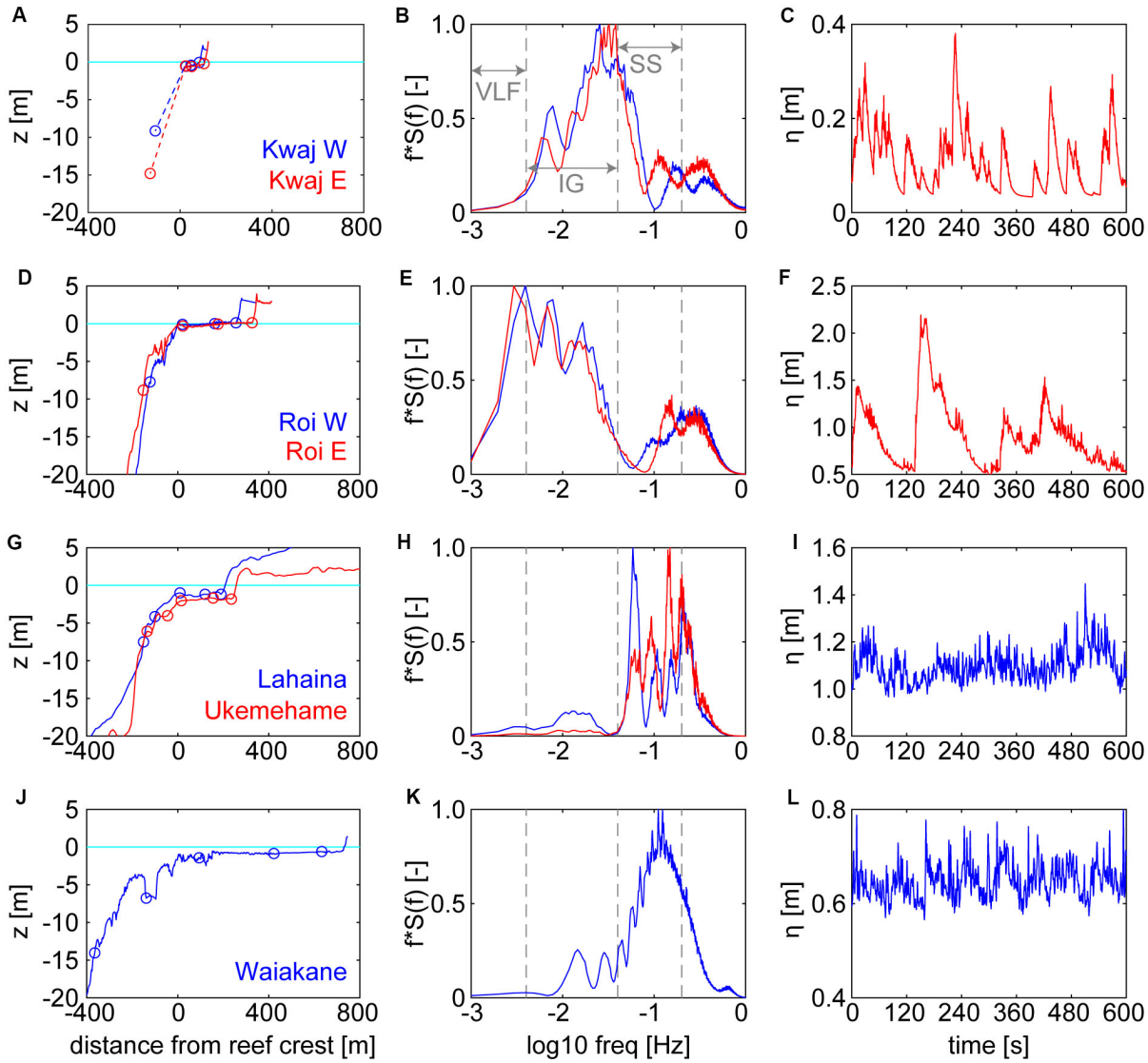

FIGURE 1 | Varying reef geometries, and the subsequent wave energy partitioning and wave characteristics. **(A,D,G,J)** Reef bathymetric profiles and sensor locations (circles) with distance from the reef crest (positive is toward shore) and colors corresponding to sites. For Kwajalein reefs, the dashed line indicates region where no bathymetry was available. **(B,E,H,K)** Mean variance-preserved energy density spectra from the inner reef-flat sites, normalized by the maximum mean energy; colors correspond to sites in left-hand column. Gray vertical dashed lines indicate frequency bands of sea-swell (SS), infragravity (IG), and very-low frequency (VLF) waves. **(C,F,I,L)** examples of 600 s time series for water levels to show the types of irregular waves at each site; for rows that display two sites, only one example is shown for clarity, but it is representative of the wave character at the site not shown.

Infragravity Bore Detection

The IG wave skewness, *Sk*, and asymmetry, *As*, were found using the third order moments of the band-pass filtered (IG frequencies) water level, η (after Pomeroy et al., 2015):

$$Sk = \frac{\langle \tilde{\eta}^3 \rangle}{\langle \tilde{\eta}^2 \rangle^{3/2}} \quad (1)$$

$$As = \frac{\langle \mathcal{H}(\tilde{\eta})^3 \rangle}{\langle \tilde{\eta}^2 \rangle^{3/2}} \quad (2)$$

Where $\langle\ \rangle$ designates the time average over each water level (η) burst, $\mathcal{H}$ is the Hilbert transform, and the "∼" indicates the deviation from the burst mean. This formulation assumes that the free-surface elevation can be used as a proxy for velocity patterns under the wave. Overall, the degree of irregularity derived from surface elevation follows the same trend as that from near-bed velocities, but the magnitudes of the skewness and asymmetry tend to be over-predicted when relying on the surface elevation (Michallet et al., 2011). Here, we consider IG waves with $As < -0.25$ to be bores (pitched onshore), and IG waves with $Sk > 0.5$ to be strongly peaked.

In addition, each individual IG wave with height > 0.05 m was analyzed to quantify the number and size of the short-period "secondary" waves riding on the IG waves (**Figure 2**). For each

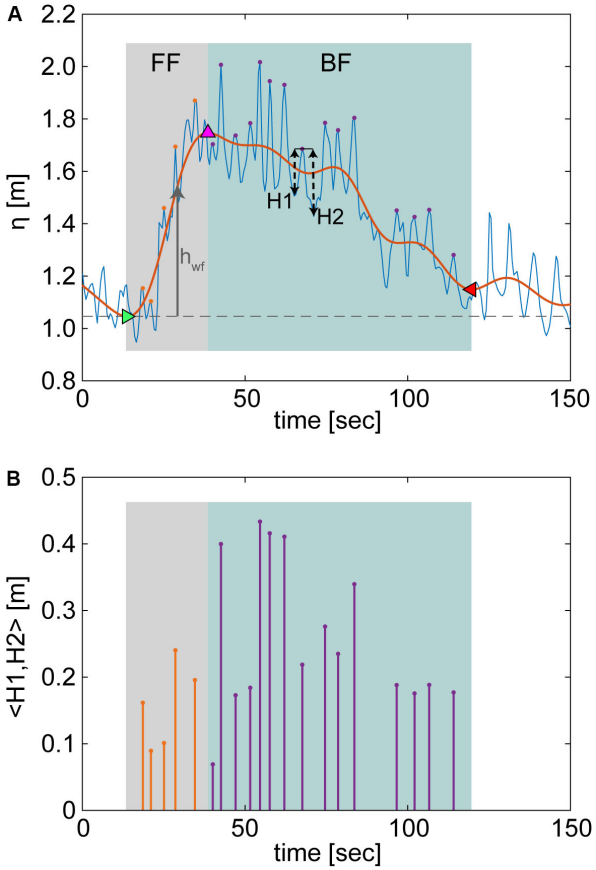

FIGURE 2 | Individual infragravity (IG) waves evaluated for different waveform geometries and characteristics. **(A)** An example IG wave with full water level (blue line) and the IG waveform (orange line), with the leading trough (green triangle), peak (pink triangle), and trailing trough (red triangle) of the waveform also indicated. For each IG wave over 0.05 m in trough-to-peak height, we cataloged the number and heights of each of the short-period waves riding on the front face ("FF") and back face ("BF") sections and the corresponding IG waveform height (h_{wf}, gray arrow) above the leading trough water level (gray dashed line) for each of these secondary waves. The secondary short-period wave heights were found by averaging the vertical distances from the peak to the leading ("H1") and trailing troughs ("H2"). Only secondary waves with periods > 1.5 s and mean heights > 0.05 m were considered. The resulting secondary wave heights for the example are shown in **(B)** for both the FF (orange stems) and BF (purple stems).

hourly water level burst, a band-pass filter was performed using cut-off frequencies of 0.004 and 0.04 Hz to separate the IG signal. We identified trough-peak pairs with heights > 0.05 m in this band-pass filtered water level. Each waveform's trailing trough was found by iteratively evaluating the troughs after the peak and, once the vertical distance between the leading and trailing trough was less than twice the standard deviation of the front-facing height, that trailing trough was considered the end point of the waveform. This criterion ensures that the trailing trough is sufficiently close (in vertical distance) to the leading trough, but also allows the trailing trough to be more elevated than the leading one, which was often the case (e.g., **Figure 2A**).

When IG waves are pitched onshore (negatively asymmetrical), the back face of the wave gradually trails off and it is not always clear what point should mark the true termination of a waveform. As such, our algorithm is conservative and tends to terminate the waveforms earlier than would be done by visual inspection. The portion of the IG wave from the leading trough to peak was considered the front face ("FF") and the section from the peak to the trailing trough the back face ("BF"). For both the FF and BF sections of the waveform, the unfiltered water level was used to identify the presence and heights of the short-period secondary waves (**Figure 2A**). The number of secondary waves for the FF and BF wave sections were cataloged, as well as their heights, which we defined as the average between the leading trough-to-peak ("H1") and trailing trough-to-peak height ("H1" and "H2," respectively; **Figure 2B**). We only considered secondary waves that met 3 criteria: (1) mean heights > 0.05 m; (2) periods > 1.5 s; (3) for FF secondary waves, H2/H1 > 0.5, and for BF secondary waves, H1/H2 > 0.5, to account for the changing IG waveform. For each secondary wave, the corresponding IG waveform height above the leading trough, h_{wf}, was recorded (**Figure 2A**).

RESULTS

General Reef Characteristics

The 7 reef transects were taken from 4 different islands, each with different reef morphologies, in terms of reef flat depth, width, roughness, and fore-reef slope (**Figure 1** and **Table 1**). The Kwajalein reef had the shallowest and narrowest reef flat, which was also a relatively smooth pavement-like substrate (**Figure 1A**). The majority of incident wave energy was dissipated at the reef crest, with large infragravity waves over the reef flat. Because the reef platform is so narrow, it cannot support VLF motions (**Figure 1B**). When onshore-pitched, bore-like waves occurred at this site, they tended to have periods in the "high" IG band, ∼50–100 s (**Figure 1C**). The Roi-Namur reef flat is similarly shallow and smooth, but 2–3x wider than the Kwajalein reef flat and with slightly steeper fore reefs (**Figure 1D** and **Table 1**). At these sites, wave energy over the reef flat extended from the IG into the VLF band (**Figure 1E**). Pitched onshore, highly skewed waves were more common at this site and were generally larger and longer period (∼200–300 s), in the "low" IG band (**Figure 1F**). The two Maui reefs, Lahaina and Ukumehame are of medium width, but have deeper reef flats and more gently sloping fore reefs (**Figure 1G** and **Table 1**). The deeper reef-flat water depths allowed the majority of wave energy to remain in the SS band, with only a small amount of IG wave energy at Lahaina (**Figure 1G**). At these Maui sites, IG bores were rare and had small amplitudes (**Figure 1I**). The last site at Waiakane, Molokai, has a relatively gradual fore-reef slope and a moderately deep, but very broad reef flat (more than 2x the width of our other sites; **Figure 1J**). Again, much of the reef-flat wave energy was condensed into the SS band due to the deeper depths (**Figure 1H**). Small IG bores occurred at this site, but they were uncommon and smaller than the SS waves (**Figure 1L**).

Wave Transformation

The majority of incoming wave energy was dissipated at the reef crest and continued to decrease across the reef flat with distance from the reef crest (**Figure 3A**). The shallower reef flats (Kwajalein and Roi-Namur sites) saw the greatest drop in proportion of SS wave energy, and a corresponding large increase in the fraction of IG energy (**Figures 3B,C**). The Roi-Namur reef flats were the only sites with a notable increase in VLF wave energy (**Figure 3D**), due to their shallow water depths, strong offshore waves, and sufficiently broad reef platforms to support standing waves and other VLF patterns (Cheriton et al., 2016; Gawehn et al., 2016). There is considerable scatter in the range of IG and VLF wave energy at the Kwajalein and Roi-Namur innermost reef flat sites (± 1 standard deviation in **Figures 3C,D**); this arises because these sites were subject to a greater range of offshore wave forcing.

The deeper reef flats of Lahaina and Ukumehame also had a decrease in SS wave energy and an increase in IG energy toward shore, but with less change over the same distance from the reef crest (**Figures 3B,C**). The broad reef flat of Waiakane exhibited an overall slight decrease in wave energy from the reef crest toward shore, but this site stands out among all our sites

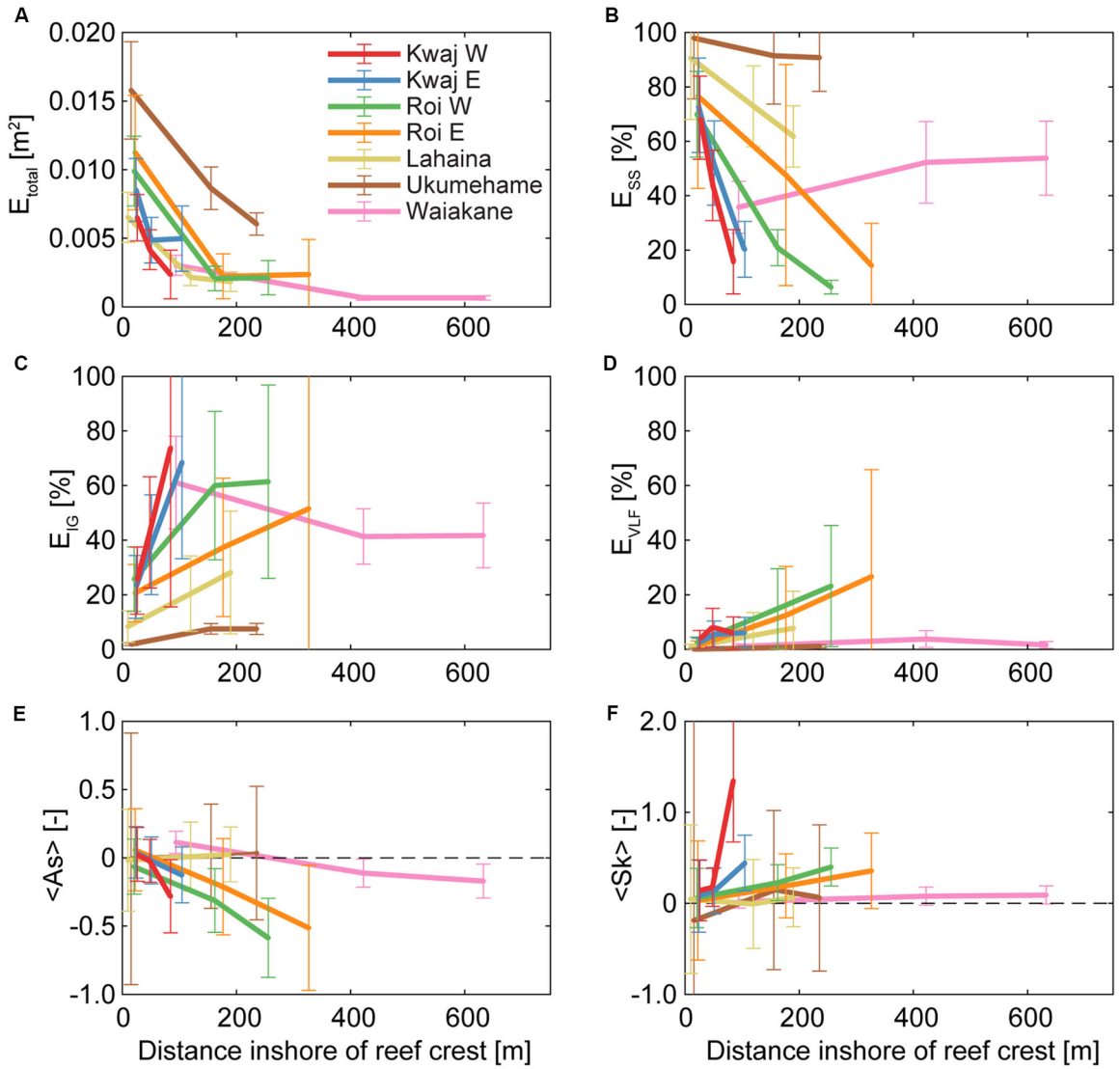

FIGURE 3 | Wave transformation, energy partitioning, and irregularity with distance across the reef flat. For all panels, the error bars indicate the mean ± one standard deviation and the colors correspond to the sites listed in **(A)**. **(A)** Mean wave energy across all frequencies. The fraction of total wave energy in the **(B)** sea-swell (SS), **(C)** infragravity (IG), and **(D)** very-low-frequency (VLF) bands. The mean **(E)** asymmetry and **(F)** skewness are also shown. Results were constrained to mean reef-flat water levels between the (site-specific) 40th and 60th-percentiles, and fore-reef wave power (Hs^2*T_p) between 3 and 30 m^2 s. There is large scatter in the IG and VLF wave energies because of the range of wave conditions captured. With distance from the reef crest toward shore, overall wave energy decreases, the proportion of IG and VLF wave energy increases, and IG waves generally become increasing pitched forward (negatively asymmetrical) and peaked (positively skewed).

for exhibiting an increase in proportional SS wave energy from the outer to the mid reef flat, which is sustained toward shore. We attribute this SS wave energy to wind-generated waves over the reef flat. The Waiakane reef is exposed to strong diurnal wind patterns, and because its broad reef flat provides sufficient fetch, these wind-generated short-period waves contribute to the increase in proportion of short-period wave energy over the outer portion of the reef flat, which is then maintained across the reef flat. These short-period, wind-generated wave heights over the Waiakane reef vary with a diurnal pattern, with maximum reef-flat wave heights coinciding with the peak diurnal winds (data not shown). At both Kwajalein and Roi-Namur, IG wave skewness and (negative) asymmetry increased with distance from the reef crest (**Figures 3E,F**). The deeper reefs of Lahaina, Ukumehame, and Waiakane had no significant change in IG wave skewness across their reef flats, and Waiakane only had a slight decrease in asymmetry (from positive to ∼0).

Infragravity Asymmetry and Skewness

Reef flat IG wave asymmetry and skewness are strongly controlled by both geomorphic features of the reef as well as reef flat submergence and offshore wave forcing. We defined bores as waves with negative asymmetry (pitched onshore) of $As < -0.25$, and strongly peaked waves as those with $Sk > 0.5$. The largest IG waves occurred on the reefs with the steepest fore-reefs: Kwajalein W, Kwajalein E, Roi-Namur W, and Roi-Namur E (**Figures 4A–G**). The most pitched-onshore IG waves occurred on the Kwajalein and Roi-Namur inner reef flats. But strongly asymmetrical IG bores only coincided with low reef-flat submergence at the Kwajalein reefs, whereas at the Roi-Namur sites, these IG bores occurred across a range of water levels (**Figures 4H–K**). With increasing reef-flat submergence, greater fore-reef wave heights were required to produce pitched-onshore IG waves at the inner reef flat (**Figures 4H–N**). At the Kwajalein and Roi-Namur sites, the majority of IG bores (>60%) were strongly peaked as well. Highly skewed ($Sk > 0.5$) IG waves were most prevalent on the narrow Kwajalein reef flats, also during conditions of low reef submergence (**Figures 4O,P**). Skewed IG waves also occurred on the Roi-Namur W inner reef during large offshore wave conditions. In general, IG waves on the deeper reefs of Lahaina, Ukumehame, and Waiakane were smaller and were less irregular.

The relationship between reef flat submergence and inner reef-flat IG wave heights was examined relative to the fore-reef wave heights, Hs_{fr}, for the four reefs with the largest IG waves: Kwajalein W, Kwajalein E, Roi-Namur W, and Roi-Namur E (**Figure 5**). To allow comparison to previous laboratory and modeling study results (e.g., Yao et al., 2018; Masselink et al., 2019), an adjusted reef flat submergence of h_{reef-a} was calculated by shifting the fore-reef tide levels according to the h_{reef} when fore-reef tide = 0 (the intercept of a linear fit). Though the absolute IG wave heights were greatest on Roi-Namur, the largest IG waves relative to the fore-reef wave heights, Hs_{IG}/Hs_{fr}, occurred on Kwajalein (**Figure 5**), which is unexpected given the slightly steeper fore-reef at the Roi-Namur sites. The narrow reef platform of Kwajalein also had a fairly linear relationship between Hs_{IG}/Hs_{fr} and relative reef submergence, h_{reef-a}/Hs_{fr},

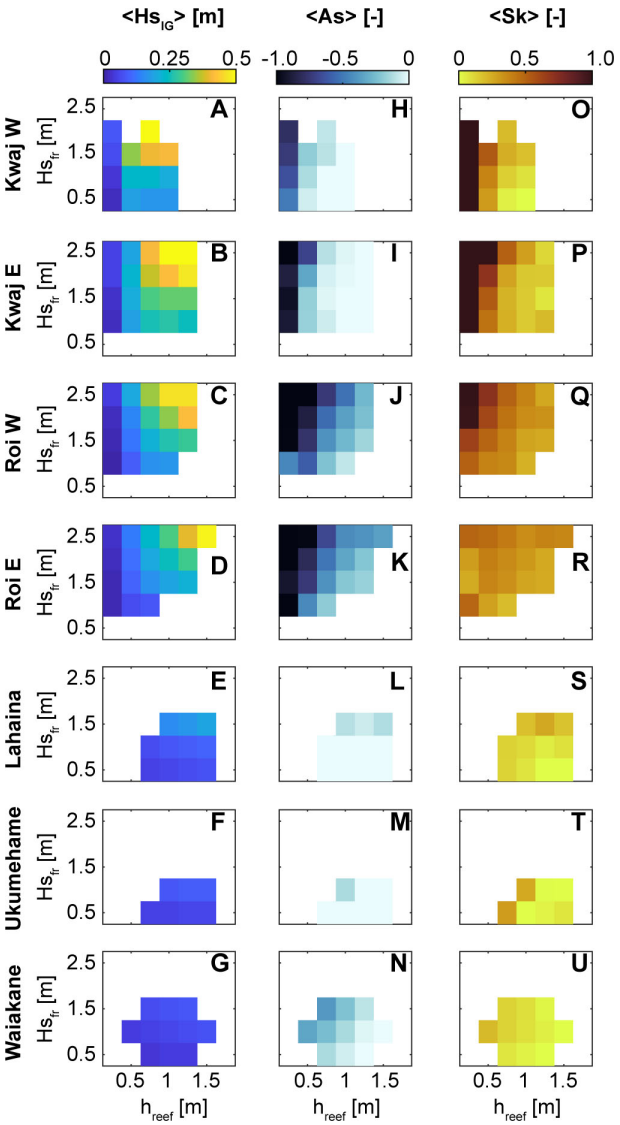

FIGURE 4 | Mean height (Hs_{IG}), asymmetry (As), and skewness (Sk) of inner reef-flat infragravity (IG) waves with different reef submergence (h_{reef}) and fore-reef wave heights (Hs_{fr}). Each row is a different site. Values are only displayed if there were at least 10 water level bursts for the given h_{reef} and Hs_{fr} levels. **(A–G)** Mean IG wave heights. **(H–N)** Mean asymmetry of the IG waves; darker blue indicate more steep-faced, bore-like waves. **(O–U)** Mean skewness of the IG waves; darker reds indicate more peaked waves. Lower reef flat submergence and larger offshore waves generally produce the most negatively asymmetrical (pitched onshore) and positively skewed IG waves in the inner reef flat.

such that greater reef-flat submergence consistently resulted in larger IG waves (**Figures 5A,B**). This was not the case on Roi-Namur, where, in the absence of energetic offshore wave forcing, greater h_{reef-a} only led to larger IG waves to a certain point ($h_{reef-a}/Hs_{fr} \sim 0.75$), after which the relative IG wave heights no longer increased with greater h_{reef-a} (**Figures 5C,D**).

The degree of negative asymmetry and positive skewness for the reef-flat IG waves generally increases with decreasing

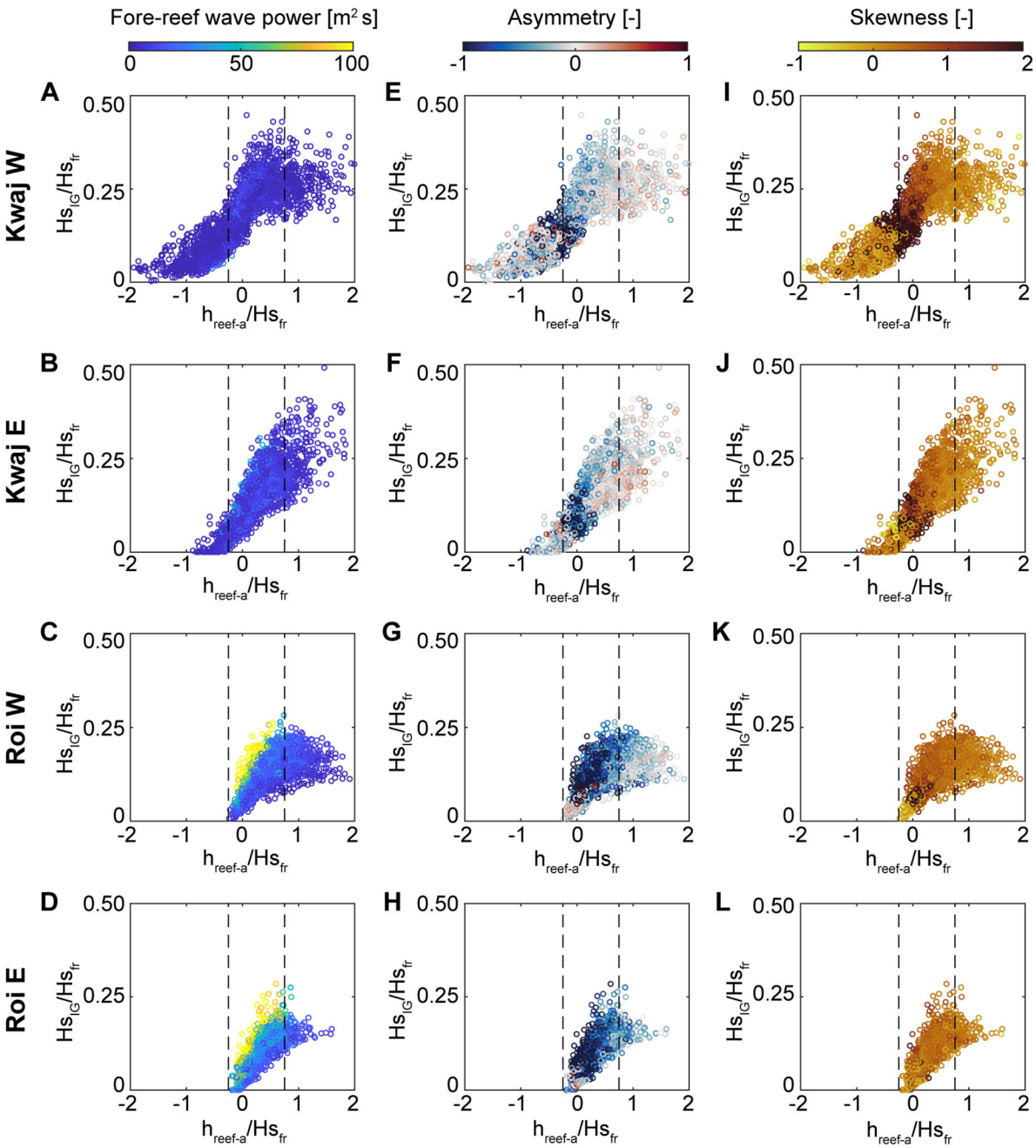

FIGURE 5 | Evaluation of the relationship between mean reef-flat infragravity wave heights (Hs_{IG}) and the ratio of the water level relative to the reef flat (h_{reef-a}), normalized by fore-reef wave heights (Hs_{fr}) for the four sites with large infragravity waves: Kwajalein W, Kwajalein E, Roi-Namur W, and Roi-Namur E reefs (each site is a row). The h_{reef-a} is the reef submergence related to fore-reef water levels above and below the mean; this was done in order to allow comparison with previous modeling results from Masselink et al. (2019). **(A–D)** Color-scale indicates the fore-reef wave power. **(E–H)** Color-scale indicates asymmetry, with darker blues indicating more pitched-onshore, bore-like IG waves. **(I–L)** Color-scale indicates skewness, with darker reds indicating more peaked waves. Masselink et al. (2019) reported the largest reef flat IG waves occur when the ratio of h_{reef-a} to Hs_{fr} was between –0.25 and 0.75 (vertical dashed lines). In general, with increasing h_{reef-a}/Hs_{fr}, the relative reef-flat Hs_{IG} become larger, and less pitched-onshore (asymmetry is less negative), and skewness lessens. Although we find the –0.25 to 0.75 window to encompass the largest relative IG waves on the Roi-Namur reef flats, the largest IG waves on the Kwajalein reefs extend beyond this window. The prevalence of IG waves with $As > 0$ (pitched offshore) at the Kwajalein reefs is due to shoreline IG wave reflection.

relative reef flat water levels (**Figures 5E–L**), with the majority (90%) of highly skewed IG bores occurring between relative reef-flat submergence levels of –0.3 and 0.3 for Kwajalein W, 0 and 0.4 for Kwajalein E, and between 0 and 0.6 for both Roi-Namur sites. Many of the IG waves at the Kwajalein inner reef flat sites displayed positive asymmetry (pitched

offshore), suggesting shoreline reflection of the pitched-onshore IG waves. Using a flume and numerical model, van Dongeren et al. (2007) found a relationship between the proportion of reflected IG waves and a modified surf similar parameter, $\beta_H = (h_x/\omega)\sqrt{g/H_{IG}}$, where h_x is the bed slope and ω is the radial frequency of the IG waves; here, we use the IG wave heights and frequencies from the mid reef-flat sites. A threshold of $\beta_H \sim 1.25$ was found to represent the transition from a less-reflective to a more-reflective shoreline regime (van Dongeren et al., 2007). Using the H_{IG} and ω from the mid reef flat sites, only the two Kwajalein reefs had reflection regimes at the shoreline: Kwajalein W had a relatively steep bed slope from the mid to the inner reef flat, and 78% of the time $\beta_H > 1.25$, while Kwajalein E had a reflection regime 26% of the time; the remainder of the sites only exceeded this threshold < 3% of the time.

Secondary Waves

Large IG waves provide a short-lived increase in water level that could potentially allow for the transmission of larger secondary waves over reef flats. To evaluate the effect of the added water level from the IG wave on the growth of these secondary waves, we focused on the inner reef-flat sites with large IG waves: the four Kwajalein and Roi-Namur reefs. We note that these short-period secondary waves are distinct from SS waves, with nearly all (>99%) cataloged secondary waves having periods < 5 s. In order to minimize the effects of overall reef-flat submergence, we constrained the data to times when the inner reef-flat h_{reef} was within a 0.1 m window, with ranges between 0.2 and 0.8 m investigated; the results from the intermediate h_{reef} window of 0.5–0.6 m are shown in **Figure 6**. The secondary waves were most prevalent on the lower portion of both the FF and BF of the IG waveform, which is not unexpected because this region

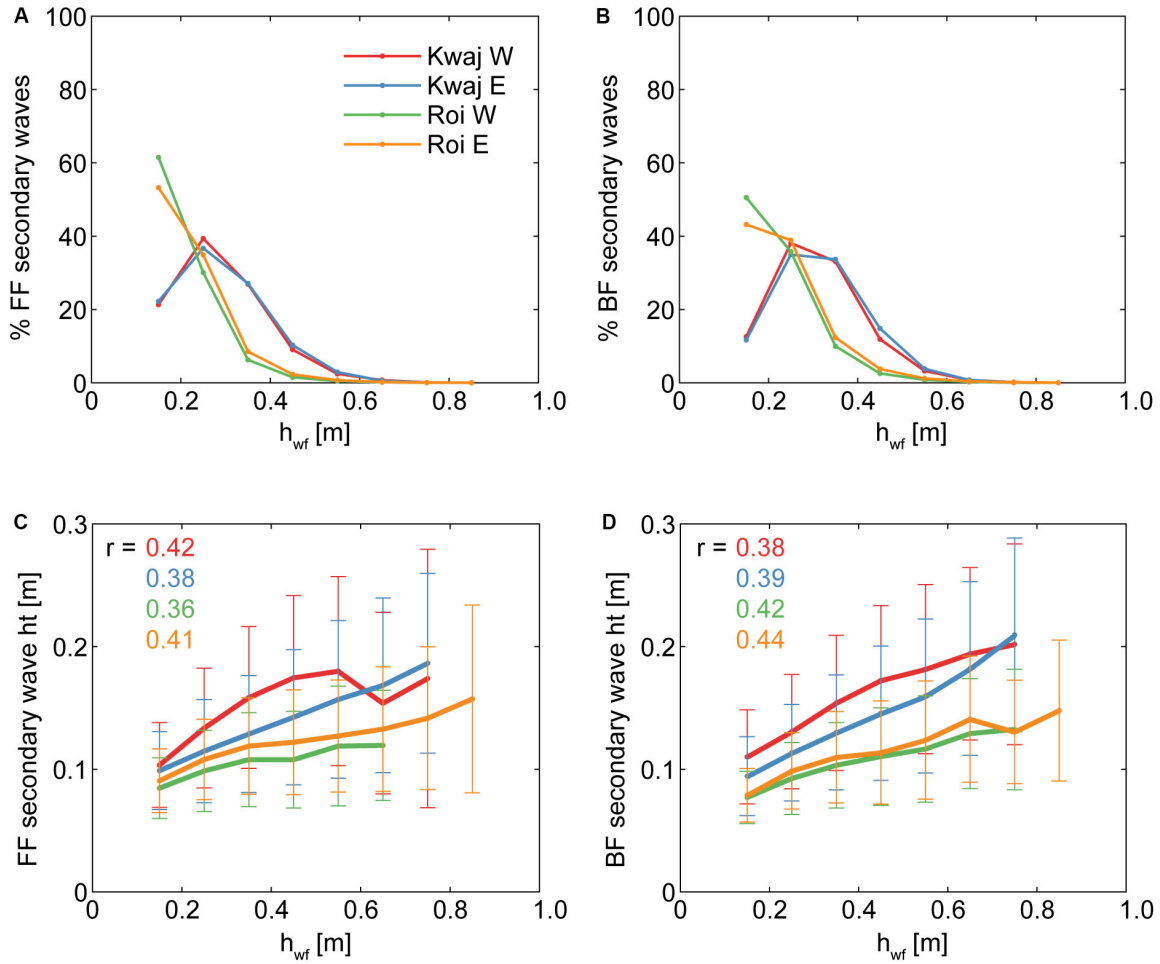

FIGURE 6 | The effects of infragravity ("IG") waves on the prevalence and heights of secondary short-period waves at the inner reef flat for the four sites with the largest IG waves. For all panels, the colors correspond to sites in **(A)**, and reef-flat water levels were constrained to a 0.1 m window ($0.5 < h_{reef} < 0.6$ m). The % of all secondary waves that occurred at different heights along the IG waveform, h_{wf} (see **Figure 2A**), for **(A)** the front face ("FF") and **(B)** the back face ("BF") of the IG waves. The mean ± one standard deviation of the secondary wave heights according to h_{wf} for **(C)** the FF and **(D)** the BF of the IG waves, with correlation coefficient, r, given for each site. The lower portions of the IG waves have the greatest number of secondary SS waves, but the largest ones occur higher up on the IG wave, independent of overall reef-flat water levels.

of the wave has the longest duration compared to the short-lived peak, allowing for a greater number of individual short-period fluctuations (**Figures 6A,B**). However, the secondary waves that were higher up on the IG waveform tended to be larger, with a moderate correlation (**Figures 6C,D**). This effect of larger secondary waves occurring on the higher portions of IG waves was greatest for the Kwajalein reefs, where, for intermediate h_{reef}, the secondary waves would be expected to be 0.1 m larger if they are riding on a 0.6 m waveform elevation, instead of closer to the troughs at 0.2 m elevation. Thus, it appears that large IG waves can support the transmission of larger secondary waves over the reef flat independent of overall water levels, but the effect is small compared to the overall IG wave heights.

DISCUSSION

Reef Morphological Controls on Infragravity Waves

Laboratory and modeling work has put forth two dominant morphological controls on reef-flat IG wave regimes: the reef-flat submergence and the slope of the fore reef (Quataert et al., 2015; Pearson et al., 2017; Yao et al., 2018; Chen et al., 2019; Masselink et al., 2019). Although physically or numerically simulated reefs allow for holding certain reef geometries constant while varying others, field-based studies utilizing natural reefs, of course, do not allow for the same level of control and manipulation. Nevertheless, the *in situ* observations from our 7 reefs generally support the findings that reef flat submergence and the slope of the fore reef are the first-order controls on the resulting IG wave field over the reef flat (**Table 2**). Our sites could be grouped according to fore-reef slope and reef-flat water depth, with Ukumehame, Lahaina, and Waiakane representing less-steep fore reefs and deeper reef flats and the four Kwajalein and Roi-Namur sites representing reefs with steeper fore reefs and shallower reef flats (**Figure 1** and **Table 1**). These groupings also capture the difference in IG wave energy observed at the sites, with the steep fore-reef and shallow reef-flat sites having much greater IG wave energy over the reef flats that became dominant toward the shoreline (**Figures 4A–G**). Although Ukumehame and Lahaina were subject to considerably less energetic offshore wave forcing, there were several large wave events at Waiakane (Hs_{fr} > 2 m) and these did not result in reef-flat IG waves of similar magnitude to those on the Kwajalein or Roi-Namur reef flats under similar Hs_{fr}. Interestingly, the Kwajalein reef flats had the largest relative IG waves, despite having slightly less steep fore-reef slopes than Roi-Namur (**Figures 4**, **5** and **Table 1**).

A modeling study by Chen et al. (2019) found that steeper fore reefs can reduce the asymmetry of reef-flat IG waves. To evaluate this for our *in situ* observations, we compared the IG wave asymmetry from the Roi-Namur W and Lahaina sites, which have similar reef-flat widths, but the Roi-Namur W fore-reef slope is approximately twice as steep (**Table 1**). Taking all the offshore wave power ($wp_{off} = Hs^{2} * Tp$) and mean reef-flat water depth (h_{avg}) combinations during a large wave event (wp_{off} > 15 m^2 s) at Lahaina, we then found all the corresponding occurrences at Roi-Namur W when wp_{off} was within 5 m^2 s and the h_{avg} was within 0.05 m of the Lahaina conditions; for any matches, we averaged the inner reef-flat IG wave *As*. Under approximately equivalent offshore wave forcing and reef flat water levels, the Roi-Namur W inner reef-flat IG waves were more negatively asymmetrical in 76% of the cases (n = 56). Our results are somewhat confounded by the different bed roughness of the two reefs, which may account for the disagreement with the proposition that steeper fore-reefs produce less asymmetrical IG waves on the reef flat. The Lahaina reef flat has relatively high rugosity, and would be expected to have a bed wave friction factor, f_w, on par with those derived for other Hawaiian reefs of $\sim$ 0.2 (e.g., Falter et al., 2004; Lowe et al., 2005). In contrast, the Roi-Namur W reef flat is relatively smooth, with an estimated $f_w \sim 0.1$ (Cheriton et al., 2016). It is possible that the smoother reef flat may explain why Roi-Namur W consistently has more asymmetrical IG reef-flat waves than Lahaina, despite its steeper fore reef, but the effects of bed roughness on resulting IG wave asymmetry are reported to be less influential than the fore-reef slope (Quiroga and Cheung, 2013; Chen et al., 2019).

Although fore-reef slope and reef submergence strongly govern the reef-flat IG wave field, the width of the reef flat may also be an important factor (**Table 2**). The width of a reef flat can vary from tens of meters to more than 1 km (Quataert et al., 2015) and affects both the resonant frequency modes possible over the reef flat (Péquignet et al., 2009), as well as the potential for wave energy dissipation by bottom friction (van Dongeren et al., 2013). At the Kwajalein and Roi-Namur reefs, the fore-reef slope and level of reef submergence were roughly equivalent, but their reef-flat widths varied by a factor of 3 (**Table 1**). On the narrow Kwajalein reefs, IG waves were larger relative to fore-reef wave heights, and more predominantly skewed compared to those on Roi-Namur (**Figures 4**, **5**). Because the Kwajalein reef flats are so narrow, the longest-period waves that can be supported by the reef platform are in the IG band; thus, with larger incident waves, energy transfer into lower-frequency bands over these narrow reef flats is constrained to the IG band, possibly accounting for the larger IG waves, despite the less steep fore-reef slope.

TABLE 2 | Summary of relationships found between reef characteristics and resulting infragravity (IG) waves at the inner reef flat.

	Steeper α	**Increasing L**	**Increasing h_{reef}**	**Increasing Hs_{VLF}/Hs_{IG}**
As	More pitched-onshore[a]	More pitched-onshore	Less pitched-onshore	More pitched-onshore
Sk	More peaked	Less peaked	Less peaked	Less peaked[a]
Hs_{IG}/Hs_{fr}	Larger	Smaller[a]	Smaller	Smaller[a,b]

Reef characteristics (top row) include: fore-reef slope (α), reef width (L), submergence level (h_{reef}), and the proportion of very-low frequency (VLF) motion energy to IG wave energy (Hs_{VLF}/Hs_{IG}) on the reef flat. The IG wave characteristics considered (left column) are: asymmetry (As), skewness (Sk), and wave height relative to the fore-reef wave height (Hs_{IG}/Hs_{fr}). [a]Trend is inconclusive, more data needed. [b]Narrower reef flats do not support VLF motions.

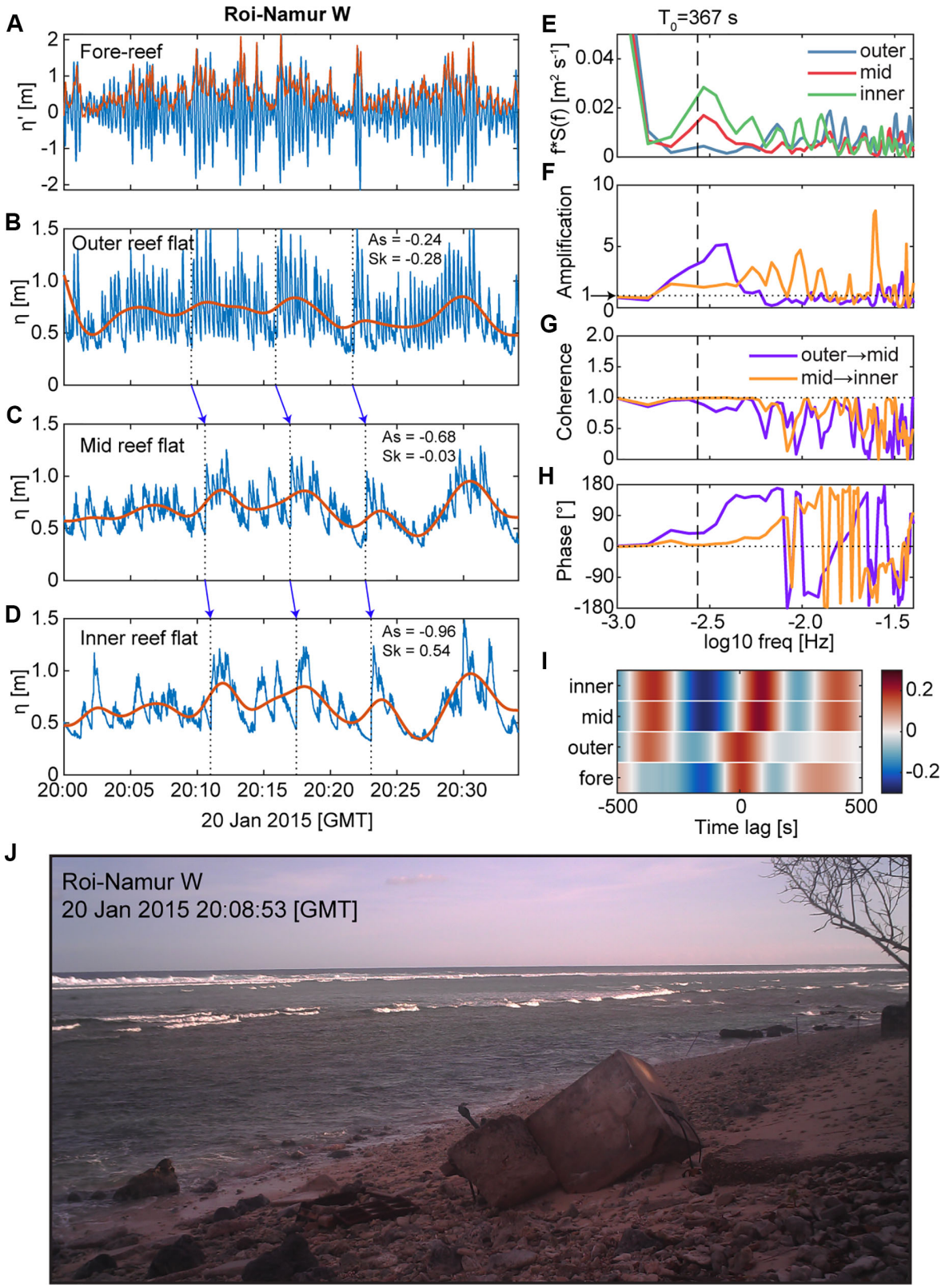

FIGURE 7 | An example of how large very-low frequency ("VLF") motions can facilitate the growth of large infragravity ("IG") bores on reef flats, using observations from Roi-Namur W during a large offshore wave event on 20 January 2015. **(A)** Fore-reef water levels relative to the mean (blue) with the sea-swell ("SS") wave

(Continued)

FIGURE 7 | Continued
envelope (red) overlaid. Reef-flat water levels (blue) and the low-pass filtered VLF water levels (red line) shown for the **(B)** outer, **(C)** mid, and **(D)** inner reef flat. Dashed lines and corresponding blue arrows highlight a few selected leading edges of wave packets that transform into steep, asymmetrical IG bores by the inner reef flat. **(E)** Variance-preserving energy density spectra from the reef flat water levels shown in **(B–D)** over the IG and VLF bands; the fundamental resonant frequency (T_0) is indicated by the dashed line. **(F)** Amplification in energy across the reef flat. **(G)** Coherence between the spectra. **(H)** The phase between the spectra. **(I)** Cross-correlation between the fore-reef wave envelope shown in **(A)** and the reef flat water levels for different time lags. **(J)** Photo taken from a shore-mounted camera during the water level bursts shown in **(A–D)** showing the shore-parallel crests of large IG bores propagating toward shore. There is strong evidence for VLF resonance or standing wave behavior: the reef flat water levels display amplification and strong coherence near T_0, and a near-zero lag and strong cross-correlation between the mid and inner reef flat. The resulting IG bores at the inner reef flat had heights of >0.8 m.

The most strongly skewed IG waves occurred on Kwajalein W, which had a disproportionately steep reef-flat slope compared to our other sites (**Table 1**). In contrast, on the wider Roi-Namur reef flats, IG waves were predominantly asymmetrical (pitched onshore) and less peaked. When the leading edge of a bore is large compared to overall water depths ($Hs_{IG}/h_{reef} > 0.75$), the bore is considered to be turbulent (Peregrine, 1966). For the IG bore waves on Kwajalein W and E, 94 and 73%, respectively, of these bores meet this criterion for fully turbulent breaking bores. However, on Roi-Namur W and E, the majority of IG bore waves (81 and 78%, respectively) had Hs_{IG}/h_{reef} between 0.28 and 0.75, so they are considered to be in a transitional regime, in which the bores exhibit both turbulent breaking and undular waveforms (Peregrine, 1966). The Kwajalein and Roi-Namur reef flats have similar bed roughness, but the wider reef flats of Roi-Namur allow for greater frictional dissipation of the low-frequency waves as they travel shoreward, which may both dampen the IG wave amplitudes and also enhance asymmetry of the waves. In addition, the Roi-Namur reef flats are sufficiently wide to allow for VLF waves. There, when reef-flat submergence increases, the resonance frequencies of the reef increase to the high-VLF band ($500 < T_0 < 300$ s, for $h_{reef} > 0.5$ m), becoming more easily excitable by the offshore wave groups, which have dominant periods on the order of minutes (Roi-Namur W mean $T_{dom,At} = 179 \pm 142$ s; Roi-Namur E mean $T_{dom,At} = 214 \pm 178$ s). Thus, our results highlight the importance of reef-flat width and bed slope, in addition to fore-reef slope and reef-flat submergence, to the resulting IG wave field on reef flats, supporting previous results that found reef-flat width an important geomorphic control on extreme runup on reef-lined coastlines (Quataert et al., 2015; Pearson et al., 2017).

Infragravity Wave-Wave Capture

Energetic VLF motions on the reef flat may enhance IG wave-wave capture over the reef flat. This phenomenon was observed during large wave events at our two Roi-Namur sites (**Figures 7**, **8**). As the large, incident SS wave groups on the fore reef excited a corresponding fluctuation in VLF motions over the reef flat, the short-period waves riding on the crests of these longer-period fluctuations merged into increasingly tall and pitched-forward IG bores (**Figures 7A–D**, **8A–D**). Energy spectra from the outer, mid, and inner reef flat show maxima centered on the resonance period T_0, with amplifications > 1, and strong coherence (**Figures 7E–G**, **8E–G**). The phase between the spectra indicate a phase lag between the outer and mid reef, but near-zero phase lag between the mid and inner reef (**Figures 7H**, **8H**), which is also indicated by the cross-correlation between the fore-reef wave envelope and the reef flat η records (**Figures 7I**, **8I**). As such, the strong VLF motions during these examples were likely standing waves with possible resonant behavior over the reef flat.

A shore-mounted camera system captured a photo of the large IG bores propagating across the Roi-Namur W reef flat during the example η record (**Figure 7J**); the shore-parallel bore wave crests extended across the reef area and appeared to have been breaking in the nearshore. It is possible that not only do VLF waves support IG wave-wave capture, but that the IG wave-wave capture, in turn, enhances energy in lower-frequencies, leading to increasing VLF wave heights toward shore, similar to the SS wave-wave capture facilitating transfer of energy into lower frequencies in plane beach environments (Tissier et al., 2015; Tissier et al., 2017). The heights of the VLF waves in our two examples increase from the outer to the inner reef flat with a $\Delta Hs_{VLF} = 0.17$ m for the Roi-Namur W example (**Figure 7**) and $\Delta Hs_{VLF} = 0.53$ m for Roi-Namur E example (**Figure 8**).

A similar phenomenon of wave-crest merging has been well documented for plane beaches (e.g., Huntley and Bowen, 1975; Sénéchal et al., 2001), but remains poorly understood (Bertin et al., 2018). Wave-wave capture occurs when irregular waves travel at different speeds (celerity) over sufficient distance to catch up to each other. Low-frequency waves can cause modulations in water levels that drive changes in wave celerity in the nearshore (e.g., Longuet-Higgins and Stewart, 1960; Phillips, 1981; Kenyon et al., 1983). Laboratory experiments by Tissier et al. (2015) demonstrated that SS bores riding on the IG wave crests over plane beaches propagate faster than those on the troughs, and the SS wave merging is enhanced at the IG wave crest. Further work by Tissier et al. (2017) found that the initial merging point for the SS waves was located where the ratio of IG to SS wave heights was ∼ 1, indicating that SS bore-bore capture occurs where IG waves already dominate. Extrapolating these results to reef-flat environments, we might expect IG wave-wave capture to be most likely where VLF wave energy begins to equal or exceed IG wave energy, i.e., $Hs_{VLF}/Hs_{IG} \geq 1$.

The Hs_{VLF}/Hs_{IG} ratio at the outer and inner reef-flat sites are well correlated, increasing and decreasing together (**Figures 9A,B**), with a similar robust positive correlation between the outer and mid reef-flat sites (not shown). Though the outer reef flat Hs_{VLF}/Hs_{IG} rarely exceeded 1, by the mid and inner reef flat, this threshold was regularly exceeded, particularly during low h_{reef}. An increasing Hs_{VLF}/Hs_{IG} ratio is moderately negatively correlated with IG wave asymmetry at the shoreline (**Figures 9C,D**). No

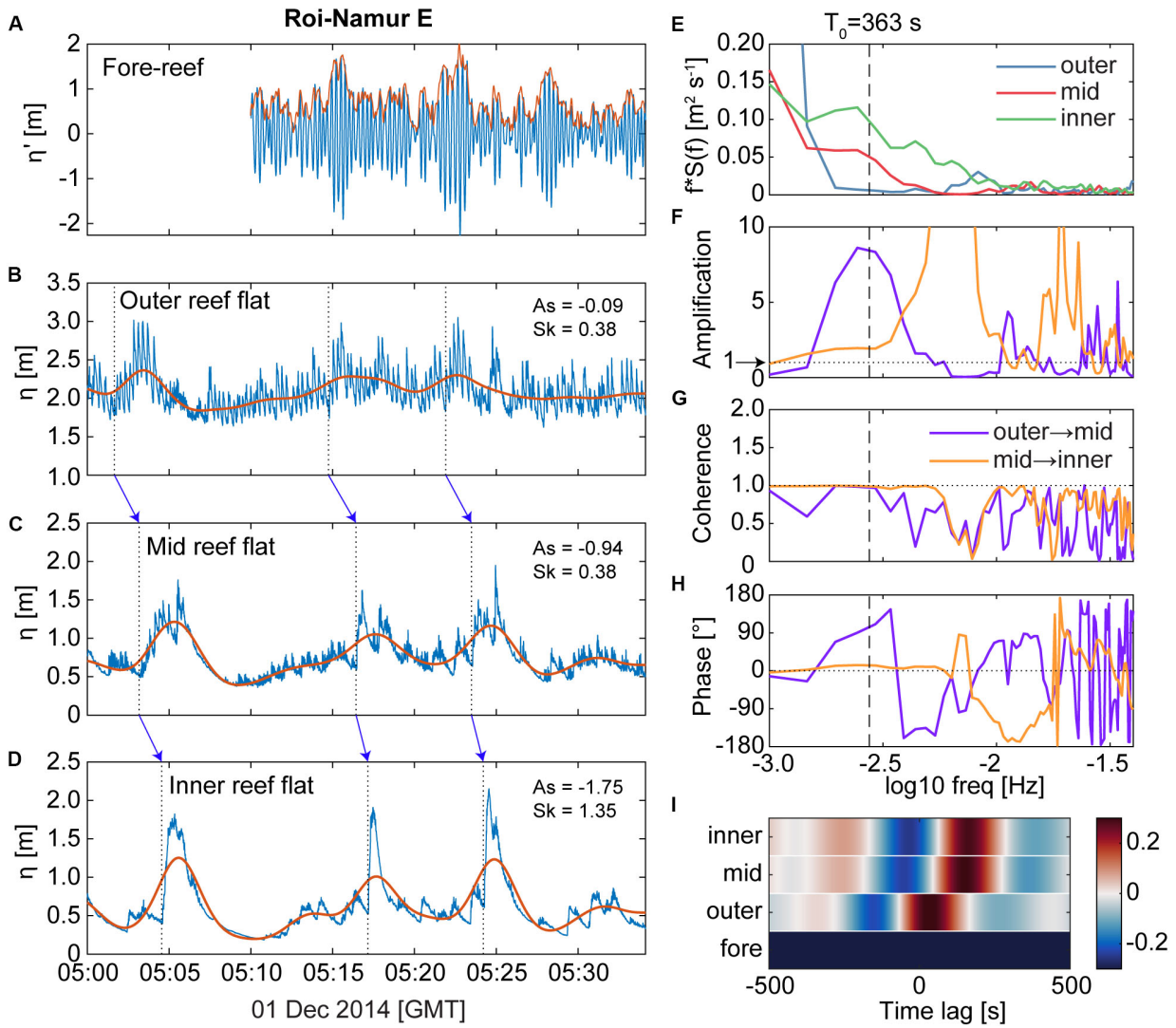

FIGURE 8 | Another example of how large, very-low frequency ("VLF") motions can facilitate the growth of large infragravity ("IG") bores on reef flats, using observations from Roi-Namur E during a large offshore wave event on 1 December 2015. **(A)** Fore-reef water levels relative to the mean (blue) with the sea-swell ("SS") wave envelope (red) overlaid. Due to data fouling of the Roi-Namur E fore-reef pressure sensor, these fore-reef water levels are taken from the AWAC pressure sensor, which did not begin its burst sampling till 10 min past the hour (see section Materials and Methods). Reef-flat water levels (blue) and the low-pass filtered VLF water levels (red line) shown for the **(B)** outer, **(C)** mid, and **(D)** inner reef flat. Dashed lines and corresponding blue arrows highlight a few selected leading edges of wave packets that transforms into a steep, asymmetrical IG bores by the inner reef flat. **(E)** Variance-preserving energy density spectra from the reef flat water levels shown in **(B–D)** over the IG and VLF bands; the fundamental resonant frequency (T_0) is indicated by the dashed line. **(F)** Amplification in energy across the reef flat. **(G)** Coherence between the spectra. **(H)** The phase between the spectra. **(I)** Cross-correlation between the outer reef-flat water level and the mid and inner reef flat water levels for different time lags; the available fore-reef water level did not correlate well with the reef flat water levels. No photo was available for this site. Similar to the example shown in **Figure 7**, there is strong evidence for VLF resonance or standing wave behavior: the reef flat water levels display amplification and strong coherence near T_0, and a near-zero lag and strong cross-correlation between the mid and inner reef flat. The resulting IG bores at the inner reef flat had heights > 1 m.

corresponding relationship was found between Hs_{VLF}/Hs_{IG} and IG wave skewness. When $Hs_{VLF}/Hs_{IG} > 1$ at the inner reef flat, the resulting IG waves were pitched-onshore bores ($As < -0.25$) 98% of the time at Roi W, and 93% of the time at Roi E. Thus, when VLF motions are energetic relative to IG waves, this leads to more negatively asymmetrical IG waves at the shoreline, but the mechanism underlying this connection is unclear.

To quantify IG wave-wave capture, we used the ratio of number of individual VLF wave crests to number of individual IG wave crests, nc_{VLF}/nc_{IG}, within a given burst record; with increasing IG wave merging, the number of IG wave crests approaches the number of VLF wave crests toward shore (e.g., **Figures 8B–D**, **9B–D**). With increasing nc_{VLF}/nc_{IG}, the IG waves on the inner reef flat were increasingly pitched onshore (negatively asymmetrical; **Figures 9E,F**). This suggests that larger

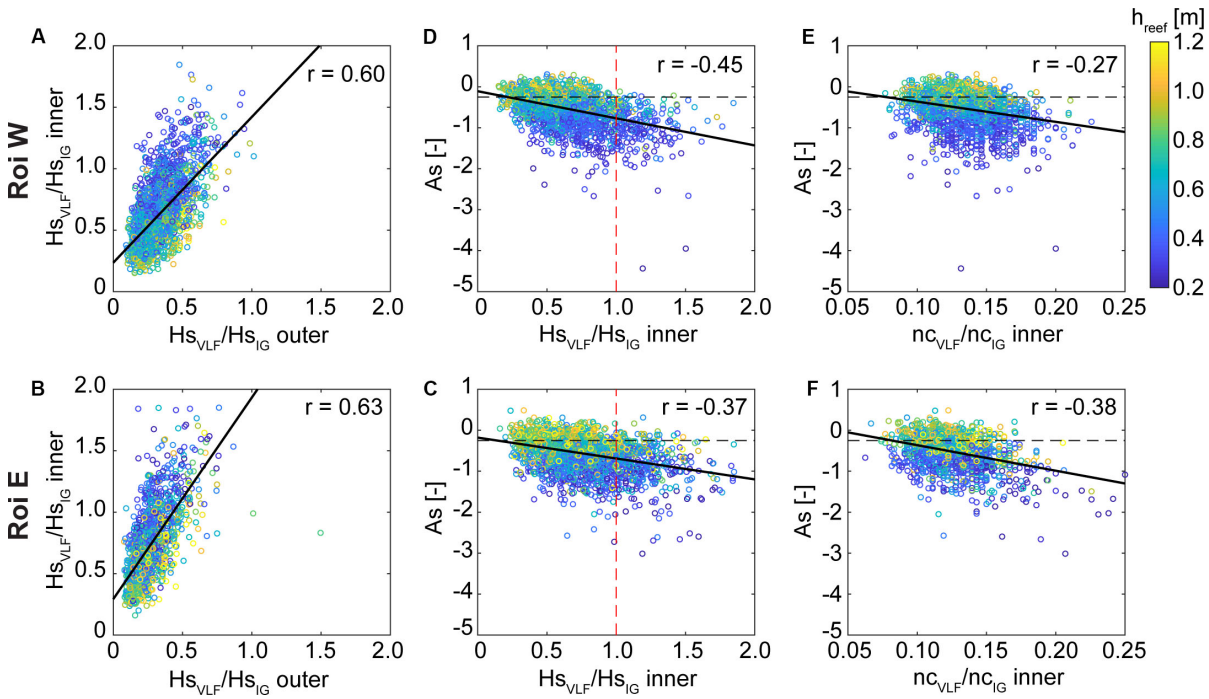

FIGURE 9 | Relationship between very-low-frequency ("VLF") wave energy and resulting nearshore infragravity ("IG") wave asymmetry on the Roi-Namur W (Top) and Roi-Namur E (Bottom) reef flats. Color-scale for all panels is the mean reef-flat submergence, h_{reef}. **(A,B)** Relationship between the VLF and IG wave height ratio (Hs_{VLF}/Hs_{IG}) on the outer and inner reef flat. **(C,D)** Inner reef-flat IG wave asymmetry according to VLF and IG wave height ratio. The threshold of $Hs_{VLF}/Hs_{IG} = 1$ is indicated by the red dashed line, and the IG bore criterion $As = -0.25$ is indicated by the black dashed line. **(E,F)** Inner reef-flat IG wave asymmetry according to ratio of number of VLF wave crests to number of IG wave crests (nc_{VLF}/nc_{IG}), cataloged from each individual burst record. The IG bore criterion $As = -0.25$ is indicated by the black dashed line. For each panel, the correlation coefficient, r, is given (corresponding $p < 0.005$ for all; degrees of freedom = 1920 for Roi W and 1,323 for Roi E), as well as a linear regression (black line) using an iteratively reweighted least squares with bisquare weighting, to show the trend.

VLF waves result in more bore-like IG waves and also enhance IG wave-wave capture over reef flats, but it is unclear if these two phenomenon are linked. Lower h_{reef} is likely also an important control on the degree of IG wave asymmetry, as greater bottom friction may cause the shoreward-propagating IG wave to rapidly decelerate, resulting in a steepening of the wave leading edge. Lower h_{reef} may also facilitate more frequent wave-wave captures in the nearshore, as has been observed on plane beaches (Stringari and Power, 2019).

CONCLUSION

In situ wave observations from 7 different fringing reef flats of varying geomorphologies are presented to evaluate under what conditions low-frequency waves occur and what factors influence their asymmetry and skewness (**Table 2**). Our observations from natural environments demonstrate that fore-reef slope and reef-flat submergence are fundamental controls on subsequent reef flat IG and VLF waves, supporting previous findings from modeling and laboratory studies (Yao et al., 2018; Chen et al., 2019; Masselink et al., 2019). In general, steeper fore-reef slopes and lower reef-flat submergence result in larger IG reef-flat waves that are more pitched onshore (negatively asymmetrical) and peaked (positively skewed). Our results also highlight the importance of reef-flat width and slope as morphological controls on reef-flat IG wave heights, asymmetry, and skewness; these aspects of reef-flat geometries have also been shown to be important in shoreline runup (Quataert et al., 2015; Pearson et al., 2017). Though the Kwajalein reefs had less steep fore-reefs than the Roi-Namur sites, they had the largest IG waves relative to offshore wave forcing and reef flat water levels, and these were also the narrowest reef flats. The Kwajalein reef-flat IG bores were also strongly skewed, which may be due to the steeper reef-flat bed slope. It is unclear if fore-reef slope is important in the resulting irregularity of IG waves. Comparing our two reefs with similar reef-flat widths during approximately equivalent incident waves and reef-flat water levels, the site with a much steeper fore-reef (Roi-Namur W) had more pitched-onshore IG waves in the majority (76%) of cases compared to the site with a gentler fore-reef slope (Lahaina), however, these sites also had different bed roughnesses.

We observed IG wave-wave capture leading to large, asymmetrical bores at the shoreline. Increasing VLF wave energy was associated with more negatively asymmetrical IG waves, particularly at lower reef submergence. In addition, more frequent IG wave-wave capture was correlated with more pitched-onshore IG waves. Although the link between these two phenomena remains unclear, a similar phenomenon has been reported for plane beaches, whereby IG wave motions enhance

SS bore-merging in the surf zone. Thus, we posit that VLF waves over reef flats may facilitate IG bore merging, and this may lead to larger, more pitched-onshore bores at the shoreline.

It is important to understand how low-frequency waves propagate and evolve over reef flats, as these waves can not only dominate at the shoreline, but as they evolve into increasingly irregular waveforms, these bores play a critical role in extreme shoreline events such as large runup, island overwash, and subsequent flooding during large wave events (Nwogu and Demirbilek, 2010; Roeber and Bricker, 2015; Shimozono et al., 2015; Ning et al., 2019). There is increasing evidence that bore-bore capture over natural beaches governs the majority of extreme shoreline runup and breaking wave heights (García-Medina et al., 2017; Bergsma et al., 2019; Stringari and Power, 2019). Given our observations, we hypothesize that IG bore-bore capture over reef flats may play an equally important role in shoreline hazards for reef-lined coasts.

DATA AVAILABILITY STATEMENT

The datasets analyzed in this study can be found in the USGS Cross-Reef Wave and Water Level Database at https://doi.org/10.5066/P9RYN5NH.

AUTHOR CONTRIBUTIONS

OC performed the analyses and wrote the manuscript with CS. KR assisted with data collection, processing, and evaluation.

FUNDING

This work was funded by the U.S. Geological Survey's Coastal/Marine Hazards and Resources Program and the U.S. Department of Defense's Strategic Environmental Research and Development Program.

ACKNOWLEDGMENTS

We would like to thank the US Army-Kwajalein Atoll and the University of Western Australia for their support of this project. We also thank M. Buckley, C. Johnson, J. Logan, T. Reiss, J. Logan, and Captain Joe Reich for their field work support. We are grateful to J. Logan and K. Cumming for their help with bathymetric profile processing. Any use of trade, firm, or product names is for descriptive purposes only and does not imply endorsement by the U.S. Government.

REFERENCES

Bayliss-Smith, T. P. (1988). The role of hurricanes in the development of reef islands, Ontong Java Atoll, Solomon Islands. *Geogr. J.* 154, 377–391. doi: 10.2307/634610

Bergsma, E. W. J., Blenkinsopp, C. E., Martins, K., Almar, R., and Melo de Almeida, L. P. (2019). Bore collapse and wave run-up on a sandy beach. *Cont. Shelf Res.* 174, 132–139. doi: 10.1016/j.csr.2019.01.009

Bertin, X., de Bakker, A., van Dongeren, A., Coco, G., Andre, G., Ardhuin, F., et al. (2018). Infragravity waves: from driving mechanisms to impacts. *Earth Sci. Rev.* 177, 774–799.

Buckley, M. L., Lowe, R. J., Hansen, J. E., van Dongeren, A. R., and Storlazzi, C. D. (2018). Mechanisms of wave-driven water level variability on reef-fringed coastlines. *J. Geophys. Res. Oceans* 123, 3811–3831. doi: 10.1029/2018JC013933

Chen, H., Jiang, D., Tang, Z., and Mao, H. (2019). Evolution of irregular wave shape over a fringing reef flat. *Ocean Eng.* 192, 106544. doi: 10.1016/j.oceaneng.2019.106544

Cheriton, O. M., Storlazzi, C. D., and Rosenberger, K. J. (2016). Observations of wave transformation over a fringing coral reef and the importance of low-frequency waves and offshore water levels to runup, overwash, and coastal flooding. *J. Geophys. Res. Oceans* 121, 3121–3140. doi: 10.1002/2015JC011231

Elgar, S., Gallagher, E. L., and Guza, R. T. (2001). Nearshore sandbar migration. *J. Geophys. Res. Oceans* 106, 11623–11627. doi: 10.1029/2000JC000389

Etienne, S., and Terry, J. P. (2012). Coral boulders, gravel tongues and sand sheets: features of coastal accretion and sediment nourishment by cyclone tomas (March 2010) on Taveuni Island. *Fiji. Geomorph.* 175-176, 54–65. doi: 10.1016/j.geomorph.2012.06.018

Falter, J. L., Atkinson, M. J., and Merrifield, M. A. (2004). Mass-transferlimitation of nutrient uptake by a wave-dominated reef flat community. *Limnol. Oceanogr.* 49, 1820–1831. doi: 10.4319/lo.2004.49.5.1820

García-Medina, G., Özkan-Haller, H. T., Holman, R. A., and Ruggiero, P. (2017). Large runup controls on a gently sloping dissipative beach. *J. Geophys. Res. Oceans* 122, 5998–6010. doi: 10.1002/2017JC012862

Gawehn, M., van Dongeren, A., van Rooijen, A., Storlazzi, C. D., Cheriton, O. M., and Reniers, A. (2016). Identification and classification of very low frequency waves on a coral reef flat. *J. Geophys. Res. Oceans* 121, 7560–7574. doi: 10.1002/2016JC011834

Grasso, F., Michallet, H., and Barthélemy, E. (2011). Sediment transport associated with morphological beach changes forced by irregular asymmetric, skewed waves. *J. Geophys. Res. Oceans* 116:C03020. doi: 10.1029/2010JC006550

Hoefel, F., and Elgar, S. (2003). Wave-induced sediment transport and sandbar migration. *Science* 229, 1885–1887. doi: 10.1126/science.1081448

Huntley, D. A., and Bowen, A. J. (1975). "Comparison of the hydrodynamics of steep and shallow beaches," in *Nearshore Sediment Dynamics and Sedimentation*, eds J. R. Hails and A. Carr (London: Wiley), 69–109.

Kench, P. S., Nichol, S. L., Smithers, S. G., McLean, R. F., and Brander, R. W. (2008). Tsunami as agents of geomorphic change in mid-ocean reef islands. *Geomorphology* 95, 361–383. doi: 10.1016/j.geomorph.2007.06.012

Kenyon, K., Sheres, D., and Bernstein, R. (1983). Short waves on long waves. *J. Geophys. Res.* 88, 7589–7596. doi: 10.1029/JC088iC12p07589

Longuet-Higgins, M. S., and Stewart, R. W. (1960). Changes in the form of short gravity waves on long waves and tidal currents. *J. Fluid Mech.* 8, 565–583. doi: 10.1017/S0022112060000803

Lowe, R. J., Falter, J. L., Bandet, M. D., Pawlak, G., Atkinson, M. J., Monismith, S. G., et al. (2005). Spectral wave dissipation over a barrier reef. *J. Geophys. Res. Oceans* 110:C04001. doi: 10.1029/2004JC002711

Masselink, G., Tuck, M., McCall, R., van Dongeren, A., Ford, M., and Kench, P. (2019). Physical and numerical modeling of infragravity wave generation and transformation on coral reef platforms. *J. Geophys. Res. Oceans* 124, 1410–1433. doi: 10.1029/2018JC014411

Michallet, H., Cienfuegos, R., Barthélemy, E., and Grasso, F. (2011). Kinematics of waves propagating and breaking on a barred beach. *Eur. J. Mech. B* 30, 624–634. doi: 10.1016/j.euromechflu.2010.12.004

Ning, Y., Liu, W., Sun, Z., Zhao, X., and Zhang, Y. (2019). Parametric study of solitary wave propagation and runup over fringing reefs based on Boussinesq wave model. *J. Marine Sci.* 24, 512–525. doi: 10.1007/s00773-018-0571-571

Nwogu, O., and Demirbilek, Z. (2010). Infragravity wave motions and runup over shallow fringing reefs. *J. Waterway Port Coast. Ocean Eng.* 136, 295–305. doi: 10.1061/(ASCE)WW.1943-5460.0000050

Pearson, S. G., Storlazzi, C. D., van Dongeren, A. R., Tissier, M. F. S., and Reniers, A. J. H. M. (2017). A Bayesian-based system to assess wave-driven flooding hazards on coral reef-lined coasts. *J. Geophys. Res. Oceans* 122, 10099–10117. doi: 10.1002/2017JC0132304

Péquignet, A. C. N., Becker, J. M., Merrifield, M. A., and Aucan, J. (2009). Forcing of resonant modes on a fringing reef during tropical storm Man-Yi. *Geophys. Res. Lett.* 36:L03607. doi: 10.1029/2008GL036259

Peregrine, D. H. (1966). Calculations of the development of an undular bore. *J. Fluid Mech.* 25, 321–330. doi: 10.1017/S0022112066001678

Phillips, O. M. (1981). The dispersion of short wavelets in the presence of a dominant long wave. *J. Fluid Mech.* 107, 465–485. doi: 10.1017/S0022112081001869

Pomeroy, A., Lowe, R., Symonds, G., van Dongeren, A., and Moore, C. (2012). The dynamics of infragravity wave transformation over a fringing reef. *J. Geophys. Res.* 117:C11022. doi: 10.1029/2012JC008310

Pomeroy, A. W. M., van Dongeren, A., Lowe, R. J., van Thiel de Vries, J. S. M., and Roelvink, J. (2012). Low frequency wave resonance in fringing reef environments. *Proc. Int. Conf. Coastal Eng.* 33, 1–10. doi: 10.9753/ice.v33.currents.25

Pomeroy, A. W. M., Lowe, R. J., Dongeren, A. R., Ghisalberti, M., Bodde, W., and Roelvink, D. (2015). Spectral wave-driven sediment transport across a fringing reef. *Coast. Eng.* 98, 78–94. doi: 10.1016/j.coastaleng.2015.01.005

Quataert, E., Storlazzi, C. D., van Rooijen, A., Cheriton, O. M., and van Dongeren, A. (2015). The influence of coral reefs and climate change on wave-driven flooding of tropical coastlines. *Geophys. Res. Lett.* 42, 6407–6415. doi: 10.1002/2015GL064861

Quiroga, P. D., and Cheung, K. F. (2013). Laboratory study of solitary-wave transformation over bed-form roughness on fringing reefs. *Coast. Eng.* 80, 35–48. doi: 10.1016/j.coastaleng.2013.05.002

Roeber, V., and Bricker, J. D. (2015). Destructive tsunami-like wave generated by surf beat over a coral reef during Typhoon Haiyan. *Nat. Comm.* 6:7854. doi: 10.1038/ncomms8854

Ruessink, B. G., van den Berg, T. J. J., and van Rijn, L. C. (2009). Modeling sediment transport beneath skewed asymmetric waves above a plane bed. *J. Geophys. Res. Oceans* 114:C11021. doi: 10.1029/2009JC005416

Scoffin, T. (1993). The geological effects of hurricanes on coral reefs and the interpretation of storm deposits. *Coral Reefs* 12, 203–221. doi: 10.1007/BF00334480

Sénéchal, N., Dupuis, H., Bonneton, P., Howa, H., and Pedreros, R. (2001). Observation of irregular wave transformation in the surf zone over a gently sloping sandy beach on the French Atlantic coastline. *Oceanol. Acta* 324, 545–556. doi: 10.1016/S0399-1784(01)01171-9

Shimozono, T., Tajima, Y., Kennedy, A. B., Nobuoka, H., Sasaki, J., and Shinji, S. (2015). Combined infragravity wave and sea-swell runup over fringing reefs by super typhoon Haiyan. *J. Geophys. Res. Oceans* 120, 4463–4486. doi: 10.1002/2015JC010760

Silva, P. A., Abreu, T., van der, A. D., Sancho, F., Ruessink, B. G., van der Werf, J., et al. (2011). Sediment transport in nonlinear skewed oscillatory flows: transkew experiments. *J. Hydraul. Res.* 49, 72–80. doi: 10.1080/00221686.2011.592681

Stoddart, D. R. (1971). "Coral reefs and islands and catastrophic storms," in *Applied Coastal Geomorphology*, ed. J. A. Steers (London: Palgrave Macmillan), 155–197. doi: 10.1007/978-1-349-15424-1_10

Stringari, C. E., and Power, H. E. (2019). Quantifying bore-bore capture on natural beaches. *arXiv* [Preprint]. Available online at: https://arxiv.org/abs/1909.11279 (accessed October 28, 2019).

Tissier, M., Bonneton, P., and Ruessink, G. (2017). Infragravity waves and bore merging. *Proc. Coast. Dyn.* 209, 451–460.

Tissier, M. F. S., Bonneton, P., Michallet, H., and Ruessink, B. G. (2015). Infragravity-wave modulation of short-wave celerity in the surf zone. *J. Geophys. Res. Oceans* 120, 6799–6814. doi: 10.1002/2015JC010708

van Dongeren, A., Battjes, J., Janssen, T., van Noorloos, J., Steenhauer, K., Steenbergen, G., et al. (2007). Shoaling and shoreline dissipation of low-frequency waves. *J. Geophys. Res.* 112:C02011. doi: 10.1029/2006JC003701

van Dongeren, A., Lowe, R., Pomeroy, A., Trang, D. M., Roelvink, D., Symonds, G., et al. (2013). Numerical modeling of low-frequency wave dynamics over a fringing coral reef. *Coast. Eng.* 73, 178–190. doi: 10.1016/j.coastaleng.2012.11.004

Yao, Y., He, F., Tang, Z., and Liu, Z. (2018). A study of tsunami-like solitary wave transformation and run-up over fringing reefs. *Ocean Eng.* 149, 142–155. doi: 10.1016/j.oceaneng.2017.12.020

Conflict of Interest: The authors declare that the research was conducted in the absence of any commercial or financial relationships that could be construed as a potential conflict of interest.

Copyright © 2020 Cheriton, Storlazzi and Rosenberger. This is an open-access article distributed under the terms of the Creative Commons Attribution License (CC BY). The use, distribution or reproduction in other forums is permitted, provided the original author(s) and the copyright owner(s) are credited and that the original publication in this journal is cited, in accordance with accepted academic practice. No use, distribution or reproduction is permitted which does not comply with these terms.

frontiers in Marine Science

ORIGINAL RESEARCH
published: 10 June 2020
doi: 10.3389/fmars.2020.00445

Shoreline Variability at a Reef-Fringed Pocket Beach

Johan Risandi[1,2,3,4], Jeff E. Hansen[1,2], Ryan J. Lowe[1,2,3,5] and Dirk P. Rijnsdorp[2,5]*

[1] School of Earth Sciences, The University of Western Australia, Crawley, WA, Australia, [2] Oceans Institute, The University of Western Australia, Crawley, WA, Australia, [3] ARC Centre of Excellence for Coral Reef Studies, Crawley, WA, Australia, [4] Marine Research Center, Ministry for Marine Affairs and Fisheries, Jakarta, Indonesia, [5] Oceans Graduate School, The University of Western Australia, Crawley, WA, Australia

Pocket beaches bound by headlands or other geologic features are common worldwide and experience constrained alongshore transport that influences their morphological changes. Pocket beaches fringed by shallow reefs have not been well-studied, yet can be commonly found throughout temperate and tropical regions. The presence of a reef is expected to drive distinct hydrodynamic processes and shoreline responses to offshore waves and water levels, which is investigated in this study. To examine the drivers of shoreline variability, a 20-month field study was conducted on a reef-fringed pocket beach in southwestern Australia (Gnarabup Beach), using a series of *in situ* wave and water level observations, topographic surveys, as well as video shoreline monitoring. The results indicate that the beach as a whole (alongshore averaged) was in a mostly stable state. However, we observed substantial spatial variability of the local shorelines in response to offshore wave and water levels across a range of time-scales (from individual storms to the seasonal cycle). We observed local regions of beach rotation within cells that were partitioned by the headlands and offshore reefs. The shoreline response was also dictated by the combination of offshore waves and water level which varied seasonally, with the shoreline generally eroding with lower water levels for the same wave height. Despite the contrasting responses in different alongshore locations of the beach, the overall beach volume of the pocket beach was largely conserved.

Keywords: rocky reef, pocket beach, coastal erosion, beach rotation, Western Australia

OPEN ACCESS

Edited by:
Juan Jose Munoz-Perez, University of Cádiz, Spain

Reviewed by:
Tim Poate, University of Plymouth, United Kingdom
Donatus Bapentire Angnuureng, University of Cape Coast, Ghana

****Correspondence:***
Johan Risandi
johan.risandi@research.uwa.edu.au

Specialty section:
This article was submitted to Coastal Ocean Processes, a section of the journal Frontiers in Marine Science

Received: *28 February 2020*
Accepted: *20 May 2020*
Published: *10 June 2020*

Citation:
Risandi J, Hansen JE, Lowe RJ and Rijnsdorp DP (2020) Shoreline Variability at a Reef-Fringed Pocket Beach. Front. Mar. Sci. 7:445. doi: 10.3389/fmars.2020.00445

INTRODUCTION

Pocket beaches, in which a stretch of sandy shoreline is bounded by headlands or other features that impede alongshore sediment transport, occur globally across a wide range of wave exposure regimes. Due to how these beaches are bound by barriers to sediment transport, they are often considered to be largely closed systems. Pocket beaches can be dominated by both cross-shore transport processes, that are primarily controlled by the incident wave energy (Harley et al., 2011; Blossier et al., 2017a), or alongshore transport that may cause beach rotation (Dehouck et al., 2009; Daly et al., 2014). In addition to limiting or preventing broad-scale alongshore transport, headlands or other bounding structures can introduce alongshore wave energy gradients (e.g., by shadowing obliquely incident waves), and act as wave reflectors particularly in the case of low frequency (infragravity waves) which can result in standing edge waves (e.g., Özkan-Haller et al., 2001; Masselink et al., 2004) along the pocket beach. Most research has focused on pocket beaches

that are located along open coastlines (e.g., Vousdoukas et al., 2009; Horta et al., 2018). However, pocket beaches are also commonly fringed by coral or rocky reefs that create a semi-protected lagoon, which may have a significant influence on the beach morphodynamics processes.

For reef-fronted beaches, the general physical mechanisms that drive the hydrodynamic processes can be similar to those in other coastal environments in which wave breaking results in wave-driven currents (Monismith et al., 2013). These wave-driven currents are generated by radiation stress gradients dominated by wave breaking, resulting in wave setup gradients across the reef that can drive onshore mass fluxes over the reef if a lagoon is present (e.g., Gourlay and Colleter, 2005; Taebi et al., 2011; Lowe and Falter, 2015). While these same processes occur in open coast sandy beaches, reef environments also have additional complexity associated with steep slopes and high bottom roughness that can modify the nearshore hydrodynamics.

Along reef-fringed beaches, the importance of low-frequency infragravity (IG) waves with periods between 25 and 600 s has been highlighted in a number of studies (e.g., Hardy and Young, 1996; Péquignet et al., 2009; Pomeroy et al., 2012; Buckley et al., 2018). This is mostly a result of the dissipation of groups of sea-swell (periods < 25 s) waves by the shallow reef that leads to the generation of IG waves through both a breakpoint forcing mechanism (Symonds et al., 1982) and the "release" of incident bound waves (Baldock, 2012). Due to their long wave lengths and typically smaller amplitudes than incident sea-swell, IG waves generally do not break and thus can have a significant influence on shoreline water level variability, including being a potential primary driver of beach erosion (Ford et al., 2013; Becker et al., 2016).

The dynamics of both sea-swell and IG waves along reef-fronted coastlines depend strongly on the submergence depth of the reef, which modulates the amount of depth-induced breaking over the reef and causes less dissipation (more transmission) occurring with greater submergence (e.g., Lowe et al., 2009). Any (offshore) process that alters water levels relative to the reef depth can, in turn, regulate the amount of wave energy that reaches reef-fringed coastlines. Reef fringed shorelines can be exposed to a range of sources of offshore water level variability over a range of time scales. These includes processes such as tides and atmospheric surges, as well as seasonal to longer-term changes in sea level. For example, in micro-tidal southwestern Australia, water level fluctuations associated with the strength of the Leeuwin Current (a poleward flowing eastern boundary current) result in seasonal and interannual sea-level variations with a range of 10s of cm, which is of the same order of magnitude as the microtidal tidal range of the region (Smith et al., 1991; Feng et al., 2003; Pattiaratchi and Eliot, 2008). In a reef-fringed beach of South West Australia (∼200 km from the study site descried here), Segura et al. (2018) found that these seasonal and inter-annual sea-level fluctuations were the dominant factor that determined the seasonal variability of the shoreline.

Despite pocket beaches influenced by reef systems being relatively common globally (Short, 1999), only a limited number of studies have investigated the processes governing morphodynamic changes within such sites, such that it still remains unclear how pocket beach shorelines generally behave relative to other classes of beaches (Norcross et al., 2002; Jeanson et al., 2013). Here we quantify the shoreline variability at Gnarabup Beach, a reef-fringed pocket beach in the Margaret River region of southwestern Australia, using a sequence of topographic measurements and daily video derived shorelines spanning a period of approximately 20 months between November 2015 and July 2017. Using this detailed data set, we investigate the processes that drive the shoreline variability along this reef-fringed pocket beach over a range of time-scales (from storm to seasonal), including the influence of large swell from the Southern Ocean and offshore water level fluctuations.

FIELD OBSERVATION AND METHODS

Description of the Study Area

Gnarabup Beach is a 1.5 km long pocket beach located in southwestern Australia (**Figure 1**). The beach is fronted by limestone reefs that are located ∼600 m offshore and become partially exposed at low water levels forming a semi-protected lagoon; hereinafter, just referred to as 'lagoon' (see **Figure 1A**). Two channels (up to 8 m deep) separate the reefs from the headlands and each other. Together, the reefs occupy approximately one-third of the length between the headlands that bound the pocket beach. The study site experiences variable hydrodynamic conditions over the seasonal cycle from the austral summer (November–February) to winter (June–September). The site is exposed to consistent swell year-round from the Southern Ocean with offshore significant wave heights averaging ∼2.3 m but can occasionally exceed 8 m during large conditions (especially during austral winter months). The tides at the site are micro-tidal, with a mean tidal range of 0.36 m and a maximum spring tidal range up to ∼1.25 m observed during the study period. Offshore water levels vary seasonally (up to 0.2 m) due to variations in the strength of the Leeuwin Current (Feng et al., 2003). The beach is composed of medium to coarse carbonate sands. The lagoon seafloor consists of a mix of carbonate sands, seagrass, and patchy limestone outcrops (particularly onshore of the two main reefs).

In situ Observations

In situ observations of waves and water levels were collected at nine locations for a total of 16 months between November 2015 and August 2017. Observations were made almost continuously for the 15 months between November 2015 and January 2017, and for another month from end of June to July 2017. Pressure sensors (sampling continuously either at 1 or 2 Hz) were deployed at eight sites (depths ranging from ∼1.7 to 3.6 m, see **Table 1**) within the lagoon and were organized into one alongshore and two cross-shore transects (**Figure 1A**). Offshore of the southern reef (in ∼18 m depth), a Nortek AWAC recorded wave conditions incident to the study area. The instruments were bottom-mounted on aluminum frames weighed down with lead and were serviced approximately every 3 months based on battery

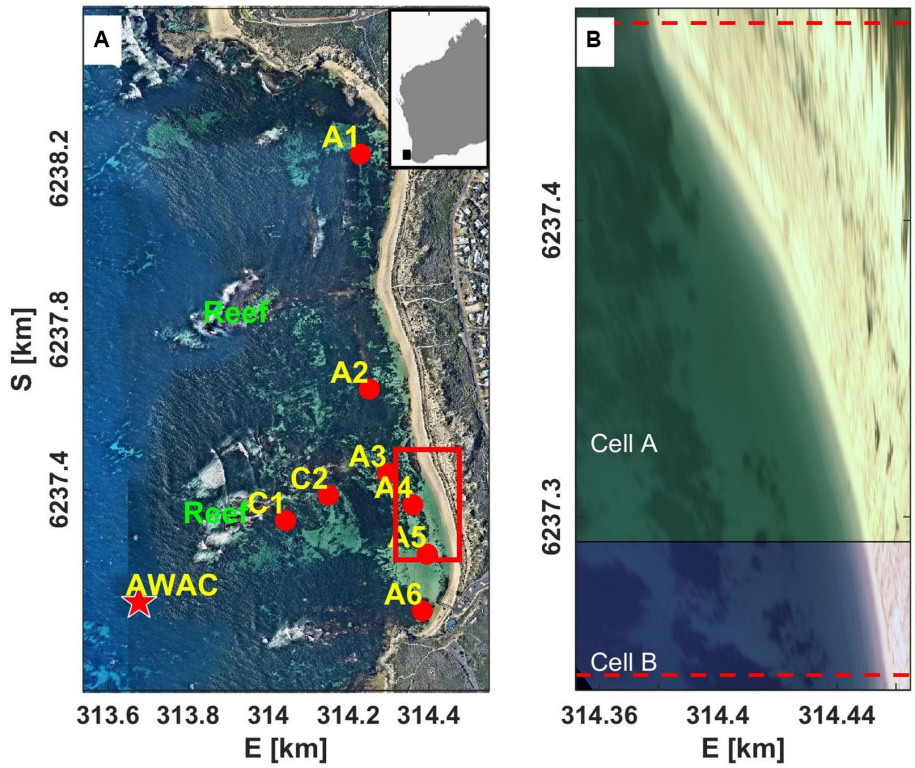

FIGURE 1 | (A) Aerial photo of the study area with 2 main offshore reefs around 600 m from the shoreline (source: www.nearmap.com). The red star denotes the location of the AWAC, the red circles denote locations of the pressure gauges. The red rectangle is the coverage area of video camera. The insert at top right corner shows the location of Gnarabup beach at the southwest coast of Western Australia. **(B)** The coverage area at the south of the beach from the image rectification process (red box in **Figure 1A**) used in this study and the 2 parts, i.e. **(A,B)**, at Cell 3 (see **Figure 7B** for the description) separated by a black line that represents the location of a node (center of beach rotation). The red dashed lines denote the border of 5 m farthest points used to identify shoreline rotation in **Figure 7C**). The coordinate system is in UTM (Universal Transverse Mercator) Zone 50.

life. Among the 15 months of nearly continuous data, there were some occasional gaps in the instrument records; for example, between April and May 2016 when the AWAC was overturned due to a large storm. The AWAC was also not deployed from February to June 2017. To provide a continuous estimate of the wave conditions at this site, data were approximated using empirical relationships derived between observations from a directional wave buoy operated by the Western Australia Department of Transport (DoT) deployed in 48 m depth offshore of Cape Naturaliste approximately 50 km NW of the study site. During overlapping periods, the wave heights at the two sites were strongly correlated (**Figure 2A**, $R_{Hs-Gna} = 0.93$), which allowed us to fill data gaps based on a linear relationship observed between the buoy and AWAC,

$$H_{s,Gna} = 0.8952 H_{s,Nat} - 0.0978 \quad (1)$$

where $H_{s,Gna}$ is offshore wave height at Gnarabup Beach and $H_{s,Nat}$ is offshore wave height at Cape Naturalist.

Datum-referenced tidal and non-tidal water levels were recorded by a tide gauge operated by DoT located in Port Geographe, approximately 45 km north of the study site. Gaps in the offshore Gnarabup water levels (when the AWAC was not properly functioning or not deployed) were estimated from the Port Geographe tide gauge based on a linear correlation observed between these sites (**Figure 2B**, $R_{WL-Gna} = 0.93$):

$$WL_{Gna} = 0.9753 WL_{Geo} - 0.0515 \quad (2)$$

where WL_{Gna} and WL_{Geo} are water level fluctuations at Gnarabup Beach and Port Geographe, respectively.

Wave statistical properties at the AWAC site were determined based on 2400 sample burst recorded at 1 Hz every other hour. AWAC measurements were processed using the Nortek Storm software, which calculates the wave spectrum based on the acoustically tracked sea surface, pressure fluctuations, and near-surface velocity signals. At the lagoon sites with pressure sensors, spectral estimates of the sea-swell (SS, periods < 25 s) and infragravity (IG, periods 25–600 s) wave height and frequency were made using hourly records (3600 or 7200 samples based on instrument sampling frequency) using linear wave theory. Non-tidal water level variations at frequencies longer than the tides (i.e., subtidal water levels) were obtained by low-pass filtering hourly averaged water level signal using a PL66TN filter with a half-power cutoff period of 33 h (Beardsley et al., 1983). Additionally, wave setup at the lagoon sites was estimated by comparing the depth difference between the sensors located at the reef and the

TABLE 1 | Site names, instrument type, and approximate mean depth during the study period.

Site name	Instrument type November 2015–January 2017	Date range	Mean depth (m)
Offshore	Nortek	D1 = 12/11/15–2/11/16	18.0
	AWAC	D2 = 27/6/17–20/8/17	
Lagoon			
A1	RBR solo	D1 = 11/11/15–24/1/16	3.5
		D2 = 9/2/16–20/7/16	
		D3 = 14/9/16–6/1/17	
		D4 = 28/6/17–25/7/17	
A2	RBR solo	D1 = 11/11/15–20/1/16	2.7
		D2 = 14/9/16–11/1/17	
		D3 = 28/6/17–25/5/17	
A3	RBR solo	D1 = 11/11/15–30/1/16	1.7
		D2 = 9/1/16–23/7/16	
		D3 = 13/9/16–2/2/17	
		D4 = 27/6/17–20/7/17	
A4	RBR solo	D1 = 11/11/15–25/1/16	2.5
		D2 = 9/2/16–2/7/16	
		D3 = 14/9/16–30/12/16	
		D4 = 27/6/17–21/7/17	
A5	RBR solo	D1 = 11/11/15–24/1/16	2.6
		D2 = 14/9/16–20/1/17	
		D3 = 27/6/17–21/7/17	
A6	RBR solo	D1 = 11/11/15–30/1/16	3.0
		D2 = 9/2/16–4/7/16	
		D3 = 13/9/16–2/2/17	
		D4 = 27/6/17–22/7/17	
C1	RBR solo	D1 = 11/11/15–21/1/16	3.6
		D2 = 9/2/16–18/7/16	
		D3 = 13/9/16–2/2/17	
		D4 = 28/6/17–25/7/17	
C2	RBR solo	D1 = 11/11/15–27/1/16	3.4
		D2 = 12/2/16–6/6/16	
		D3 = 13/9/16–2/2/17	
		D4 = 28/6/17–25/7/17	

The D1–D4 refers to the deployment periods in between servicing.

one offshore, as described in e.g., Mory and Hamm (1997) and Beetham et al. (2016),

$$\bar{\eta} = \bar{h} - (\bar{h}_0 + \Delta h) \tag{3}$$

where $\bar{\eta}$ is the wave setup at the lagoon sites; $\bar{h}$ is the mean depth at the lagoon site; $\bar{h}_0$ is the depth at the offshore AWAC (with overbars indicating hourly averaging); and Δh is the difference in elevation between the offshore sensor and the lagoon sensors. The depth difference was calculated assuming a flat sea surface during periods with minimal incident wave energy and periods with small tidal residual (see section "Intertidal Beach Morphology").

Video Shoreline Detection

At the southern end of the beach, an elevated camera was installed to quantify the shoreline variability. The video system consisted of a Point Gray Blackfly 5 MP video camera with 12.5 mm fixed-focal-length lens that was mounted on a light pole 15.9 m above mean sea level. Every other hour during daylight, the system collected 10 min of video recording at 1.5 Hz. Time exposure (timex) images were produced by averaging the 900 video frames recordings from which the average shoreline position could be extracted (see Holman and Stanley, 2007). Between November 2015 and July 2017, there were 3390 timex images collected by the video system from which ∼97% were useable for shoreline detection.

The timex images were transformed onto a horizontal plane and rectified by taking into account the tidal level to increase the accuracy of the shoreline position on the rectified images (Bryan et al., 2008; Blossier et al., 2017b). Due to the decrease in pixel resolution with increasing distance from the camera, the usable area of the rectified images was 112 m in the cross-shore and 250 m in the alongshore (indicated by the red rectangle on **Figure 1A**).

Numerous algorithms have been developed to detect shoreline position from timex images automatically (e.g., Uunk et al., 2010; Almar et al., 2012; Simarro et al., 2015). At Gnarabup, the white sand and clear water, coupled with the variability in atmospheric conditions and lighting, resulted in no single methodology from those available in the published literatures working optimally for all images. As a result, we relied on an algorithm that sequentially adopted four methods; the maximum grayscale intensity (Holland et al., 1997), the color channel divergence method that identifies the difference between red and blue channels (Turner et al., 2004), pixel intensity clustering which is based on the hue saturation value (Aarninkhof, 2003), and the Otsu method that works on the black and white color model (Otsu, 1979). Each method was applied to the cross-shore array of pixels of each images and the predicted shorelines from each method were evaluated using a multi-criterion analysis (e.g., Longley et al., 2005).

The shoreline of an image was selected among the four detection methods based on the following criteria. First, the cross-shore difference in the detected shoreline position between adjacent shoreline points was calculated. If the difference between adjacent shoreline points was greater than 5 m, the detected shoreline was automatically discarded. This approach was designed to capture erroneous shorelines in which points of the detected shoreline were either anomalously too far offshore or inland. Second, of the remaining shorelines that were not removed due to the first criterion, the shoreline was selected whose alongshore averaged position was the closest to the alongshore averaged position of a reference shoreline. The reference shoreline was the average shoreline position of a random sampling of 150 hand digitized shorelines spanning all weather conditions. In some cases, often during low light, none of the four automatically detected shorelines met the above criterion, in these cases the shoreline was digitized manually. The multi-criterion analysis showed almost all of the shorelines (∼90%) were predicted using HSV, RGB and grayscale methods (i.e., each method could predict ∼30% of the total shorelines), and the remaining shorelines were predicted using Otsu method. Overall, the combined algorithm was able to accurately detect

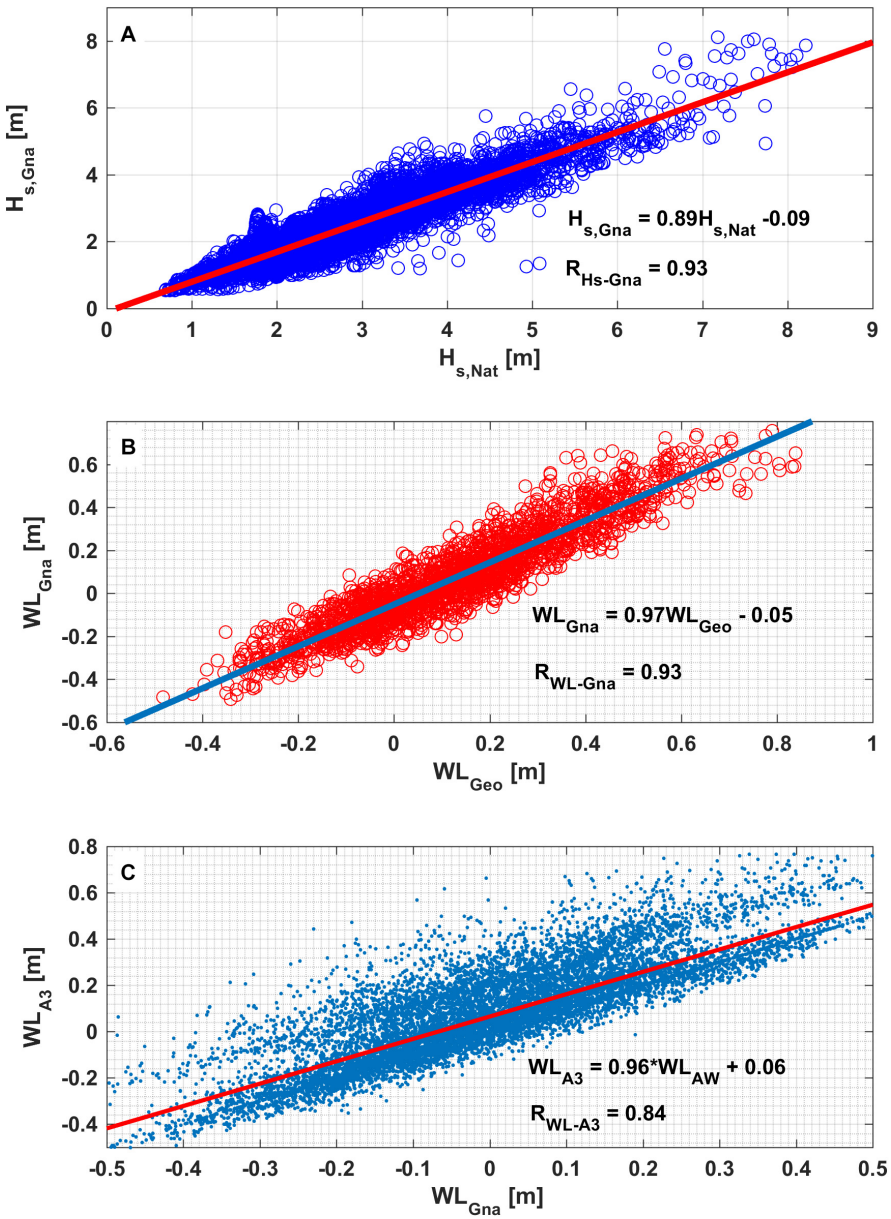

FIGURE 2 | Relationships between **(A)** offshore wave heights at Cape Naturaliste (H_{Nat}) and Gnarabup (H_{Gna}), **(B)** offshore water level elevations at Busselton (WL_{Bus}) and Gnarabup beach (WL_{Gna}), and **(C)** offshore water level at Gnarabup beach (from AWAC and Busselton tide station) and inside the lagoon at A3.

76% of the shorelines from the 3277 images, the remaining shorelines required assistance from manual digitization. All of the automatically detected shorelines were also manually checked to ensure their quality.

Intertidal Beach Morphology

As the shoreline recorded from a timex image reflects the position of the waterline with all water level contributions included (tidal and non-tidal), any shoreline position change between successive timex images does not necessarily reflect changes in the beach morphology. To estimate the position of the daily (datum-based) shoreline, the horizontal excursion of the shoreline, in combination with the recorded water levels, were used to reconstruct the intertidal beach morphology. Datum-based water levels recorded by the pressure sensors were estimated by determining the deployment depth of the sensor relative to the Australian Height Datum (AHD, representing approximately mean sea level). This was done by comparing the measured hourly-averaged water levels at site A3, which was close to shore and had the longest recorded time series, with the hourly average water levels recorded at the Port Geographe tide gauge that were referenced to AHD. To minimize the contribution of wave- and/or wind-driven setup and other non-tidal water levels, the comparison was made only for hours when the tidal residuals

measured at Port Geographe were less than 0.1 m and the offshore waves recorded by the AWAC were less than 1.5 m. As the deployment location and depth varied slightly between each deployment, this analysis was conducted independently for each deployment period lasting several months. For instances when the water level data was not available from site A3 (e.g., February–June 2017), the water level at that position was estimated from the AWAC water level, given that this water level was found to be well-correlated with the water level measured at A3, R_{WL-A3} = ∼0.84 (**Figure 2C**).

The deployment depth (relative to AHD) for each instrument was estimated from the average bottom elevation (tide removed) from all periods where the tidal residuals and wave heights were less than a threshold (less than 0.1 and 1.5 m, respectively). This resulted in a total of 22 estimates of the instrument depth (with a standard deviation of 0.17 m) for the four deployments (for which the tidal residual ranged from 0.02 to 0.1 m and incident wave height ranged from 0.54 to 1.37 m). The AHD shoreline elevation from each timex image in between November 2015 to July 2017 was assumed to be equivalent to the recorded AHD elevation from the hourly water level at site A3. The daily intertidal beach morphology was then reconstructed by linearly interpolating the horizontal and vertical positions of the hourly shorelines. From the reconstructed beach morphology, the location of the 0 m AHD contour was extracted for each day and used in all subsequent analysis (**Figure 3A**). This approach was acceptable for 488 of the 504 days. For the remaining 16 days, none of the video derived shorelines spanned the 0 m AHD contour (i.e., water levels never exceeded or dropped below 0 m). For these days, the shoreline position was estimated by extrapolating the beach slope estimated from the range of elevations covered. The regression models used in the beach extrapolation were generated from monthly cross-shore profiles and the corresponding elevations as illustrated in **Figure 3B**. The modeled curves were used to extend the shape of daily intertidal bathymetry to obtain a shoreline position at a reference elevation (0 m).

In addition to the video-derived shorelines, seven topographic beach surveys were conducted between December 2015 and July 2017 using a backpack-mounted Differential Global Navigation Satellite System (DGNSS) receiver. Following the method of Segura et al. (2018), for each survey the complete 1.5 km beach was traversed by foot in a series of cross- and alongshore lines each spaced ∼30 m apart and spanning −0.5 to 5 m AHD. The points from the DGNSS receiver (collected at 2 Hz) were organized into a triangular irregular network (TIN) and subsequently interpolated onto a 2 m regular grid. The sub-aerial beach volume from each survey was estimated using trapezoidal integration (e.g., Roy, 2010) with 2 m grid cell size calculated over 49,485 m^2 of beach area with −1 m AHD as the lowest elevation. To evaluate the quality of the video derived shorelines we compared the daily 0 m contour shorelines extracted from the video system with those estimated from the DGNSS backpack survey for 4 days during which both data sets were available. The average (across the four surveys) root mean square error (RMSE) calculated over the 250 m alongshore stretch of beach common

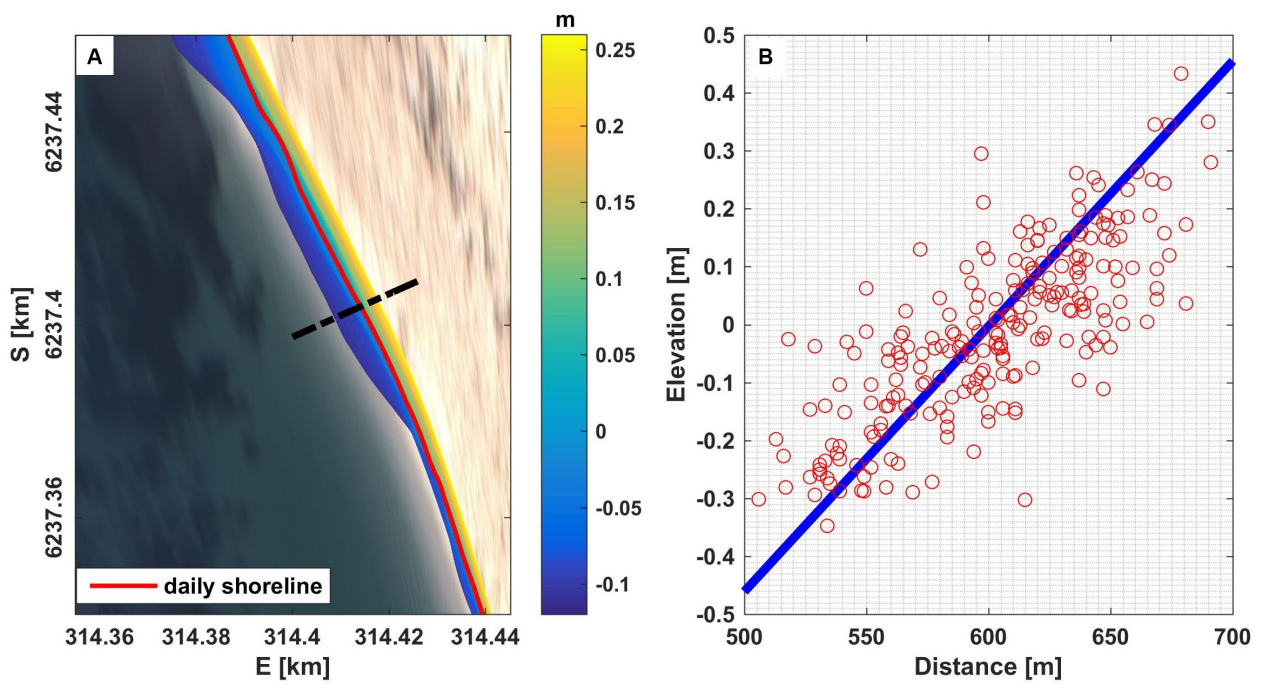

FIGURE 3 | (A) Daily intertidal bathymetry on 16 November 2015, the red line represents the shoreline at 0 m and the dashed black line is the location cross-section profile at **(B)**. **(B)** A modeled cross-section profile at S 6237.4 km in November 2015 (blue line), red dots are the corresponding shoreline positions recorded during the month.

to both data sets was 1.71 m (average bias of 3.82 m). The difference between the shorelines is potentially a result of image rectification errors (e.g., Tian et al., 2002; Girard, 2018) as well as interpolation of the survey data (to extract the 0 m contour) which was produced from cross-and alongshore transects spaced ∼30 m apart.

RESULTS

Hydrodynamic Conditions

During the study period, the offshore significant sea-swell (SS) wave heights at the offshore AWAC averaged 2.3 m (**Figure 4A**), with a mean direction from the southwest and west. Wave heights were lower (higher) during the austral summer (winter) months, with episodic, high-energy winter storms causing large wave events (i.e., reaching up ∼8 m in July 2016). From the wave spectrum at the AWAC between November 2015 and July 2017 (**Figure 5A**) the incident waves were dominated by sea-swell waves with peak period of 5–20 s. We identified 75 days of energetic wave events (daily average H_s higher than 3.5 m) that mainly occurred during winter with maximum daily average H_s of 6.9 m on 31 July 2016. Stormy days also occurred in spring and autumn for example two consecutive days of storm in the beginning of October 2016 (see **Figure 4A**). The hourly offshore mean water level reached a maximum of 1.05 m above AHD, with a range of 1.62 m over the study period (**Figure 4B**). The offshore non-tidal water level variations reached a maximum value of up to 0.62 m above AHD and a minimum of −0.17 m AHD. The two reefs shelter the beach creating a semi-protected lagoon, and the daily-averaged significant wave height never exceeded 1.5 m within the lagoon, even when the offshore waves reached 8.4 m (**Figure 4D**).

Inside the lagoon, as wave energy within the SS band dissipated, the wave spectrum became increasingly dominated by IG waves, particularly at site A6 in the protected southern corner of the lagoon (see **Figures 5B–D**). Similar to other reef environments, SS waves were mostly depth-limited in the lagoon (Lowe et al., 2009) with the breaking index (the ratio between wave height and local water depth) of ∼0.4 for all sites (**Figure 6A**). In contrast, the IG waves in the lagoon did not appear to display any depth limitation on water depth over the study period (**Figure 6B**). The IG waves were typically less than 0.5 m and showed less spatial variability among sensors inside the lagoon (**Figure 4E**). Within the lagoon, the IG waves made a significant contribution to the total wave energy, especially at the most protected area at the south (site A6) where the SS waves were smallest (**Figure 4F**). Both the SS and IG wave heights were strongly correlated with the offshore waves (R_{SS} = 0.83 and R_{IG} = 0.81, respectively).

Time-series of wave setup at site A3 are shown in **Figure 4G**. Note that there were only small differences in setup between A3 and the other lagoon sites. This is likely because the setup in the lagoon was dictated by breaking on the offshore reefs rather than breaking inside the lagoon, with maximum RMSE among sites relative to A3 of only 0.016 m with maximum bias of less than 1 cm (% error among sites relative to A3 of 7.7–31.5%, highest at A1) over the study period (not shown). The maximum daily wave setup over the 15 months (November 2015 to January 2017) reached 0.32 m at site A3, which coincided with a large wave event on 1 October 2016 when the daily significant wave height at the AWAC site was 5.8 m. Wave setup at all sites was very strongly correlated (R_η of ∼0.85 to ∼0.95) with the off-shore wave height squared (proportional to the incident wave energy) (**Table 2**).

Beach Dynamics

Sub-aerial beach dynamics were quantified using the daily video-derived shorelines, which supplemented by less frequent DGNSS backpack-based surveys of the entire 1.5 km beach. While the video-derived shorelines were available almost every day, they only captured the southern 250 m of the beach. As a result, the complete topographic surveys of the beach, while being much less frequent, provide valuable additional context to the video shorelines.

Topographic Beach Surveys

Over the 20 months (from December 2015 to July 2017), the total sub-aerial beach volume averaged over the entire 1.5 km beach was largely conserved (**Figure 7A**, the blue line). Relative to the initial total beach volume (in December 2015) of ∼195,000 m^3 (calculated over 49,485 m^2 of beach area with −1 m AHD as the lowest elevation), the maximum total beach volume changes were ∼23,100 m^3 (∼15.4 m^3/m), which is equivalent to ∼11.8% of the total initial beach volume (**Figure 7A**). However, despite the total beach volume being mostly conserved, there was considerable alongshore variability in the seasonal erosion and accretion patterns over the study period (**Figure 8**).

To investigate these erosion/accretion patterns in further detail, we divided the beach into three cells based on the patterns in the beach elevation changes (**Figure 8**, with boundaries generally aligning with the alongshore locations of the reefs). The volume changes indicate that each cell is semi-closed, as evident by small volume within Cell 1 to Cell 3 in **Figure 7A**, with a local out of phase erosion/accretion response within each cell (**Figure 8**). The elevation changes over the two summer seasons within the study period (**Figures 8A,D**) showed similar patterns, characterized by sand deposition at the northern and southern corners of the beach, accretion of the salient that formed where the northern reef attaches to the coast at the boundary between Cell 1 and 2, and erosion of the salient that formed where the southern reef attaches to the coast at the boundary between Cell 2 and 3.

The beach evolution in transitional seasons (spring and autumn), showed different behavior. During spring between September to November 2016 (**Figure 8C**), both the northern salient (boundary between Cell 1 and 2) and the corners of the beach near the headlands accreted; whereas the southern salient (boundary between Cell 2 and 3) eroded. The sand volume during the period decreased by ∼3,500 m^3 (around −2.4 m^3/m or −1.8% of total beach volume, **Figure 7A**), which is likely related to the high wave heights in October to November 2016 that reached 5.8 m (see **Figure 7D**). In contrast, between February to June (autumn) 2017, the beach exhibited erosion at both salients and

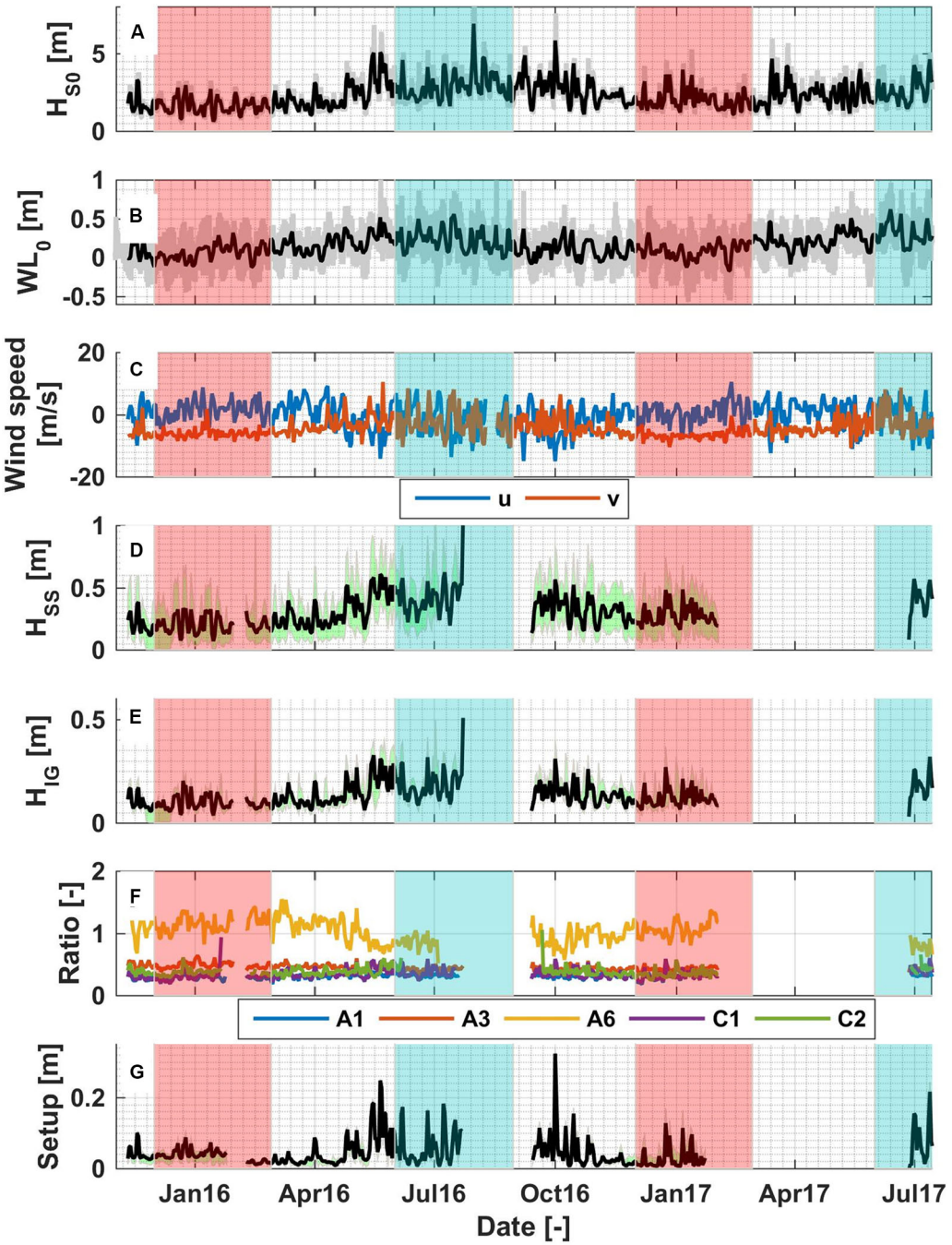

FIGURE 4 | Daily average (solid black line) and hourly (solid gray line) **(A)** offshore significant wave height. **(B)** Non-tidal (solid black line, filtered using PL66TN with a half-power cutoff period of 33 h) and hourly water level (solid gray line) variations. **(C)** East (*u*, blue line) and north (*v*, red line) components of daily wind speed. **(D)** Daily sea-swell (SS) and **(E)** infragravity (IG) wave heights at site A3, chosen to represent the conditions inside the lagoon. **(F)** Ratio between IG and SS at selected observation points. **(G)** Daily wave setup at A3. Gray lines and green areas at figure **(D,E,G)** denote the range of value among the sensors inside the lagoon. Transparent red and blue regions denote periods of the austral summer and winter, respectively.

deposition at all embayments (**Figure 8E**). The autumn profile showed a slight decrease (−0.87%) of the total beach volume (**Figure 7A**). During autumn 2017, the daily wave heights were relatively higher (average of 2.3 m), compared to that of the summer (average of 2.1 m).

The winter (June to August) beach elevation patterns (**Figures 8B,F**) showed an opposite response to the summer patterns (**Figures 8A,D**). Sediment accumulated in the southern portion of each cell, with erosion on the northern ends; during this period there was additional ∼18,000 m^3 (9.3%) of sand

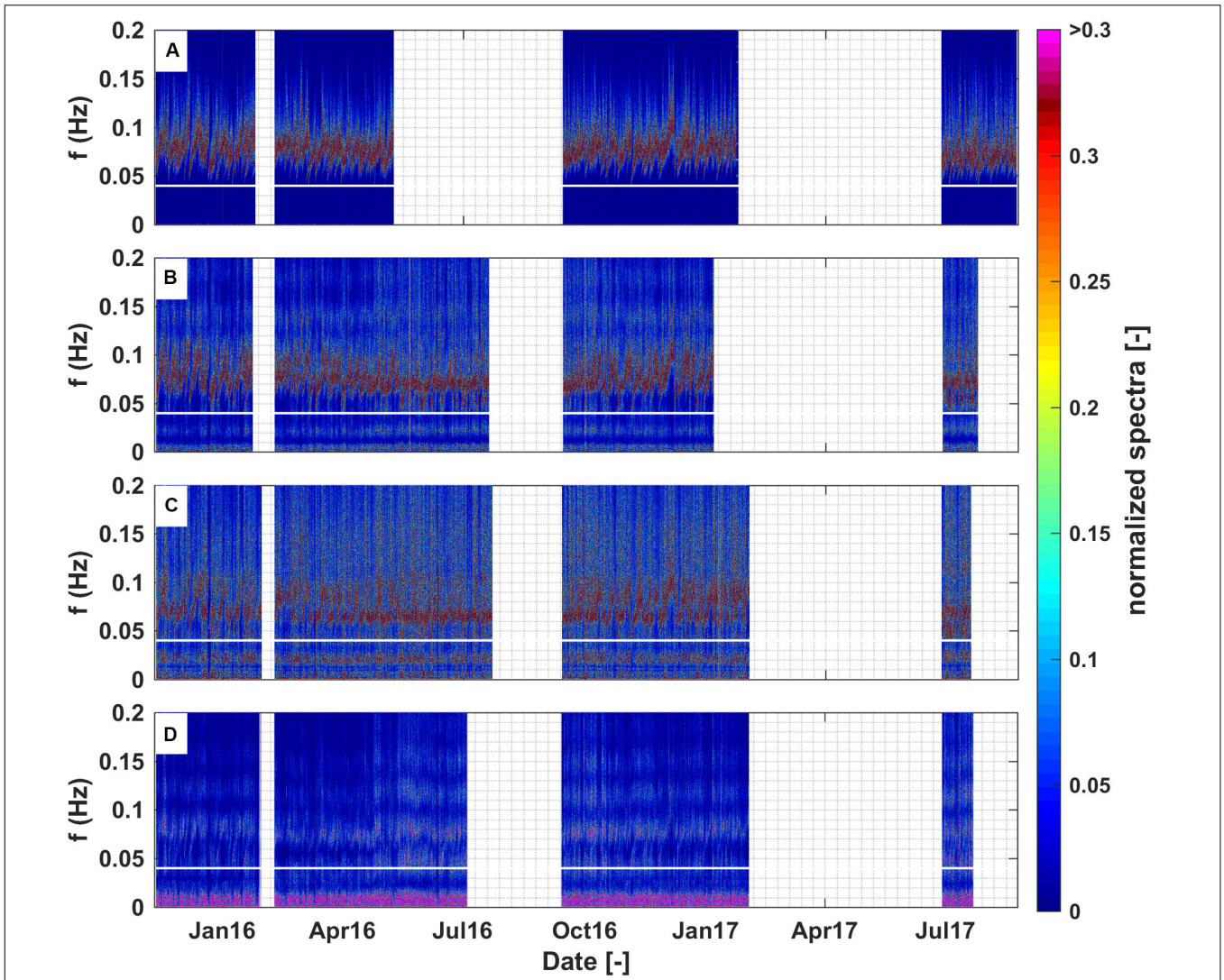

FIGURE 5 | Time series of normalized energy density spectra (against the maximum value of each hourly spectra) at **(A)** offshore, **(B)** A1, **(C)** A3, and **(D)** A6 (see **Figure 1A** for site descriptions) with spectra resolution of 0.0005 Hz. The horizontal white line on the figures represents the separation frequency (fsplit of 0.04 Hz) for the short-wave and infragravity bands. Blank parts on the figures denote the periods without observation.

added to the overall beach volume, mostly deposited on the lower beach between 0 and −1 m elevations, thus indicating some flattening of the beach.

Video Shoreline Observations

The video monitoring captured daily shoreline movements in the central and northern portion of Cell 3 where images were obtained (see **Figure 1A**, red box). Consistent with the topographic surveys, the video observations indicated shoreline rotation within Cell 3, and we thus used the nodal point (derived from the topographic beach surveys) to divide the cell into two sections within the camera's field of view (hereinafter referred to Cell 3A and Cell 3B, **Figure 1B**, note the camera's field of view only captured the northern portion of Cell 3B close to the nodal point). The temporal mean shoreline position averaged over the 20 month period was removed from the daily shoreline position yielding daily relative shoreline positions (**Figure 7B**). The shoreline movements were characterized by short term oscillations over days-to-weeks, which were superimposed on longer time-scale (seasonal) cycle (**Figures 7B,C**). Given that the data from the topographic surveys indicated that similar beach rotation patterns occurred over the entire beach (**Figure 8**), we would expect both Cells 1 and 2 to show rotational responses that were similar to Cell 3.

The shoreline rotation signal within Cell 3 becomes even more apparent (**Figure 7C**) within timeseries of the monthly-averaged northern and southern limits of the shoreline positions within the cell. In the rectified images, these locations coincide with y = 0–5 m (Cell 3B) and y = 245–250 m (Cell 3A) (see red dashed lines in **Figure 1B**). The offshore wave and water level conditions (**Figure 4**) influenced the change of shoreline positions, resulting in both an in-phase (uniform) and out-phase

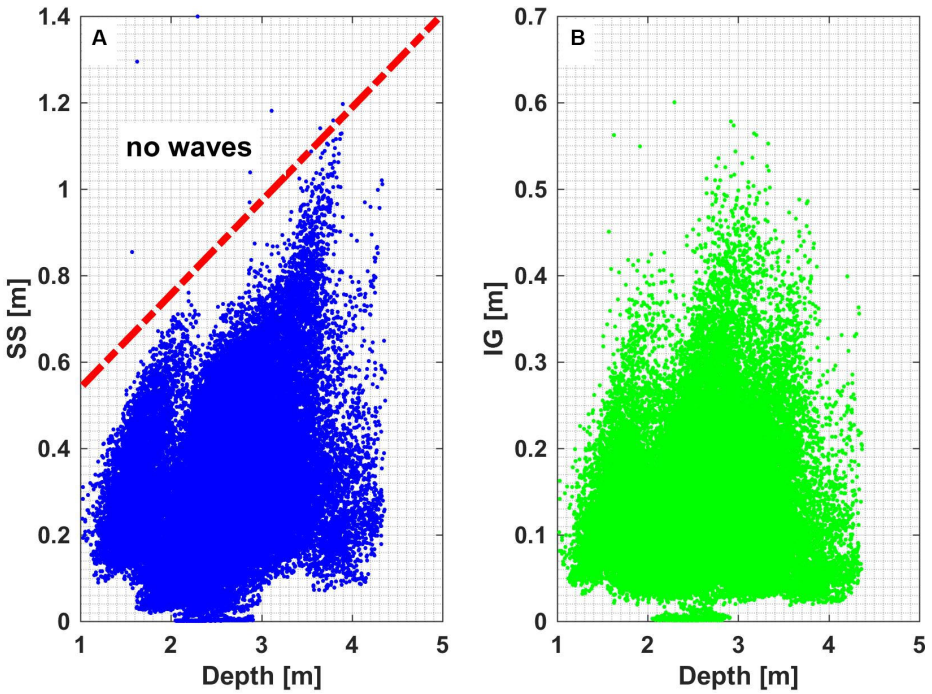

FIGURE 6 | Correlation between water depth and **(A)** sea-swell significant wave heights as well as **(B)** infragravity significant wave heights at all observed points inside the lagoon. The red dashed line in **(A)** represents a sea-swell wave height to depth ratio (γ) of 0.39.

(rotational) response at the extreme ends of Cell 3A and Cell 3B (**Figure 7C**). In December 2015–February 2016 (summer), the wave energy was the lowest of all the seasons over the study period (with daily H_{s0} of 1.6 m on average), and the shoreline across both Cells 3A and 3B was accreted (except for in the very early summer where Cell 3B was eroded), with larger accretion in Cell 3A suggesting northward alongshore transport (**Figure 7C**). In December 2016–February 2017 (Summer), most of the shoreline was consistently eroded across both Cells 3A and B with greater erosion at Cell 3A (~ -4 m) compared to that of Cell 3B, which could be due to some southward alongshore sediment transport. The subtle differences in the shoreline responses during the summers of 2016 and 2017 appears to be due to the differences in the average offshore wave conditions between these years. Compared to the summer of 2016, the summer of 2017 experienced larger waves (average H_s of 2.1 m versus 1.6 m in the summer of 2016). This could be partially attributed to stronger local wind conditions in 2017 (average of 7.7 m/s) than the average value of 7.0 m/s in 2016 (**Figures 4A,C**).

TABLE 2 | Summary of correlation coefficient between offshore wave energy ($\sim H^2$) and setup at observed locations for all observation period and every season.

Seasons	A1	A2	A3	A4	A5	A6	C1	C2
All	0.92	0.92	0.91	0.92	0.95	0.85	0.92	0.91
Summer 2016	0.84	0.94	0.78	0.77	0.90	0.60	0.87	0.90
Fall 2016	0.95	N/A	0.96	0.96	N/A	0.96	0.96	0.94
Winter 2016	0.88	N/A	0.92	0.91	N/A	0.90	0.90	0.75
Spring 2016	0.97	0.98	0.98	0.98	0.98	0.63	0.96	0.98
Summer 2017	0.88	0.98	0.97	0.96	0.95	0.92	0.94	0.97

N/A shows when the data is not available.

During the winter (June–August) seasons, the shoreline responded more consistently at Cells 3A and 3B, with both sub-cells showing rapid erosion and recovery (**Figures 7B,C**). The shorelines showed a slight counter-clockwise rotation at the beginning of the winter of 2016 and then demonstrated an in-phase (uniform) response during the remainder of the winter of 2016 before the shoreline began to rotate counter-clockwise after July 2016 (**Figures 7B,C**).

The shoreline patterns in autumn (March–May) were opposite to that of spring (August–November) in which during both periods, the daily offshore wave height was moderate (2–4 m). Shoreline patterns in autumn 2016 showed the shoreline rotated clockwise, in which Cell 3B was more accreted than Cell 3A. However, during spring (around September to early-October 2016), when the daily wave heights decreased, the sediment tended to move back to Cell 3A; as a result, Cell 3B became eroded and the shoreline rotated anti-clockwise (**Figure 7C**).

During large wave events (defined as days with offshore $H_s > 3.5$ m), which mainly occurred during winter months but also occasionally in other seasons (**Figure 4A**), the entire shoreline in Cell 3 mostly retreated up to 10 m. But it often quickly recovered as wave energy decreased; for example, during the storms on 31 July 2016 with average daily offshore wave height of 5.8 m (**Figure 4A**). During some storm events, we observed a rotational response, i.e., accretion within one portion of Cell 3 while the other portion became eroded; however, there

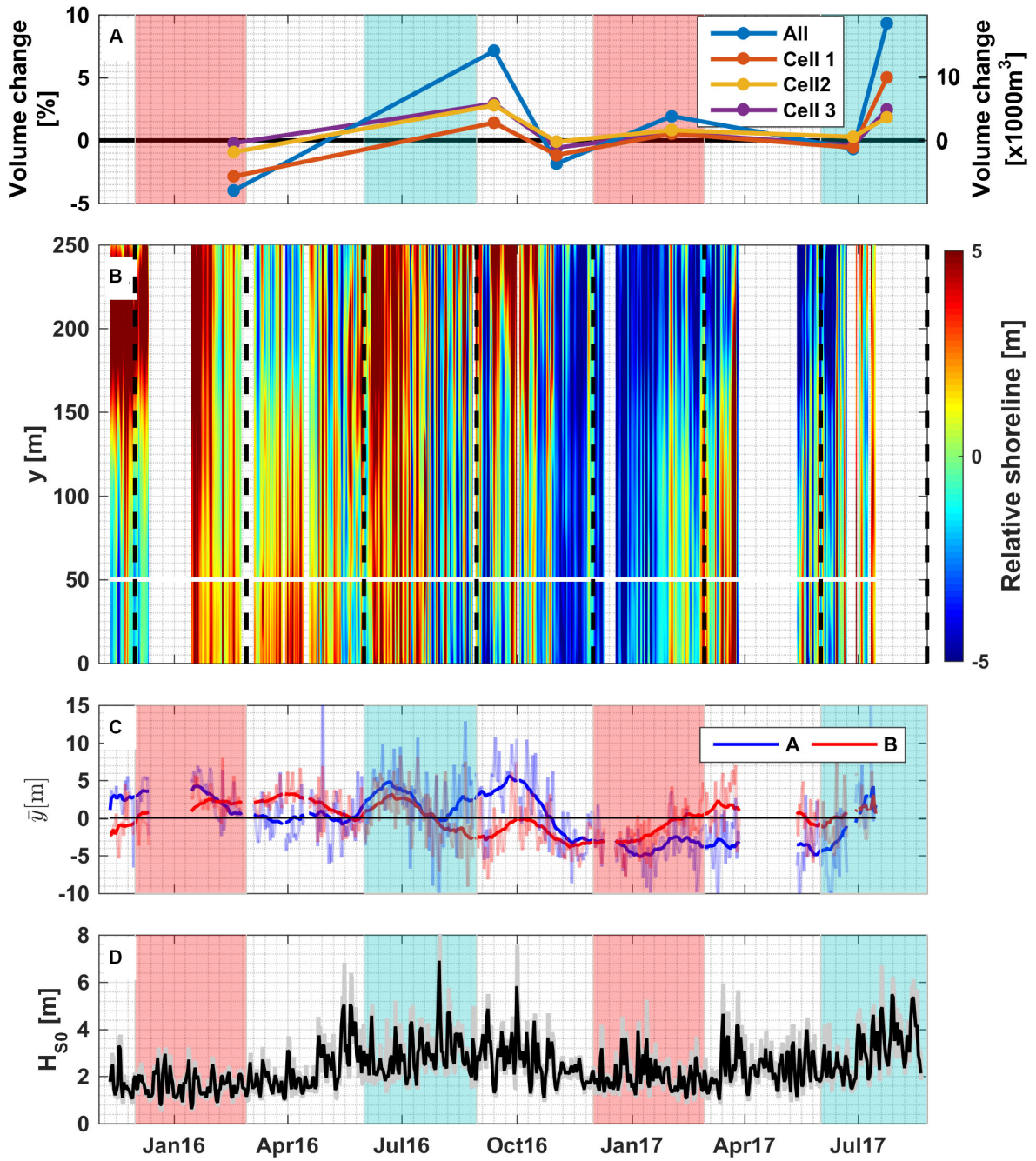

FIGURE 7 | (A) Volume change of the beach between successive topographic surveys in 2015–2017, relative to the initial beach volume in December 2015. The respective primary and secondary *y*-axis show the beach volume change in percentage relative to initial total beach volume and in 1000 cubic meters. **(B)** Daily shoreline positions (colors) relative to the mean position over the entire observation period along the 250 m alongshore stretch of beach. A white horizontal line shows the boundary between Cell 3A and B. **(C)** Daily (thin) and monthly averaged (bold) shoreline positions at 5 m farthest points from the node of part **(A)** (blue) and **(B)** (red) which refer to dashed red lines at **Figure 1B**. Gaps in **(B,C)** are the periods when video images were unavailable. **(D)** Daily average (solid black line) and hourly (solid gray line) offshore significant wave height. Transparent red and blue regions as the vertical black dashed lines denote periods of the austral summer and winter, respectively.

were inconsistent responses in shoreline rotation to individual storms. Examples include the days of 16 May (H_s = 5 m) and 7 June 2016 (H_s = 4.6 m) where Cell 3A accreted, whereas on 15 March (H_s = 4.6 m) and 13 July 2017 (H_s = 4.6 m) Cell 3B accreted. Over the full record correlations between Hs > 3.5 m and shoreline at 3A–3B were very weak with $R < 0.1$ ($p > 0.05$).

The shoreline positions during the observation period were very weakly correlated to the main offshore hydrodynamic

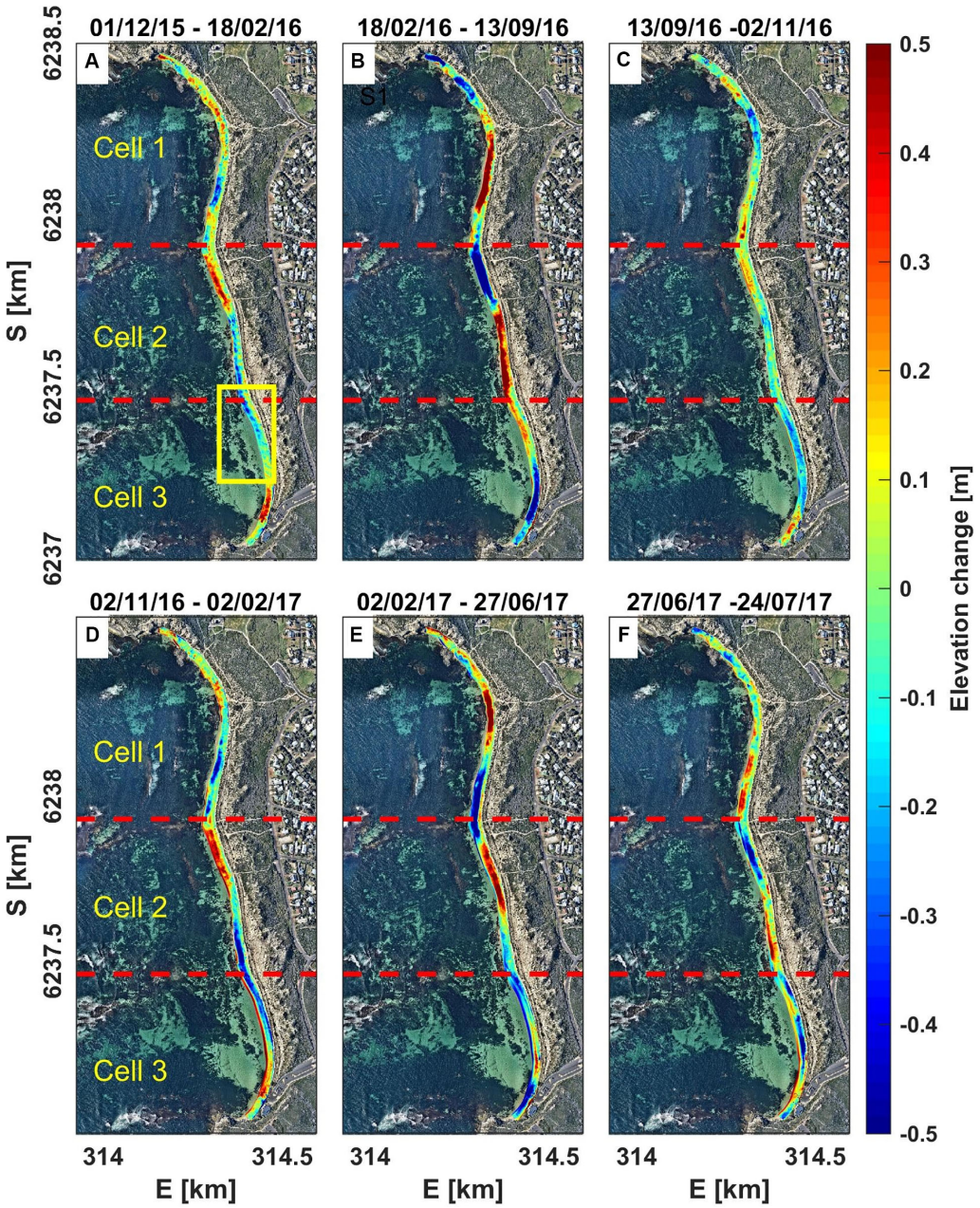

FIGURE 8 | Beach elevation changes within period of **(A)** 01/12/2015-18/02/2016, **(B)** 18/02/2016-13/09/2016, **(C)** 13/09/2016-02/11/2016, **(D)** 02/11/2016-02/02/2017, **(E)** 02/02/2017-27/06/2017, **(F)** 27/06/2017-24/07/2017, separated into three cells (Cell 1-Cell 3) based on the position of anti-nodes located behind the offshore reefs (red-dashed lines). The yellow box in figure **(A)** is the area covered by video camera system.

forcing, including wave height and direction as well as subtidal water level (that modulates wave transmission across the reefs) ($|R| < 0.3$, $p < 0.05$). However, if the correlations were computed between the shoreline positions and wave heights from each season independently, we found greater correlations. This especially occurred during summer and winter, with $R = -0.55$ and -0.48 at Cell 3A as well as $R = -0.55$ and -0.42 at Cell 3B (with all $p < 0.05$), respectively. Similarly, correlation coefficients with the offshore water level were larger in summer (Cell 3A of ∼0.26 and Cell 3B of ∼0.37, all $p < 0.05$) but slightly weaker in winter (Cell 3A of 0.16 $p > 0.05$ and Cell 3B of 0.32 with $p < 0.05$). During transitional seasons, autumn and spring, the shoreline positions were weakly correlated with the offshore hydrodynamics. Correlations remained low between shoreline position and offshore wave direction over the entire data set or by seasons ($R < 0.14$ for entire years and seasonal, $p < 0.05$ at Cell 3A for all years and spring). Although there were appreciable fluctuations in the shoreline position at individual

locations, overall, there was a balance between erosion and accretion indicating the beach is in dynamic equilibrium with no significant net trend in erosion or accretion (**Figure 7B**).

Given the role of offshore water level in modulating wave breaking over reef platforms (e.g., Lowe et al., 2005), it is expected that the offshore water level fluctuations at the site would have an impact on the shoreline dynamics. To examine the shoreline response to both offshore waves and water levels, the shoreline position from the northern and southern 5 m of the camera's field of view (transparent lines in **Figure 7C**) were organized into 0.2 m bins of daily averaged offshore wave height and 0.1 m bins of daily averaged offshore water level. All daily shoreline positions that occurred with the corresponding wave and water level bins were averaged within each bin (**Figure 9**). While there was significant scatter, in general, we see a trend of greater erosion for the same wave height, with lower water level, and vice-versa. The greatest shoreline accretion occurred at the higher water levels. For example, in both Cells 3A and B for offshore wave heights between 2 and 2.5 m, we generally observed shoreline accretion during high water levels and erosion for low water levels. By further relating the erosion and accretion patterns of Cell 3A and B to larger offshore wave heights (>3.5 m) and the corresponding subtidal water levels across study period, we found that accretion at both Cells 3A and B mostly occurred during high subtidal water levels (average of 0.32 m); for example, on 1 October 2016 (daily H_s ∼5.8 m and subtidal water level ∼0.3 m). In contrast, when the subtidal water level was lower (average of 0.21 m), erosion occurred across the entire shoreline, for example, on 9 August 2016 (daily H_s ∼4.2 m and subtidal water level ∼0 m). During intermediate subtidal water levels (in between 0.21 and 0.32 m), we identified a rotational response with accretion at one of the cell followed by erosion at the other cell.

DISCUSSION

This study investigated the shoreline and beach elevation changes at a reef fronted pocket beach at Gnarabup Beach in southwestern Australia. The site receives substantial offshore wave energy. Strong wave breaking occurs over the reefs, where significant energy is generated at the infragravity frequencies. Infragravity waves contribute to a large portion of the total wave energy inside the lagoon, similar to what has been found at coral reef sites (e.g., Taebi et al., 2011; Torres-Freyermuth et al., 2012; Péquignet et al., 2014). The site also features substantial seasonal non-tidal water level variability, with fluctuations which can be as large as the tide.

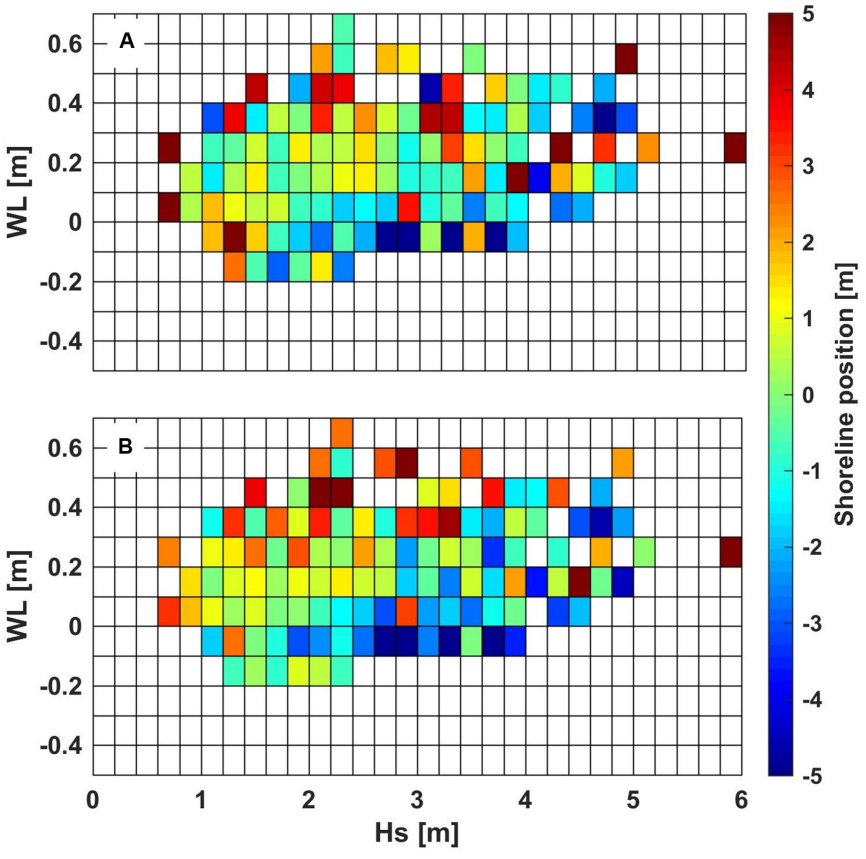

FIGURE 9 | Offshore subtidal water level (bin size 0.1 m, y-axis) and significant wave height (bin size 0.2 m, x-axis) compared to average shoreline positions at **(A)** Cell 3A and **(B)** 3B. The colors denote to the averaged shoreline position of all daily shorelines within each respective bin or the shoreline position in the event only one daily shoreline position fell within a bin.

At Gnarabup Beach, seasonal shoreline changes mostly consisted of beach rotation with differing areas of the 1.5 km pocket beach experiencing in and out of phase patterns of erosion and accretion represented by beach surveys (**Figures 7A**, **8**) and also the video analysis (**Figures 7B,C**). The video derived shorelines for the southern portion of the beach showed considerable temporal and spatial variability. Similar to the research conducted by Norcross et al. (2002) at a reef-fringed pocket beach in Hawaii, we also found weak bivariate correlations between the observed hydrodynamic forcing (waves and water levels) and shoreline position. This was potentially caused by the complexity of beach geometry whereby the presence of the reefs and headlands caused a non-linear response of the shoreline to the offshore forcing. As such, the video records indicate the shoreline positions had no consistent relationship with the offshore forcing conditions (see **Figure 9**). While in many cases the shoreline was in an eroded state during low subtidal water level, we also found during larger wave events ($>$3.5 m) the shorelines showed variable erosion and accretion patterns at different subtidal water levels. Considering Gnarabup beach is a pocket beach with minimum sediment exchange between the beach and adjacent areas; the shoreline accretion (instead of the expected erosion) at all of the sub-regions during larger wave events could be explained as follows. Energetic waves with high subtidal water level occurring mainly during winter would likely contribute to beach flattening and/or dune erosion as the waves erode a higher part of the beach and further deposited the eroded material seaward. As evidence of that, beach topography surveys collected around winter indicated additional sand within the system instead of erosion (see **Figure 7A**), which could have potentially come from the upper beach area. Evidence of beach flattening is also seen in the topographic beach surveys in Cell 3 (blue color in **Figures 8D,F**), where the upper part of the beach was eroded.

The patterns of beach erosion and recovery, as observed in both the beach surveys and video shoreline data, indicate that seasonal beach rotation occurs within the study area. This is similar to what was found by Jeanson et al. (2013) for another reef fronted pocket beach. Instead of the whole beach rotating in a pattern that commonly occurs in pocket beaches (e.g., Ranasinghe et al., 2004; Castelle and Coco, 2012; Do et al., 2016), at this reef-fringed pocket beach the rotation occurred in clusters (cells). This is associated with the presence of offshore fringing reefs that partly connected to the shore, creating quasi-headlands within the pocket beach that could partially-impede the alongshore sediment transport.

Furthermore, the existence of fringing reefs creates a narrow offshore gap, i.e., the width between the southern headland and the southern fringing reefs is only ∼230 m, protecting the beach which can likely explain why the beach was not very sensitive to changes in the wave direction. While literature on open-coast beaches has often identified a strong influence of offshore wave direction on shoreline rotational response (e.g., Turki et al., 2013; Daly et al., 2015; Luccio et al., 2019), at Gnarabup beach the beach rotation was more strongly controlled by the interaction between the offshore hydrodynamic conditions and the reef morphology.

CONCLUSION

A series of field observations over 20 months were used to assess the behavior of an embayed pocket beach fringed by rocky reefs in southwestern Australia. Despite the high incident wave energy at the site, most of the incoming wave energy was dissipated by the shallow reefs, resulting in relatively low wave energy conditions along the shoreline. Seasonal beach surveys over the entire 1.5 km of the beach and daily video derived shorelines over the southern 250 m of beach indicate the shoreline shows both patterns of rotation as well as uniform erosion and accretion. Over the entire study period, the beach experienced large (up to 10 m) erosion caused by storms, yet, the erosion events were quickly followed by recovery that caused the shoreline position was largely stable. The video derived daily shorelines also reveal differing shoreline response based on the combination of offshore waves and water levels (which vary as a result of seasonal variations in the Leeuwin Current). In general, at comparable wave height conditions, the beach tended to be more eroded during low water levels compared to during high water levels. This pattern, while somewhat counterintuitive, may have resulted from both beach flattening and rotation of the shoreline. The study shown the complexity of beach dynamics within a reef-fringed pocket beach whereby the wave energy at the shoreline is strongly modulated by offshore wave conditions but also reef submergence.

DATA AVAILABILITY STATEMENT

The datasets used in this study are available on request to the corresponding author.

AUTHOR CONTRIBUTIONS

JR conducted beach morphology surveys, analysis of the video imagery and wrote the initial draft of the manuscript. JH conducted the *in situ* deployments and analysis, installed the video system, and assisted JR in the writing of the manuscript. RL and DR assisted in the data interpretation in a writing of the manuscript.

FUNDING

This work was supported by the Western Australia Department of Transport, Shire of Augusta Margaret River, and Australia Awards Scholarship.

ACKNOWLEDGMENTS

The authors are grateful to Peter Kovesi and Karin Bryan for fruitful discussions and the help on the video rectification, also Carlin Bowyer, Anton Kuret, and Rebecca Green for assisting with the field experiments.

REFERENCES

Aarninkhof, S. G. J. (2003). *Nearshore Bathymetry Derived From Video Imagery*. Delft: TU Delft.

Almar, R., Ranasinghe, R., Senechal, N., Bonneton, P., Roelvink, D., Bryan, K. R., et al. (2012). Video-based detection of shorelines at complex meso–macro tidal beaches.(Report). *J. Coast. Res.* 28, 1040–1048. doi: 10.2112/jcoastres-d-10-00149.1

Baldock, T. E. (2012). Dissipation of incident forced long waves in the surf zone—Implications for the concept of "bound" wave release at short wave breaking. *Coast. Eng.* 60, 276–285. doi: 10.1016/j.coastaleng.2011.11.002

Beardsley, R. C., Mills, C. A., Rosenfeld, L. K., Bratkovich, A. W., Erdman, M. R., Winant, C. D., et al. (1983). *CODE-1: Moored Array and Large-Scale Data Report*. Woods Hole, MA: Woods Hole Oceanographic Institution.

Becker, J. M., Merrifield, M. A., and Yoon, H. (2016). Infragravity waves on fringing reefs in the tropical pacific: dynamic setup. *J. Geophys. Res. Oceans* 121, 3010–3028. doi: 10.1002/2015jc011516

Beetham, E., Kench, P. S., O' Callaghan, J., and Popinet, S. (2016). Wave transformation and shoreline water level on funafuti atoll. Tuvalu. *J. Geophys. Res. Oceans* 121, 311–326. doi: 10.1002/2015jc011246

Blossier, B., Bryan, K. R., Daly, C. J., and Winter, C. (2017a). Shore and bar cross-shore migration, rotation, and breathing processes at an embayed beach. *J. Geophys. Res. Earth Surface* 122, 1745–1770. doi: 10.1002/2017jf004227

Blossier, B., Bryan, K., Daly, C., and Winter, C. (2017b). Spatial and temporal scales of shoreline morphodynamics derived from video camera observations for the island of Sylt, German Wadden Sea. *Geo Mar. Lett.* 37, 111–123. doi: 10.1007/s00367-016-0461-7

Bryan, K. R., Salmon, S. A., and Giovanni, C. (2008). "Measuring storm run-up on intermediate beaches using video," in *Coastal Engineering* ed. J. M. Smith (Singapore: World Scientific Publishing), 854–864.

Buckley, M. L., Lowe, R. J., Hansen, J. E., Van Dongeren, A. R., and Storlazzi, C. D. (2018). Mechanisms of wave-driven water level variability on reef-fringed coastlines. *J. Geophys. Res. Oceans* 123, 3811–3831. doi: 10.1029/2018JC013933

Castelle, B., and Coco, G. (2012). The morphodynamics of rip channels on embayed beaches. *Cont. Shelf Res.* 43, 10–23. doi: 10.1016/j.csr.2012.04.010

Daly, C. J., Bryan, K. R., and Winter, C. (2014). Wave energy distribution and morphological development in and around the shadow zone of an embayed beach. *Coast. Eng.* 93, 40–54. doi: 10.1016/j.coastaleng.2014.08.003

Daly, C. J., Winter, C., and Bryan, K. R. (2015). On the morphological development of embayed beaches. *Geomorphology* 248, 252–263. doi: 10.1016/j.geomorph.2015.07.040

Dehouck, A., Dupuis, H., and Sénéchal, N. (2009). Pocket beach hydrodynamics: the example of four macrotidal beaches, Brittany, France. *Mar. Geol.* 266, 1–17. doi: 10.1016/j.margeo.2009.07.008

Do, K., Kobayashi, N., Suh, K.-D., and Jae-Youll, J. (2016). Wave transformation and sand transport on a macrotidal pocket beach. *J. Waterway PortCoast. Ocean Eng.* 142:04015009. doi: 10.1061/(ASCE)WW.1943-5460.0000309

Feng, M., Meyers, G., Pearce, A., and Wijffels, S. (2003). Annual and interannual variations of the leeuwin current at 32°S. *J. Geophys. Res. Oceans* 108:3555. doi: 10.1029/2002jc001763

Ford, M., Becker, J., and Merrifield, M. (2013). Reef flat wave processes and excavation pits: observations and implications for majuro atoll. Marshall Islands. *J. Coast. Res.* 29, 545–554. doi: 10.2112/jcoastres-d-12-00097.1

Girard, C. M. (2018). *Processing of Remote Sensing Data*. Boca Raton, FL: CRC Press.

Gourlay, M. R., and Colleter, G. (2005). Wave-generated flow on coral reefs—an analysis for two-dimensional horizontal reef-tops with steep faces. *Coast. Eng.* 52, 353–387. doi: 10.1016/j.coastaleng.2004.11.007

Hardy, T. A., and Young, I. R. (1996). Field study of wave attenuation on an offshore coral reef. *J. Geophys. Res. Oceans* 101, 14311–14326. doi: 10.1029/96jc00202

Harley, M. D., Turner, I. L., Short, A. D., and Ranasinghe, R. (2011). A reevaluation of coastal embayment rotation: the dominance of cross-shore versus alongshore sediment transport processes, Collaroy-Narrabeen Beach, southeast Australia. *J. Geophys. Res. Earth Surface* 116:F04033. doi: 10.1029/2011JF001989

Holland, K. T., Holman, R. A., Lippmann, T. C., Stanley, J., and Plant, N. (1997). Practical use of video imagery in nearshore oceanographic field studies. *Oceanic Eng. IEEE J.* 22, 81–92. doi: 10.1109/48.557542

Holman, R. A., and Stanley, J. (2007). The history and technical capabilities of Argus. *Coast. Eng.* 54, 477–491. doi: 10.1016/j.coastaleng.2007.01.003

Horta, J., Oliveira, S., Moura, D., and Ferreira, Ó (2018). Nearshore hydrodynamics at pocket beaches with contrasting wave exposure in southern Portugal. *Estuar. Coast. Shelf Sci.* 204, 40–55. doi: 10.1016/j.ecss.2018.02.018

Jeanson, M., Anthony, E. J., Dolique, F., and Aubry, A. (2013). Wave characteristics and morphological variations of pocket beaches in a coral reef–lagoon setting. Mayotte Island, Indian Ocean. *Geomorphology* 182, 190–209. doi: 10.1016/j.geomorph.2012.11.013

Longley, P., Goodchild, M., Maguire, D., and Rhind, D. (2005). "New developments in geographical information systems: principles, techniques, management and applications," in *Geographical Information Systems: Principles, Techniques, Management and Applications*, 2nd Edn. Abridged, eds P. Longley, M. Goodchild, D. Maguire and D. Rhind (New Jersey, United States: John Wiley & Sons Inc), 404.

Lowe, R. J., and Falter, J. L. (2015). Oceanic forcing of coral reefs. *Annu. Rev. Mar. Sci.* 2015, 43–66. doi: 10.1146/annurev-marine-010814-015834

Lowe, R. J., Falter, J. L., Atkinson, M. J., and Monismith, S. G. (2009). Wave-driven circulation of a coastal reef-lagoon system. *J. Phys. Oceanogr.* 39, 873–893. doi: 10.1175/2008jpo3958.1

Lowe, R. J., Falter, J. L., Bandet, M. D., Pawlak, G., Atkinson, M. J., Monismith, S. G., et al. (2005). Spectral wave dissipation over a barrier reef. *J. Geophys. Res. Oceans* 110:C04001. doi: 10.1029/2004jc002711

Luccio, D. D., Benassai, G., Paola, G. D., Mucerino, L., Buono, A., Rosskopf, C. M., et al. (2019). Shoreline rotation analysis of embayed beaches by means of in situ and remote surveys. *Sustainability* 11:725. doi: 10.3390/su11030725

Masselink, G., Russell, P., Coco, G., and Huntley, D. (2004). Test of edge wave forcing during formation of rhythmic beach morphology. *J. Geophys. Res.* 109. doi: 10.1029/2004jc002339

Monismith, S., Herdman, L., Ahmerkamp, S., and Hench, J. (2013). Wave transformation and wave-driven flow across a steep coral reef. *J. Phys. Oceanogr.* 43, 1356–1379. doi: 10.1175/jpo-d-12-0164.1

Mory, M., and Hamm, L. (1997). Wave height, setup and currents around a detached breakwater submitted to regular or random wave forcing. *Coast. Eng.* 31, 77–96. doi: 10.1016/S0378-3839(96)00053-1

Norcross, Z. M., Fletcher, C. H., and Merrifield, M. (2002). Annual and interannual changes on a reef-fringed pocket beach: kailua Bay. Hawaii. *Mar. Geol.* 190, 553–580. doi: 10.1016/S0025-3227(02)00481-4

Otsu, N. (1979). A threshold selection method from gray-level histograms. *IEEE Trans. Syst. Man. Cybernet.* 9, 62–66. doi: 10.1109/tsmc.1979.4310076

Özkan-Haller, H. T., Vidal, C., Losada, I. J., Medina, R., and Losada, M. A. (2001). Standing edge waves on a pocket beach. *J. Geophys. Res. Oceans* 106, 16981–16996. doi: 10.1029/1999jc000193

Pattiaratchi, C., and Eliot, M. (2008). "Sea level variability in south-west australia: from hours to decades," in *Coastal Engineering* ed. J. M. Smith (Singapore: World Scientific Publishing), 1186–1198.

Péquignet, A. C. N., Becker, J. M., and Merrifield, M. A. (2014). Energy transfer between wind waves and low-frequency oscillations on a fringing reef, I pan, G uam. *J. Geophys. Res. Oceans* 119, 6709–6724. doi: 10.1002/2014jc010179

Péquignet, A. C. N., Becker, J. M., Merrifield, M. A., and Aucan, J. (2009). Forcing of resonant modes on a fringing reef during tropical storm Man-Yi. *Geophys. Res. Lett.* 36:L03607.

Pomeroy, A., Lowe, R., Symonds, G., Van Dongeren, A., and Moore, C. C. C. (2012). The dynamics of infragravity wave transformation over a fringing reef. *J. Geophys. Res. Oceans* 117:C11022. doi: 10.1029/2012jc008310

Ranasinghe, R., McLoughlin, R., Short, A., and Symonds, G. (2004). The Southern Oscillation Index, wave climate, and beach rotation. *Mar. Geol.* 204, 273–287. doi: 10.1016/S0025-3227(04)00002-7

Roy, S. K. (2010). *Fundamentals of Surveying*. New Delhi: Asoke L. Ghosh.

Segura, L. E., Hansen, J. E., and Lowe, R. J. (2018). Seasonal Shoreline Variability Induced by Subtidal Water Level Fluctuations at Reef-Fringed Beaches. *J. Geophys. Res. Earth Surface* 123, 433–447. doi: 10.1002/2017JF004385

Short, A. D. (1999). *Handbook of Beach and Shoreface Morphodynamics*. Chichester, NY: John Wiley.

Simarro, G., Bryan, K. R., Guedes, R. M. C., Sancho, A., Guillen, J., and Coco, G. (2015). On the use of variance images for runup and shoreline detection. *Coast. Eng.* 99, 136–147. doi: 10.1016/j.coastaleng.2015.03.002

Smith, R., Huyer, A., Godfrey, J., and Church, J. (1991). The leeuwin current off Western Australia, 1986-1987. *J. Phys. Oceanogr.* 21, 323–345. doi: 10.1175/1520-0485(1991)021<0323:tlcowa>2.0.co;2

Symonds, G., Huntley, D. A., and Bowen, A. J. (1982). Two-dimensional surf beat: long wave generation by a time-varying breakpoint. *J. Geophys. Res. Oceans* 87, 492–498. doi: 10.1029/JC087iC01p00492

Taebi, S., Lowe, R., Pattiaratchi, C., Ivey, G., and Symonds, G. (2011). *The Response of The Wave-Driven Circulation at Ningaloo Reef, Western Australia, to a Rise in Mean Sea Level*. Barton, ACT: Engineers Australia.

Tian, Z. Z., Kyte, M. D., and Messer, C. J. (2002). parallax error in video-image systems. *J. Transport. Eng.* 128, 218–223. doi: 10.1061/(ASCE)0733-947X2002128:3(218)

Torres-Freyermuth, A., Mariño-Tapia, I., Coronado, C., Salles, P., Medellín, G., Pedrozo-Acuña, A., et al. (2012). Wave-induced extreme water levels in the puerto morelos fringing reef lagoon. *Nat. Hazards Earth Syst. Sci.* 12, 3765. doi: 10.5194/nhess-12-3765-2012

Turki, I., Medina, R., Gonzalez, M., and Coco, G. (2013). Natural variability of shoreline position: observations at three pocket beaches. *Mar. Geol.* 338, 76–89. doi: 10.1016/j.margeo.2012.10.007

Turner, I. L., Aarninkhof, S. G. J., Dronkers, T. D. T., and McGrath, J. (2004). CZM applications of argus coastal Imaging at the Gold Coast, Australia. *J. Coast. Res.* 20, 739–752. doi: 10.2112/1551-5036(2004)20[739:caoaci]2.0.co;2

Uunk, L., Wijnberg, K. M., and Morelissen, R. (2010). Automated mapping of the intertidal beach bathymetry from video images. *Coast. Eng.* 57, 461–469. doi: 10.1016/j.coastaleng.2009.12.002

Vousdoukas, M. I., Velegrakis, A. F., Dimou, K., Zervakis, V., and Conley, D. C. (2009). Wave run-up observations in microtidal, sediment-starved pocket beaches of the eastern mediterranean. *J. Mar. Syst.* 78, S37–S47. doi: 10.1016/j.jmarsys.2009.01.009

Conflict of Interest: The authors declare that the research was conducted in the absence of any commercial or financial relationships that could be construed as a potential conflict of interest.

Copyright © 2020 Risandi, Hansen, Lowe and Rijnsdorp. This is an open-access article distributed under the terms of the Creative Commons Attribution License (CC BY). The use, distribution or reproduction in other forums is permitted, provided the original author(s) and the copyright owner(s) are credited and that the original publication in this journal is cited, in accordance with accepted academic practice. No use, distribution or reproduction is permitted which does not comply with these terms.

frontiers in Marine Science

BRIEF RESEARCH REPORT
published: 15 July 2020
doi: 10.3389/fmars.2020.00546

Distant-Source Swells Cause Coastal Inundation on Fiji's Coral Coast

Moritz Wandres[1], Jérôme Aucan[2], Antonio Espejo[1], Naomi Jackson[1], Antoine De Ramon N'Yeurt[3] and Hervé Damlamian[1]*

[1] Geoscience, Energy and Maritime (GEM) Division, Pacific Community (SPC), Suva, Fiji, [2] Laboratoire d'Ecologie Marine Tropicale des Océans Pacifique et Indien (ENTROPIE), Institut de Recherche pour le Développement (IRD), Nouméa, New Caledonia, [3] Pacific Centre for Environment and Sustainable Development (PaCE-SD), The University of the South Pacific, Suva, Fiji

Distant-source swells are known to regularly inundate low-lying Pacific Island communities. Here we examine extreme total water level (TWL) and inundation driven by a distant-source swell on Fiji's Coral Coast using observations and a phase-resolving wave model (XBeach). The objective of this study is to increase understanding of swell-driven hazards in fringing reef environments to identify the contribution of wave setup and infragravity waves to extreme TWL and to investigate coastal flooding during present and future sea levels. The maximum TWL near the shore was caused by compounding mechanisms, where tides, wave setup, infragravity waves, and waves in the sea swell frequencies contributed to the TWL. Waves and wave setup on the reef were modulated by offshore wave heights and tides with increased setup during low tide and increased wave heights during high tide. Numerical simulations were able to reproduce the mechanisms contributing to the extreme TWL and allowed an estimation of the inundation extent. Simulations of the same swell under the RCP8.5 sea-level rise scenario suggest the area of inundation would increase by 97% by 2100. A comparison between the numerical model, a multiple linear regression model, and two commonly used parametric models reveals that both XBeach and the linear regression model are better suited to reproduce the nearshore wave setup and TWL than the empirical equations. The results highlight the need for customized, site-specific coastal hazard assessments and inundation forecast systems in the South Pacific.

Keywords: coastal inundation, infragravity waves, wave setup, distant swells, coastal flooding, XBeach, multiple linear regression, climate change

OPEN ACCESS

Edited by:
Andrew W. M. Pomeroy, The University of Western Australia, Australia

Reviewed by:
Rodolfo Silva, National Autonomous University of Mexico, Mexico
Alec Torres-Freyermuth, National Autonomous University of Mexico, Mexico

****Correspondence:***
Moritz Wandres
moritzw@spc.int

Specialty section:
This article was submitted to Coastal Ocean Processes, a section of the journal Frontiers in Marine Science

Received: *03 March 2020*
Accepted: *15 June 2020*
Published: *15 July 2020*

Citation:
Wandres M, Aucan J, Espejo A, Jackson N, De Ramon N'Yeurt A and Damlamian H (2020) Distant-Source Swells Cause Coastal Inundation on Fiji's Coral Coast. Front. Mar. Sci. 7:546. doi: 10.3389/fmars.2020.00546

INTRODUCTION

Coastal inundation can cause shoreline changes (e.g., erosion), destruction of infrastructure, contamination of freshwater reserves and agricultural land, and even loss of lives (Hoeke et al., 2013; Storlazzi et al., 2018; Smith and Juria, 2019). It is, therefore, critical for decision makers to have access to detailed coastal hazard and risk information to adequately manage coastal areas. In the tropical Pacific, coastal inundation is commonly associated with unusually high astronomical tides and storm surges from tropical cyclones (McInnes et al., 2014). The risk of inundation from distant-source swells is less well studied (Hoeke et al., 2013). Consequently, regional meteorological services often fail to warn communities of imminent swell-driven inundation

(Bosserelle et al., 2015a; Winter et al., 2020). Hoeke et al. (2013) investigated a series of inundation events in low-lying island communities in the western Pacific that were caused by swell waves generated by extra-tropical storms in the north Pacific. Although the flooding caused severe impacts to five Pacific Island nations, tide gauges failed to record evidence of extreme sea levels. The authors argue that tide gauges and satellite altimetry often fail to capture wave contributions to total water level (TWL) and, consequently, miss many inundation events. A recent study projects that many atolls will become uninhabitable over the coming decades due to wave-driven inundation exacerbated by increased sea levels (Storlazzi et al., 2018). Inundation risk assessments and future early warning systems should, therefore, consider the wave contributions to extreme TWLs (Hoeke et al., 2013).

There are two major wave-driven processes that contribute to the TWL on reef-lined coasts. First, dissipation of swells due to breaking causes wave setup (η_{wave}, elevation of the mean still water surface) from the excess momentum flux in the water column (Becker et al., 2014). Second, swell dissipation over coral reefs generates infragravity (IG) waves (bore-like uprush of individual waves on the beach) (e.g., Baldock, 2012; Pomeroy et al., 2012) that significantly contribute to the total wave run-up (e.g., Van Dongeren et al., 2013). η_{wave} has been found to reach up to one third of the incident wave heights $(H_{s,inc})$ along coastlines of tropical and subtropical islands (Munk and Sargent, 1948; Tait, 1972; Vetter et al., 2010). Both IG waves and η_{wave} have been shown to cause morphological changes (e.g., Kench et al., 2017) and coastal inundation (e.g., Ford et al., 2018) along fringing reef coastlines.

Recent work has investigated the importance of wave contributions to flooding at inter-annual to decadal time scales in the context of sea-level rise (Rueda et al., 2017; Vitousek et al., 2017; Storlazzi et al., 2018; Vousdoukas et al., 2018). Vitousek et al. (2017) investigated projected changes in coastal flooding on a global scale using sea-level projections combined with wave, tide, and storm surge models. The authors estimate a doubling of the frequency of extreme water levels in the tropics by no later than 2050. Vousdoukas et al. (2018) investigated global projections of extreme sea levels based on a probabilistic approach and estimate that, for a large part of the tropics, once-in-a-century extreme sea levels would become annual by 2050. To provide a large-scale estimate of potential future extreme TWLs, these global studies are generally based on empirical equations to calculate η_{wave} and neglect wave run-up. For example, Vousdoukas et al. (2018) calculated η_{wave} using a generic approximation, where η_{wave} is 2% of $H_{s,inc}$, and Vitousek et al. (2017) calculated η_{wave} based on the 2% exceedance run-up on dissipative beaches (Stockdon et al., 2006). Although these global assessments serve as useful first-order inundation hazard estimates, they neglect wave run-up due to incident IG waves and may significantly misrepresent extreme TWL and inundation hazard. Furthermore, these studies drew their wave information from coarse global wave simulations and neglected regional features, such as nearshore bathymetry, geomorphology, or local winds. To accurately quantify the wave contribution to extreme TWL at a particular coastline, hydrodynamic models at high spatial and temporal resolutions or observational methodologies should be applied (Hoeke et al., 2011, 2013; McInnes et al., 2014; Winter et al., 2020).

In the present study, we examine extreme TWL driven by a distant-source swell in May 2018 on Fiji's Coral Coast (**Figure 1**) using observations from an offshore wave buoy and a pressure sensor on the reef flat. The objective of this study is to increase our understanding of swell-driven hazards in fringing reef environments and to identify the contribution of η_{wave} and IG waves to extreme TWLs and coastal inundation on reef-lined islands. The inundation extent under present and future sea levels is simulated using a high-resolution numerical model (XBeach; Roelvink et al., 2009) to demonstrate how increased sea levels can modify the relative contribution of the different components. Finally, we compare the XBeach simulations with two empirical equations and a multiple linear regression model to investigate their suitability to reproduce the extreme TWL.

METHODOLOGY

Study Site

Fiji's Coral Coast in the south of the main island of Viti Levu is a major tourist area critical for the economy and development of the country (Harrison and Prasad, 2013). Although the area is known to be frequently flooded by distant-source swells, these events often remain undocumented and have received limited attention in the peer-reviewed literature (e.g., Hoeke et al., 2013; McInnes et al., 2014; Bosserelle et al., 2015a).

Viti Levu features a semi-diurnal tide with 1.2 m amplitude. The wave climate is dominated by long-period southwesterly swells generated by storms in the Southern Ocean and Tasman Sea and by shorter period east-southeasterly waves generated by the trade winds. The annual mean significant wave height (H_s) is 2.15 m with a 99th percentile H_s of 3.93 m; 90% of times large wave heights (i.e., waves exceeding the 99th percentile) are generated by Southern Ocean swells. The annual mean peak period (T_P) is 13 s (Bosserelle et al., 2015b).

Observations

Offshore wave conditions off Cuvu on Fiji's Coral Coast (**Figure 1**) were recorded using a Sofar Spotter wave buoy deployed at 200 m water depth. The wave buoy measured the full directional wave spectrum at a frequency resolution of 0.0098 Hz and a frequency range of 0.033–1 Hz (i.e., wave periods between 1 and 30 s) at a sampling rate of 2.5 Hz. Half-hourly bulk statistics (i.e., H_s, mean period (T_m), T_P and directions θ as well as directional spreads) were automatically calculated onboard and transmitted in near real-time via an iridium satellite connection while the full spectral data was stored internally and downloaded after retrieval.

The nearshore TWL was recorded using an RBR Duo pressure sensor (**Figure 1**) programmed to continuously sample at 1 Hz. Water levels were corrected for ambient atmospheric pressure (Fofonoff and Millard, 1983) using data from a nearby automated

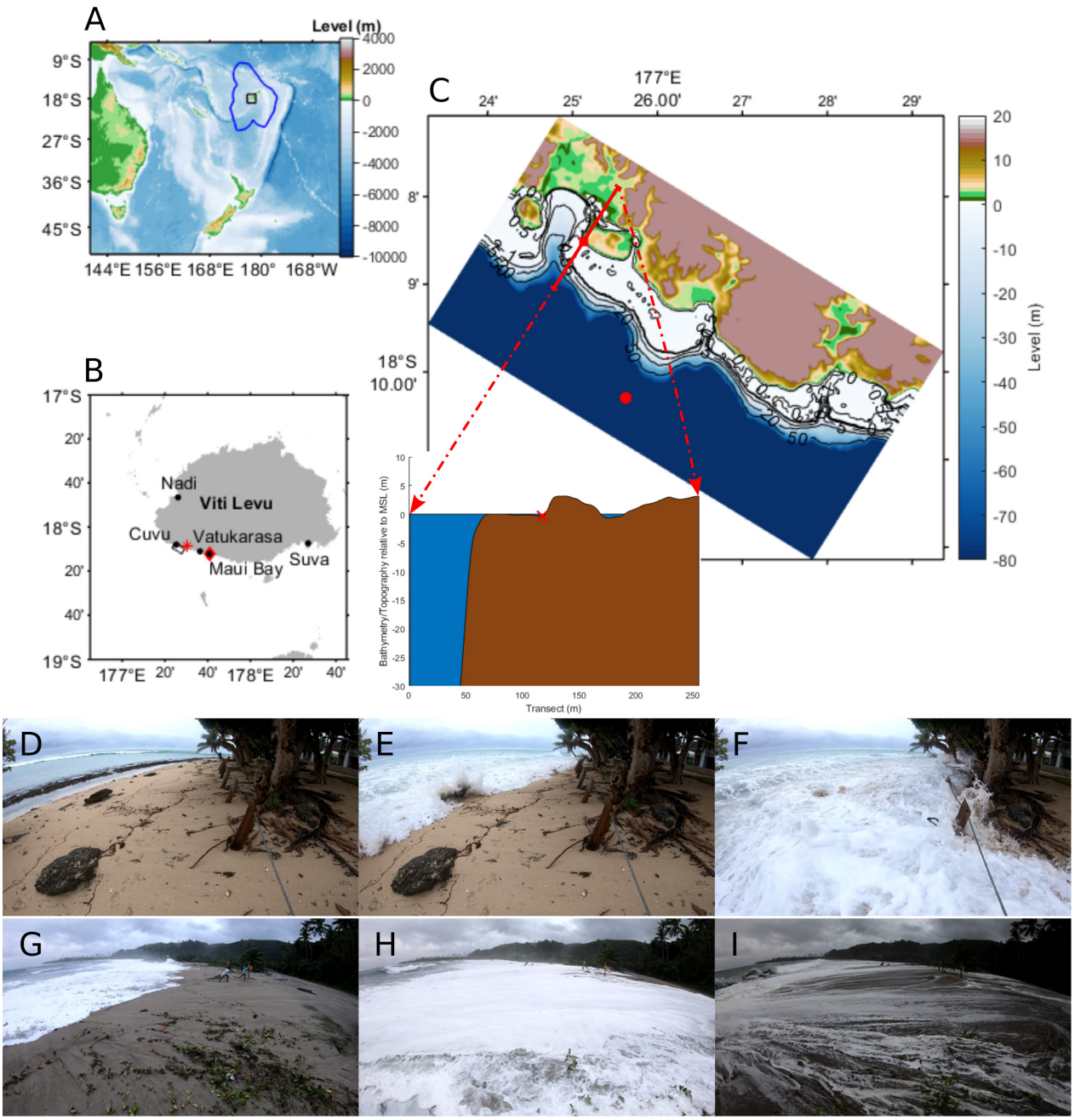

FIGURE 1 | (A) Map of the southwest Pacific. Blue lines indicate Fiji's exclusive economic zone, and black lines indicate the extent of **(B)** the map of Fiji's capital island Viti Levu. Black box by Cuvu indicates the extent of **(C)** the model domain with a reef transect (red line) over the area where the pressure sensor (red square and red x) was deployed. **(D–F)** Incoming bore-like inundation from an infragravity wave in Maui Bay. **(G–I)** Inundation of the beach and Queens Highway, Viti Levu's major highway along the south coast. The red diamond in Maui Bay **(B)** indicates the location of the tide gauge. The red asterisk indicates the location of the automated weather station (AWS). The red circle **(C)** indicates the location of the wave buoy, and the red square/x **(C)** indicates the location of the pressure sensor.

weather station (**Figure 1** and **Supplementary Figure S1**). η_{wave} and IG wave heights were calculated from the water-level time series. η_{wave} was calculated as the difference between the predicted tide and the 1-h mean observed water level. The water level time series was decomposed into short and IG waves using a continuous wavelet transform with a frequency range for short waves in the sea and swell frequency bands between $f_{min} = 0.033$ and $f_{max} = 0.6$ Hz (wave periods between 1.67 and 30 s) and IG waves within lower frequencies between $f_{min} = 0.0036$ and $f_{max} = 0.033\ Hz$ (wave periods between 30 s and ~5 min). Significant wave heights of short ($H_{s,SW}$) and IG waves ($H_{s,IG}$) were calculated from the partially integrated power spectrum:

$$H_s = 4\sqrt{\int_{f_{min}}^{f_{max}} E(f)\,df}. \quad (1)$$

Tidal harmonics were derived from past (December 17, 2013–September 30, 2014) water-level measurements at a nearby tide gauge in Maui Bay (**Figure 1**) using the Unified Tidal Analysis and Prediction (UTide) software (Codiga, 2011).

Models

Multiple Linear Regression Model

Statistical models are often applied as computationally efficient alternatives to numerical models (e.g., Camus et al., 2014; Cid et al., 2017). Here, we investigated the relationship between observed incident H_s and tide level (η_{tide}) (predictor variables) and $H_{s,SW}$, $H_{s,IG}$, η_{wave}, and TWL (response variables) on the reef by performing a multiple linear regression analysis:

$$Y = a_1 + \beta_1 X_1 + \beta_2 X_2 + \beta_3 X_1 X_2, \quad (2)$$

where Y is the response variable ($H_{s,SW}$, $H_{s,IG}$, η_{wave}, or TWL) and X_1 and X_2 are the predictor variables (offshore H_s and η_{tide}, respectively). a_1, $\beta_1, \ldots, \beta_3$ are the regression coefficients.

Numerical Model (XBeach)

We simulated the swell using the XBeach model (Roelvink et al., 2009) in surfbeat mode. XBeach is a coupled wave and circulation model that resolves the complete wave transformation (e.g., swash hydrodynamics) including wave-group forcing and resulting IG waves through the non-linear shallow water equations. The model combines the time-varying wave-action balance with a dissipation model to derive the wave-group forcing (Roelvink et al., 2009). Surface rollers inducing a shoreward shift in wave forcing are resolved using a roller model. Long- and cross-shore currents as well as wave-current interaction in the wave boundary layer and resulting changes in wave-averaged bed shear stress are also accounted for. Despite being originally developed for mild sloping beaches, XBeach has since been successfully adapted and applied to fringing reef environments (Pomeroy et al., 2012; Van Dongeren et al., 2013; Buckley et al., 2014; Quataert et al., 2015; Rueda et al., 2019). This has been achieved by including a bottom friction dissipation term in the short-wave energy balance and by increasing the bottom friction coefficient for flow (cf), which is associated with currents and IG wave action, and the incident short wave dissipation (fw) (Van Dongeren et al., 2013; Quataert et al., 2015). Furthermore, XBeach was recently improved to better predict the groupiness of the short waves and the resulting IG waves by implementing the "single-dir" option and by improving the propagation scheme for the wave-action balance (Roelvink et al., 2018). In the present study, we apply this new feature to our simulations.

We simulated the time span of May 25–29, 2018, and stored the free surface TWL (zs), maximum TWL (maxzs), and Hrms wave height.

The wave model was forced at the boundary with hourly parametric wave conditions (H_s, T_P, θ_P, and directional spread) measured by the wave buoy. η_{tide} was calculated from historic tidal records at Maui Bay (see section "Study Site"). Meteorological sea level anomalies (e.g., wind setup and inverted barometric effect) were not taken into account in the numerical model to isolate wave-driven effects on the reef.

Bathymetry and topography data were obtained from a range of different surveys and data sets: Bathymetry data in the deep water (i.e., off the reef edge) were collected using boat-mounted multi- and single-beam sensors. The bathymetry on the reef platform (shallower than ∼10–15 m) and the topography data were derived from satellite imagery. The dissipation of waves across a reef is extremely sensitive to the geomorphology (i.e., reef slope, water depth, reef width, or bed friction) (Rueda et al., 2019). Initial attempts to validate the model failed due to inaccuracies in the satellite-derived bathymetry on the reef flat. A detailed real-time kinematic (RTK) positioning survey on the reef and along the beach allowed us to correct the satellite data. All data were tied to ground control points, which were referenced to a primary benchmark in Maui Bay, which, in turn, was linked to a tide gauge in Maui Bay. All data (including the water levels in this study) are referenced to the local mean sea level.

All data were collated and interpolated onto a 10-m resolution grid (940 by 515 grid points; **Figure 1**). As η_{wave}, wave breaking, and other effects, such as the generation of IG waves, is highly dependent on the reef slope, it can be assumed that the response of wave-driven inundation to sea-level rise is non-linear. We, therefore, simulated the May 2018 swell with current sea levels derived from the Maui Bay tide gauge and with increased water levels (0.84 m), corresponding to the likely global mean sea-level rise under the representative concentration pathway (RCP) 8.5 (Portner et al., 2019).

A multivariate sensitivity analysis was performed to find ideal values for the slope of the breaking wave front in the roller model (β), the breaker parameter (γ) (Roelvink, 1993), the bottom friction coefficient for flow (cf), and the short wave friction coefficient (fw). Previous studies (Lowe et al., 2007; Van Dongeren et al., 2013) indicate that the short wave friction coefficient and bottom friction coefficient for swell should be considered independently. Other parameters were set to default (e.g., Roelvink et al., 2009). The sensitivity analysis was performed as follows: (1) An 11-h time period (May 27, 2018, 5:44 until 16:44 UTC) was simulated 36 times. (2) Each of the 36 model runs was simulated with different model parameters (i.e., cf = 0.005, 0.05, and 0.02; fw = 0, 0.3, and 0.6; β = 0.1 and 0.3; and γ = 0.4 and 0.6). (3) For each simulation, the root mean square error (RMSE) was calculated for $\bar{\eta}$, $H_{s,SW}$, and $H_{s,IG}$. The lowest RMSE averaged across $\bar{\eta}$, $H_{s,SW}$, and $H_{s,IG}$ was found for γ = 0.6, β = 0.3, fw = 0.3, and cf = 0.005, and these values were applied to the simulation of the entire swell. Although the fw value agreed with previous findings, the cf value was lower than expected when comparing to similar studies (e.g., Péquignet et al., 2011). It is well documented that small changes in reef composition can have large effects on the bottom roughness and, in turn, change the nearshore hydrodynamics (e.g., Osorio-Cano et al., 2019;

Reguero et al., 2019). Fiji, like many Pacific Island countries has reported coastal degradation over recent years. A study investigating the benthic habitat of the reef at a nearby site on the Coral Coast estimated about ∼48% of algae cover, ∼19% of sand and gravel cover, and only ∼7.5% of coral cover on the reef flat (Singh et al., 2019). It is, therefore, feasible that a developed coastal area, such as the Coral Coast, would have reduced friction coefficients compared to more pristine and less degraded coral reefs (e.g., Van Dongeren et al., 2013; Rogers et al., 2017).

Empirical Models

Because many large-scale studies of coastal flooding and extreme TWLs employ empirical formulations to derive η_{wave} and maximum TWLs, we compared the multiple linear regression model and the XBeach simulations with two empirical solutions. We applied the same methodologies as Vitousek et al. (2017) and Vousdoukas et al. (2018) to reproduce the η_{wave} and TWL. Vousdoukas et al. (2018) used a generic approximation of η_{wave}, where

$$\eta_{wave} = 0.2\ H_{s,Offshore} \tag{3}$$

while Vitousek et al. (2017) calculate η_{wave} using the empirical relationship for the 2% exceedance run-up on dissipative beaches (Stockdon et al., 2006):

$$\eta_{wave} = 0.016\sqrt{H_s L_0}, \tag{4}$$

where L_0 is the wavelength obtained using linear wave theory for deep water $L_0 = gT^2/(2\pi)$.

Both define the maximum TWL as

$$TWL_{max} = MSL + \eta_{tide} + \eta_{wave}. \tag{5}$$

RESULTS

Offshore Waves

To understand the nature of the May 2018 swell, the atmospheric and wave conditions in the swell-generation zone were analyzed. Regional wind, mean sea-level pressure, and wave conditions for the time of the big wave event were extracted from the European Centre for Medium-Range Weather Forecasts (ECMWF) ERA5 reanalysis data set (European Centre for Medium-Range Weather Forecasts [ECMWF], 2019). The swell originated in the Southern Ocean and Tasman Sea, where strong winds exceeding 25 m/s acted over a wind fetch of over 2000 km between 35 and 55°S from May 23–25, 2018 (**Supplementary Figure S2**). The strong winds were the result of a low-pressure system (<980 hPa minimum pressure) tracking south of New Zealand while a large stable high-pressure system (>1030 hPa maximum pressure) covered the extent of Australia. Maximum H_s in the swell-generation area exceeded 6 m while peak periods of the northward propagating swell exceeded 15 s (**Supplementary Figure S3**).

The swell reached the Coral Coast around 22:00 (UTC) on May 24, 2018, when the wave buoy recorded an increase in H_s, T_m, and T_P. The swell was characterized by two distinct peaks in H_s. The first peak in H_s (4.67 m) occurred around 9:45 (UTC) on May 25, and the second peak (4.91 m) was recorded at 11:20 (UTC) on May 27 (**Figure 2A**). As such, the maximum H_s exceeded the 99th percentile H_s (Bosserelle et al., 2015b) by 25%. The maximum observed T_P exceeded 17 s. The swell direction remained constant from the southwest between 190° and 220° throughout the entire event. The maximum recorded single wave height (derived from the vertical water displacement) was 9.32 m at 10:21 (UTC) on May 25.

Nearshore Waves and Water Levels

The largest instantaneous TWL was recorded during the second peak of the swell on May 27, 2018, at high tide (2.03 m above MSL, **Figure 2B**). Consistent with previous findings (e.g., Becker et al., 2016) IG and short wave heights followed the tidal signal with the largest wave heights during high tides and smallest wave heights during low tides (**Figures 2C,D**). On the reef flat, the height of IG waves exceeded the height of short waves significantly throughout the entire period with the maximum IG H_s of 0.79 m during the second peak of the swell. The maximum H_s of the short waves was 0.35 m (**Figure 2E**). η_{wave} also followed a tidal signal with the maximum setup observed during low tides and lower η_{wave} during high tides. The maximum η_{wave} was 0.91 m and occurred during the second peak of the swell. The out-of-phase signals of η_{wave} and wave heights resulted in similar TWL increases during high and low tides. The max 2% total non-tidal water level was 1.42 m, and the maximum observed non-tidal water level was 1.64 m above η_{tide} and occurred during low tide. During high tide, when the η_{wave} decreased to 0.25 m, the observed non-tidal water level was still 1.62 m above η_{tide} due to the large IG and short waves (**Figure 2F**).

The contribution of the different components (tide, short waves, IG waves, and setup) to the maximum instantaneous TWL was examined by calculating the percentage of each component to the hourly maximum observed water level (**Figure 2G**). Between May 24 and 29, 2018, tides on average contributed to 55% of the maximum recorded TWL, η_{wave} to 25%, IG waves to 11%, and short waves to 9%; however, the contribution varied significantly. Unsurprisingly, before the swell reached Fiji (before May 25, 2018), the TWL was largely tidally dominated (85–90%) as the offshore waves were small. As $H_{s,inc}$ increased with the arrival of the swell, the contribution of the tides to the TWL decreased and the contribution of setup, short, and IG waves increased. Particularly during low tides, η_{wave} contributed the most to the maximum TWL while short and IG waves superseded the contribution of η_{wave} during high tide. On May 27, even at high tide, η_{tide} only contributed to ∼47% of the maximum TWL while η_{wave} (10%), IG waves (24%), and short waves (19%) accounted for the rest.

Linear and Multiple Linear Regression Analysis

$H_{s,inc}$ was positively correlated to $H_{s,SW}$ ($\rho = 0.57$), $H_{s,IG}$ ($\rho = 0.32$), and setup ($\rho = 0.62$). Tides were positively correlated to $H_{s,SW}$ ($\rho = 0.66$) and $H_{s,IG}$ ($\rho = 0.84$) and negatively correlated to setup ($\rho = -0.73$). All correlations were statistically significant with p-values lower than 0.05.

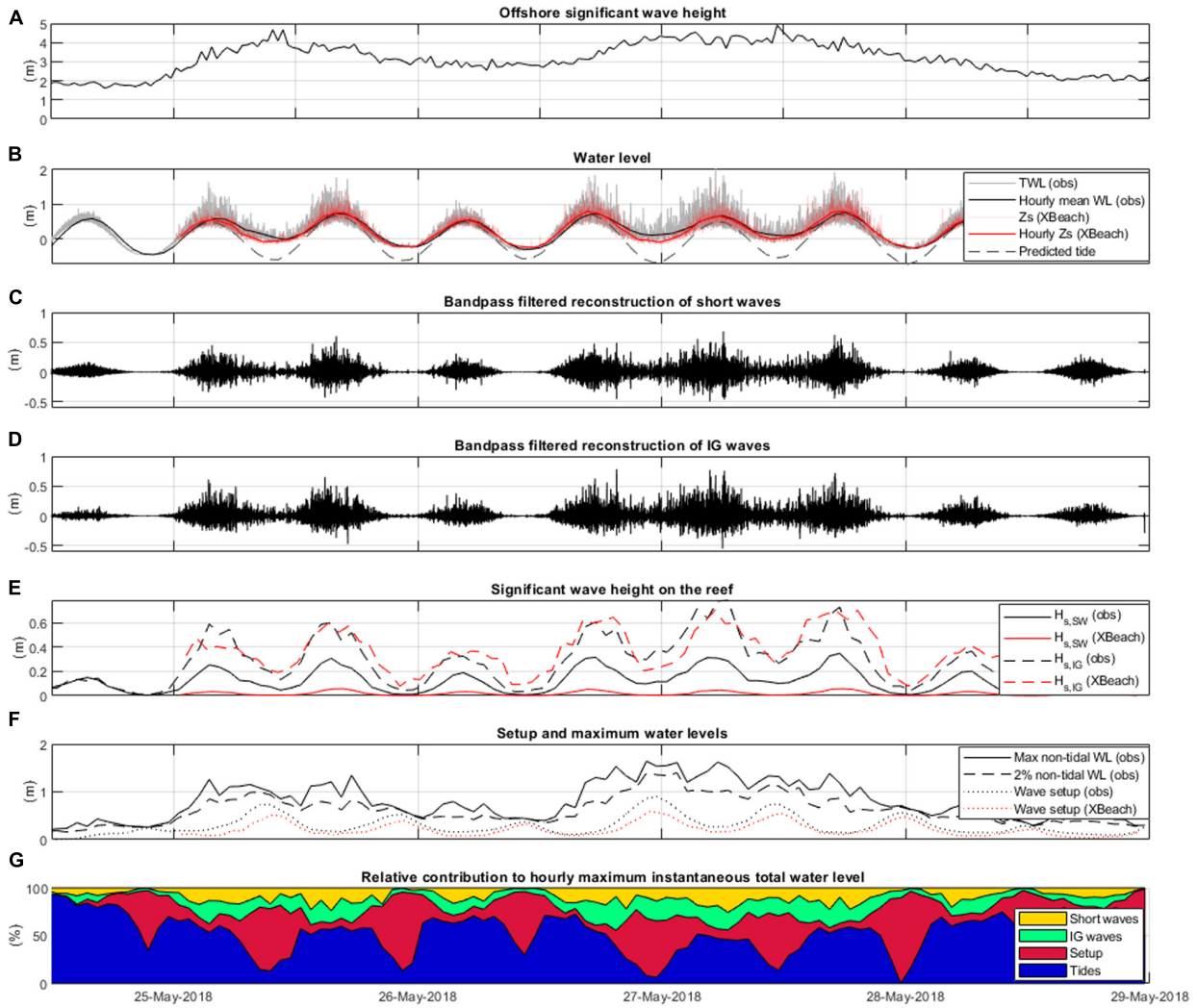

FIGURE 2 | (A) Observed offshore significant wave height. **(B)** Observed total water level (TWL, gray) and hourly mean water level (black). Predicted tides (black striped line). Simulated TWL (light red) and hourly mean water level (red). **(C)** Wavelet-filtered signal of the short waves. **(D)** Wavelet-filtered signal of the infragravity waves. **(E)** Observed (black) and simulated (red) $H_{s,IG}$ (striped line) and $H_{s,SW}$ (solid line). **(F)** Observed hourly maximum non-tidal water level (solid black line), hourly 2% non-tidal water level (black striped line), hourly η_{wave} (black dotted line), and simulated η_{wave} (red dotted line). **(G)** Relative contribution of short waves, infragravity waves, set up, and tide to the hourly maximum instantaneous TWL.

To better explain these relationships, we performed a multiple linear regression analysis where offshore H_s and η_{tide} were the independent variables and where $H_{s,SW}$, $H_{s,IG}$, η_{wave}, and hourly maximum instantaneous TWL were the dependent response variables (**Figure 3**). We found highly statistically significant (p-values < 0.05) linear relationships between the predictor and the response variables: $H_{s,SW}$ $\left(R^2 = 0.88\right)$, $H_{s,IG}$ $\left(R^2 = 0.86\right)$, η_{wave} $\left(R^2 = 0.92\right)$, and the hourly maximum instantaneous TWL $\left(R^2 = 0.91\right)$. This implies that 91% of the hourly maximum TWL near the shore can be explained by the incident wave heights and the tides.

Numerical Model Results

The XBeach model was able to accurately reproduce the nearshore water levels and waves (RMSE = 0.12 m) (**Figure 2B**). $H_{s,IG}$ (**Figure 2C**) and the η_{wave} (**Figure 2D**) were captured well with RMSEs of 0.07 and 0.12 m, respectively; however, the peaks in η_{wave} were slightly underestimated. Simulated $H_{s,SW}$ were systematically smaller than the observed (RMSE of 0.16 m). This underestimation in η_{wave} and $H_{s,SW}$ is likely responsible for the overall underestimation of TWLs (**Figure 2B**).

We performed a multivariate sensitivity analysis (**Supplementary Figures S4, S5**) to evaluate the model response to changes in friction coefficients. Simulated η_{wave} was mainly sensitive to the wave friction coefficient while IG wave heights were sensitive to both bottom friction coefficient for flow and short wave friction coefficient (**Supplementary Figures S4, S5**). In comparison, wave heights and η_{wave} were less sensitive to β and γ .

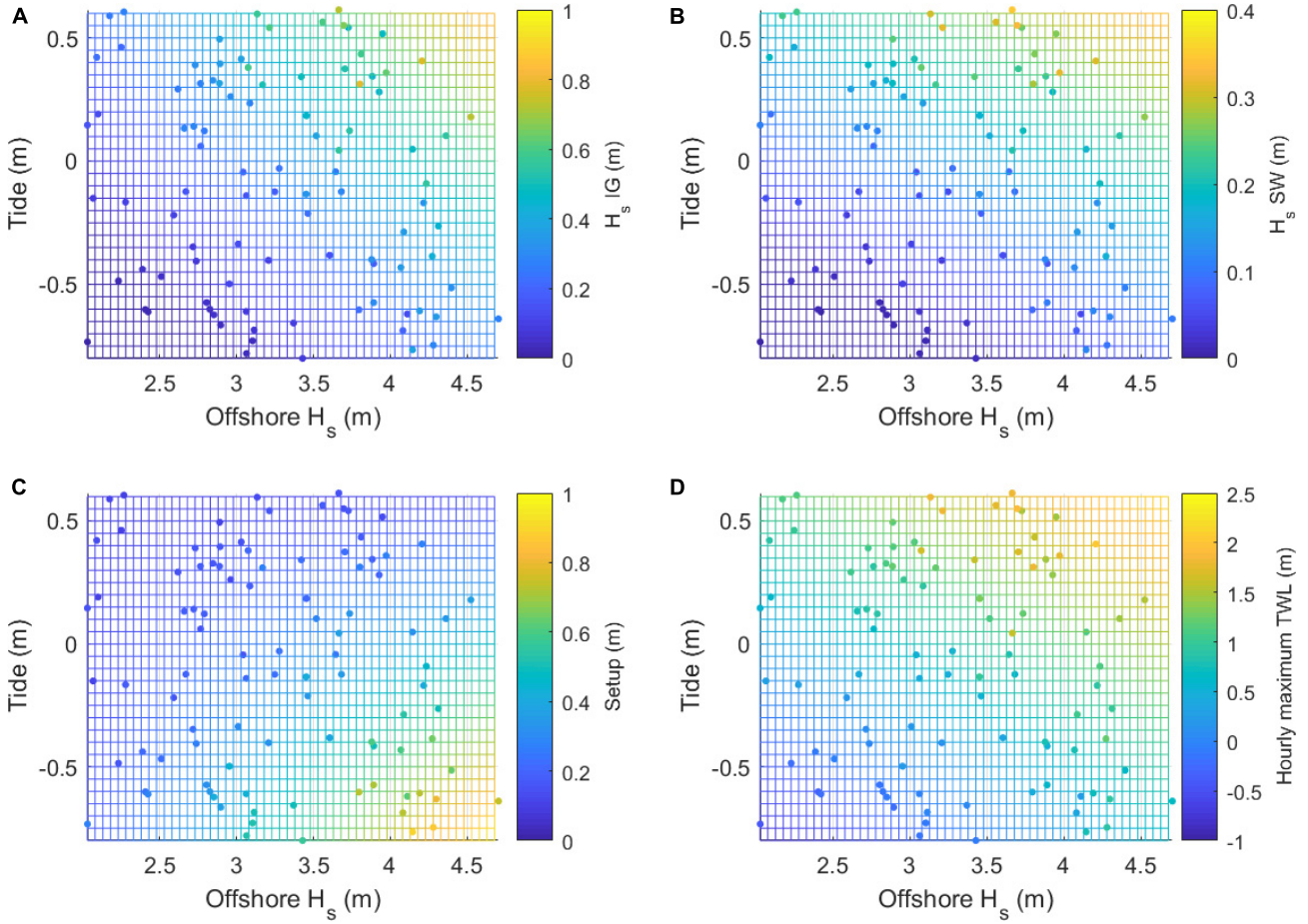

FIGURE 3 | Observed relationship between tide and offshore H_s and **(A)** $H_{s,IG}$, **(B)** $H_{s,SW}$, **(C)** η_{wave}, and **(D)** hourly maximum instantaneous water level. The grid represents the multiple linear regression model.

The simulations were used to assess the inundation extent and showed that the flooding was mainly limited to the immediate coastline and only few inhabited areas (**Supplementary Figure S6A**). This estimation agrees with verbal witness accounts that pointed out water depth and water marks on land and stated most damage and impact during the swell occurred on buildings in immediate proximity to the ocean. The simulated inundation extent was calculated by summing up all inundated grid points. Throughout the swell, an area of 67,620 m^2 within the model domain was flooded.

The simulation with increased mean sea levels suggests the inundated area would be ∼97% larger (133,110 m^2) and include large areas of the coastal settlements under the RCP 8.5 scenario (**Supplementary Figure S6B**). Although the simulation did not account for future changes in wave climate, coral cover, bathymetry, topography, or potential adaptation measures, it serves as a first estimate of changing hazards due to climate change. The maximum $H_{s,IG}$ increased by 28% while the maximum η decreased by ∼61%. $H_{s,SW}$ also increased (by 244%); however, as the model failed to accurately simulate $H_{s,SW}$ under current sea levels, the projected changes might be inaccurate.

Comparison of Different Approaches to Estimate TWL

Comparison between the empirical formulas, the multiple linear regression model, and the XBeach simulations (**Figure 4**) show clear limitations of the empirical formulations. Setup was tidally modulated, and the parametric equations, which are functions of just $H_{s,inc}$, were not able to capture the tide-induced variability in setup. This resulted in a significant overestimation of η_{wave} during low tides as well as during most high tides (**Figure 4A**). Although the TWL_{max} predictions were better than the predictions of η_{wave}, maximum water levels were too low compared to the observations (**Figure 4B**). The XBeach simulation performed better than the empirical formulations and was able to capture η_{wave} and maximum water levels well despite slightly underestimating the TWL (**Supplementary Table S7**). The multiple linear regression model was able to reproduce the observations most closely, which is not surprising as the model was trained with the observations from this particular event.

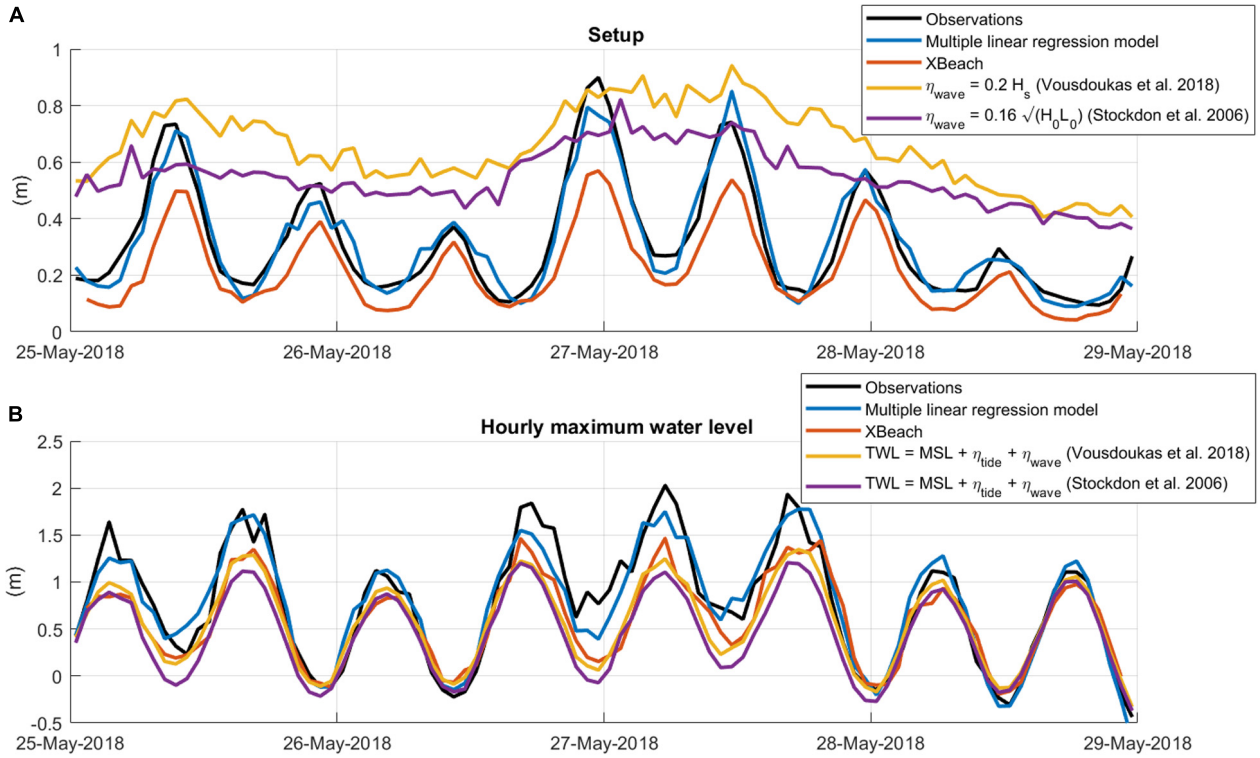

FIGURE 4 | (A) Observed and simulated wave setup using different models and empirical formulations. **(B)** Observed and simulated maximum TWL using different models and empirical formulations.

DISCUSSION AND CONCLUSION

In the present study, we investigated a large swell in May 2018 that was generated by an extra-tropical low-pressure system in the Southern Ocean and Tasman Sea. The waves generated by the system propagated through the South Pacific and caused extreme TWLs and coastal inundation along Fiji's Coral Coast. The maximum TWL near the shore was caused by several compounding mechanisms, namely η_{tide} (55% average contribution to the maximum TWL), η_{wave} (25% average contribution to the maximum TWL), IG waves (11% average contribution to the maximum TWL), and short waves (9% average contribution to the maximum TWL). Consistent with previous findings (e.g., Péquignet et al., 2011; Pomeroy et al., 2012; Becker et al., 2016, 2014) results indicated that $H_{s,SW}$, $H_{s,IG}$, and η_{wave} on the reef were modulated by $H_{s,inc}$ and η_{tide}. Consequently, the maximum hourly instantaneous TWL could be described as a function of η_{tide} and $H_{s,inc}$.

Simulations of the swell with the numerical model XBeach were able to reproduce the main mechanisms contributing to the extreme TWL and the inundation extent. Simulations of the same event under the RCP8.5 sea-level scenario suggest an increase in inundation area by 97%. Although the contribution of η_{wave} to the maximum TWL decreased (by 61%), the contribution of waves (both short and IG waves) increased.

A comparison between a multiple linear regression model, XBeach, and two empirical equations to estimate η_{wave} and maximum TWL (Vitousek et al., 2017; Vousdoukas et al., 2018), reveals that both XBeach and the linear regression model were better suited to reproduce the nearshore water levels than the empirical formulations.

The benefit of the linear regression model is its ease of use as it does not rely on computationally expensive simulations. The linear relationship between $H_{s,inc}$, η_{tide}, and nearshore TWL could be a useful tool to efficiently forecast extreme TWLs along the Coral Coast. However, it does not provide any information about inundation or wave run-up. Furthermore, although the model performed well for the event with which it was trained, it is yet to be tested against different swells (e.g., different wave period or direction).

The numerical model XBeach, on the other hand, is well established and tested in fringing reef environments (Van Dongeren et al., 2013; Buckley et al., 2014). Although XBeach is a useful tool to examine single events, it is less suitable as an operational forecast system due to the high computational cost. However, recent advances in hybrid-downscaling of coastal flood models (e.g., Camus et al., 2011; Rueda et al., 2019, 2016) could provide an adequate solution for operational forecast systems in the region. In this study, the model slightly underpredicted $H_{s,SW}$ and the maximum TWL. Although the best available bathymetry and topography data were used to set up the model, some of the model error may still be attributed to the lack of better baseline data (e.g., Lidar topography and bathymetry). Another possible solution to improve the model could be to apply a varying friction

coefficient depending on marine habitat across the model domain (Passeri et al., 2018). Coral reefs are complex systems in terms of geometry and bottom roughness; hence, incorporating this complexity into the numerical model might improve the results (e.g., Osorio-Cano et al., 2019; Reguero et al., 2019; Silva et al., 2019).

The results presented here highlight the need for customized, locality-specific coastal hazard assessments and inundation forecast systems based on observational data in the South Pacific as the commonly applied empirical equations often fail to capture the complex physical processes within reef environments. Localized inundation thresholds (Smith and Juria, 2019), downscaled numerical models, and *in situ* wave and sea-level observations are critical tools to understand swell-driven hazard in fringing reef environments. Decision makers are urged to invest in regional coastal monitoring programs, including long-term observations and downscaled models, to find adequate solutions to mitigate the inundation risks Pacific Island nations will face over the coming decades.

DATA AVAILABILITY STATEMENT

The datasets generated for this study are available on request to the corresponding author.

AUTHOR CONTRIBUTIONS

MW conceived the study and performed most of the simulations, analysis, and writing and some of the field data collection. JA assisted with field work and data analysis. AE assisted with writing and data analysis. NJ assisted with field work and provided the model grid. AD assisted with field work and writing. HD contributed data and other information and assisted with modeling, writing, and analysis. All authors contributed to the article and approved the submitted version.

FUNDING

MW, AE, NJ, and HD were funded through the Coastal Inundation Forecast Demonstration Project (CIFDP) funded by the World Meteorological Organization (WMO) and the Korean Government and through the Climate and Oceans Support Program in the Pacific (COSPPac) funded by the Australian Government. AD was funded through a JEAI grant from the French Research Institute for Sustainable Development (IRD) to the University of the South Pacific.

ACKNOWLEDGMENTS

The authors thank the World Meteorological Organization (WMO) and the Korean Government for providing some of the funds for this study through the Coastal Inundation Forecast Demonstration Project. The authors further thank the Australian Government and the Climate and Oceans Support Program in the Pacific (COSPPac), as well as the Pacific Centre for Environment and Sustainable Development (PaCE-SD) for providing some of the funds for the fieldwork. The authors express their gratitude to the team at the Fiji Meteorological Service and the Fiji Navy for assisting with the fieldwork. The authors also thank the Fiji Meteorological Service for providing access to the wind and sea level pressure data. Last, a big *vinaka vaka levu* to Adrien Lauranceau-Moineau, Donato Roqica, Judith Giblin, Maleli Turagabeci, Poate Degei, Salesh Kumar, and Zulfikar Begg for their assistance with the field data collection and to Jens Krüger for providing the images in **Figure 1**.

SUPPLEMENTARY MATERIAL

The Supplementary Material for this article can be found online at: https://www.frontiersin.org/articles/10.3389/fmars.2020.00546/full#supplementary-material

REFERENCES

Baldock, T. E. (2012). Dissipation of incident forced long waves in the surf zone—Implications for the concept of "bound" wave release at short wave breaking. *Coast. Eng.* 60, 276–285. doi: 10.1016/j.coastaleng.2011.11.002

Becker, J. M., Merrifield, M. A., and Ford, M. (2014). Water level effects on breaking wave setup for Pacific Island fringing reefs. *J. Geophys. Res. Ocean.* 119, 914–932. doi: 10.1002/2013JC009373

Becker, J. M., Merrifield, M. A., and Yoon, H. (2016). Infragravity waves on fringing reefs in the tropical Pacific: dynamic setup. *J. Geophys. Res. Ocean.* 121, 3010–3028. doi: 10.1002/2015JC011516

Bosserelle, C., Kruger, J., Movono, M., and Reddy, S. (2015a). Wave inundation on the Coral Coast of Fiji. *Australas. Coasts Ports Conf.* 2015, 96–101.

Bosserelle, C., Reddy, S., and Lal, D. (2015b). *WACOP Wave Climate Reports*. Suva: Secretariat of. the Pacific Community.

Buckley, M., Lowe, R., and Hansen, J. (2014). Evaluation of nearshore wave models in steep reef environments. *Ocean Dyn.* 64, 847–862. doi: 10.1007/s10236-014-0713-x

Camus, P., Méndez, F. J., Losada, I. J., Menéndez, M., Espejo, A., Pérez, J., et al. (2014). A method for finding the optimal predictor indices for local wave climate conditions. *Ocean Dyn.* 64, 1025–1038. doi: 10.1007/s10236-014-0737-2

Camus, P., Mendez, F. J., and Medina, R. (2011). A hybrid efficient method to downscale wave climate to coastal areas. *Coast. Eng.* 58, 851–862. doi: 10.1016/j.coastaleng.2011.05.007

Cid, A., Camus, P., Castanedo, S., Méndez, F. J., and Medina, R. (2017). Global reconstructed daily surge levels from the 20th Century Reanalysis (1871–2010). *Glob. Planet. Change* 148, 9–21. doi: 10.1016/j.gloplacha.2016.11.006

Codiga, D. L. (2011). *Unified Tidal Analysis and Prediction Using the UTide Matlab Functions*. Rhode Island: University of Rhode Island.

European Centre for Medium-Range Weather Forecasts [ECMWF] (2019). *ERA5, Reanalysis datasets*. Reading: ECMWF.

Fofonoff, P., and Millard, R. C. J. (1983). Algorithms for computation of fundamental properties of seawater. *Paper Presented at the UNESCO Technical Paper in Marine Science*, (London: UNESCO).

Ford, M., Merrifield, M. A., and Becker, J. M. (2018). Inundation of a low-lying urban atoll island: majuro, Marshall Islands. *Nat. Hazards* 91, 1273–1297. doi: 10.1007/s11069-018-3183-5

Harrison, D., and Prasad, B. (2013). "The contribution of tourism to the development of fiji and other Pacific Island Countries," in *Handbook of Tourism Economics*, ed. C. Tisdell (Singapore: World Scientific), 741–761. doi: 10.1142/9789814327084_0032

Hoeke, R., Storlazzi, C., and Ridd, P. (2011). Hydrodynamics of a bathymetrically complex fringing coral reef embayment: wave climate, in situ observations,

and wave prediction. *J. Geophys. Res. Ocean.* 116, 1–19. doi: 10.1029/2010JC006170

Hoeke, R. K., McInnes, K. L., Kruger, J. C., McNaught, R. J., Hunter, J. R., and Smithers, S. G. (2013). Widespread inundation of Pacific islands triggered by distant-source wind-waves. *Glob. Planet. Change* 108, 128–138. doi: 10.1016/j.gloplacha.2013.06.006

Kench, P. S., Beetham, E., Bosserelle, C., Kruger, J., Pohler, S. M. L., Coco, G., et al. (2017). Nearshore hydrodynamics, beachface cobble transport and morphodynamics on a Pacific atoll motu. *Mar. Geol.* 389, 17–31. doi: 10.1016/j.margeo.2017.04.012

Lowe, R. J., Falter, J. L., Koseff, J. R., Monismith, S. G., and Atkinson, M. J. (2007). Spectral wave flow attenuation within submerged canopies: implications for wave energy dissipation. *J. Geophys. Res.* 112:C05018. doi: 10.1029/2006JC003605

McInnes, K. L., Walsh, K. J. E., Hoeke, R. K., O'Grady, J. G., Colberg, F., and Hubbert, G. D. (2014). Quantifying storm tide risk in Fiji due to climate variability and change. *Glob. Planet. Change* 116, 115–129. doi: 10.1016/j.gloplacha.2014.02.004

Munk, W. H., and Sargent, M. C. (1948). Adjustment of Bikini Atoll to ocean waves. *EOS Trans. Am. Geophys. Union* 29, 855–860. doi: 10.1029/TR029i006p00855

Osorio-Cano, J. D., Alcérreca-Huerta, J. C., Mariño-Tapia, I., Osorio, A. F., Acevedo-Ramírez, C., Enriquez, C., et al. (2019). Effects of roughness loss on reef hydrodynamics and coastal protection: approaches in Latin America. *Estua. Coasts* 42, 1742–1760. doi: 10.1007/s12237-019-00584-4

Passeri, D. L., Long, J. W., Plant, N. G., Bilskie, M. V., and Hagen, S. C. (2018). The influence of bed friction variability due to land cover on storm-driven barrier island morphodynamics. *Coast. Eng.* 132, 82–94. doi: 10.1016/j.coastaleng.2017.11.005

Péquignet, A. C., Becker, J. M., Merrifield, M. A., and Boc, S. J. (2011). The dissipation of wind wave energy across a fringing reef at Ipan. *Guam. Coral Reefs* 30, 71–82. doi: 10.1007/s00338-011-0719-5

Pomeroy, A., Lowe, R., Symonds, G., Van Dongeren, A., and Moore, C. (2012). The dynamics of infragravity wave transformation over a fringing reef. *J. Geophys. Res. Ocean.* 117, 1–17. doi: 10.1029/2012JC008310

Portner, H. O., Roberts, D. C., Masson-Delmotte, V., Zhai, P., Tignor, M., Poloczanska, E., et al. (2019). *IPCC The Ocean and Cryosphere in a Changing Climate Summary for Policmakers*. IPCC Spec. Rep. Ocean Cryosph. a Chang. Clim. SPM-1-SPM-42. Geneva: IPCC.

Quataert, E., Storlazzi, C., van Rooijen, A., Cheriton, O., and van Dongeren, A. (2015). The influence of coral reefs and climate change on wave-driven flooding of tropical coastlines. *Geophys. Res. Lett.* 42, 6407–6415. doi: 10.1002/2015GL064861

Reguero, B. G., Secaira, F., Toimil, A., Escudero, M., Díaz-Simal, P., Beck, M. W., et al. (2019). The risk reduction benefits of the mesoamerican reef in Mexico. *Front. Earth Sci.* 7:125. doi: 10.3389/feart.2019.00125

Roelvink, D., McCall, R., Mehvar, S., Nederhoff, K., and Dastgheib, A. (2018). Improving predictions of swash dynamics in XBeach: the role of groupiness and incident-band runup. *Coast. Eng.* 134, 103–123. doi: 10.1016/j.coastaleng.2017.07.004

Roelvink, D., Reniers, A., van Dongeren, A., van Thiel de Vries, J., McCall, R., and Lescinski, J. (2009). Modelling storm impacts on beaches, dunes and barrier islands. *Coast. Eng.* 56, 1133–1152. doi: 10.1016/j.coastaleng.2009.08.006

Roelvink, J. A. (1993). Dissipation in random wave groups incident on a beach. *Coast. Eng.* 19, 127–150. doi: 10.1016/0378-3839(93)90021-Y

Rogers, J. S., Monismith, S. G., Fringer, O. B., Koweek, D. A., and Dunbar, R. B. (2017). A coupled wave-hydrodynamic model of an atoll with high friction: mechanisms for flow, connectivity, and ecological implications. *Ocean Model.* 110, 66–82. doi: 10.1016/j.ocemod.2016.12.012

Rueda, A., Cagigal, L., Pearson, S., Antolínez, J. A. A., Storlazzi, C., van Dongeren, A., et al. (2019). HyCReWW: a hybrid coral reef wave and water level metamodel. *Comput. Geosci.* 127, 85–90. doi: 10.1016/j.cageo.2019.03.004

Rueda, A., Gouldby, B., Méndez, F. J., Tomás, A., Losada, I. J., Lara, J. L., et al. (2016). The use of wave propagation and reduced complexity inundation models and metamodels for coastal flood risk assessment. *J. Flood Risk Manag.* 9, 390–401. doi: 10.1111/jfr3.12204

Rueda, A., Vitousek, S., Camus, P., Tomás, A., Espejo, A., Losada, I. J., et al. (2017). A global classification of coastal flood hazard climates associated with large-scale oceanographic forcing /704/106/829/2737 /704/4111 /141 /129 article. *Sci. Rep.* 7, 1–8. doi: 10.1038/s41598-017-05090-w

Silva, R., Chávez, V., Bouma, T. J., van Tussenbroek, B. I., Arkema, K. K., Martínez, M. L., et al. (2019). The incorporation of biophysical and social components in coastal management. *Estua. Coasts* 42, 1695–1708. doi: 10.1007/s12237-019-00559-5

Singh, A. A., Maharaj, A., Kumar, M., Singh, P., Singh, S., Muller-Karger, F. E., et al. (2019). Developing high resolution baseline coast resource maps using world view 2 imagery for a coastal village in fiji. *Front. Mar. Sci.* 6:207. doi: 10.3389/fmars.2019.00207

Smith, G., and Juria, N. (2019). Diagnosis of historical inundation events in the Marshall Islands to assist early warning systems. *Nat. Hazards* 99, 189–216. doi: 10.1007/s11069-019-03735-9

Stockdon, H. F., Holman, R. A., Howd, P. A., and Sallenger, A. H. (2006). Empirical parameterization of setup, swash, and runup. *Coast. Eng.* 53, 573–588. doi: 10.1016/j.coastaleng.2005.12.005

Storlazzi, C. D., Gingerich, S. B., Van Dongeren, A., Cheriton, O. M., Swarzenski, P. W., Quataert, E., et al. (2018). Most atolls will be uninhabitable by the mid-21st century because of sea-level rise exacerbating wave-driven flooding. *Sci. Adv.* 4, 1–10. doi: 10.1126/sciadv.aap9741

Tait, R. J. (1972). Wave set-up on coral reefs. *J. Geophys. Res.* 77, 2207–2211. doi: 10.1029/JC077i012p02207

Van Dongeren, A., Lowe, R., Pomeroy, A., Trang, D. M., Roelvink, D., Symonds, G., et al. (2013). Numerical modeling of low-frequency wave dynamics over a fringing coral reef. *Coast. Eng.* 73, 178–190. doi: 10.1016/j.coastaleng.2012.11.004

Vetter, O., Becker, J. M., Merrifield, M. A., Pequignet, A. C., Aucan, J., Boc, S. J., et al. (2010). Wave setup over a Pacific Island fringing reef. *J. Geophys. Res. Ocean.* 115:C12066. doi: 10.1029/2010JC006455

Vitousek, S., Barnard, P. L., Fletcher, C. H., Frazer, N., Erikson, L., and Storlazzi, C. D. (2017). Doubling of coastal flooding frequency within decades due to sea-level rise. *Sci. Rep.* 7, 1–9. doi: 10.1038/s41598-017-01362-7

Vousdoukas, M. I., Mentaschi, L., Voukouvalas, E., Verlaan, M., Jevrejeva, S., Jackson, L. P., et al. (2018). Global probabilistic projections of extreme sea levels show intensification of coastal flood hazard. *Nat. Commun.* 9:2360. doi: 10.1038/s41467-018-04692-w

Winter, G., Storlazzi, C., Vitousek, S., van Dongeren, A., McCall, R., Hoeke, R., et al. (2020). Steps to develop early warning systems and future scenarios of storm wave-driven flooding along coral reef-lined coasts. *Front. Mar. Sci.* 7:199. doi: 10.3389/fmars.2020.00199

Conflict of Interest: The authors declare that the research was conducted in the absence of any commercial or financial relationships that could be construed as a potential conflict of interest.

Copyright © 2020 Wandres, Aucan, Espejo, Jackson, De Ramon N'Yeurt and Damlamian. This is an open-access article distributed under the terms of the Creative Commons Attribution License (CC BY). The use, distribution or reproduction in other forums is permitted, provided the original author(s) and the copyright owner(s) are credited and that the original publication in this journal is cited, in accordance with accepted academic practice. No use, distribution or reproduction is permitted which does not comply with these terms.

frontiers in Marine Science

ORIGINAL RESEARCH
published: 22 October 2020
doi: 10.3389/fmars.2020.513020

Spectral Wave-Driven Bedload Transport Across a Coral Reef Flat/Lagoon Complex

Kurt J. Rosenberger[1], Curt D. Storlazzi[1], Olivia M. Cheriton[1], Andrew W. M. Pomeroy[2,3], Jeff E. Hansen[2], Ryan J. Lowe[2] and Mark L. Buckley[2]*

[1] U.S. Geological Survey, Pacific Coastal and Marine Science Center, Santa Cruz, CA, United States, [2] UWA Oceans Institute, University of Western Australia, Crawley, WA, Australia, [3] Australian Institute of Marine Science (AIMS), Townsville, QLD, Australia

Coral reefs are an important source of sediment for reef-lined coasts and help to maintain beaches by providing protection though dissipation of wave energy. Understanding the mechanisms that deliver sediment to the coast from coral reefs and quantifying the total volume of sediment generated at coral reefs are critical for projecting future coastal change. A month-long hydrodynamics and sediment transport study on a fringing reef/lagoon complex in Western Australia indicates that lower frequency wave energy constituents are important to the total bedload transport of sediment across the reef flat and lagoon to the shoreline. The reef flat and the lagoon are characterized by distinctly different transport regimes, resulting in an offset in the timing of bedform migration between the two. Short-term storage of sediment occurs on the reef flat, which is subsequently transported into the lagoon when offshore wave heights increase and strong currents due to wave breaking at the reef crest develop. This sudden influx of sediment is correlated with an increase in bedform migration rates in the lagoon. Infragravity wave energy on the reef flat and lagoon make an important contribution to the migration of bedforms and resultant bedload transport. Given the complexity of the hydrodynamics of fringing reefs, the transfer of energy to lower frequency bands, as well as accurate estimates of sources and sinks of sediment, must but considered in order to correctly model the transport of sediment from the reef to the coast.

Keywords: coral, reef, sediment, bedform, bedload, migration

OPEN ACCESS

Edited by:
William J. Skirving, National Oceanic and Atmospheric Administration (NOAA), United States

Reviewed by:
Anne-Christine Pequignet, Met Office, United Kingdom
Dano Roelvink, IHE Delft Institute for Water Education, Netherlands

****Correspondence:***
Kurt J. Rosenberger
krosenberger@usgs.gov

Specialty section:
This article was submitted to Coral Reef Research, a section of the journal Frontiers in Marine Science

Received: *18 November 2019*
Accepted: *28 September 2020*
Published: *22 October 2020*

Citation:
Rosenberger KJ, Storlazzi CD, Cheriton OM, Pomeroy AWM, Hansen JE, Lowe RJ and Buckley ML (2020) Spectral Wave-Driven Bedload Transport Across a Coral Reef Flat/Lagoon Complex. Front. Mar. Sci. 7:513020. doi: 10.3389/fmars.2020.513020

INTRODUCTION

The importance of coral reefs in protecting and supplying sediment to reef-lined coasts is becoming widely recognized, as highlighted by many recent studies (Pomeroy et al., 2017; Cuttler et al., 2018b; Reguero et al., 2019; Storlazzi et al., 2019). The precise mechanisms by which sediment is transported across a reef to the shoreline, however, are still not well understood. Sediment is transported as both suspended load and bedload, and laboratory studies have suggested that in a reef environment, the bedload component dominates (Pomeroy et al., 2015a). There have been few studies on the bedload transport of sediment in reef environments. Cacchione et al. (1999) considered bedform migration in a reef channel off Kailua, Oahu, and found that the net transport direction varied according to the seasonality of the trade winds. Becker et al. (2007) investigated the migration of bedforms in Waimea Bay on the island of Oahu using imagery at low tide, when

the beach was exposed. Although they compared seabed response to predicted forcing using a numerical model, they did not attempt to calculate the volume of resultant transport by migrating bedforms. Cuttler et al. (2018a) estimated migration rates and sediment flux from *in situ* data within the lagoon on Ningaloo reef, but lacked data from the reef flat, and therefore did not have estimates of transport from the reef flat to the lagoon.

Seaward of the reef crest, in deep water, incident sea-swell (*SS*) waves (peak period, T_p = 5–25 s) dominate. However, depth-limited wave breaking limits *SS* wave heights shoreward of the reef crest and surfzone generated infragravity (*IG*) waves (T_p = 25–250 s) become a large proportion of the total wave energy (Pomeroy et al., 2012; Buckley et al., 2018). As such, infragravity waves likely make important contributions to the transport of sediment on reef flats and lagoons (Pomeroy et al., 2015a), but this has yet to be demonstrated with field observations. Most sediment transport models rely on bulk statistics of monochromatic waves such as significant wave height and peak period or an idealized spectrum such as JONSWAP to empirically relate wave hydrodynamics to the resultant transport of sediment (Traykovski, 2007; Soulsby et al., 2012; Deltares Systems, 2019). These representations of the wave field do not account for infragravity waves and, therefore, may not accurately describe the resultant sediment transport in environments with a high proportion of the total wave energy in the *IG* band, such as occurs on reefs.

Numerous models of both equilibrium and dynamic bedform development and change have been proposed, mostly from data acquired on sandy coasts (Grant and Madsen, 1979; Nielsen, 1981; Wiberg and Harris, 1994; Styles and Glenn, 2002; Soulsby and Whitehouse, 2005; O'Donoghue et al., 2006; Traykovski, 2007; Wengrove et al., 2018). Many of these models primarily depend upon the horizontal wave-orbital excursion length to predict bedform dimensions, which is only a function of the wave forcing. Some models use the mobility parameter, Ψ, which is dependent on the grain density (Camenen, 2009). Given that grain density of carbonate sediment can be less than typical quartz beach sediment (Cuttler et al., 2017), we propose this to be an important factor in predicting bedform geometry (and subsequent bedload transport) on coral reefs. The Shields parameter is often used to distinguish between and predict wave- (θ_{wv}) and current-dominated (θ_{cur}) transport in coastal regions (Soulsby et al., 2012; Kramer and Winter, 2016). The advantage of using the Shields parameter is that it includes the non-dimensional grain size, D_*, which accounts for the relative grain density. Soulsby et al. (2012) determined critical Shields parameters for the initiation of motion (θ_{crit}), the washout of bedforms (θ_{wo}), and the initiation of sheetflow conditions (θ_{sf}) based on D_* using data from multiple field experiments. Equations for the aforementioned parameters can be found in **Appendix A**.

In this study we present the results of a month-long field study on the hydro and sediment dynamics across a fringing reef/lagoon system in Western Australia. The goal was to make highly detailed measurements of the currents, waves, and suspended and bedload transport across the reef and lagoon to better constrain the processes responsible for shoreward transport of sediment. The objectives of this paper are to (1) Quantify the time variation and total bedload transport by characterizing the migration of bedforms, (2) Compute the relative contribution of sea-swell and lower-frequency constituents to shear stresses on the seafloor, (3) Relate the observed forcing to bedform migration, (4) Determine how lower-frequency motions on the reef contribute to the total bedload transport, and (5) Evaluate how well current equilibrium models of bedform development predict the dimensions of bedforms observed in the coral reef environment. We found that the mechanisms responsible for bedform migration differ greatly from the reef flat to the lagoon, and that lower-frequency constituents of wave forcing on the reef need to be accounted for to properly predict timing and rates of sediment transport by bedforms. It should be noted that bedload transport alone does not account for all of the flux of sediment across the reef toward the shore, and that suspended load can also represent a significant portion of that flux. The contribution of the suspended load will be addressed in a separate manuscript.

STUDY AREA

Ningaloo Reef in northern Western Australia is the largest fringing reef in Australia, spanning 260 km of the coast, and lies within UNESCO's Ningaloo Coast World Heritage Area. Many recent studies have focused on a section of reef near Jurabi (21°52′6.03″S, 113°58′58.26″E, **Figure 1**) that is approximately 4 km in the alongshore dimension, extends 2.0–2.5 km from the shoreline, and has a ∼500 m wide reef flat that is submerged approximately 0.6–1.5 m at mean sea level (Pomeroy et al., 2015b, 2018; Cuttler et al., 2017, 2018a,b). The shorewardmost portion of the reef is characterized by a large, sandy lagoon that averages 3 m deep and is bounded to the north and south by channels up to 6 m deep. One of the most significant features of the coastline is a large promontory, or salient, which is aligned with the central axis of the reef, as is the case with many sections of Ningaloo Reef (Cuttler et al., 2018a).

There is a trend of decreasing median grain size from the reef crest, shoreward through the lagoon to the beach with the sediment on the southern side of the lagoon slightly coarser than on the northern side (Cuttler et al., 2017). The sediment at the edges of the reef-lagoon system primarily consists of coralline algae and reworked coral-derived grains. The greatest number of foraminifera and mollusk fragments are found in the northwest corner of the study area and quartz is only a dominant constitute near the shoreline (Cuttler et al., 2017).

Tides in the region are characterized as semidiurnal transitioning between microtidal and macrotidal; in the study area tides are mixed semidiurnal, with a spring range of more than 1.5 m and a mean range of 0.9 m (Taebi et al., 2011). Significant wave heights offshore of the study area typically range from 1 to 2 m, and average wave periods are 11–15 s. Infrequent (every 1–2 y) tropical cyclones that occur along the northwest shelf of Australia can expose the reef to large (>5 m) waves (Drost et al., 2017; Cuttler et al., 2018a), and occasional Southern Ocean swell events can exceed 4 m. Currents on the reef are

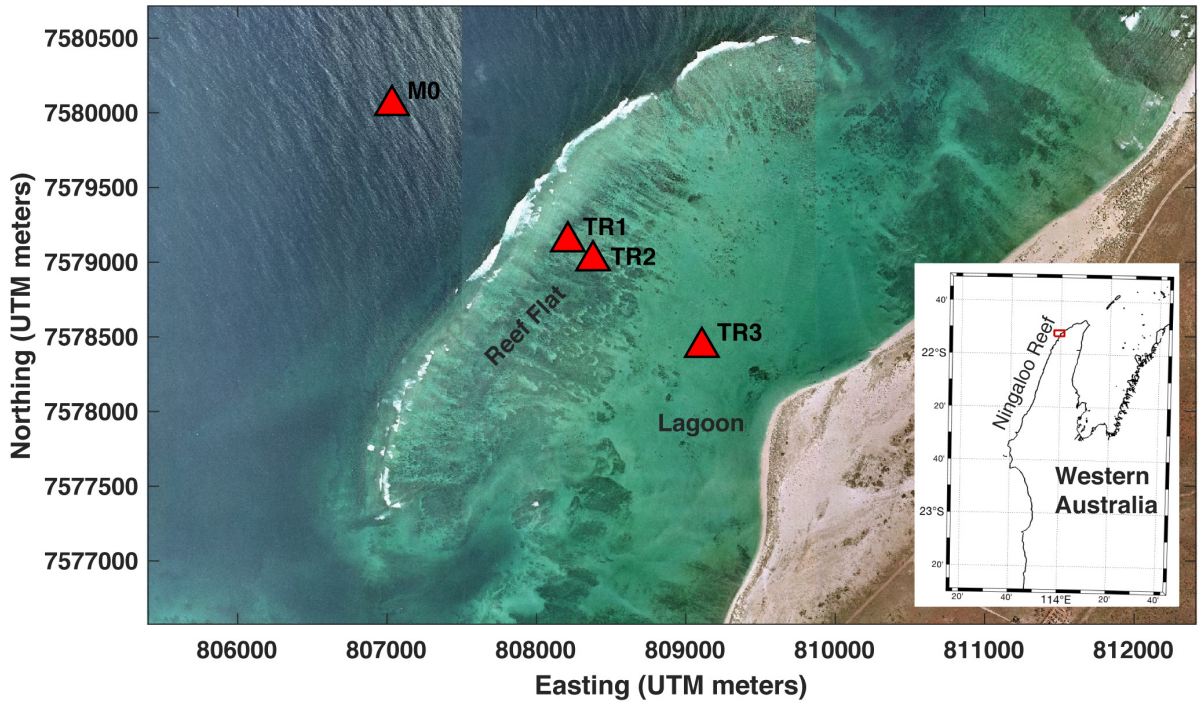

FIGURE 1 | Aerial image of the study area showing the location of the instrument packages (red triangles) used in this study.

predominantly driven by cross-shore gradients in water level induced by setup when offshore waves break at the reef crest. This process is modulated by the tides, as the degree of wave breaking dissipation, and hence wave energy transmitted onto the reef, is influenced by tidal depth variations at the reef crest (Pomeroy et al., 2018).

METHODS

Field Methods

Three hydrodynamic and sediment dynamic tripods with multiple instrument packages were deployed across the fringing reef flat off Jurabi for a 33-day period from 21 May to 23 June 2016. Two tripods (TR1, TR2; **Figure 1**) were located on the reef flat 0.4 and 0.6 km from the reef crest in ∼1.5 m water depth. A third tripod (TR3, **Figure 1**) was positioned in the lagoon in ∼3 m water depth, 1.5 km from the reef crest and 0.65 km from the salient. Each tripod had a downward-looking Nortek 1 MHz pulse-coherent acoustic Doppler current profiler (ADP), a Seapoint optical backscatter sensor (OBS), an RBR, Ltd. pressure-based wave and water level gauge, and three Echologger AA400 downward-looking 450 kHz acoustic altimeters (**Table 1**). The ADP continuously sampled current profiles of the bottom 65 cm of the water column at 1 Hz (in 2-cm vertical bins), and logged data from the OBS located 0.40 m above the bottom (mab). The wave gauge continuously sampled water levels at 1 mab at 4 Hz. The continuous measurements of currents (U, V, and W) by current meters and high-accuracy water level (P) enabled wave energy data to be parsed into sea-swell (T = 5–25 s, 'SS'), infragravity (T = 25–250 s, 'IG') and very-low frequency (T > 250 s, 'VLF') bands. The altimeters were spaced 6.5 cm apart in a line oriented perpendicular to the reef crest and shoreline (in-line with the dominant wave direction) to measure bedform migration and collected bursts of 10 samples of range to bottom every 10 min. A Nortek AWAC ADCP tide/wave gauge was deployed offshore in 20 m water depth on the fore reef approximately 1 km seaward of the reef crest to provide hourly measurements of incident wave parameters. A meteorological station measuring wind speed, direction and barometric pressure was deployed on the shore for the study period.

Analysis Methods

Grain-size distributions of surface sediment grab samples and from sediment collected in sediment traps at each location were determined using a Beckman LS-13-320 laser diffraction particle size analyzer. The grain density (or particle density) of samples from sediment traps was directly measured in the laboratory using a method derived from the American Society for Testing and Materials, ASTM D854 (ASTM International, 2010).

Identification of individual bedforms in the acoustic altimeter data (i.e., range to seabed, or bed level) was performed manually, as the data contained some noise and the shape of the features varied enough that algorithms designed to search for one type of bedform would invariably neglect others; this ensured that all migrating ripples were detected. Ripple speed was calculated using the change in arrival time of a given feature identified between adjacent altimeters. Bedload sediment flux

TABLE 1 | Instrumentation used in the experiment.

Instrument type	Locations	Variables measured	Sampling scheme	Height above bottom (m)
ADP	Reef crest, reef flat, lagoon	U,V,W (profile), P	1 Hz continuous	1
Wave gauge	Reef crest, reef flat, lagoon	P	4 Hz continuous	0.95
Altimeter	Reef crest, reef flat, lagoon	Range to bed	10 samples/10 min	0.87
ADP/Wave gauge	Fore reef	U,V,W,P, Directional waves	1024 samples/1 h	0.5

was determined from bedform migration using a method similar to Traykovski et al. (1999), except that migration rates at each timestep of bed elevation measurement were not available. Instead, we integrated the accumulation of sediment between troughs of each bedform using the time for adjacent troughs to pass by an altimeter.

The continuous 1-Hz current and water level data were parsed into one-hour bursts for spectral analysis. A frequency-space FFT filter was applied to each burst of current and water level data to obtain data filtered into SS, IG, and VLF bands. Hourly time series of bulk wave statistics such as significant wave height (H_s), mean period (T_m), and peak period (T_p) were then calculated for each frequency band using the Oceanlyz wave toolbox in Matlab (Karimpour and Chen, 2017). Near-bottom wave orbital velocity (U_{orb}, per Wiberg and Sherwood, 2008) and depth-averaged velocity (U_{mean}) were calculated on the filtered data from each band as well. Wave asymmetry and skewness were also calculated for each frequency band following Pomeroy et al. (2015a). The Grant and Madsen model (GM94) for combined waves and currents (Madsen, 1994) was used to determine shear velocity (U_*) in each band of filtered data, and the formulations of Soulsby et al. (2012) were used to calculate the Shields parameters (see **Appendix A**). Current speed at 15 cm above bottom from the downward profiling ADCP data were used in the calculations of Sheilds parameters, U_{orb}, and GM94; this height was chosen to account for variability in bed height.

RESULTS

Forcing Conditions

Meteorological conditions during the 6-week study period were generally calm; no frontal systems or cyclones passed through the region. The winds were light to moderate (0–10 m/s) and were typically onshore or obliquely onshore, with a stronger down-coast component (**Figure 2A**). A diurnal sea breeze was prevalent during the latter part of the study period (2016 Year Day (YD) 162-170). The offshore waves comprised of Southern Ocean swell from the southwest with heights (H_{m0}) consistently above 1 m and average T_p of between 10–20 s (**Figure 2B**). Two larger swell events impacted the study area on 2016 YD 150-152 and 2016 YD 158-162 (**Figure 2C**), with a period of elevated wave height and period in between the events. The beginning of the second swell event was marked by a bimodal wave distribution, with short-period wind waves (∼5 s) and long-period swell (∼20 s) occurring simultaneously. Waves near the reef crest were tidally modulated, with larger wave heights at higher tides when incident waves energy propagated more efficiently onto the reef (**Figures 2D,E**). T_p near the reef crest (TR1) varied from 5–20 s, with longer period waves occurring during times of elevated offshore incident wave energy; T_m were much shorter, averaging around 5 s (**Figure 2D**). The tidal range during the measurement period varied from 0.75 to 1.5 m (**Figure 2F**).

Reef Hydrodynamics

Waves

The hydrodynamics varied from the reef crest to the lagoon (**Figures 3–5**). H_s was generally highest near the reef crest (ranging from 0.10 to 0.65 m), and was at times almost twice as high as in the lagoon (ranging from 0.10 to 0.46 m). Tidal modulation of wave height is evident at all sites on the reef and in the lagoon. Offshore swell events were not as apparent in wave height on the reef; the average H_s on the reef was only slightly elevated during the two swell events of the study period, as indicated within the low-pass filtered time series (**Figure 3A**). The incident wave direction was almost exclusively out of the west-northwest, averaging 260 degrees, and did not vary more than 20 degrees except for short periods of a few hours (not shown).

A gradient in the relative contribution of the lower frequency motions was present across the reef and lagoon. SS-band motions dominate the spectrum near the reef crest (TR1), in H_s, U_{mean}, and U_{orb} (**Figure 3**). U_{mean} and U_{orb} in the IG band represented a significant portion of the total velocity, particularly during periods of increased incident wave energy, even if the H_s in this band were small relative to the total H_s. Otherwise, when waves were moderate or calm, energy due to SS-band waves was dominant and typically elevated, and seemingly enough to keep sediment in motion (as noted in elevated backscatter). Apart from a small contribution to U_{mean} during swell events, energy in the VLF band was substantially lower, and often negligible. Wave asymmetry and skewness were quite variable at both TR1 and TR2 (**Figures 3**, **4**, respectively), with the most significant changes in these parameters (particularly in the SS-band wave skewness) occurring during swell events. Asymmetry of the total, unfiltered wave record at TR2 did show some significant increases on a semi-tidal basis (approximately diurnal), particularly during periods of sustained incident waves not associated with swell events (shaded light blue).

The IG component relative to the other frequencies was greater for U_{mean} and U_{orb} in the lagoon than on the reef, though its amplitude was small (**Figure 5**). However, the amplitude of the IG and VLF U_{mean} in the lagoon was nearly as high as on the outer reef flat near the reef crest, though SS amplitude was considerably smaller. The amplitude and variance of asymmetry in the IG band was higher than both the SS band and the unfiltered data. Skewness of both SS and IG were consistently

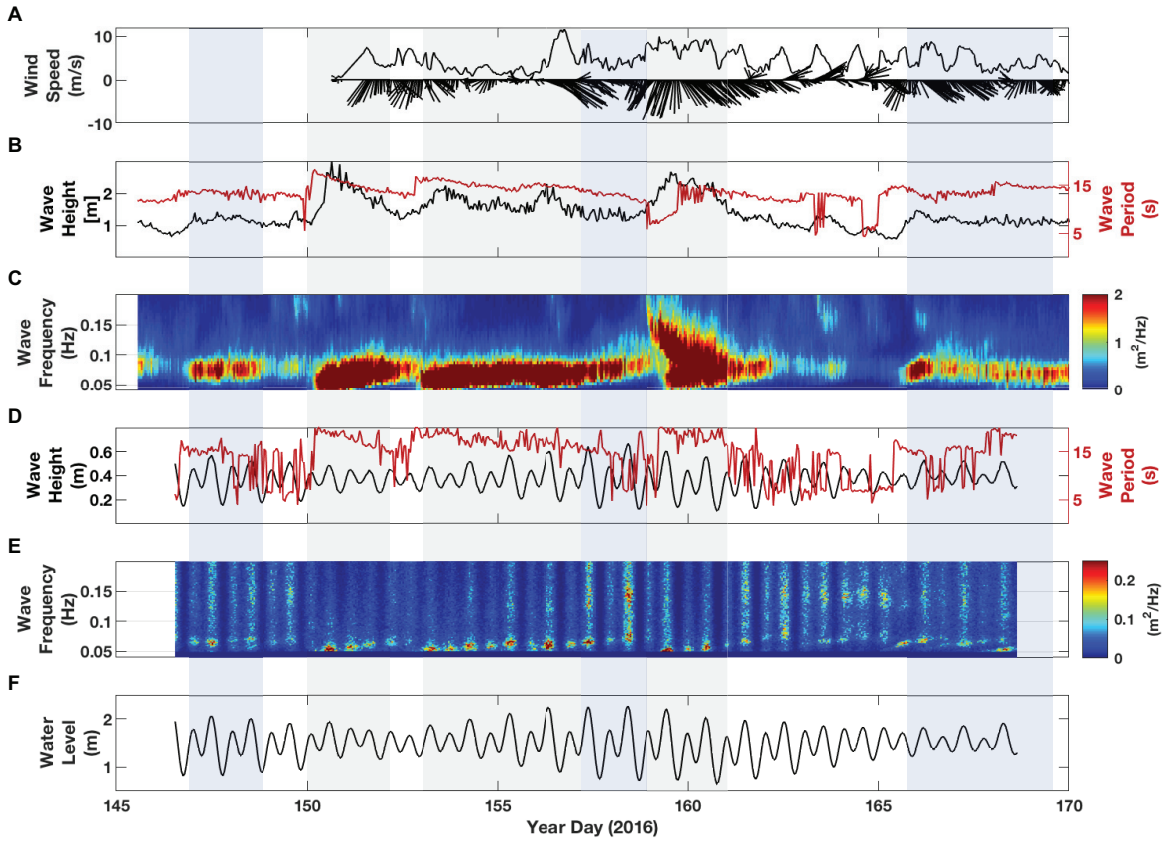

FIGURE 2 | Meteorologic and oceanographic forcing during the measurement period. **(A)** Wind speed and 3-h average wind vectors measured at the shoreline. **(B)** Offshore significant wave height and peak wave period. **(C)** Offshore wave spectral energy density at station M0. **(D)** Wave height and period near the reef crest at station TR1. **(E)** Wave spectral density near the reef crest. **(F)** Water level on the reef. The time frames shaded in gray represent "swell events" where offshore wave heights were greater than 1.5 m and wave periods were longer than 13 s. The areas shaded in blue represent time frames where there were consistent offshore waves heights greater than 1 m with periods greater than 12 s.

higher than the unfiltered data, as well. However, overall the variance of asymmetry and skewness was lower in the lagoon than on the reef crest, and there was almost no detectable change in these parameters during swell events, in contrast to the reef crest. Wave asymmetry and skewness did not increase toward the shore at this site, in contrast to the results of Cheriton et al. (2016), which may be due to the increase in water depth from the reef flat to the lagoon.

Currents

Currents on the reef respond both to water levels and incident H_s. U_{mean} was usually strongest on the reef flat (**Figure 4B**) and weakest in the lagoon (**Figure 5B**), however, there were instances when the reverse was also observed (such as YD 163-165). Strong U_{mean} developed during both swell events (YD 150-152 and 158-162), with the wave setup gradients generated by the breaking waves driving a net onshore flow across the reef that returned to the channels on either side of the reef. The currents also tended to occur at lower water levels due to greater wave dissipation at the reef crest. This was evident during both swell events and average wave conditions alike, such as YD 145-150. The response time of setup-driven U_{mean} on the reef was rapid; U_{mean} across the reef increased from near-zero to peak flow within 1 day (YD 150) and this increase coincided first with the arrival of longer-period incident waves, and secondly with higher-amplitude waves (**Figure 4B**). U_{mean} receded quickly as incident wave energy decreased. The current direction was almost exclusively toward the shore (averaging 100 deg T), except during periods of very weak flow (not shown).

Sediment Dynamics

Sediment Characteristics

Cuttler et al. (2017) calculated a range of grain density of 2.51–2.76 g/cm^3 for the bioclastic sediment on Ningaloo reef from bottom grab samples. We determined grain densities of 1.92, 2.08, and 2.5 g/cm^3 and median grain sizes of 0.95, 0.86, and 0.67 mm from samples collected at sites TR1, TR2 and TR3, respectively; these were used to calculate the Shields parameters at each site.

Bed Elevation Changes Across the Reef/Lagoon

Bed elevation changes varied considerably across the reef/lagoon complex. Near the reef crest at Site TR1, there was little apparent

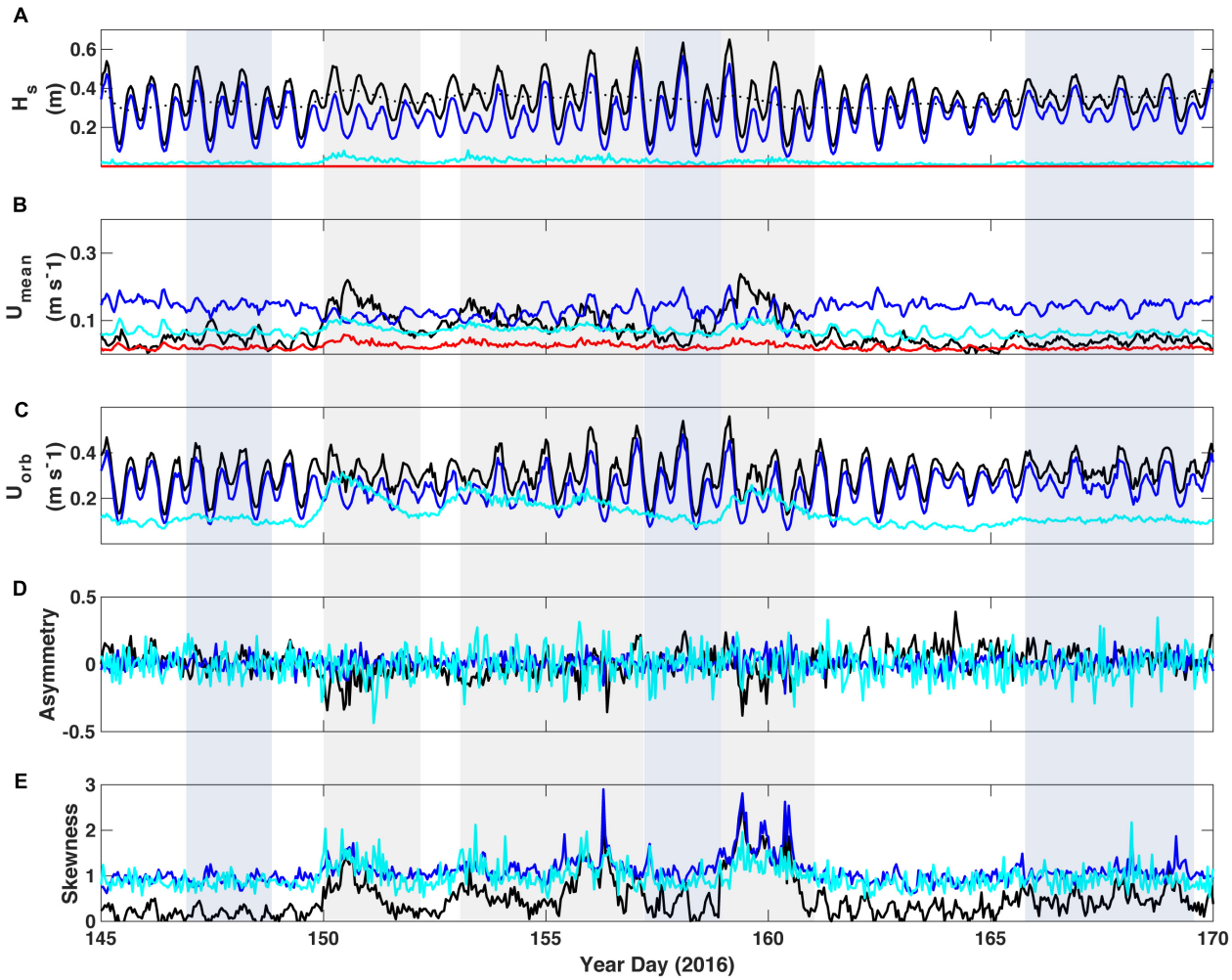

FIGURE 3 | Wave and current parameters delineated by spectral bandwidth at TR1 on the outer reef flat near the reef crest. **(A)** Significant wave height; the black dotted line denotes the 40-h low-pass filtered wave height. **(B)** Burst mean near-bed current speed and **(C)** Near-bed wave-orbital velocity from 10 cm above bottom. **(D)** Wave asymmetry. **(E)** Wave skewness. Black = unfiltered data, blue = sea-swell band, cyan = infragravity band, and red = very-low frequency band. Parameters were calculated from hour-long bursts of continuous data; mean current speed of unfiltered data was derived from the vector sum of the burst mean U and V. Energy in the VLF band was significantly lower, if not zero, and is therefore not plotted in U_{orb}, asymmetry or skewness.

accumulation or loss of sediment; the bed level rarely varied more than a few centimeters (**Figure 6C**). When bed level variation did occur, the variation was detected across all three altimeters simultaneously. This represented whole-scale bed change and not the formation or propagation of bedforms. We interpret that sheet-flow conditions (or suspended sediment transport) dominated at TR1 due to the absence of bedforms, despite a clear source of sediment.

The greatest variability in bed elevation was observed on the inner reef flat, Site TR2 (**Figure 6D**). On multiple occasions, sediment accumulated (indicated by an increase in bed elevation across all three altimeters, **Figure 6D**) and bedforms developed, migrated, and were washed out (indicated by differential changes in bed elevation between adjacent altimeters; **Figure 6D**). We interpret this to mean that sediment was eroded down to reef pavement at this site. A baseline layer of ∼5 cm of sediment subsequently accumulated under moderate forcing conditions, on top of which bedforms of up to 7.8 cm in amplitude developed and migrated. The migration of bedforms was highly variable and dependent upon wave energy. Bedforms typically migrated for a short period of time and then stalled. Thus bedform migration peaked when H_s was consistent and moderate in amplitude. All of the accumulated sediment (bedforms and the baseline layer) was completely washed off the reef flat when strong currents developed and coincided with larger *in situ* H_s. This was a rapid process; on two occasions the reef flat was completely stripped of accumulated sediment in less than 1 day (YD 150 and 158). The baseline layer would redevelop once the offshore H_s decreased, strong currents over the reef ceased, and moderate wave conditions returned. The bedforms returned to equilibrium conditions within several days to a week.

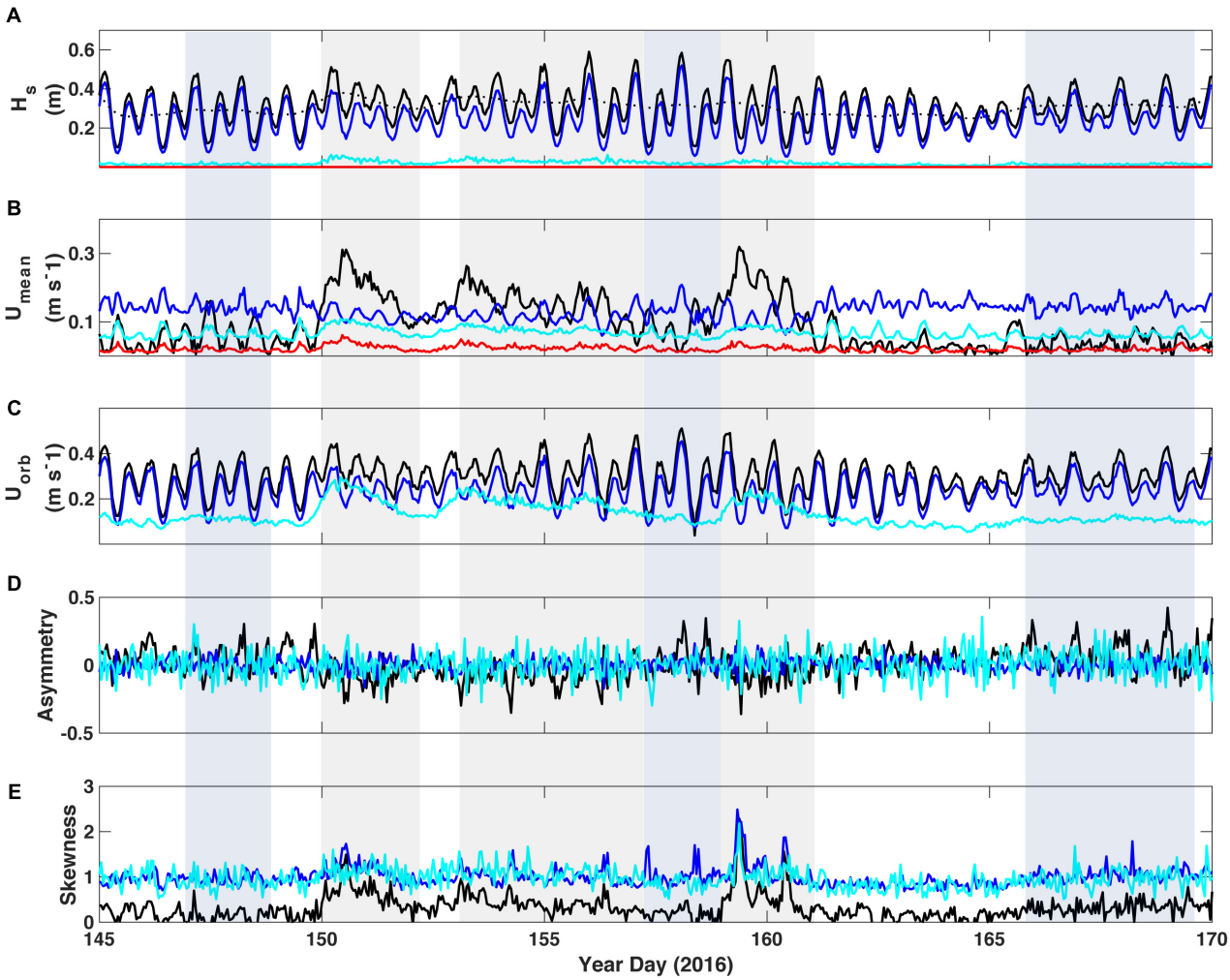

FIGURE 4 | Wave and current parameters delineated by spectral bandwidth at TR2 on the mid-reef flat. **(A)** Significant wave height; the black dotted line denotes the 40-h low-pass filtered wave height. **(B)** Burst mean near-bed current speed and **(C)** Near-bed wave-orbital velocity from 10 cm above bottom. **(D)** Wave asymmetry. **(E)** Wave skewness. Black = unfiltered data, blue = sea-swell band, cyan = infragravity band, and red = very-low frequency band. Parameters were calculated from hour-long bursts of continuous data; mean current speed of unfiltered data was derived from the vector sum of the burst mean U and V. Energy in the VLF band was significantly lower, if not zero, and is therefore not plotted in U_{orb}, asymmetry or skewness.

In the lagoon, bedforms appeared to be present throughout the study (i.e., the washout of bedforms that was observed on the inner reef flat did not occur), and there was little variability in average bed elevation (**Figure 6E**). The migration of bedforms was highly variable, and usually only occurred during periods of largest offshore H_s. There were extended periods where seemingly no bedform migration occurred; this is explored further below.

The discrepancy in sediment response between TR1 and TR2, despite similar hydrodynamics is confounding, and our primary explanation is the presence/absence of vegetation and/or reef roughness elements that act to trap sediment. It is possible that the lower frequency waves at the reef crest form in standing waves, and that Site TR1 sits at an antinode. To investigate this, we calculated coherence between horizontal velocity and pressure, vertical velocity and pressure, and horizontal and vertical velocity, both during swell events (when IG energy tends to be higher) and non-swell events. The results indicate that in the IG band, the system behaves as a progressive wave at both sites TR1 and TR2. During swell events, there is strong coherence between U and P in the IG band, and the phase is between 0 and 45 degrees, suggesting a progressive wave. There is also strong coherence between U and W in the IG band in these periods, but the phase is more like 90 degrees, again suggestive of a progressive wave (per Dean and Dalrymple, 1991). Thus, the idea of a standing wave in the IG band does not appear to be the case here.

Bedform Migration and Bedload Transport

The rate of bedform migration, as measured by sequential altimeters, was highly variable in time, and ranged from 1–14 m/d on the reef flat to 1–9 m/d in the lagoon (**Figure 7**). On the inner reef flat, the maximum in ripple migration rate

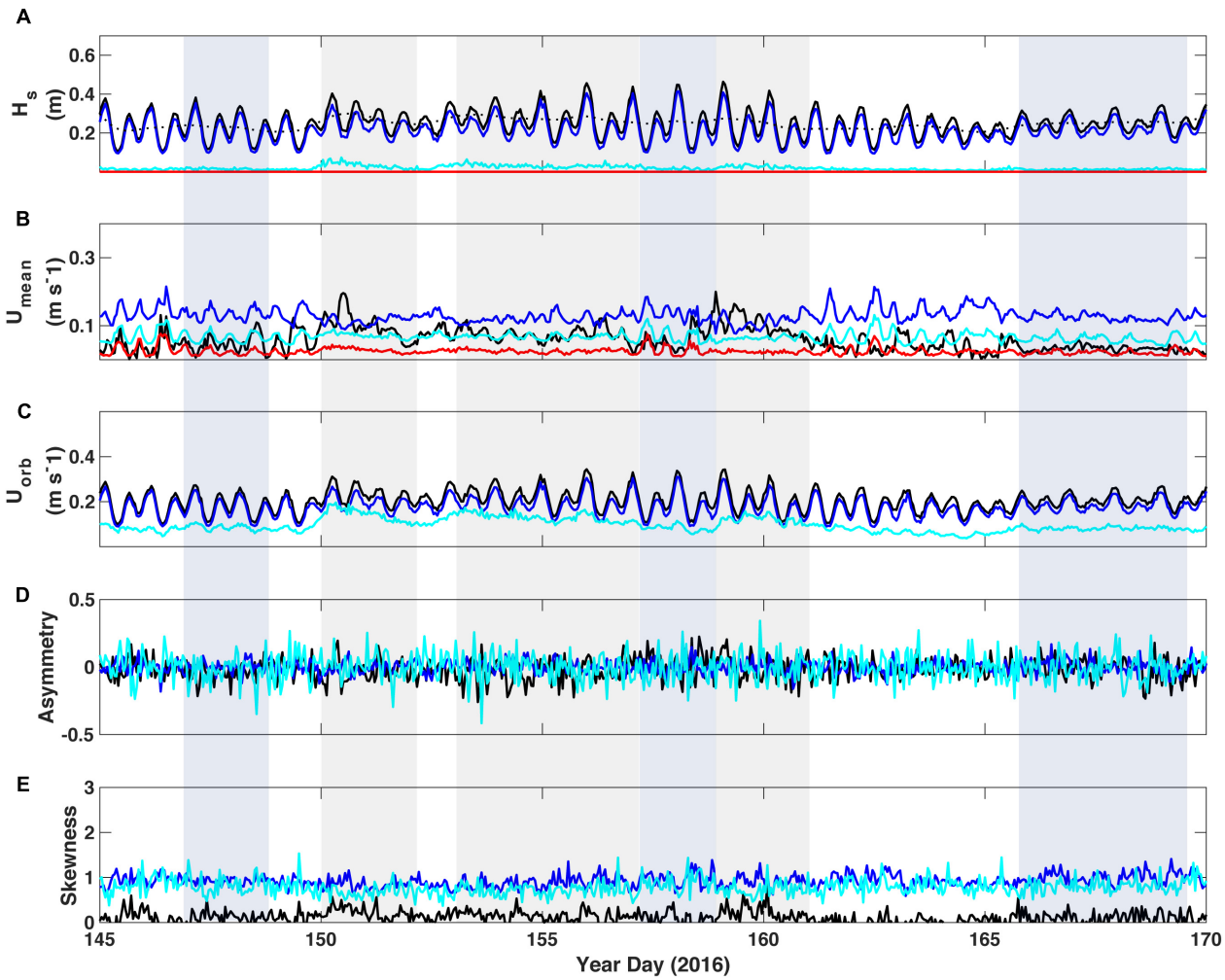

FIGURE 5 | Wave and current parameters delineated by spectral bandwidth at TR3 in the lagoon. **(A)** Significant wave height; the black dotted line denotes the 40-h low-pass filtered wave height. **(B)** Burst mean near-bed current speed and **(C)** Near-bed wave-orbital velocity from 10 cm above bottom. **(D)** Wave asymmetry. **(E)** Wave skewness. Black = unfiltered data, blue = sea-swell band, cyan = infragravity band, and red = very-low frequency band. Parameters were calculated from hour-long bursts of continuous data; mean current speed of unfiltered data was derived from the vector sum of the burst mean U and V. Energy in the VLF band was significantly lower, if not zero, and is therefore not plotted in U_{orb}, asymmetry or skewness.

did not coincide with peak incident wave energy, as these larger wave events lead to washout conditions. Migration on the inner reef flat was highly variable even when the incident wave energy was consistent, such as during the latter part of the study period (YD 165-170). Acceleration in migration rate was both gradual and sudden on the reef flat; at times migration rate gradually increased and decreased, while at other times the change in migration rate was sudden. Notably, bedforms on the reef flat were predominantly linear (i.e., not two-dimensional or bifurcated), and the orientation was almost exclusively normal to the array of transducers, as confirmed by plan-view video data of the seabed collected by the tripods (not shown). Video data also confirm that migration was exclusively toward the shoreline. Given that there was potential for bedform orientation to change over the course of the deployment, migration rates reported here represent a minimum and could have been larger if bedforms were migrating obliquely to the transducer array.

The flux of sediment toward the shore associated with bedform migration on the reef flat at TR2 ranged from 13 to 485 kg/m/d, with an average daily rate of 61 kg/m/d. This average does not include the time period after ripples had washed out on sheetflow conditions (YD 150-157). Periods of higher average sediment flux due to ripple migration did not always coincide with instantaneous peaks in ripple migration rate, highlighting the ephemeral nature of migration. Near-bottom average acoustic backscatter on the reef flat illustrates the degree to which the transport is tidal, particularly when bedforms were present. When bedforms washed out, near-bottom backscatter was consistently elevated, demonstrating a shift to transport by suspended load on the reef flat under high-energy forcing.

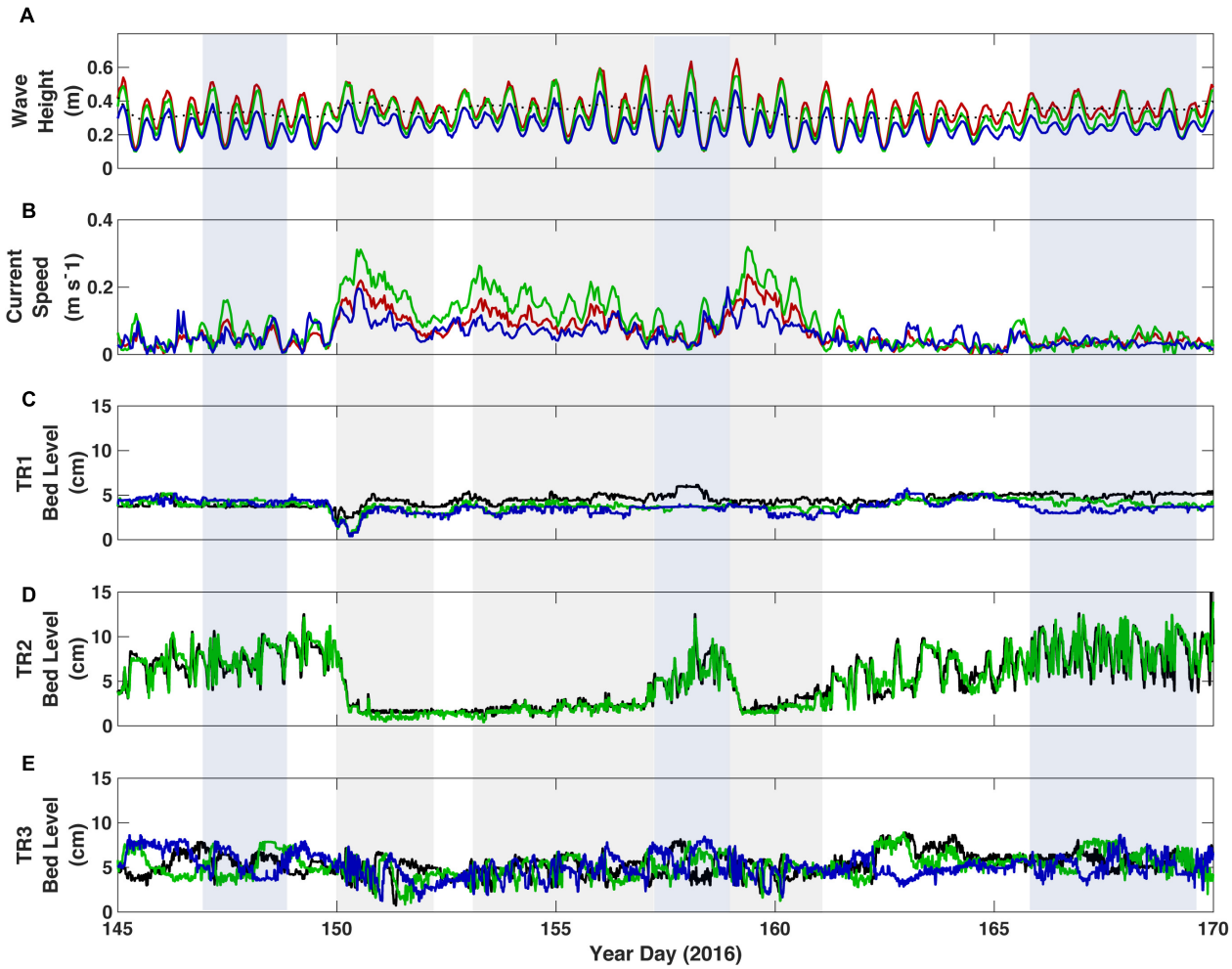

FIGURE 6 | Response of the reef to forcing. **(A)** Significant wave height; the black dotted line denotes the 40-h low-pass filtered wave height at TR1. **(B)** Depth-averaged current speed. **(C)** Bed elevation from the three in-line altimeters at TR1 on the outer reef flat near the reef crest. **(D)** Bed elevation from the two in-line altimeters at TR2 on the inner reef flat. **(E)** Bed elevation from the three in-line altimeters at TR3 in the lagoon. In A and B, color represents the site location: Red = TR1 on the outer reef flat near the reef crest, blue = TR2 on the inner reef flat, and green = TR3 in the lagoon. In panels **(C–E)** colors represent data from individual altimeters, in order from offshore to onshore, black, green and blue.

In the lagoon, bedforms appeared to be present throughout the study (i.e., washout of bedforms did not occur, as was observed on the inner reef flat), and the average bed elevation varied little. Migration would peak at the onset of a swell event, gradually slowing, and eventually ceasing altogether (**Figure 7A**). While bedform migration and transport was observed on the inner reef flat in the latter half of the study period, after the swell events, there was no detectable bedform migration in the lagoon for several days. This is not to say that there was no change in bed elevation; there was still variability of up to 5 cm in the ∼1-week period after the second swell event on YD 162-170 (**Figures 6D,E**). This change was slow and variable between altimeters such that it was difficult to identify coherent peaks in bedforms. Bedform sediment flux toward the shore was reduced in the lagoon relative to the reef flat and when bedform migration was detected ranged from 20 to 231 kg/m/d, with an average daily rate of 34 kg/m/d when migrating bedforms were detected (**Figure 6B**). The average daily rate calculated for the lagoon over the same 23-day period that bedform migration was detected on the reef flat is half as much as that measured on the reef flat (19 kg/m/d).

Near-bed suspended-sediment levels (using ADP acoustic backscatter from 10 cm above bottom as a proxy) on the reef varied with higher wave energy and enhanced currents (**Figure 7C**). Suspended sediment levels were generally higher on the reef flat than near the reef crest or in the lagoon. During periods of highest incident wave energy (such as YD 150-152 and YD 158-162), suspended sediment tended to remain elevated throughout the system. This is coincident with the period when bedforms were washed out, and suggests a transition from bedload to suspended load dominated transport. In the interim period between swell events when incident H_s were large

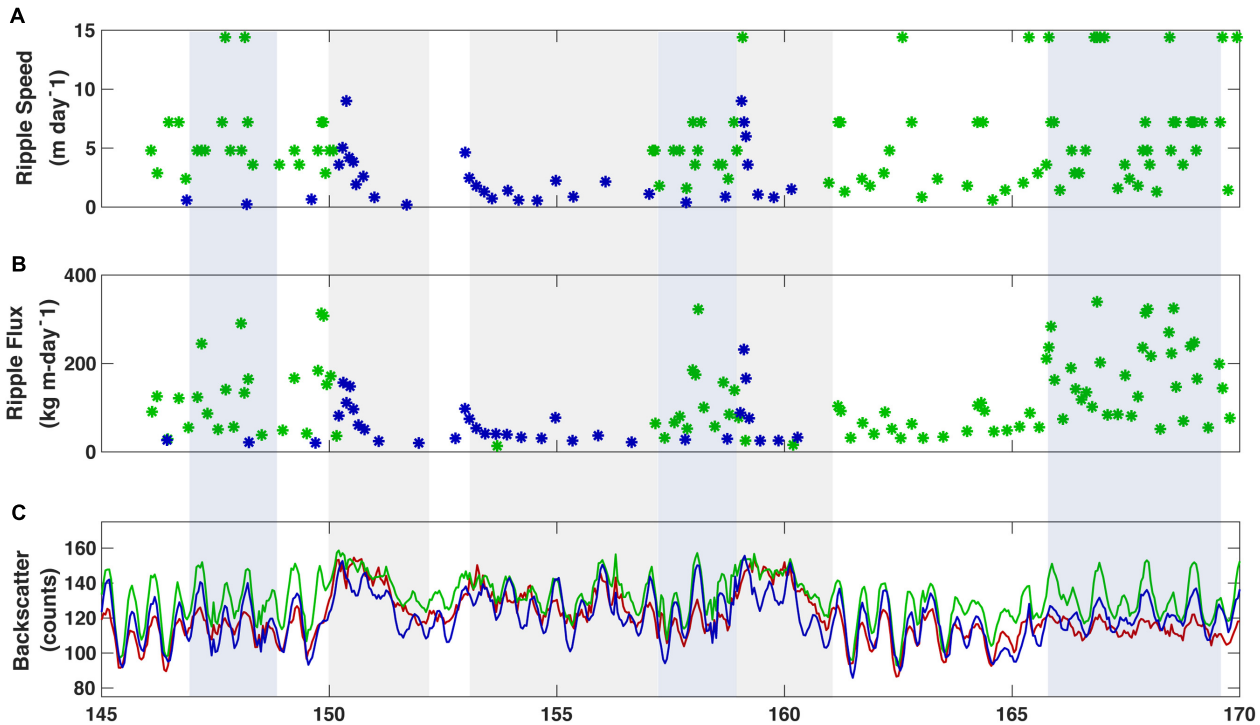

FIGURE 7 | Sediment flux parameters measured at the three sites across the reef flat and lagoon. **(A)** Bedform migration rate. **(B)** Total sediment flux by migrating bedform. **(C)** Near-bed acoustic backscatter from 10 cm above bottom, a proxy for suspended sediment. Color represents the site location: Red = TR1 on the outer reef flat near the reef crest, blue = TR2 on the inner reef flat, and green = TR3 in the lagoon.

(1–2 m), suspended sediment on the reef remained elevated in the lagoon but demonstrated more tidal variability. During periods of lower to moderate forcing, suspended sediment on the reef flat displayed a strong tidal signature; this is especially evident when bedforms were present. This is interpreted as the result of ejection of sediment higher into the water column off the faces of bedforms. The tidal nature of near-bottom suspended sediment is more prevalent in the lagoon, as the suspended load increased and decreased with the tide even during peak incident wave forcing.

DISCUSSION

Primary Modes of Transport

The dimensions and rate of change of bedforms in shelf seas has been shown to scale with the imparted shear stress whether it be due to the wave-orbital diameter or average current velocity (Baas, 1993; Traykovski, 2007; Soulsby et al., 2012), and we expect the same to be true on a coral reef. Cacchione et al. (1999) showed that bedform migration rate in a reef channel on Kailua, Oahu, was proportional to the power of the near-bottom combined wave-current speed cubed (approximately). However, in this study no clear relationship was found between migration rate and imparted shear stress due to currents alone on the reef or in the lagoon (not shown). The same was true for combined wave-current stress on the reef flat – both low and high ripple migration rates occurred over a wide range of shear stress and water levels (**Figure 8**). This was observed for the SS and the IG bands, as well as total combined shear stress, although there were more instances of moderate migration rate when compared to IG shear stress at lower water levels. A better correlation between imparted shear stress and migration rate existed in the lagoon; higher migration rates almost exclusively occurred at higher stresses and water levels, particularly for combined total shear stresses.

Given the lack of relationship between imparted shear stress and bedform migration rate on the reef flat, we postulate that the supply of sediment plays an important role in controlling migration rate. The washout of all bedforms and sediment confirms that the supply of sediment on the reef was not consistent. After the first instance of washout on YD 150, it took several days for a baseline of sediment to accumulate on the reef again, during which time migration rates were average even though incident H_s remained elevated. Similarly, after the second washout period on YD 159, the highest bedform migration rates on the reef flat did not occur until an established baseline of sediment had accumulated and incident H_s were once again elevated.

Bedform migration in the lagoon also appeared to be related to the supply of sediment, even if there was a slightly stronger relationship between migration rate and shear stress. The two periods of highest ripple migration in the lagoon occurred immediately after the reef flat had been cleared of sediment (YD 150 and YD 158, **Figure 6**). In the first event, an increase in

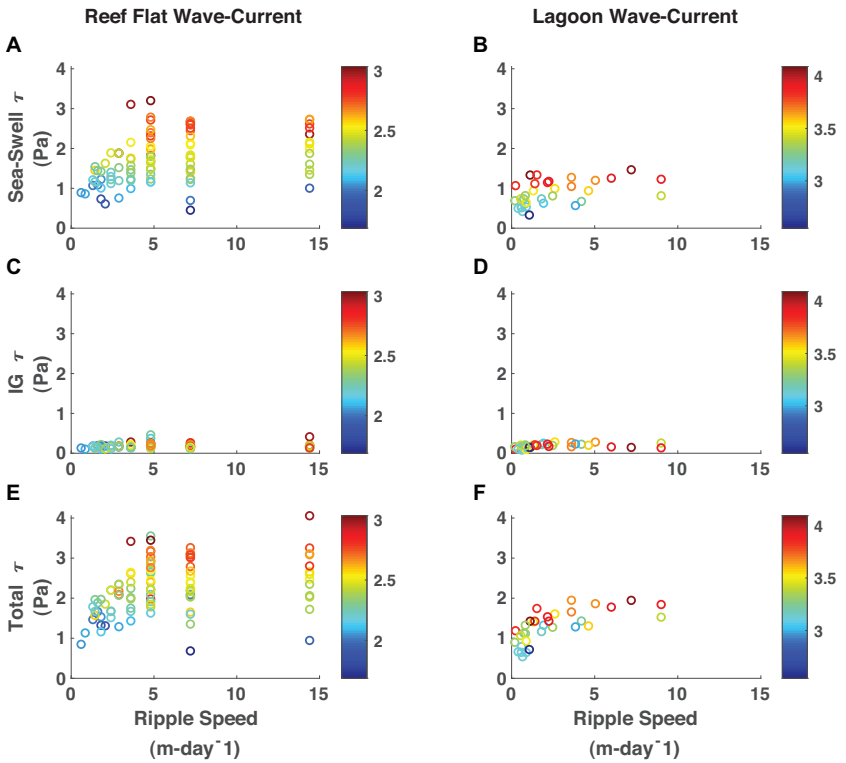

FIGURE 8 | Shear stress (τ) versus ripple speed as a function of water level. **(A)** τ due to sea-swell waves at TR2 on the inner reef flat. **(B)** τ due to sea-swell waves at TR3 in the lagoon. **(C)** τ due to infragravity waves at TR2 on the inner reef flat. **(D)** τ due to infragravity waves at TR3 in the lagoon. **(E)** Total τ at TR2 on the inner reef flat. **(F)** Total τ at TR3 in the lagoon. Color denotes the total water level, in meters.

offshore H_s began around YD 149.75 and resulted in higher U_{orb} both on the reef flat and in the lagoon (**Figure 9**). There was a corresponding migration of bedforms on the reef flat at this time, but not in the lagoon. The bed level on the reef flat dropped quickly as shear stresses due to U_{mean} increased and sediment was washed off the reef flat (YD 150.00-150.25). Once the sediment was completely washed off the reef flat and local U_{orb} began to increase with the rising tide, bedforms began to migrate quickly in the lagoon, subsequently slowing once U_{orb} began to decrease again. When the local U_{orb} increased again to the previous level, bedforms in the lagoon again began to migrate, albeit at a much slower pace. Although the shear stresses were seemingly the same, bedform migration was not nearly as prominent without an influx of new sediment.

Infragravity Contribution to Bedload Transport

In a laboratory study using a physical model of a fringing reef, Pomeroy et al. (2015a) showed that the IG component of suspended-sediment flux in a laboratory setting can be as high, if not higher, than the SS component. In our study, it does not appear from the relationships of bedform migration rate to U_* that the IG energy alone was responsible for moving sediment on the reef, but this does not mean that it is not important. Periods of enhanced bedform migration corresponded to periods of higher IG energy, both on the reef flat and in the lagoon. In particular, U_{orb} associated with IG waves comprised a significant portion of the total near-bed U_{orb} (**Figure 5**). For instance, SS-band U_{orb} during YD 152-155 were comparable to those during YD 162-165 in the lagoon, yet no detectable bedform migration was observed during the latter period. The difference is that offshore H_s, and subsequently local IG energy (both U_{mean} and U_{orb}) was elevated during the former period. This was similarly noted on the reef flat; the SS wave energy during the period of YD 160-165 was comparable to that of the period of YD 165-170, yet the sediment flux by migrating bedforms was considerably smaller during the former. IG wave energy on the reef flat was elevated during the latter period in this instance.

Perhaps more important to sediment transport than the IG energy at a given time is the increased wave asymmetry and skewness under IG waves. Wave asymmetry results in a skewed near bottom velocity distribution (Ruessink et al., 2009; Tissier et al., 2015) and can contribute to net onshore or offshore transport, depending on sediment types (Aagaard and Greenwood, 2008; de Bakker et al., 2016). A transition to higher wave asymmetry and skewness toward the shore (particularly in the IG and VLF frequency bands) has been shown to occur in reef environments (Cheriton et al., 2016; Pomeroy et al., 2015a). Thus, while the shear stress associated with individual IG waves may not be high enough to mobilize sediment alone, the contribution of IG waves with higher asymmetry to the background SS energy may result in bedload transport both on the reef flat and in the lagoon.

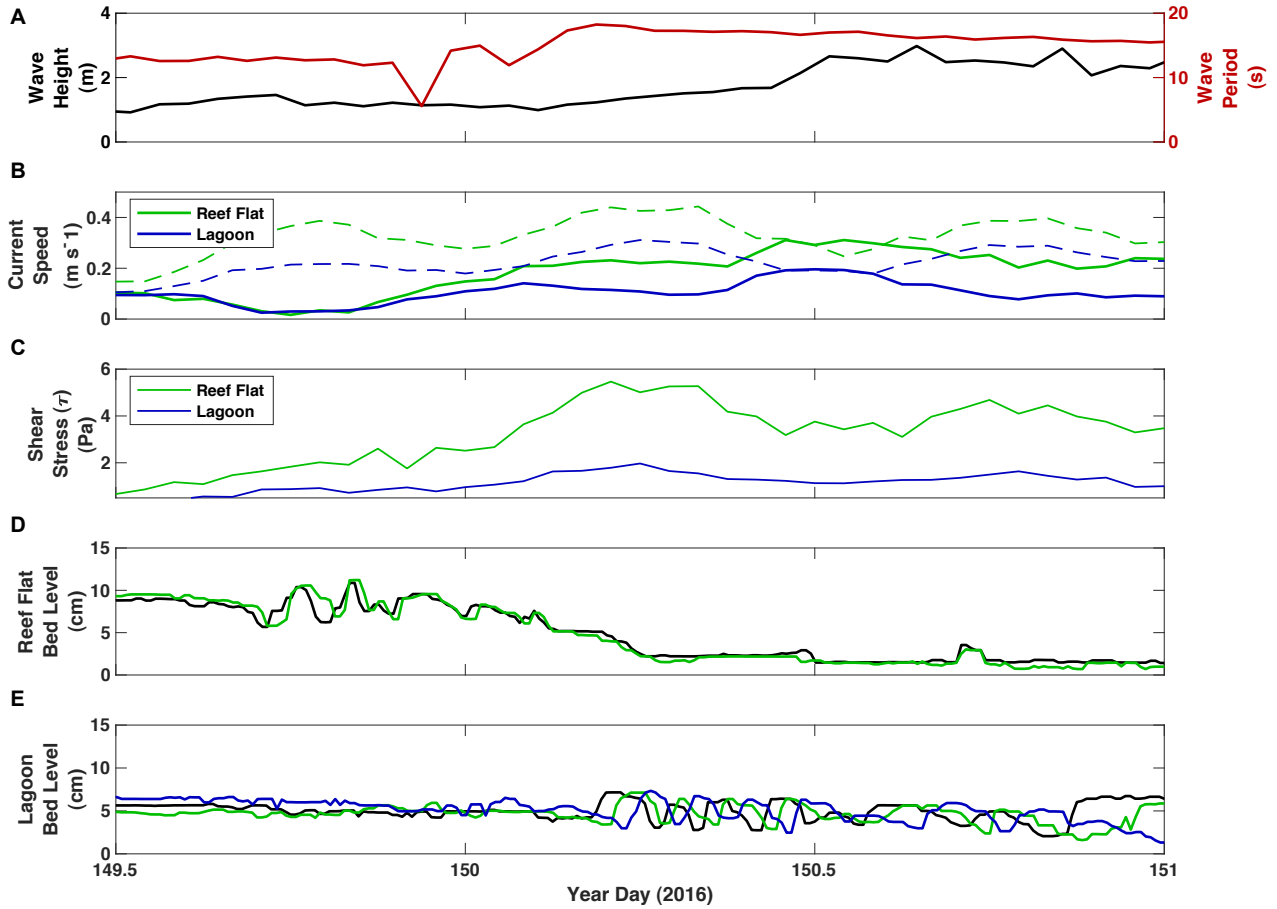

FIGURE 9 | Wave and current parameters and bed elevation from TR2 on the inner reef flat and TR3 in the lagoon during a transition period when ripples on the reef flat were washed out and sediment input to the lagoon peaked. **(A)** Offshore significant wave height (black) and peak wave period (red). **(B)** Burst mean current speed (solid) and wave orbital velocity (dashed) on the reef. **(C)** Total shear stress (τ) **(D)** Bed altimetry at TR2 on the inner reef flat. **(E)** Bed altimetry at TR3 in the lagoon. Colors in panels **(D,E)** represent data from individual altimeters, in order from offshore to onshore, black, green and blue.

Wave- vs. Current-Dominated Transport

The Soulsby et al. (2012) critical Shields parameters were accurate predictors of washout and sheetflow conditions at the reef flat site (**Figure 10**). The washout of bedforms coincided with current Shields parameter (θ_{cur}) surpassing the washout Shields parameter (θ_{wo}), and when θ_{cur} dropped below θ_{wo} around YD 157, bedforms began to form again on the reef flat. The timing of the wave Shields parameter (θ_{wv}) surpassing the critical Shields parameter for sediment mobilization (θ_{crit}) was consistent with bedform migration on the reef flat. The Shields parameter did not seem to be an accurate predictor of sediment behavior at the reef crest, however. Even though sediment was not observed to accumulate at the reef crest (presumably due to sheetflow conditions), θ_{cur} only exceeded θ_{wo} on two occasions. Nevertheless, θ_{wv} was often above critical for sediment movement at this location.

In the lagoon, θ_{wv} rarely exceeded θ_{crit}, demonstrating that waves alone were probably not responsible for bedload sediment movement. The timing of when θ_{cur} exceeded θ_{crit} matched the timing of bedform migration well. Peaks in θ_{cur} generally did not correspond to peaks in θ_{wv}, again demonstrating that U_{mean} was mainly dependent upon mean wave-driven currents and not SS-band velocities that peaked at high tides. The Shields parameter for currents in the lagoon never exceeded θ_{wo}, despite the drop in average bed level that occurred on occasion (such as YD 152 and YD 158), indicating net loss of the sediment in the lagoon.

Applicability of Equilibrium Bedform Models

We could only to test predictors for bedform height, η, as we only have data from vertical altimeters. The Wiberg and Harris ('W-H') formula (that depends only on wave height and wave-orbital diameter) generally overestimated η on the reef flat by a factor of two (**Figure 11**). The O'Donaghue formula ('OD'), which uses the mobility parameter, Ψ, which is a function of the non-dimensional grain size, over-predicted η almost by an order of magnitude. The Styles and Glenn ('S-G') formula is the best predictor for η, albeit often under-predicting it. In the lagoon, the S-G formula was the best predictor, with both the W-H and OD formulae greatly overpredicting

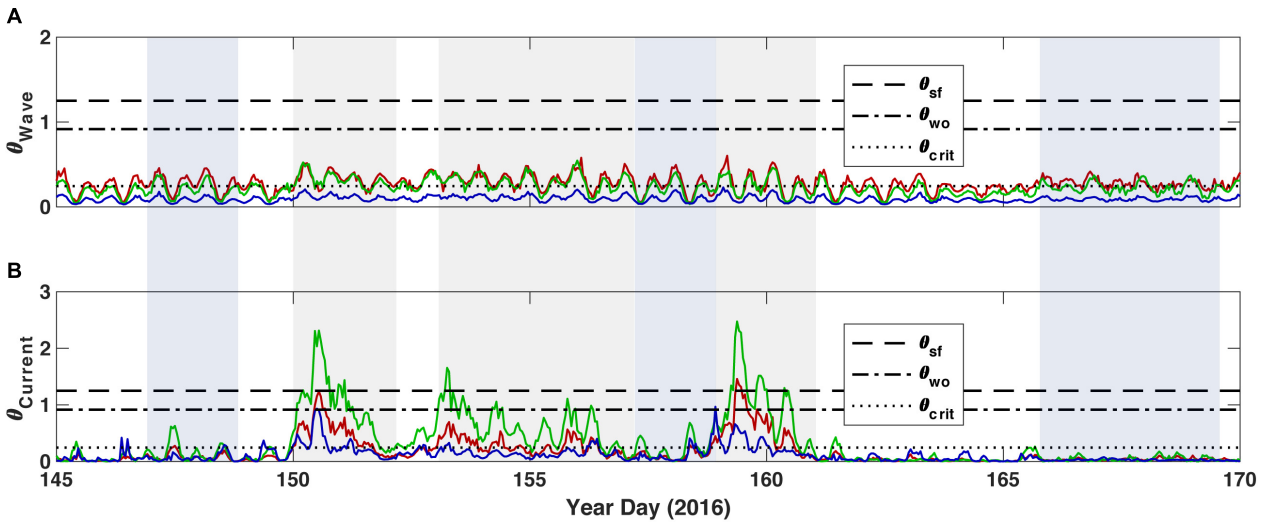

FIGURE 10 | Shields parameters by forcing mechanism for the three sites. **(A)** Waves. **(B)** Currents. Color represents the site location: Red = TR1 on the outer reef flat near the reef crest, green = TR2 on the inner reef flat, and blue = TR3 in the lagoon.

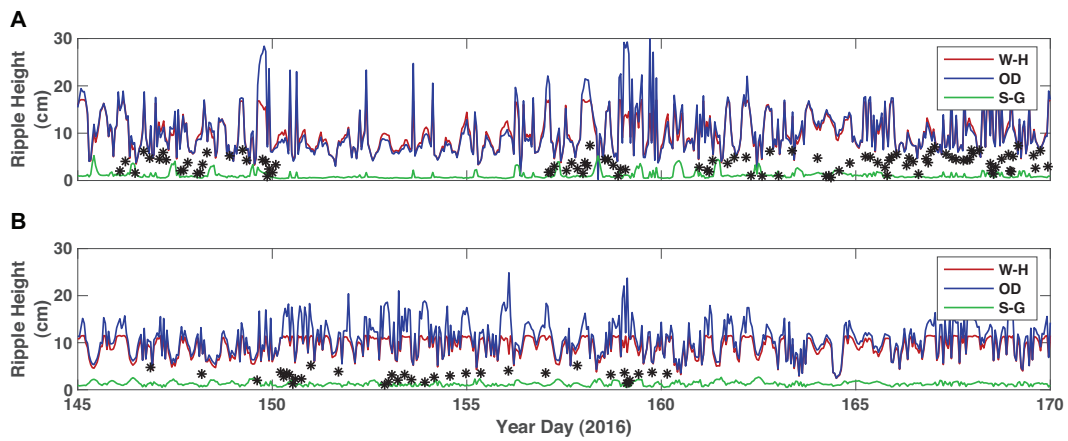

FIGURE 11 | Comparison of measured and modeled equilibrium bedform dimensions. **(A)** TR2 on the inner reef flat. **(B)** TR3 in the lagoon. Color represents the equilibrium bedform model: Red = Wiberg and Harris, 1994, green = Styles and Glenn (2002), and blue = O'Donoghue et al. (2006). Black stars denote ripple amplitudes as measured by altimeter.

η. These models of bedform development assume unlimited sediment supply. This is clearly not the case on the reef flat at Ningaloo where all sediment on the flat appears to be stripped off during large wave events. It isn't until the system reaches equilibrium conditions (such as the latter 2 weeks) that we would expect an equilibrium model to accurately predict bedform development.

Gradients in Accumulation and Bedload Transport

A gradient in the volume of bedload transport from the inner reef to the lagoon suggests that not all of the bedload constituent reaches the salient at the shoreline. Total bedload transport over the study period was calculated to be 1,565 and 485 kg/m, on the reef flat and in the lagoon, respectively, while the estimated yearly transport was 2×10^4 and 7×10^3 kg/m on the reef flat and in the lagoon, respectively. Thus, the shoreward bedload transport over the reef flat is more than 3 times that of the lagoon. Modeled circulation patterns on the reef show strong return flow through the north and south channels via the lagoon (Cuttler et al., 2018b). This does not mean that all the sediment is being exported out of the reef system through the channels. At least some of this excess sediment is most likely being spread out on either side of the salient, eventually being transported toward the shore by asymmetrical waves. Indeed, Cuttler et al. (2018b) showed that mean wave direction north and south of the salient is normal to the shoreline, not the reef crest, and hence the refraction of waves affects the direction of bedload transport and bedform migration. Shoreline accretion rates of ∼1 m/year were estimated by Cuttler et al. (2018a). Assuming a beach slope of 45

degrees, mean depth of the lagoon of 3 m, and a bulk density of sediment of 1,600 kg/m^3, a total of 7,200 kg of sediment would be required to accrete 1 m of shoreline (in the alongshore direction) out 1 m. A mean daily bedload transport rate of 34 kg/m/d in the lagoon over a year-long period results in 12,645 kg of transport over 1 m of reef flat, 1.75 times the previously noted shoreline accretion rates.

Nevertheless, there is a large discrepancy in bedload transport rate on the reef flat (61 kg/m/d) and previously reported estimates of sediment production on the reef by bioerosion (5 kg/m/d, per Langdon, 2012). The fact that wave and current energy was comparable on the reef flat near the reef crest and near the lagoon, but that no apparent sediment accumulation was occurring near the reef crest, indicates that some sediment storage occurs on the reef flat. It has been shown that high roughness due to the presence of coral can significantly reduce both mean and oscillatory flow, thus reducing near-bottom shear stresses (Pomeroy et al., 2017). Higher roughness due to coral rubble and vegetation on the reef flat at Ningaloo may contribute to this process, thus allowing sediment to accumulate and bedforms to develop on the reef flat.

Estimating the area of the reef flat to be ∼2 km^2 and assuming the accumulation of sediment across the entire reef flat is comparable to that of our site TR2 (∼5 cm), the volume of sediment washed off the reef in one large wave event would be ∼10^5 m^3. This is an overestimate of sediment contribution to the lagoon during washout events, given that sediment did not cover the entire reef flat at all times. Nevertheless, sediment at this site was replaced within a few days once waves and currents subsided on the reef flat. So the question is, from where is this sediment coming? Sediment production from bioerosion of reef framework alone cannot produce this volume in such a short period. Is it possible that sediment is being brought up the fore reef and over the reef crest? If so, is it possible that that sediment was once washed off the reef and out through the channels, thereby being recycled in the system? More study on the sources and sinks of sediment in a fringing reef with a lagoon and channels will help to answer these important questions.

CONCLUSION

Understanding the transport of sediment in coral reef environments is critical to forecasting future change on coral-reef-lined coasts. Models that rely solely on bulk wave statistics or idealized spectra may not accurately describe the forcing on reefs and, therefore, may incorrectly estimate the pathways and rates of sediment transport from the reef to the shoreline. Low-frequency IG-band motions may or may not mobilize sediment alone depending on the reef geometry, but the combination of IG-band motions with incident SS-band motions is clearly important in mobilizing sediment as well to the migration of bedforms on the seafloor toward the shoreline. Ignoring the IG constituent could result in underestimation of bedload transport on a coral reef.

Bedload transport on the Ningaloo Reef flat alternates between being predominantly current-driven during large swell events when washout of bedforms occurs, and wave-driven during average offshore wave conditions when bedform migration is greatest. Transport in the lagoon is due to a combination of current and wave forcing; bedform migration occurs when the summation of the two exceeds the sediment's critical shear stress.

Existing equilibrium models of bedform development do not predict the observed dimensions of bedforms either on the reef flat or in the lagoon, although the Styles and Glenn (2002) formulae that employs the observed sediment grain density perform the best. This discrepancy may also be due to the fact that these models use bulk wave statistics and not the full energy spectrum in their formulations and therefore do not account for the lower-frequency, IG-band energy that commonly occurs on reefs. Variations in the supply of sediment also affect the accuracy of an equilibrium model. Nevertheless, using accurate estimates of grain density may be important not only for modeling the formation of bedforms, but also for predicting washout conditions on a reef.

Sediment budgets of bedload transport across Ningaloo Reef indicate that although large volumes of sediment are transported across the reef flat, not all of the sediment migrates to the shoreline. The source of the relatively large volumes of sediment that accumulates on reef flat is still not well understood. It is possible that sediment is being recycled in the system; sediment is brought up onto the reef by large waves, transported across the reef by SS- and IG-band energy, and a percentage is then exported from the reef system through adjacent channels. Despite seemingly similar hydrodynamic conditions and sources of sediment between two nearby sites on the reef flat, we still don't fully understand why bedforms generate at one site and not the other. More research on the sources and sinks of carbonate sediment on reefs would help answer some of these questions.

Although this study has demonstrated that IG waves are important to bedload transport in a coral reef/lagoon complex, the results here may or may not apply to the great variety of geometries in coral reef environments observed around the world. The average water depth, reef flat width, and fore-reef slope all factor into the proportion of IG energy that exists on the reef flat (Cheriton et al., 2020). Incorporating low-frequency energy, wave asymmetry and skewness, and accurate estimates of grain density will greatly improve future models of sediment transport on coral reefs. In addition, better relationships between bedform migration and input forcing could be made with more comprehensive sonar measurements (spatially and temporally) of bedforms and their transformation and migration, such as could be made with time series of sector scanning sonar data. Given how important sediment supply is to bedform formation and migration, more studies on the sources and supply of sediment on coral reefs (including studies of sediment dynamics on the fore reef) will be necessary to accurately forecast the bedload constituent.

DATA AVAILABILITY STATEMENT

The datasets analyzed in this manuscript are available from ScienceBase at doi: 10.5066/P9PEIA2S.

AUTHOR CONTRIBUTIONS

KR performed the analyses and wrote the manuscript with CS, OC, AP, JH, RL, and MB. All authors contributed to the article and approved the submitted version.

FUNDING

This work was funded by the U.S. Geological Survey's Coastal/Marine Hazards and Resources Program, the Western Australia Marine Science Institute (WAMSI) Dredging Science Node (Theme 2/3), an Australian Research Council Future Fellowship (FT110100201), and an Australian Research Council Discovery Project grant (DP140102026).

ACKNOWLEDGMENTS

We would like to thank Carlin Bowyer (UWA), Anton Kuret (UWA), and Joshua Logan (USGS) for their logistical and field work in support of this project. We also would like to thank Bruce Jaffe (USGS) for an initial review of this manuscript, and Chris Sherwood (USGS) for his routines and insight into the calculation of modeled bedform dimensions. Any use of trade, firm, or product names is for descriptive purposes only and does not imply endorsement by the U.S. Government.

REFERENCES

Aagaard, T., and Greenwood, B. (2008). Infragravity wave contribution to surf zone sediment transport — The role of advection. *Mar. Geol.* 251, 1–14.

ASTM International (2010). *Standard Test Methods for Specific Gravity of Soil Solids by Water Pycnometer*. West Conshohocken, PA: ASTM International.

Baas, J. H. (1993). *Dimensional Analysis of Current Ripples in Recent and Ancient Depositional Environments*. Ph.D. Thesis, University of Utrecht, The Netherlands, 199.

Becker, J. M., Firing, Y. L., Aucan, J., Holman, R., Merrifield, M., and Pawlak, G. (2007). Video-based observations of nearshore sand ripples and ripple migration. *J. Geophys. Res.* 112:C01007. doi: 10.1029/2005JC003451

Buckley, M. L., Lowe, R. J., Hansen, J. E., van Dongeren, A. R., and Storlazzi, C. D. (2018). Mechanisms of wave-driven water level variability on reef-fringed coastlines. *J. Geophys. Res. Oceans* 123, 3811–3831. doi: 10.1029/2018JC013933

Cacchione, D., Richmond, B., Fletcher, C., Tate, G., and Ferreira, J. (1999). "Sand transport in a reef channel off Kailua, Oahu, Hawaii," in *Proceedings of The Non-Steady State of the Inner Shelf and Shoreline: Coastal Change on the Time Scale of Decades to Millennia in the Late Quaternary, Abstracts with Programs*, (Honolulu: University of Hawaii).

Camenen, B. (2009). Estimation of the wave-related ripple characteristics and induced bed shear stress. *Estar. Coast Shelf Sci.* 553–564. doi: 10.1016/j.ecss.2009.07.022

Cheriton, O. M., Storlazzi, C. D., and Rosenberger, K. J. (2016). Observations of wave transformation over a fringing coral reef and the importance of low-frequency waves and offshore water levels to runup, overwash, and coastal flooding. *J. Geophys. Res. Oceans* 121, 3121–3140. doi: 10.1002/2015JC011231

Cheriton, O. M., Storlazzi, C. D., and Rosenberger, K. J. (2020). In situ observations of wave transformation and infragravity bore development across reef flats of varying geomorphology. *Front. Mar. Sci.* 7:351. doi: 10.3389/fmars.2020.00351

Cuttler, M. V. W., Hansen, J. E., Lowe, R. J., and Drost, E. J. F. (2018a). Response of a fringing reef coastline to the direct impact of a tropical cyclone. *Limnol. Ocean. Lett.* 3, 31–38. doi: 10.1002/lol2.10067

Cuttler, M. V. W., Hansen, J. E., Lowe, R. J., Trotter, J. A., and McCulloch, M. T. (2018b). Source and supply of sediment to a shoreline salient in a fringing reef environment. *Earth Surf. Process. Landforms* 44, 552–564. doi: 10.1002/esp.4516

Cuttler, M. V. W., Lowe, R. J., Falter, J. L., and Buscombe, D. (2017). Estimating the settling velocity of bioclastic sediment using common grain-size analysis techniques. *Sedimentology* 64, 987–1004. doi: 10.1111/sed.12338

de Bakker, A. T. M., Brinkkemper, J. A., van der Steen, F., Tissier, M. F. S., and Ruessink, B. G. (2016). Cross-shore sand transport by infragravity waves as a function of beach steepness. *J. Geophys. Res. Ear. Surf.* 121, 1786–1799.

Dean, R. D., and Dalrymple, R. A. (eds) (1991). "Water wave mechanics for engineers and scientists," in *Advanced Series on Ocean Engineering*, Vol. 2, (Singapore: World Scientific Publishing Co. Ltd).

Deltares Systems (2019). *Delft3D-WAVE User Manual, V 3.05, Deltares, Boussinesqweg, 1 2629 HV*. Delft: Deltares Systems.

Drost, E. J. F., Lowe, R. J., Ivey, G. N., Jones, N. L., and Pequignet, C. A. (2017). The effects of tropical cyclone characteristics on the surface wave fields in Australia's North West region. *Cont. Shelf Res.* 35–53. doi: 10.1016/j.csr.2017.03.006

Grant, W. D., and Madsen, O. S. (1979). Combined wave and current interaction with a rough bottom. *J. Geophys. Res.* 84, 1797–1808. doi: 10.1029/JC084iC04p01797

Karimpour, A., and Chen, Q. (2017). Wind wave analysis in depth limited water using OCEANLYZ, a MATLAB toolbox. *Comput. Geosci.* 181–189. doi: 10.1016/j.cageo.2017.06.010

Kramer, K., and Winter, C. (2016). Predicted ripple dimensions in relation to the precision of in situ measurements in the southern North Sea. *Ocean Sci.* 12, 1221–1235. doi: 10.5194/os-12-1221-2016

Langdon, M. W. (2012). *The Ecology of the Grazing Urchin Echinometramathaei at Ningaloo Marine Park*. Murdoch University.

Madsen, O. S. (1994). "Spectral wave-current bottom boundary layer flows. Coastal Engineering 1994," in *Proceedings, 24th International Conference Coastal Engineering Research Council*, New York, NY, 384–398.

Nielsen, P. (1981). Dynamics and geometry of wave-generated ripples. *J. Geophys. Res.* 86, 6467–6472.

O'Donoghue, T., Doucette, J. S., van der Werf, J. J., and Ribberink, J. S. (2006). The dimensions of sand ripples in full-scale oscillatory flows. *Coast. Eng.* 997–1012. doi: 10.1016/j.coastaleng.2006.06.008

Pomeroy, A., Lowe, R., Symonds, G., Van Dongeren, A., and Moore, C. (2012). The dynamics of infragravity wave transformation over a fringing reef. *J. Geophys. Res.* 117:C11022. doi: 10.1029/2012JC008310

Pomeroy, A. W. M., Lowe, R. J., Dongeren, A. R., Ghisalberti, M., Bodde, W., and Roelvink, D. (2015a). Spectral wave-driven sediment transport across a fringing reef. *Coast. Eng.* 98, 78–94. doi: 10.1016/j.coastaleng.2015.01.005

Pomeroy, A. W. M., Lowe, R. J., Ghisalberti, M., Storlazzi, C. D., Cuttler, M., and Symonds, G. (2015b). "Mechanics of sediment suspension and transport within a fringing reef," in *Proceedings of the Coastal Sediments Conference, 2015*, (Singapore: World Scientific Publishing).

Pomeroy, A. W. M., Lowe, R. J., Ghisalberti, M., Storlazzi, C. D., Symonds, G., and Roelvink, D. (2017). Sediment transport in the presence of large reef bottom roughness. *J. Geophys. Res. Oceans* 122, 1347–1368.

Pomeroy, A. W. M., Lowe, R. J., Ghisalberti, M., Winter, G., and Storlazzi, C. D. (2018). Spatial variability of sediment transport processes over intra- and subtidal time-scales within a fringing coral reef. *J. Geophys. Res. Ear. Surf.* 123, 1013–1010. doi: 10.1002/2017JF004468

Reguero, B. G., Secaira, F., Toimil, A., Escudero, M., Díaz-Simal, P., Beck, M. W., et al. (2019). The risk reduction benefits of the mesoamerican reef in Mexico. *Front. Earth Sci.* 7:125. doi: 10.3389/feart.2019.00125

Ruessink, B. G., van den Berg, T. J. J., and van Rijn, L. C. (2009). Modeling sediment transport beneath skewed asymmetric waves above a plane bed. *J. Geophys. Res.* 114:C11021. doi: 10.1029/2009JC005416

Soulsby, R. L., and Whitehouse, R. J. S. (2005). *Prediction of Ripple Properties in Shelf Seas. Mark 1 Predictor*. Report TR150. Wallingford: HR Wallingford.

Soulsby, R. L., Whitehouse, R. J. S., and Marten, K. V. (2012). Prediction of time-evolving sand ripples in shelf seas. *Cont. Shelf Res.* 47–62. doi: 10.1016/j.csr.2012.02.016

Storlazzi, C. D., Reguero, B. G., Cole, A. D., Lowe, E., Shope, J. B., Gibbs, A. E., et al. (2019). *Rigorously Valuing the Role of U.S. Coral Reefs in Coastal Hazard Risk Reduction*. U.S. Geological Survey Open-File Report 2019–1027. Reston: U.S. Geological Survey.

Styles, R., and Glenn, S. M. (2002). Modeling bottom roughness in the presence of wave-generated ripples. *J. Geophys. Res.* 107:3110. doi: 10.1029/2001JC000864

Taebi, S., Lowe, R. J., Pattiaratchi, C. B., Ivey, G. N., Symonds, G., and Brinkman, R. (2011). Nearshore circulation in a tropical fringing reef system. *J. Geophys. Res. Oceans* 116:C02016. doi: 10.1029/2010JC006439

Tissier, M. F. S., Bonneton, P., Michallet, H., and Ruessink, B. G. (2015). Infragravity-wave modulation of short-wave celerity in the surf zone. *J. Geophys. Res. Oceans* 120, 6799–6814.

Traykovski, P. (2007). Observations of wave orbital scale ripples and a non-equillibrium time-dependent model. *J. Geophys. Res. Oceans* 112, 1–19. doi: 10.1029/2006JC003811

Traykovski, P., Hay, A. E., Irish, J. D., and Lynch, J. F. (1999). Geometry, migration, and evolution of wave orbital ripples at LEO-15. *J. Geophys. Res. Oceans* 104, 1505–1524. doi: 10.1029/1998JC900026

Wengrove, M. E., Foster, D. L., Lippmann, T. C., de Schipper, M. A., and Calantoni, J. (2018). Observations of time-dependent bedform trans- formation in combined wave-current flows. *J. Geophys. Res. Oceans* 123, 7581–7598. doi: 10.1029/2018JC014357

Wiberg, P. L., and Harris, C. K. (1994). Ripple geometry in wave-dominated environments. *J. Geophys. Res.* 99, 775–789. doi: 10.1029/93JC02726

Wiberg, P. L., and Sherwood, C. R. (2008). Calculating wave-generated bottom orbital velocities from surface wave parameters. *Comput. Geosci.* 34, 1243–1262. doi: 10.1016/j.cageo.2008.02.010

Conflict of Interest: The authors declare that the research was conducted in the absence of any commercial or financial relationships that could be construed as a potential conflict of interest.

Copyright © 2020 Rosenberger, Storlazzi, Cheriton, Pomeroy, Hansen, Lowe and Buckley. This is an open-access article distributed under the terms of the Creative Commons Attribution License (CC BY). The use, distribution or reproduction in other forums is permitted, provided the original author(s) and the copyright owner(s) are credited and that the original publication in this journal is cited, in accordance with accepted academic practice. No use, distribution or reproduction is permitted which does not comply with these terms.

APPENDIX A: DEFINITIONS OF PARAMETERS USED IN CALCULATIONS

$\psi_w = \frac{U_w^2}{D_*}$ the mobility parameter, where U_w is the orbital velocity

$D_* = d_{50}\left[g\left(s-1\right)/\upsilon^2\right]^{\frac{1}{3}}$ the non-dimensional grainsize

where, s= ρ_{sed}/ρ_{water} is the relative sediment density, and υ is the viscosity of the seawater

The Shields parameters were calculated following Soulsby et al. (2012):

$$\theta_{cur} = \frac{C_d \mathcal{U}^2}{g\left(s-1\right)d_{50}}, C_d = \left[\frac{0.40}{ln\left(h/z_0\right)-1}\right]^2$$

where $z_0 = d_{50}/12$,

and $\mathcal{U}$ is the depth averaged velocity

$$\theta_{wo} = 2.26\times D_*^{-1.3}, \quad \theta_{sf} = 1.66\times D_*^{-1.3}, for D_* > 1.58$$

$$\theta_{wo} = 0.916, \quad \theta_{sf} = 1.25, for D_* \leq 1.58$$

The wave skewness and asymmetry were calculated following Pomeroy et al. (2015a):

$$Sk = \frac{\left\langle \tilde{u}^3 \right\rangle}{\left\langle \tilde{u}^2 \right\rangle^{3/2}}$$

$$As = \frac{\left\langle H\left(\tilde{u}^3\right)\right\rangle}{\left\langle \tilde{u}^2 \right\rangle^{3/2}}$$

where $\tilde{u}$ is the near-bed oscillatory velocity, and H is the Hilbert transform.

frontiers in Marine Science

ORIGINAL RESEARCH
published: 29 October 2020
doi: 10.3389/fmars.2020.538675

Hydrodynamic Drivers and Morphological Responses on Small Coral Islands—The Thoondu Spit on Fuvahmulah, the Maldives

C. Gabriel David and Torsten Schlurmann*

Faculty of Civil Engineering and Geodetic Sciences, Ludwig-Franzius-Institute for Hydraulic, Estuarine and Coastal Engineering, Leibniz University Hannover, Hannover, Germany

Assessing the resilience of islands toward altered ocean climate pressures and providing robust adaptation measures requires an understanding of the interaction between morphological processes and the underlying hydrodynamic drivers. In this sense, this study presents changing sediment volumes on various temporal scales for the fringing reef island Fuvahmulah. Based on three field campaigns, conducted over 2 years, aerial imagery provides information on marine aggregates of the island's beaches. In addition, high resolution climate reanalysis data serves as input into an empirical and a numerical approach. Together, both approaches describe the driving processes behind volumetric seasonal and interannual changes: On the one hand, the empirical method quantifies sediment transport rates for calcareous sediments over the whole time span of the data set by considering wind and swell waves from multiple directions. On the other hand, the numerical method gives insights into the complexity of currents induced by dominant wave components. Combining these methods facilitates hindcasting and predicting morphological changes under varying wave climate, assessing sediment pathways over the whole reef, and describing the seasonal and interannual evolution of the sand spit Thoondu. As a result, this study reveals sediment distribution on different spatio-temporal scales and elucidates their significance in the design of conventional and alternative low-regret coastal adaptation.

Keywords: low-lying islands, morphology, coral reefs, global climate data, sand spit, Maldives, coastal management, climate change adaptation

OPEN ACCESS

Edited by:
Curt D. Storlazzi, United States Geological Survey (USGS), United States

Reviewed by:
Matthew John Eliot, Seashore Engineering, Australia
Peng Yao, Hohai University, China

****Correspondence:***
C. Gabriel David
david@lufi.uni-hannover.de

Specialty section:
This article was submitted to Coastal Ocean Processes, a section of the journal Frontiers in Marine Science

Received: *28 February 2020*
Accepted: *29 September 2020*
Published: *29 October 2020*

Citation:
David CG and Schlurmann T (2020) Hydrodynamic Drivers and Morphological Responses on Small Coral Islands—The Thoondu Spit on Fuvahmulah, the Maldives. Front. Mar. Sci. 7:538675. doi: 10.3389/fmars.2020.538675

1. INTRODUCTION

Small islands and atolls are exposed to sea level rise and associated impacts, as they lie only a few meters above mean sea level, while being fully surrounded by water. Thus, the fifth assessment report of the Intergovernmental Panel on Climate Change (IPCC) came to the conclusion that communities of small islands are particularly vulnerable to these impacts due to their inherent lack of means for retreat (Nurse et al., 2014). The Special Report Ocean and Cryosphere (SROCC) of the IPCC further finds that coastal risks for low-lying areas will increase, historically rare extreme sea level events will become common by 2100 under all climate change projection pathways, and that there are limits to any coastal protection within the current or following century (Oppenheimer et al., in press). Over a time span of decades, this could translate to uninhabitable atolls, as global

warming will be accompanied by stronger and more frequent sea-borne hazards (Storlazzi et al., 2015, 2018).

Reef islands are mainly vulnerable to shoreline erosion, inundation (including overwash), and saline intrusion (Nurse et al., 2014). These impacts are triggered by storm events and the rising sea levels (Ferrario et al., 2014). Tropical storms develop, among other factors, above a sea-surface temperature (SST) threshold of 27 °C (Tory and Frank, 2010). Thus, the frequency as well as intensity of tropical cyclones will increase within the 20° band around the equator in the face of global warming (Emanuel, 1988).

With climate change induced warming, reefs are more susceptible to coral bleaching. Therefore, higher water temperatures affect coral health directly (Pisapia et al., 2019). Corals are important for the livelihood of the accommodated reef islands. The reef is the major contributor of wave attenuation and thus protection of the inhabited island (Ferrario et al., 2014; Harris et al., 2018), because healthy coral reefs serve as natural buffers to shelter susceptible small coral islands from direct wave attack and consequent erosion (Narayan et al., 2016; Oppenheimer et al., in press). An ongoing increase of water levels in the face of climate change implies coral reefs might reach their biophysical limit of ecosystem-based protection within this century (Oppenheimer et al., in press).

But observations have shown that shorelines of reef islands respond individually to sea level rise impacts: while on the Solomon islands, severe shoreline recession and disappearing islands have been registered (Albert et al., 2016), net land area changes vary for other islands in the central and western Pacific, including positive sediment budgets despite sea level rise (McLean and Kench, 2015). Other coral reef islands have even formed and developed naturally during higher sea levels than the current mean sea level (East et al., 2018). This shows that sediment erosion and accretion is highly site specific and is sensitive to multiple drivers. However, the evolution of reef islands and their natural response to changing impacts mainly depend on the reef's individual sediment production rate and the sediment distribution under the given hydrodynamic circumstances:

Coral reefs serve as sediment source for the islands they inhabit (Woodroffe et al., 1999; Ryan et al., 2019)—sediment production rates depend on coral type (Hamylton et al., 2017), sea level (Perry et al., 2011), and location of the organisms on the reef (Ryan et al., 2019). Supply rates also vary over time, due to changes in reef growth, reef ecology and climate-driven perturbations, such as ocean acidification or increasing water temperature (Andersson, 2015; Kench and Mann, 2017; Perry et al., 2018).

On the other hand, sediment entrainment, transport and (re-)distribution on the reef is generally governed by swell waves, even though wind-waves can have an influence on flow patterns occasionally (Pomeroy et al., 2015, 2018). The island's shape and location on the reef depends on the incoming waves, the reef platform (Mandlier and Kench, 2012; Kench and Mann, 2017) as well as the island's orientation toward the dominant wave direction (Shope and Storlazzi, 2019).

The high morphologic activity allows reef islands to respond dynamically to natural ocean-climate pressures. However, coastal management efforts and infrastructure development often interfere with the inherent natural processes (Kench, 2012; David et al., 2019) adding to anthropogenic ocean-climate pressures (Duvat and Magnan, 2019) instead of providing appropriate and sustainable protection of lives, livelihoods and natural environments. In contrast, a "low-regret approach" would maintain the system's abilities and support it where and when adequate. According to the IPCC (2012), low-regret measures are concepts to manage the risks of extreme events and disasters, while offering (co-)benefits to the coastal community regardless of the current or future climate scenarios. Following a so-called *"working with nature"* or *"eco-system based"* approach (Stive et al., 2013; Temmerman et al., 2013; Tessler et al., 2015), candidates for sustainable low-regret measures include sea grass stabilization to prevent erosion (Möller et al., 2014; Paul and Gillis, 2015), bio-rock materials to mimic eco-friendly artificial reefs (David et al., 2016) or large scale artificial sand deposits, being naturally distributed by tides, waves and wind force toward beaches and dunes (Stive et al., 2013). But implementing sustainable climate change adaptation measures requires understanding natural and anthropogenic ocean-climate pressures, their impacts, the subsequent response, and the underlying processes—in the case of this study with regard to the reef. Applying this knowledge limits deteriorating impacts on ecosystems and associated ecosystem services, enables tailoring appropriate coastal protection solutions to the local conditions (Schoonees et al., 2019), and thus providing low-regret solutions.

In this study, we focus on the Maldivian island Fuvahmulah in the Indian Ocean. The Maldivian islands are susceptible to increased coral bleaching (Pisapia et al., 2019; Ryan et al., 2019; Skirving et al., 2019) and Fuvahmulah is a projected hotspot for sea level rise (Dangendorf et al., 2019). In addition, storms, storm surges, and occasional tsunamis commonly batter the coasts of the Maldives as any low-lying small islands (Nurse et al., 2014). With its location close to the equator and in between the Indian Ocean Dipole (IOD), the island is also prone to experience SST-based increase of cyclone activity and altered wave climate (Saji et al., 1999; Cai et al., 2014; Kumar et al., 2019).

In front of this background, the purpose of this study is to explore the status of and processes behind sediment distribution around the island, their significance for beach formation and coastal erosion, and to elucidate the importance of morphodynamic responses to ocean-borne hazards for low-regret and nature-based climate change adaptation. This study is the first scientific examination on the status and drivers of morphological activity on Fuvahmulah, advancing the design basics for adaptation solutions to sea level rise and wave impacts on small, low-lying coral reef islands. With this, the study also aims to present valuable methods applicable for future studies on other islands:

This study presents high resolution topographic measurements from three field campaigns on the fringing coral reef island of Fuvahmulah. These measurements reveal seasonal shoreline changes and characteristic sediment depot location for the wet and dry seasons in 2017 and 2019. A process-based, empirical

method is combined with multi-directional ocean wave data of hourly resolution from a global reanalysis model (C3S, 2017). The empirical method captures the natural, monsoon-driven seasonal as well as the annual variations of the local hydro- and morphodynamic regime. In addition, numerical modeling efforts help to further analyze coral sediment entrainment, transport processes and distribution on the reef and around the island, dependent on wave directionality and forcing.

These approaches mimic the natural seasonal and annual variations of the typical local hydro- and morphodynamic regime. Considering multi-directional wave input facilitates evaluating characteristic regional and local wave climate as well as following the probable sediment pathway around the island. Compared to studies on annual or seasonal scale, the hourly temporal resolution of hydrodynamic data gives new and more detailed insights into drivers of morphodynamics on reef islands and thus improves the understanding of sediment distribution.

The results of this study facilitate the understanding of sediment transport on reefs and thereby emphasizes the necessity of this natural sediment supply for the island. Previous studies found that the reef serves as temporally varying sediment supplier (Hamylton et al., 2017; Kench and Mann, 2017; Ryan et al., 2019) and the wave climate as sediment distributor on the reef (Kench and Brander, 2006; Kench, 2012; Mandlier and Kench, 2012; Pomeroy et al., 2015, 2017; Shope and Storlazzi, 2019). This study builds on these findings, scrutinizes the influence of a varying wave climate on reef sediment pathways, and thereby showcases reef islands' capability to naturally cope with changing ocean and climate pressures on reef islands. In the face of rising seas, this potential must be considered in coastal management and improves conventional and alternative coastal protection measures for sustainable low-regret coastal adaptation.

2. METHODS

2.1. Study Site

Fuvahmulah is the biggest single reef island in the Maldives that is not part of an atoll and the third largest Maldivian island by population (∼8,510 inhabitants). The low-lying island is located in the Indian Ocean, ∼30 km south of the equator at latitude −0.30° and longitude 73.43° (**Figure 1**). Fuvahmulah is the second most southerly atoll in the Maldives, neighboring Huvadhu Atoll in the north and Addu Atoll in the south. Fuvahmulah is ∼490 km south of the capital Malé. Tide data from the University of Hawai'i sea level Center (UHSLC, Caldwell et al., 2015) shows that the tidal signal on Fuvahmulah is a mixed semidiurnal tide (see **Supplementary Material**) with a maximum tidal range of about 1.1 m. Associated tidal currents (and ocean circulation velocities) are about an order of magnitude below those induced by waves (David et al., 2019).

Fuvahmulah is protected by the fringing reef and a vegetated coastal ridge which surrounds the island. The island's community has a tendency to prefer hard-coastal infrastructure due to national guidelines, but are open toward soft coastal protection measures (Ratter et al., 2019). Today, the island is subject to erosion being introduced by the existing coastal infrastructure (David et al., 2019; Ratter et al., 2019). The seaport is in operation since late 2004, and was constructed with sheltering breakwaters and a port entrance to the north east. But Fuvahmulah also accommodates highly morphodynamic areas: One example is the beach and coastal spit Thoondu in the north. The inhabitants of Fuvahmulah strongly identify with the island in terms of weather-related, seasonally-driven hydrodynamic characteristics, and unique morphodynamic features on Thoondu and the adjacent beaches (Ratter et al., 2019).

Future risks of flooding increase on Fuvahmulah, as on any low-lying islands, because the sea level is projected to rise about 0.8–1.0 m (Magnan et al., in press) and moreover, sea level rise is accelerating in the Indian Ocean (Dangendorf et al., 2019). In the face of climate change, other factors add to the increasing risk by sea level rise: For example, the IOD is a natural oscillation of sea surface temperatures between the western Indian Ocean (50–70° E, 10° N–10°E) and the tropical southeastern Indian Ocean (90–110° E, 10° N–0°), comparable with the El Niño and La Niña oscillations (Saji et al., 1999). Above or below a threshold of ±0.4–0.7°C the dipole has noticeable implications on the climate and weather in the Indian Ocean (Saji et al., 1999; Hermes et al., 2019). The Dipole Mode Index (DMI) is an indicator for the IOD and peaked at a threshold of +2.15 °C in October 2019 (see **Supplementary Material**). A positive DMI leads to an inverse atmospheric convection, and thus winds, from east to west. Extreme, positive IOD events are projected to increase (Collins et al., in press), having an impact on the wave climate and seaborne hazards on small islands in the Indian Ocean (Kumar et al., 2019).

2.2. Wave Data

Measured wave data for the southern Maldives is scarce. Therefore, this study uses publicly available hourly data on single levels from 1979 to November 2019 (C3S, 2017), taken from the ERA5 of the European Centre for Medium-Range Weather Forecasts (ECMWF). Statistical wave data in this paper is given in mean ± standard deviation, if not stated otherwise. The global climate reanalysis model has a spatial resolution of 0.25° in both latitudinal and longitudinal direction. The hydrodynamic boundary conditions for Fuvahmulah in this study come from the node at 0° latitude and 73.5° longitude (**Figure 1**). This data describes the hydrodynamic regime and has a sufficient resolution to be used as boundary condition for regional studies. The significant wave height H_s from the ERA5 data set shows a general trend of wave heights over 1 year (**Figure 2A**) which facilitates classifying the data into wet and dry season. The significant wave height H_s is the average wave height of the 33 % highest waves in a time-series (time-domain) or the integrated energy from a wave spectrum (frequency domain). The directional components are divided in wind-wave and total swell: Here, subsets of a directional wave energy spectrum that are subject to wind forcing are defined as wind-waves. On the contrary, swell subsets are defined as the remaining part of the spectrum that are not wind-waves (Hanson and Phillips, 2001; Bidlot, 2016) and typically subject to larger wave lengths. The ERA5 data set also provides further gradation of swell partitions (with an associated subset of wave parameters), where the swell is divided into the three most energetic systems within the swell

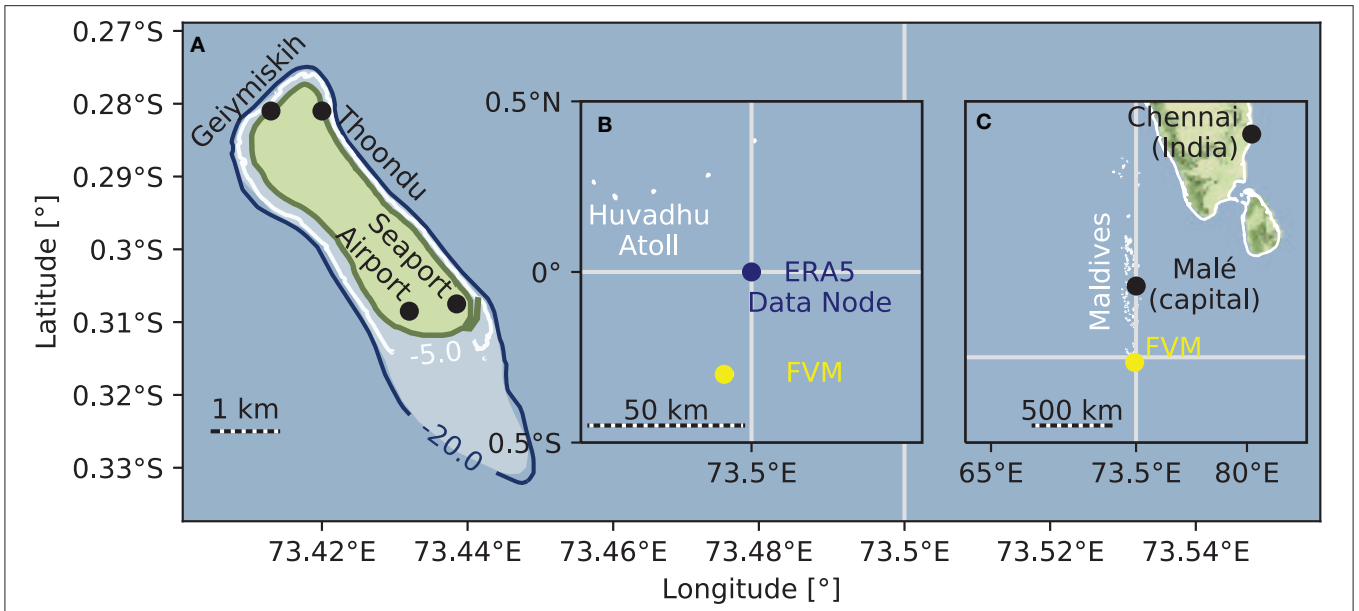

FIGURE 1 | Location of FVM. **(A)** Shows the extent of the island and the fringing reef. It also illustrates the position of the air- and seaport, as well as the beach of Thoondu and the coastal spit. The bathymetry lines come from echo-sound measurements of the first field survey (March 2017). **(B)** Shows the location of Fuvahmulah in the Indian Ocean. The data node is the virtual wave gauge at 0° latitude and 73.5° longitude. In this study, the virtual wave gauge provides information on the wave climate, based on the ERA5 data assimilation of hourly single levels from 1979 to near present (C3S, 2017, see **Figure 2**). **(C)** Shows the island location within the Maldives, Indian Ocean and the location referred to south India and Sri Lanka. Plots were generated with Matplotlib version 3.1.1 (RRID:SCR_008624) and Cartopy. Cartopy also delivered the coastlines in **(B,C)**.

partition (Bidlot, 2016). Each subset and partition contain their own parameters: significant wave height H_s, peak period T_p, mean period T_m, and peak direction θ_p. The mean period is the average time of consecutive waves to pass through a fixed point, while the peak period and direction refer to the wave period and direction associated with the highest spectral energy (C3S, 2017). The division into wind-waves and swell gives an overview of the general wave climate of Fuvahmulah (**Figures 2B–E**). This data is later used to compute and assess sediment transport processes in an approach provided by the Coastal Engineering Research Center (CERC) of the U.S. Army Corps of Engineering (CERC, 1984). The adequacy and flexibility of the CERC formulation has been proven for typical sandy shorelines (Schoonees and Theron, 1995), but application to coral reef transport is rare in literature (Shope and Storlazzi, 2019). Analyzing all peak directions θ_p of each season and wave partition will yield a pre-dominant range or significant range of peak directions $\theta_{p,sig}$. Here, this range is derived from a discrete probability distribution of the whole ERA5 time-series and contains the directions, which combined have the highest 33 % occurrence probability (see **Figure 2** and **Table 1**).

2.3. Field Campaign

Three field campaigns provided data to evaluate the seasonal and annual sedimentation processes around the island: The first campaign started in March 2017 at the end of the dry season. The second field campaign took place at the end of the wet season in September 2017, revealing seasonal variations in combination with the former measurements in March. The last field measures were taken in March and April 2019, disclosing seasonal and annual changes of sediment volumes when compared to the data recorded in 2017. The first field campaign also accommodated a bathymetric survey, recording depth profiles with a dual-frequency echo-sounder (Dr. Fahrentholz LituBox 15/200). Furthermore, the field campaigns yielded the following data sets:

2.4. Digital Elevation Models

The basis of the digital elevation models have been aerial images of the island, recorded by a DJI Phantom 4 (field campaign 1 and 2) and a DJI Phantom 4 Pro (field campaign 3). These unmanned aerial vehicles (UAVs) captured the entire coast of the island, except the beaches directly neighboring the airport. These $\sim$ 1.7 km of the total $\sim$ 11 km long coastline adjacent of the airport lie within a restricted no-fly-zone. The drones captured the accessible coast in 15 tiles, which were used throughout all three campaigns. The drones contain a built-in global navigation satellite system (GNSS) with regular GNSS precision of 2–5 m (Wing et al., 2005). This information serves as first estimation of camera locations in a geodetic reference system for the photogrammetric reconstruction of the beach. Ground control point (GCP) measured with survey grade GNSS devices improve the positioning of the final digital elevation model (DEM) in the geodetic system. Post-processing of the first two campaigns revealed a sub-par precision for the base stations of each tile in World Geodetic System 1984 (WGS84). With the base station's default survey-in time of 15 min, the vertical precision of the position was in the range of 3–7 m vertically, even though the real-time kinematic (RTK) accuracy

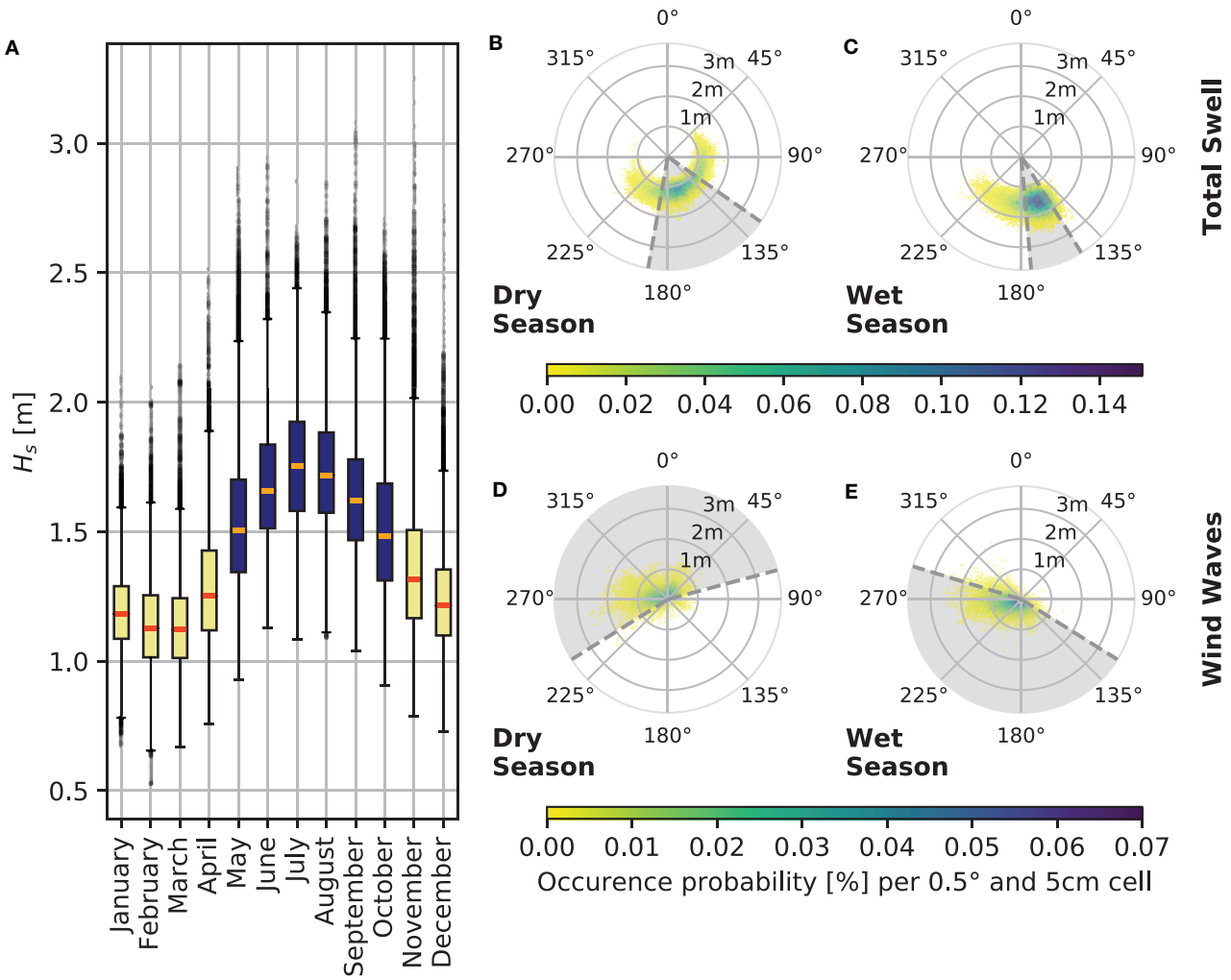

FIGURE 2 | Wave climate at the ERA5 data node (**Figure 1**) **(A)** Shows monthly box plots of hourly significant wave height H_s for a time series from 1979 to 2019. Here, blue boxes are wet season months and yellow boxes are dry season months. **(B)** Shows the discrete marginal distribution between the peak wave direction θ_p and the significant wave height H_s of the dry season, while **(C)** contains this information for the wet season. Both plots use only swell data, while **(D,E)** contain the same information for wind waves. Here, the colorbar shows the occurrence probability of each 0.5° wave direction and 0.05 m wave height cell. The gray areas visualize the significant peak direction range $\theta_{p,sig}$ for each subset, containing the directions which combined have the highest 33% occurrence probability.

of each measured tile remained within centimeter precision (equipment: Trimble 4700 and 5700 receiver, Zephyr and 13″ GPS antennas). To improve the initial positioning, the third campaign included a constant reference measurement combining a Javad Legacy GNSS base station receiver with a NAVX-3G antenna mounted on a roof. The rover consisted of a Septentrio AsteRx-U receiver and another NAVX-3G antenna, recording between 13 and 26 GCP per tile. The GCP measurements were corrected with the signal of the reference point by RTKLIB 2.4.3 b31 (RRID:SCR_018116). The aerial images and the GCPs of the third campaign were then post-processed in Agisoft Photoscan 1.4.5 build 7354 (RRID:SCR_018120) to DEMs of each tile. The DEMs have a resolution of 3.6 cm px^{-1}. Combining both the GNSS deviation and the software estimation by Photoscan, the DEMs have a total median positioning error of $\tilde{\sigma}_{DEM,3} = \pm 6.2$ cm (see **Supplementary Material**). The DEM-tiles of the third campaign then served as reference tiles for the DEMs of the other campaigns: extracting the position of unique features from each tile (for example man-made or reef structures) delivered virtual Ground Control Point (vGCP). These vGCPs were then used to correct the positions of DEMs obtained from the first two campaigns. The median relative error between the DEMs of the dry season 2019 (reference) and 2017 is $\tilde{\sigma}_{vGCP} = \pm 12.7$ cm. Between the DEMs of the dry season 2019 and wet season 2017, the median relative error is $\tilde{\sigma}_{vGCP} = \pm 13.6$ cm. The error of both GCPs and vGCPs is within the usual error range for UAV-borne photogrammetry (Casella et al., 2020).

2.5. Sediment Budgets

In the next processing step, Quantum GIS (version 3.4.11.) uses the rastered topography provided by Photoscan to calculate the

seasonal or annual changes of the coastal topography with

$$\Delta\mathrm{DEM}_{\mathrm{seasonal}} = \mathrm{DEM}_{\mathrm{wet\ season,\ 2017}} - \mathrm{DEM}_{\mathrm{dry\ season,\ 2017}} \quad (1)$$

and

$$\Delta\mathrm{DEM}_{\mathrm{interannual}} = \mathrm{DEM}_{\mathrm{dry\ season,\ 2019}} - \mathrm{DEM}_{\mathrm{dry\ season,\ 2017}} \quad (2)$$

resulting in a difference of topographic height $\Delta z_{i,j}$ for each pixel of the rastered DEM. All further post-processing (**Figure 3**) was performed with the Python module Rasterio (version 1.1.1): The total volume change in each of the ΔDEM is calculated with

$$\Delta V_{\mathrm{DEM}} = \sum_{i=1,j=1}^{i_{max},j_{max}} \Delta z_{i,j} \cdot A_{\mathrm{pixel}} \quad (3)$$

using the area A_{pixel} covered by each pixel in the raster image of each DEM and the associated $\Delta z_{i,j}$ at the pixel's position i and j within the DEM. Because the accuracy of submerged topography tends to be poor (Casella et al., 2016), wet areas were cropped from the DEMs. This results in morphological cells, dividing Fuvahmulah's coastline subsequently into 12.5 m wide sections ranging over the entire dry length of the beach (see **Figure 3B**). The dry beach length does not differ significantly between seasons—except for the northern part of Fuvahmulah. To account for varying beach lengths and to compare the sediment volumes independently of dry beach length, this study assesses the volume change of each morphological cell ΔV_{mc} over it's dry beach area A_{mc} in terms of areal sediment difference Δv_{mc} (**Figure 3**):

$$\Delta v_{\mathrm{mc}} = \frac{\Delta V_{\mathrm{mc}}}{A_{\mathrm{mc}}} \quad (4)$$

here, ΔV_{mc} equals to ΔV_{DEM} but only within the boundaries of the morphological cell (index mc). Summarizing the areal sediment volumes of each morphological cell for the entire island with the absolute areal sediment difference quantifies the morphodynamic activity and gives an estimate on the average shoreline change (index sc):

$$\overline{v}_{\mathrm{sc}} = \frac{1}{m} \cdot \sum_{m=1}^{m} \left| \frac{\Delta V_{\mathrm{mc}}}{A_{\mathrm{mc}}} \right| \quad (5)$$

Another classification of seasonal shoreline change is the island oscillation index I_o (Kench and Brander, 2006). It looks at areas which are subject to $\geq$ 50 % of the maximum shoreline change and relates them to the entire island perimeter. The results give information on the seasonal morphological activity on an island and classify specific characteristics: A high oscillation index implies coastline changes around the entire island between the seasons. Small oscillation indices indicate changes predominantly around a hotspot. Low oscillation indices are typically found on elliptical islands and indicate that large parts of the shoreline are meant to be morphologically stable (Kench and Brander, 2006), if not obstructed by coastal infrastructure (Kench, 2012). This study modifies the approach of Kench and Brander (2006) and uses the average seasonal and annual sediment difference as the volumetric change per area (**Figure 4** and Equation 4) to calculate I_o. Areas that were especially challenging to align and geo-reference in the photogrammetric process, or which were inaccessible due to no-fly-zones, are not taken into account in the sediment budget (**Figure 3**).

Obtaining total sand volumes on beaches with high seasonal differences in beach widths require interpolating the reef height between the base of the wider beach profile and the base of the plain beach (the base of a beach is also called beach toe). The location of the beach toe was derived from orthophotos at low-tide. Interpolation was done for Geiymiskih beach in the north and northwest of Fuvahmulah (**Figure 4**, profile 1). In addition, the Thoondu sand spit forms in the wet season. The wet season associated with higher waves and thus higher run-up, hampering a full reconstruction of the beach face. Therefore, the wet season Thoondu beach is interpolated between the beach crest and the beach toe (**Figure 4**, profile 2). Here, the geodetic height of the reef at the beach base was interpolated from the georeferenced 2019 measurements of the adjacent beach on the east (**Figure 4**, profile 3), where it is at $\sim$ −94.8 m. All interpolations have been done with the interpolation sub-package in SciPy version 1.3.3 (RRID:SCR_008058 under Python version 3.7.3 RRID:SCR_008394). Calculating total sand volumes on dry season beaches at Thoondu leads to further challenges (**Figure 4**, profile 3): On the one hand, large areas of the reef were covered with sand in the dry season, making vGCP assignment on the sea-side of the beach impossible. On the other hand, the land-side is densely vegetated, so that DEMs contain areas with either poor or without referencing. To overcome these challenges, six beach profiles support the estimation of sand volumes on the dry season Thoondu beach. The profiles have been manually referenced to the plain beach in wet season.

Bio-erosion at neighboring islands was assessed as $G_{\mathrm{sed}} = 3.4 \pm 0.4\,\mathrm{kg\,CaCO_3\,m^{-2}\,yr^{-1}}$ (Ryan et al., 2019). This study acknowledges the difference between gross and net carbonate production and bio-erosion (Chave et al., 1972), but in the following, *sediment production* refers to the bio-eroded marine aggregates of the reef, available to be transported toward the island. The corresponding reef area A_{reef} of the Gnaviyani Atoll is 499.2 ha and originates from shape files for the Maldives, provided by ©OpenStreetMap contributors. Combining the annual areal carbonate production rate with the reef platform gives the total annual estimate of sediment volume produced on the reef as

$$Q_{\mathrm{reef}} = \frac{G_{\mathrm{Sed}}}{\rho_{\mathrm{s}}} \cdot A_{\mathrm{reef}} \quad (6)$$

with a measured sediment density of $\rho_{\mathrm{s}} = 2\,\mathrm{g\,cm^{-3}}$.

2.6. Sediment Transport

The CERC-formulation or Shore Protection Manual (SPM)-method for longshore sediment transport (CERC, 1984) uses the longshore component of wave power as longshore wave energy flux

$$P_{y,wp} = c_b \cdot \frac{1}{8} \cdot \rho \cdot g \cdot H_{b,wp}^2 \cdot \frac{1}{2}\sin(2\theta_{b,\perp,wp}) \quad (7)$$

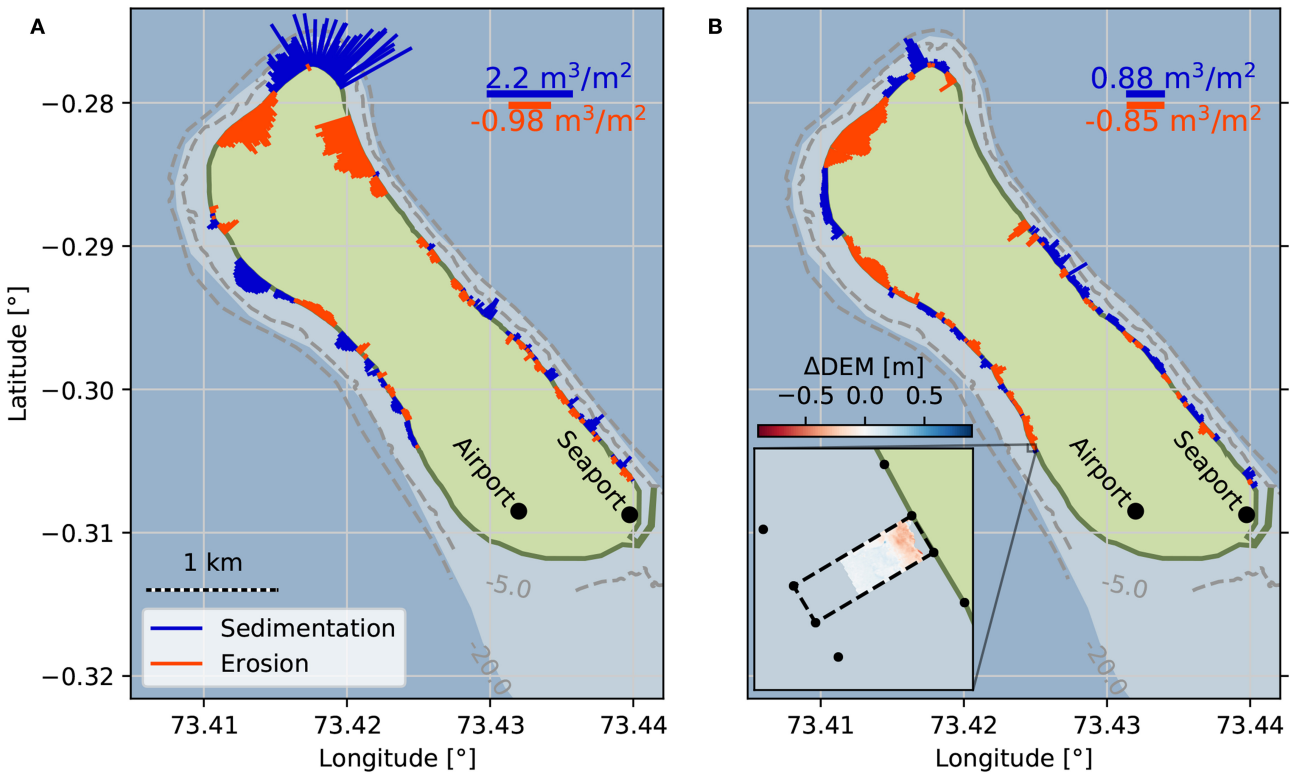

FIGURE 3 | Average areal sediment budgets from DEMs with **(A)** seasonal sediment budget from dry to wet season, based on the data of March 2017 and September 2017 and **(B)** annual sediment budget between dry season 2017 and 2019 (both recorded in March). In both subfigures, sediment accumulation for the observation period is blue, while sediment removal is red. The volumetric change of sediment [m^3] is averaged over dry beach area [m^2] (see Equation 4). Bathymetry lines (gray, dashed) come from measurements in the first field campaign (March 2017).

with c_b as the wave phase velocity, wave height $H_{b,wp}$ and incident wave angle $\theta_{b,\perp,wp}$ for each wave partition wp at the breaker point b, as well as the water density ρ and the gravitation constant $g = 9.81\,\mathrm{m\,s^{-1}}$. The shear stress of the wave-averaged transport momentum S_{xy} is the longshore transport component when considering $\theta_{b,\perp}$ with respect to beach orientation. The longshore transport component S_{xy} does not vary outside the breaker zone, so that $P = S_{xy,b} \cdot c_b = S_{xy,0} \cdot c_b$, with index 0 for deep water waves (Longuet-Higgins, 1970; Bosboom and Stive, 2015). Converting Equation (7) to deep water parameters with $n_0 = 1/2$ yields:

$$P_{y,wp} = \frac{c_b}{16} \cdot \rho \cdot g \cdot H_{0,wp}^2 \cdot \sin(2\theta_{0,\perp,wp}) \cdot n_0 \tag{8}$$

From linear wave theory, the wave velocity at the breaking point is $c_b = c_0 \cdot \tanh(k \cdot h_b)$ using the water depth of breaking waves h_b and ERA5 wave periods to calculate c_0. The echo-sounder usually recorded depths of around $h_b \approx 4.5\,\mathrm{m}$ where the boat was able to measure close to the breaker line. Further input values for incident waves are the significant wave height $H_{s,wp}$ for $H_{0,wp}$ and peak wave directions $\theta_{p,wp}$ from the ERA5 data set for each wave partition wp. With respect to the coastline normal, the incident angle from θ_p is $\theta_{0,\perp} = \theta_p - \alpha_\perp$, where the coastline normal is $\alpha_\perp$. The incident wave direction $\theta_{0,\perp}$ ranges from -90 to $90°$ with regard of the coastline normal. Values beyond this range are not considered in Equation (8). On the other hand, with $\sin(2 \cdot \theta_{0,\perp})$, oblique waves approaching the coastline normal from $\alpha_\perp = \pm 45°$ will have the greatest impact on longshore sediment transport, while waves from $\alpha_\perp = \pm 90°$ or $\alpha_\perp = 0$ will have no influence on it. The CERC-equation assumes the wave energy flux P_y being the forcing parameter behind changing beach morphology. When considering the local wave angle $\theta_{0,\perp}$ in Equation (8), the wave energy flux P_y already gives information on the expected morphodynamic response of the beach (Rutten et al., 2017). But the CERC-formulation combines the longshore energy flux (Equation 8) with sediment parameters as the *"immersed weight of sand moved"* (CERC, 1984) to translate it into volumetric sediment transport rates:

$$I_{y,wp} = \frac{K}{\rho \cdot g \cdot (\rho_s - \rho_w) \cdot (1 - \Phi)} \tag{9}$$

here with salt water density ρ_w of $1.03\,\mathrm{g\,cm^{-3}}$, sediment density ρ_s of $2\,\mathrm{g\,cm^{-3}}$, a porosity Φ of 0.2, and an empirical coefficient K. Combined, the CERC formulation reads:

$$q_{y,wp} = P_{y,wp} \cdot I_{y,wp} = \frac{K \cdot c_b}{32 \cdot (\rho_s - \rho_w) \cdot (1 - \Phi)} \cdot H_{0,wp}^2 \cdot \sin(2\theta_{0,\perp,wp}) \tag{10}$$

The empirical coefficient K is the transmission between wave-induced energy flux and sediment parameters. It accounts for the heterogeneity of beach sediments and the local coastal environments. The coefficient translates the wave energy impact on site into the site-specific sediment motion by calibration with measured data (Schoonees and Theron, 1995). In this study, K facilitates matching the measured with the calculated total sediment volume of the field campaigns in 2019. Using the CERC-formulation, the total sediment volume transported on a coast for all wave partitions is

$$Q_y = \sum_{wp=wp_{ww}}^{wp_{S3}} q_{y,wp} \tag{11}$$

with wp_{ww} for wind waves and wp_{Si} for swell waves with i for each of the three swell partitions of the ERA5 data set. With the sediment volumes measured in the 2019 dry season field campaign for the northwest (NW: 14.689 m^3) and east coast (E: 1.171 m^3), the empirical coefficient K becomes $K_{NW} = 55.89$ and $K_E = 107.26$.

When illustrating results from the CERC method based on the hourly ERA5 data between January 2016 and November 2019, this study smooths the data with a combined windowed forward and backward average filter based on

$$\overline{H_s} = \frac{1}{2}\left(\frac{1}{n}\sum_{i=0}^{n-1} H_{s-i} + \frac{1}{n}\sum_{i=0}^{n+1} H_{s+i}\right) \tag{12}$$

with a window of $n = 24\,\mathrm{h} \cdot 7\,\mathrm{d}$. Filtering was applied on H_s (depicted in Equation 12), θ_p, q_y, and Q_y (analogous to Equation 12). Smoothing accounts for a delayed response of the morphology to wave energy forcing (Rutten et al., 2017).

2.7. Modeling

This study also uses the wave data from ECMWF's global reanalysis model ERA5 as boundary condition in the phase-resolving, depth-integrated Boussinesq Ocean and Surf Zone model (BOSZ). The governing equations of BOSZ fall into the category of Boussinesq-type equations—an approximation of the Navier-Stokes equations commonly used for studies of coastal areas (Roeber et al., 2010; Roeber and Cheung, 2012). These governing equations compute dispersion accurately for water depths up to $kh \approx \pi$, with k as wave number and h the water depth (David et al., 2017). For deep waters of $kh > \pi (k = 2\pi/L)$ BOSZ starts overestimating the wavelength (L) increasingly. Previously, the numerical model has been used for example in modeling cascades to compute wave transformation and associated impacts over irregular bathymetries, such as reefs (Roeber and Bricker, 2015) and to study shorter, more non-linear wave phenomena (David et al., 2017). BOSZ uses an adaptive wetting and drying algorithm and has shown good results when benchmarked with laboratory and field data of different scenarios (Horrillo et al., 2014; Lynett et al., 2017).

In this study, the model uses the off-shore ERA5 wave data to compute wave propagation and transformation from deeper to shallow waters, leading to wave-induced currents on the reef surrounding Fuvahmulah. The reef's bathymetry originates from echo-sounder measurements recording data until a maximum depth of about 45 m. The minimum water depth from the echo-sounder depends on the required under keel clearance of the boat, being at water depths of about 4 m. As complement to the bathymetry, the DEMs (wet season, 2017) supply topographic information on the coastal and intertidal areas of the reef. The reef topography's elevation data starts approximately at around mean low tide. The Generic Mapping Tool (GMT) combines the bathymetric and topographic data, projecting it onto a computation grid with 876 × 1,274 cells and a $\Delta x, \Delta y = 7.5$ m resolution (Wessel and Luis, 2017). Off shore waters are limited to 60 m depth to maintain an effective dispersion accuracy for the governing Boussinesq-type equations. The model contains a hydrodynamic framework, providing for example water level elevation and wave-induced currents on the reef in form of depth-averaged flow velocities (for a snapshot of the free surface elevation provided by BOSZ see **Supplementary Material**). The resulting, two-dimensional velocity fields are the main drivers behind sediment transport on the beach (van Rijn, 2005), revealing areas of sediment pick-up at increased, and accretion areas at reduced velocity gradients. On Fuvahmulah, ocean circulation and tidal currents are significantly lower than those of wave-induced currents (David et al., 2019) and, in general, are of minor importance when modeling longshore sediment transport (Burcharth et al., 2007). Therefore, this study accounts for currents induced by waves from the dominant wave direction $\theta_p = 157.5 \pm 22.5°$, in a TMA-spectrum with a significant wave height $H_s = 2.3$ m, and peak period of $T_p = 17$ s over a bathymetry with constant Manning's friction of $n = 0.013\,\mathrm{s\,m^{1/3}}$. The friction parameter was chosen in accordance to another study with the same model over coral reefs (Roeber and Bricker, 2015).

3. RESULTS

3.1. Wave Climate and Tidal Regime

Fuvahmulah has two seasons: the wet or rainy season from May to October and the dry season from November to April. Between the wet and the dry season, waves differ in height as shown by the ERA5 data set (C3S, 2017) of the ECMWF (**Figure 2**). While the dry season brings northeastern winds, Fuvahmulah is subject to mainly south to southwestern Monsoons in the wet season (MEE, 2014). The Monsoons are accompanied by high waves with the highest median significant wave height in July ($\tilde{H}_{s,\mathrm{max.}} = 1.72$ m), while the highest total significant wave height was registered on November, 5th 2016 ($H_{s,\mathrm{max.}} = 3.25$ m). While this study defines November already as dry season, the wave data discloses a transition phase between wet and dry season. The lowest annual median value $\tilde{H}_{s,\mathrm{min.}} = 1.12$ m appears in March (dry season).

Observations of the wave climate during the field campaign have shown that waves approach the island from multiple directions at the same time. This is important for the further analysis and significant for the coast as well as coastal structures, because it reveals the need for multi-directional data. To analyze the multi-directional wave climate, the ERA5 data set provides hourly wave parameters, such as significant wave height H_s and

TABLE 1 | Wave parameters for the time series at the ERA5 data node (**Figure 1**).

	Dry season		Wet season	
	$\overline{H}_s$	$\theta_{p,sig}$	$\overline{H}_s$	$\theta_{p,sig}$
Swell waves	1.17 ± 0.18 m	125–190° (SE-E)	1.60 ± 0.26 m	148–175° (SE-E)
Wind waves	0.26 ± 0.28 m	238–75° (SW-E)	0.26 ± 0.28 m	122–287° (SE-W)

*The table contains the mean significant wave heights H_s as well as significant peak direction ranges $\theta_{p,sig}$ (**Figure 2**) for wind waves and swell approaching Fuvahmulah.*

peak wave direction θ_p for both wind waves and swell partitions for ocean waves from 1979 to 2019 (C3S, 2017). These parameters are used to describe the dominant features of wave heights, periods and directions:

Around Fuvahmulah, total swell has a higher seasonal variation of H_s but less spreading or directional variety of associated peak wave directions θ_p than wind waves (**Figure 2** and **Table 1**) Swell waves are rarely below 1 m in the wet season (**Figure 2**. The dominant peak direction $\theta_{p,ts}$ are coming from south to southwest in both seasons, however the dry season contains additional directional components between ∼45 and 135°, which are absent in the wet season.

Wind waves have a mean significant height of $\overline{H}_{s,\mathrm{ww}} = 0.26 \pm 0.28$ m (in both seasons, **Figure 2** and **Table 1**). The highest wind waves approach the island from west. The two significant differences among seasonal wind waves are (a) in the dry season waves reach Fuvahmulah dominantly between 238 and 75° while they approach the island with 122–287° in the wet season and (b) an additional north to west (0–90°) component in the dry season being absent in the wet season. Both differences have a considerable influence on the sediment transport in the northern part of the island and the sand spit Thoondu.

Summing up the above, the wave climate around Fuvahmulah is characterized by dominant southerly swells with noticeably higher waves in the wet season than in the dry season. The main swell direction $\theta_p \sim 157.5 \pm 22.5°$ is similar to the orientation of the large southeastern reef. Both seasons occasionally experience (wind) waves from west, however the dry season has a much higher angular spreading for both wave components. The dry season has an additional swell component from northeast to southeast and a wind-wave component coming from northern to eastern directions. These components are absent in the wet season. Analyzing the hindcast wave data reveals the difference between seasons: Monthly time series of wave heights from 1979 to 2019 show a gradual transition between wet and dry seasons without a fixed date explicitly terminating a season (**Figure 2**). Dominant south to southeastern swells and increased wave heights in the wet season define the characteristic hydrodynamic regime for the Maldives (Kench and Brander, 2006; Kench and Mann, 2017).

3.2. Sediment Budget From Measurements

The Gnaviyani Atoll has a size of 992.3 ha and consists of the island Fuvahmulah, covering an area of 493.1 ha, and the fringing reef with 499.2 ha. The coral reef is the natural sediment source for the island with an estimated annual sediment production rate of $3.4 \pm 0.4\,\mathrm{kg\,CaCO_3\,m^{-2}\,yr^{-1}}$ (Ryan et al., 2019), leading to a total sediment supply by the reef of $Q_{\mathrm{reef}} = 8,486 \pm 998\,\mathrm{m^3\,yr^{-1}}$. The total carbonate production rate of the reef depends on the eco-geomorphological zones on the reef platform. These zones are subject to different light availability, wave energy and degree of turbidity. Carbonate production is also affected by anthropogenic, natural and climate stressors that change the water quality and temperature (Hamylton et al., 2017; Ryan et al., 2019). The Gnaviyani Atoll reef is mostly sub-tidal with an inter-tidal reef-flat around Fuvahmulah. The sub-tidal reef fringes the inter-tidal plateau before it expands to an about ∼ 2.2 km long and 1.6–0.5 km wide fore reef in the south east. This southern fore reef makes about 58.8 % of the total reef area. At the southeastern tip of the fore reef, the depth is ∼ 25 m and slowly decreases to around 8–15 m until reaching the inter-tidal reef. The reef form is elliptical with the long axis approximate to the dominant swell wave direction $\theta_p \sim 157.5°$. The transition from sub-tidal fore reef to intertidal reef on the south and west side is sudden, while it is more gradual on the north and east side of Fuvahmulah. The inter-tidal reef is wider on the south and west side (around 85–145 m) than on the north and east side (around 15–25 m).

The sandy western beaches have mildly sloping equilibrium beach profiles, while the eastern beach profiles change from south to north: Long parts of the southern east coast suffer from noticeable erosion introduced after the port construction at the southeastern end of Fuvahmulah (David et al., 2019). The northern part of the east side (Thoondu) as well as the north coast is part of a highly morphodynamically active region (**Figure 3**). This region hosts coarse calcareous sediment to fine pebble stones. The beaches west and south of the airport (in the south and southwest of the island) consists of steep pebble stone beach profiles, which become sandy in front of the port breakwater (south). This sandy accumulation on the sea side of the western port breakwater and in front of the airport runway is blocked by the port infrastructure (Naeem, 2006; David et al., 2019).

3.2.1. Morphodynamic Activity and Seasonal Formation of the Thoondu Spit From Field Data

The island oscillation index I_o describes the morphodynamic activity of an entire island by comparing the island's perimeter with the coastal area encompassing more than half of the maximum (seasonal) coastline change. The coastline change is linked to the beaches' volumetric changes and—in this study—estimated by integrating seasonal and interannual sediment differences over 12.5 m wide areal increments of Fuvahmulah's coast. The underlying sediment differences required for this procedure originate from the DEMs of the UAV surveys.

Averaging these seasonal and interannual mean shoreline changes discloses a higher seasonal than interannual morphodynamic activity. This results from the seasonal mean shoreline change between the 2017 dry and wet season ($\overline{v}_{\mathrm{sc}} = 0.33\,\mathrm{m^3/m^2}$), being greater than the interannual mean shoreline changes between 2017 and 2019 ($\overline{v}_{\mathrm{sc}} = 0.15\,\mathrm{m^3/m^2}$). But shoreline changes in most coastal areas are below these mean

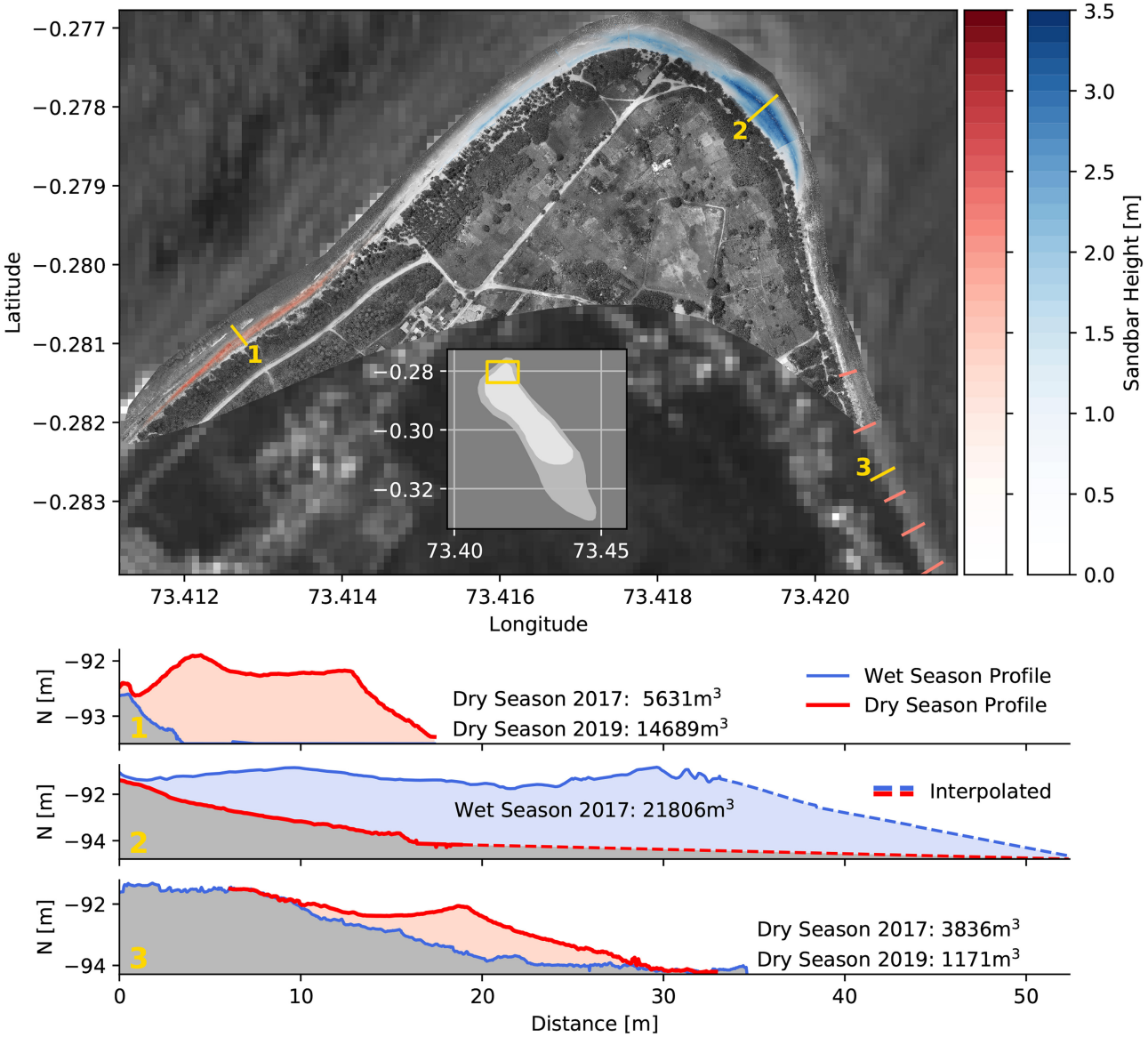

FIGURE 4 | Location of sediment volumes and profiles (orange lines) for the dry season 2017 (red colorbar) and wet season 2017 (blue colorbar) in the north of Fuvahmulah. In the dry season sand depots form at the adjacent beaches Geiymiskih Fannu in the west (profile 1) and Thoondu in the east (profile 3) of the headland. The wet season allocates sand on the north tip of the island, forming the Thoondu sand pit (profile 2). The dry season sand volume of eastern Thoondu beach (profile 3) was integrated over differences of six accuracy-improved profiles. The profile elevation *N* is given as distance to the WGS84 ellipsoid. The background satellite image contains Copernicus Sentinel data (true color, red green blue) from September 14, 2017, which is in the wet season.

values—except for the northern headland. The northern headland is Fuvahmulah's prominent morphodynamic area, but covers only a small fraction of the island's perimeter (**Figure 3**).

Using this information for the island oscillation index leads to a low I_o of $I_o = 350° - 315°/360° = 9.7\,\%$. Such low oscillation indices on elliptical islands indicate that the elongated, lateral shorelines are meant to be morphologically stable (Kench and Brander, 2006) if not obstructed by artificial interference (Kench, 2012), for example harbors, jetties or breakwaters.

Focusing on the prominent morphodynamic area in the north of Fuvahmulah discloses the seasonal formation of the Thoondu spit:

When describing the sheer amount of sediment allocation and (re-)distribution on the northern beaches from experiences and by visual inspection, beaches with a low-lying rocky bottom material in one season can be covered by meter high bulk sediment in the other season. The associated UAV measurements and DEMs reveal two distinct depots in the dry season 2017: The depot on the west side of the headland has a net volume of 5.631 m^3 and is called Geiymiskih Fannu (red area on the

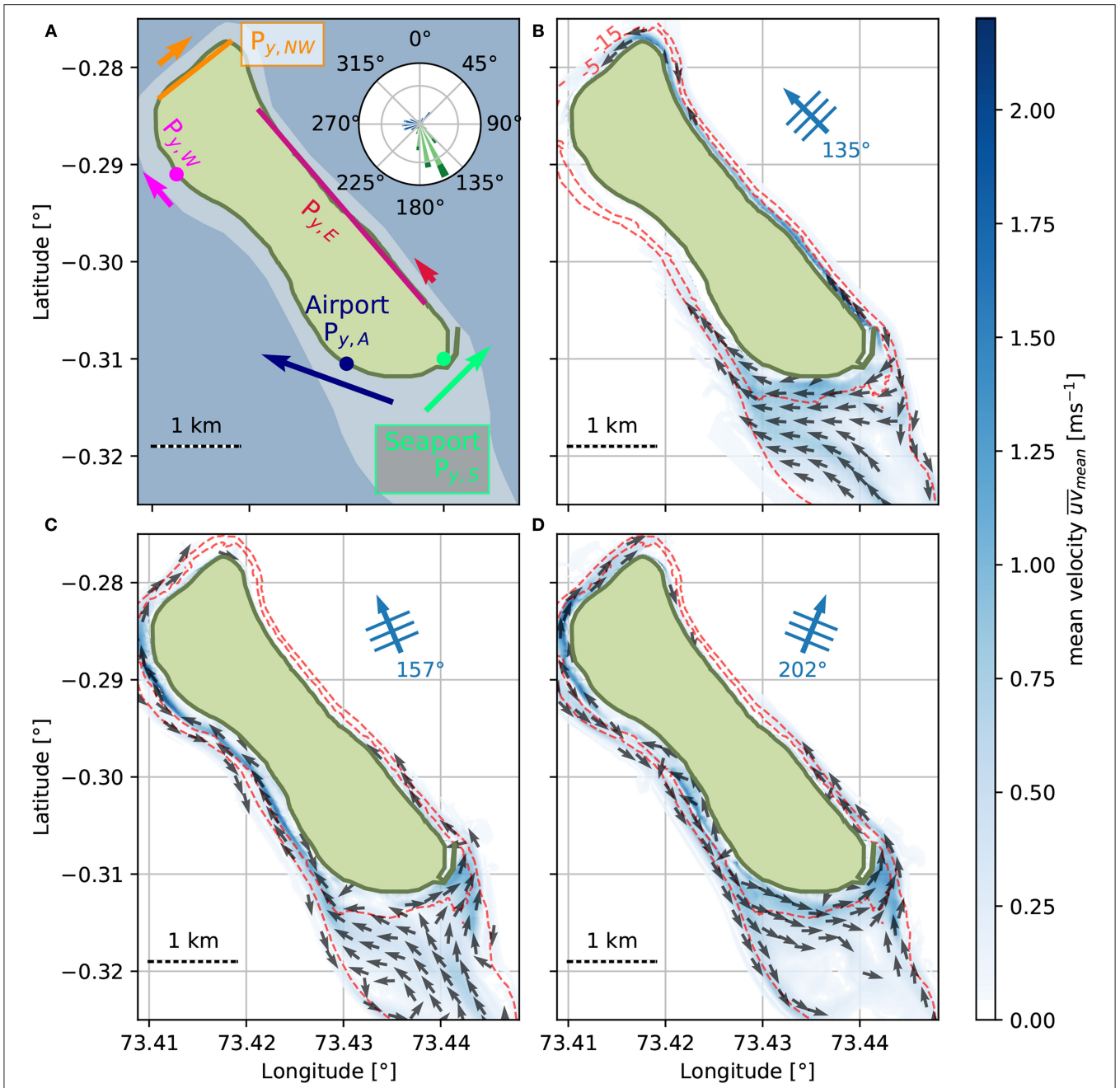

FIGURE 5 | (A) Longshore energy flux rates P_y between 2016 to 2019 indicating sediment transport direction and potential in the CERC-formulation for incoming waves between 2016 and 2019. The wave rose separates annual wind waves (blue) from swell (green). The resulting sediment transport direction is shown in front of the air- and seaport as well as for the beaches on the north and east side. The arrow lengths are in proportion to P_y calculated at each location (values in **Table 2**). **(B)** Current velocities from the depth-averaged, phase resolving numerical wave model (BOSZ) for waves approaching the island from $\theta_p = 135°$, **(C)** $\theta_p = 157.5°$ and **(D)** $\theta_p = 202°$. The background color shows the magnitude of wave induced current velocity on the reef while the arrows depict the local current direction. Dashed red contour lines are the reef depths −5 and −15 m recorded in the first field campaign (March 2017).

map and cross section 1 in **Figure 4**). The depot on the east or southeast side of the headland has a volume of 3.868 m^3 and is part of Thoondu beach (red transects on the map and cross section 3 in **Figure 4**). In total, this makes a volume of 9.499 m^3 for the dry season 2017. Later in the wet season 2017, a large sediment depot with 21.806 m^3 net volume gradually forms on the northern tip of the headland—the Thoondu spit (blue area on the map and cross section 2 in **Figure 4**). The UAV-borne data of the two field campaigns in 2017 discloses a positive seasonal sediment balance. The instantaneous records do not contain the

TABLE 2 | Beach orientation as well as longshore sediment transport directions and energy flux rates P_y, i from the CERC-formulation (**Figures 5A**, **7**, **8**).

Index *i*	Coastline parallel (°)	Longshore transport direction (°)	Mean longshore energy flux $P_{y,i}$ ($\times 10^3$) (kW m^{-1} yr^{-1})
NW	231.6	+180	4.9
E	319.3	+0	0.9
S (Seaport)	45.0	+180	14.6
A (Airport)	110.0	+0	22.3
W	139.3	+180	7.4

The longshore transport directions are expressed with respect to the coastline parallel $\alpha_\perp$.

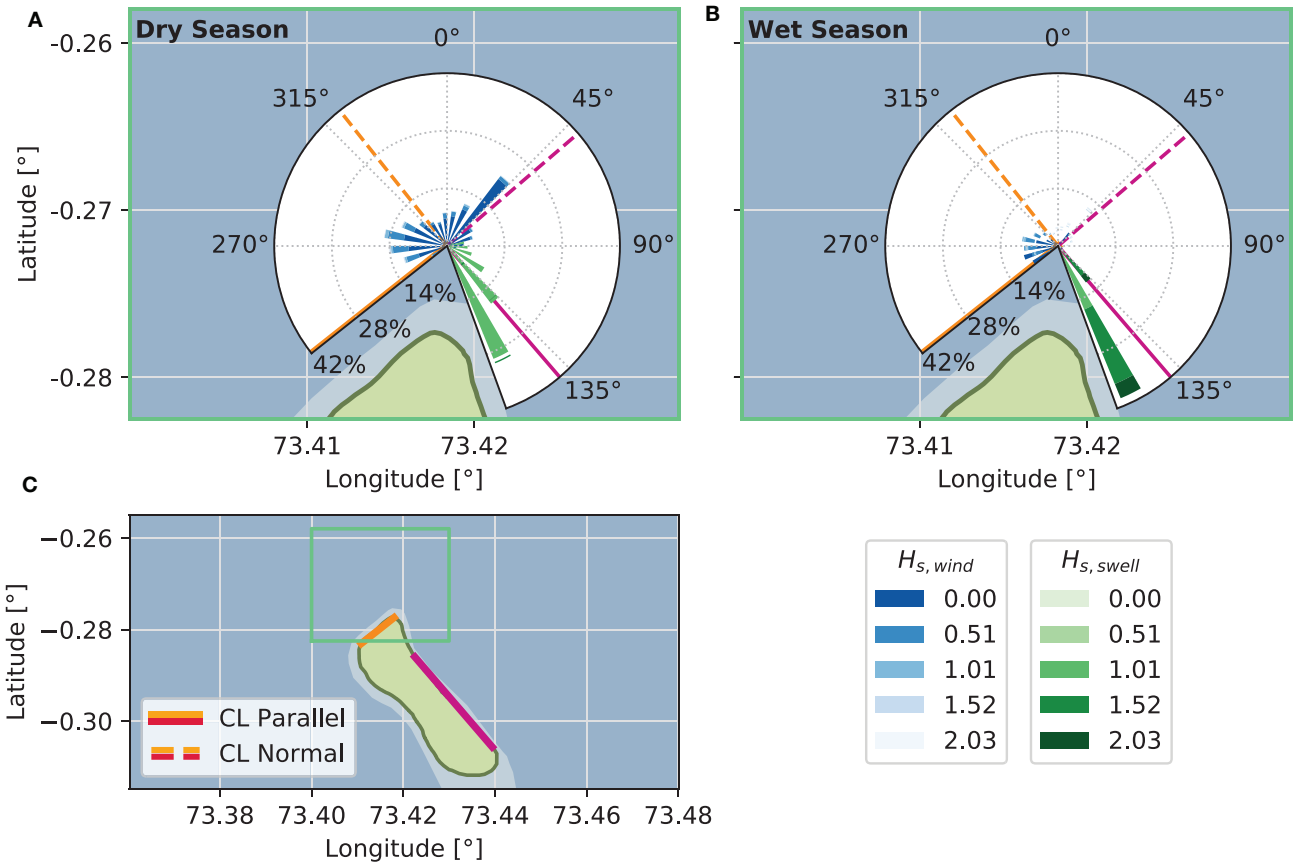

FIGURE 6 | Wave parameter input for the assessment of the evolution of the Thoondu sand spit with the CERC method for **(A)** the dry season and **(B)** the wet season. Blue and green bar plots are the wave rose for wind and swell waves. Orange and crimson lines in the wave roses mark the shoreline parallels (solid) and shoreline normals (dashed) of **(C)** the beaches Geiymiskih (orange, see also **Figure 7**) and Thoondu (crimson, see also **Figure 8**) adjacent to the northern headland.

maximum depot sizes, as the seasonal difference in sediment volume is +12.307 m^3. In the field campaign during the dry season of 2019, sediment depots formed at the same locations as in the dry season 2017. However, the depot in the west (Geiymiskih Fannu) was considerably larger when compared to 2017 (14.689 m^3), while the eastern depot was smaller (1.171 m^3, southeast Thoondu). In total, the sediment volume recorded in the dry season of 2019 is 15.860 m^3. This is an additional sediment volume of +6.361 m^3 over the dry season of 2017, while it is −5.946 m^3 less than in the wet season of 2017.

3.3. Sediment Transport From Models

In this study, two approaches help to study sediment distribution on the Gnaviyani Atoll (**Figure 5**): an empirical, process-based method—the CERC-equation—assesses the longshore transport processes, while the BOSZ model is a numerical approach to compute current pattern on the reef. For the coastlines around Fuvahmulah, the CERC-formulation (CERC, 1984) quantifies the expected longshore sediment transport rate q_y, wp as volume over time for each wave partition wp separately and also the total sediment volume Q_y transported between January 2016

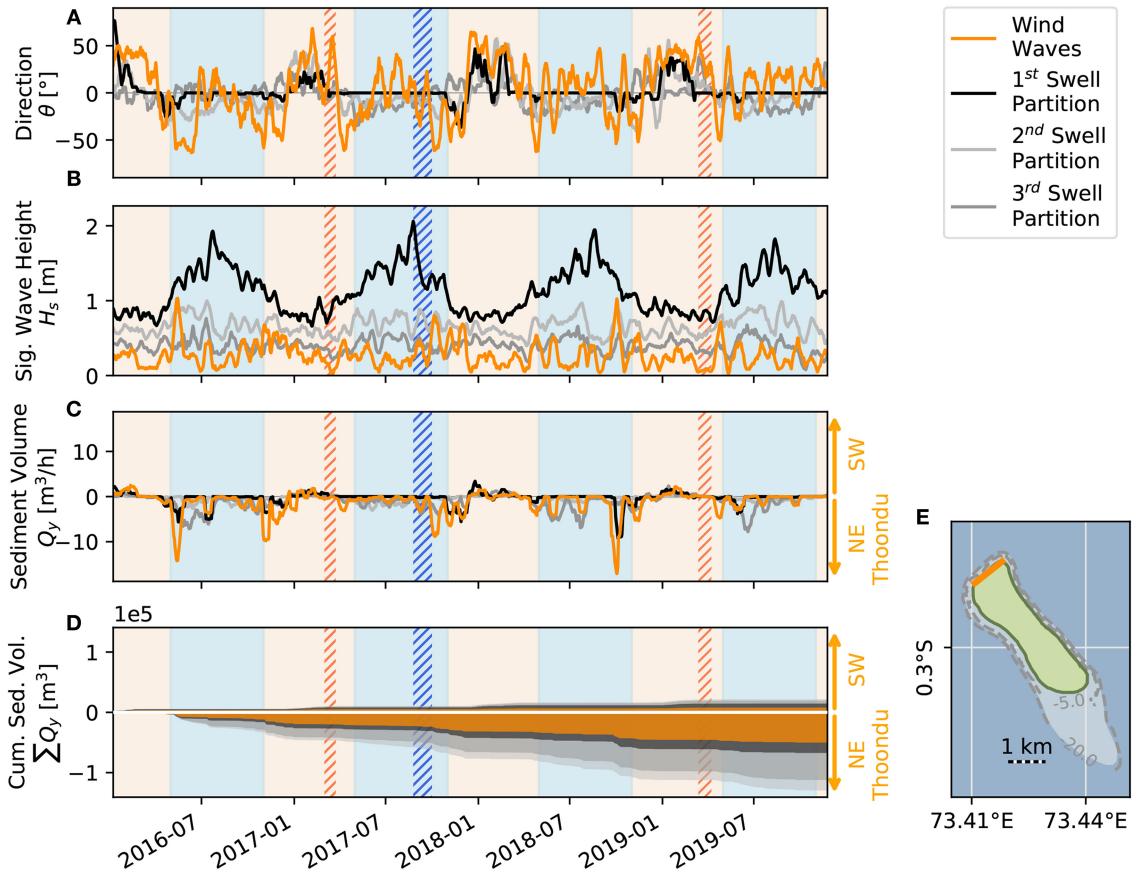

FIGURE 7 | (A) Averaged incident wave direction $\theta_{\perp,wp}$, measured as difference from the coastline normal $\alpha_{\perp}$ and **(B)** wave height $H_{s,wp}$ of each wave partition *wp* used for **(C)** longshore sediment transport rates $q_{y,wp}$ and **(D)** cumulative sediment volume $Q_{y,wp}$, transported alongshore the, marked with an orange line on the map in **(E)**. The orange line is accordance with the orange line in **Figure 6** (see **Table 3** for corresponding peak transport rate values $q_{y,max}$ and the contribution of each wave partition to Q_y). The time series shows values from January 2016 to November 2019. Positive values for $q_{y,wp}$ and $Q_{y,wp}$ indicate a transport toward southwest, while negative values lead to sediment transport toward Thoondu beach in the northeast. The time series shows the dry season with orange and the wet season with blue background. Field campaign 1 and 3 (orange hatched area) took place in March 2017 and 2019. Field campaign 2 (blue hatched area) was conducted in September 2017.

and December 2019. The numerical model depicts wave-induced currents for the dominant swell wave direction $\theta_p \sim 157°$ as well as the outer limits of the dominant swell range with 135 and 202°. The model resolves the wave interaction with the reef spatially (**Figure 2** and **Table 1**). In combination, the empirical and numerical methods can capture the spatio-temporal sediment transport over the reef.

3.3.1. Results From the Empirical Model

Considering the reef crest and reef flat as *carbonate factory for sediment supply to reef islands* (Ryan et al., 2019), the numerical model demonstrates that wave-induced currents transport sediment from the reef toward Fuvahmulah (**Figures 5B–D**). The CERC-formulation assesses longshore energy flux as driver for sediment transport rates around the island on five locations: the southern sea- and airport areas as well as the beaches on the west, northwest and east (**Figure 5A** and **Table 2**). Sediment transport splits on the southern beach into an eastern component at the seaport and a western component at the airport. The lateral beaches have a northward directed transport direction, where the CERC-equation estimates a 6.9 times larger energy transport potential on the west side when compared to the east side. Based on longshore energy fluxes, the longshore transport pattern from the CERC-formulation discloses sediment reaching the island from the southeastern reef plateau will primarily be distributed over the west side. According to the CERC-equation, sediment transport over the east side up to the northeastern headland is of minor significance. The numerical model confirms the general distribution pattern revealed by the CERC-formulation for the dominant swell components (**Figures 5B–D**). It shows that the currents flow around the southern coast and toward the north, where the Thoondu spit forms in the wet season (**Figure 4**) and hints at higher current velocities on the west side from the dominant swell wave direction $\theta_p \sim 157.5°$ (**Figure 5C**).

The beaches of the northern headland are the island's lee side. This area is sheltered against the dominant southern swells and only experiences swell impact through diffraction

and refraction occasionally—the numerical model shows the influence of dominant southern or southeastern swells, leading to currents on the northern beaches Geiymiskih Fannu and Thoondu (**Figures 5B–D**). Suspended sediment entrained in currents is swept along and transported along the west coast toward the north. There, it deposits in areas with mitigated current velocities, as seen in the dry season (**Figure 4**). While being sheltered from the dominant swell waves, data from the wave rose shows that the north coasts of Fuvahmulah dominantly experience wind waves (**Figure 6**). Wind wave induced currents lead to further sediment transport, as shown by the CERC-formulation. The CERC-equation gives further insights in the temporal scale of sediment transport on the northern beaches and facilitates assessing the intraannual evolution of the Thoondu spit (**Figure 4**). It only utilizes waves approaching the coastline normal at $\theta_{\perp} \pm 90°$, excluding swell waves approaching the island from the south (**Figure 6**):

The coastline parallel of the north coast (Geiymiskih beach) is at 231.6°, while the coastline normal is at 319.3° (**Figure 6**, **Table 2**). The combination of wave angle and height defines the amount of sediment longshore transport, peaking at $\theta_{\perp} \pm 45°$ with $\sin(2 \cdot \theta)$ in equation 10. Therefore, longshore transport rates commonly peak at the end of the wet season, with high waves and incident angles of $\theta_{\perp} \sim -50°$ (**Figure 7**). Even though swell waves are dominant around Fuvahmulah, in the CERC-formulation the main share of total longshore sediment transport comes from wind waves (36.8 %) and the second swell partition (33.8 %, **Table 3**). They appear in the wet season or in the transition between dry and wet season. Regarding the CERC-equation's longshore transport direction, only 13.6 % of the sediment longshore rate is toward the south west, while 86.4 % is toward Thoondu beach in the north east. Occasional, single events yield the highest longshore sediment transport rates on Geiymiskih beach (**Figure 7C**).

The coastline parallel of the eastern beach feeding the Thoondu spit is at 319.3°, while the coastline normal is at 49.3° (**Figure 6**, **Table 2**). Significant wave heights are from the same data base as those used at the adjacent Geiymiskih beach (**Figure 7**). Thoondu and the east side of Fuvahmulah are subject to swell waves from the south east, as well as wind waves from north west to north east (**Figures 6**, **8**)—but in contrast to Geiymiskih beach, wind waves have a small overall contribution to the total sediment transport when calculated with the CERC-equation for the east side (17.7 %). Nevertheless, Thoondu beach is prone to receive some of the dominant southeastern swell waves with $\theta_p = 135° - 180°$. However, with respect to the coastline parallel, dominant swell waves approach the beach only with $\theta_{\perp} \leq 9°$, resulting in a low contribution in the CERC-formulation. Instead, occasional first partition swell wave events trigger longshore sediment transport in the CERC-equation, followed by second partition swell waves (**Figure 8** and **Table 3**). The resulting dominant longshore sediment transport direction is toward Thoondu beach (67.9 %). The dominant sediment transport toward Thoondu is commonly found in the course of the wet season, usually peaking between July and early September. Southward components only appear in dry season.

TABLE 3 | Peak transport rates $q_{y,max}$ and the contribution of each wave partition to the total transported sediment volume Q_y in the CERC-formulation between 2016 and 2019 on the northern beaches Geiymiskih and Thoondu (NW: **Figure 7** and E: **Figure 8**).

Beach index *i*	Wave partition index *wp*	Peak sediment transport rate $q_{y,i,max.}$ ($m^3\ h^{-1}$)	Contribution to total transport volume Q_y (%)
NW	Wind waves	17.08	36.8
	1st swell partition	9.31	16.1
	2nd swell partition	7.79	33.8
	3rd swell partition	3.05	13.2
E	Wind waves	4.74	17.7
	1st swell partition	12.28	55.0
	2nd swell partition	7.89	20.1
	3rd swell partition	7.47	7.2

3.3.2. Combining Results From the Empirical and the Numerical Model

Combining insights from the empirical, process-based CERC method and the numerical BOSZ model reveals a constant sediment supply from the southern reef toward the island. Wave-induced currents transport the sediment around the island toward the island's lee side in the north. Throughout the dry season, sediment accumulates along Geiymiskih beach and at the southern end of Thoondu. Afterwards, in the wet season, the Thoondu spit forms at the northeastern end of Fuvahmulah (**Figure 4**). This formation can be elucidated with the CERC-formulation (**Figures 7**, **8**): In the wet season, the energy flux at the northern Geiymiskih beach carries sediment toward the east. At the same time, the swell dominated longshore energy flux is directed toward the north on Thoondu beach. Together, these hydrodynamic drivers transport sediment toward the north eastern headland of the island, forming the sand spit Thoondu. Inhabitants report and satellite images confirm that location and shape of the spit varies within the wet season (see **Supplementary Material**). The CERC-formulation is able to capture these changes when regarding the underlying hydrodynamic events (**Figure 9**). For example: The CERC-formulation is able to use the ERA5 climate data to explain singularities, such as those experienced on Fuvahmulah in the second half of the 2019 wet season. In September 2019, an anomaly occurred, where swell waves approached the island from $\theta_p \leq 135°$, leading to large transport rates in the CERC-equation: The highest longshore transport rate $q_{y,\max} = 8.98\,m^3\,h^{-1}$ came from swell waves with $H_s = 1.22\,m$ and $\theta_{\perp} = 79.9°$. This event is likely connected to a distinct temperature difference between the tropical eastern and western Indian Ocean, the IOD (Saji and Yamagata, 2003). The wave climate led to a beach protrusion on the edge of Geiymiskih to Thoondu beach and was well-appreciated by locals and tourists (see **Supplementary Material**). After the Thoondu spit formed in the wet season, the dry season wave climate leads to sediment depletion of the Thoondu spit, while new sediment accumulations form on Geiymiskih and Thoondu beach.

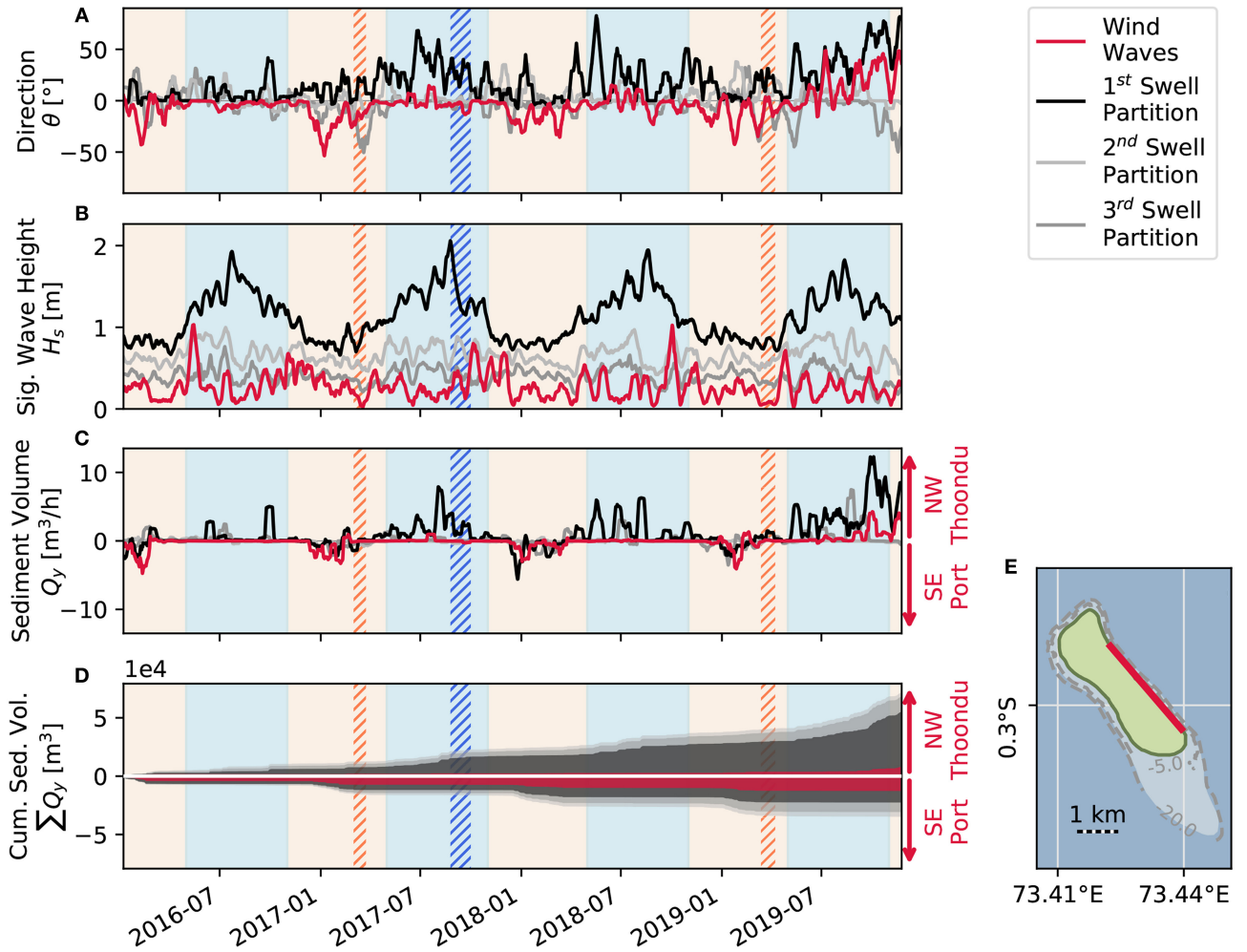

FIGURE 8 | (A) Averaged incident wave direction $\theta_{\perp,wp}$, measured as difference from the coastline normal $\alpha_{\perp}$ and **(B)** wave height $H_{s,wp}$ of each wave partition *wp* used for **(C)** longshore sediment transport rates $q_{y,wp}$ and **(D)** cumulative sediment volume $Q_{y,wp}$, transported alongshore the, marked with an crimson line on the map **(E)**. The crimson line is accordance with the crimson line in **Figure 6** (see **Table 3** for corresponding peak transport rate values $q_{y,max}$ and the contribution of each wave partition to Q_y). The time series shows values from January 2016 to November 2019. Negative values for $q_{y,wp}$ and $Q_{y,wp}$ indicate a transport toward the seaport in the southeast, while positive values lead to sediment transport toward Thoondu beach in the northwest. The time series shows the dry season with orange and the wet season with blue background. Field campaign 1 and 3 (orange hatched area) took place in March 2017 and 2019. Field campaign 2 (blue hatched area) was conducted in September 2017.

4. DISCUSSION

Sediment distribution on a reef is subject to (a) hydrodynamic forcing, for example by waves, wave transformation and tides, (b) the reef shape and bathymetry, defining wave propagation and thus current direction on the reef platform, as well as (c) sediment supply of the reef. This study used wave data from the climate reanalysis model ERA5 in the process-based, empirical CERC method and the phase-resolving, depth-integrated numerical model BOSZ to study the associated morphodynamic response on the Maldivian reef island Fuvahmulah. On this basis, the study linked these insights to comprehend measured shoreline changes on the island's beaches and the seasonal formation of the sand spit Thoondu in the north of the island.

As climate data resources have been scarce and of lower resolution, former studies usually combined significant wave heights H_s of wind waves and swell, but ignored their misalignment (Hildebrandt et al., 2019). This procedure emphasizes the dominant components but neglects the local characteristics. But the availability and constant improvement of climate reanalysis models provide more detailed boundary conditions today. The ocean wave model of ERA5 uses the wind input provided by their climate data set. However, the ERA5 wind data tends to result in underestimated significant wave heights. But compared to earlier releases of ECMWF's climate reanalysis models, the latest release of ECMWF's climate reanalysis model ERA5 improves the spatio-temporal resolution of it's predecessors with a 0.25° spatial resolution in latitudinal

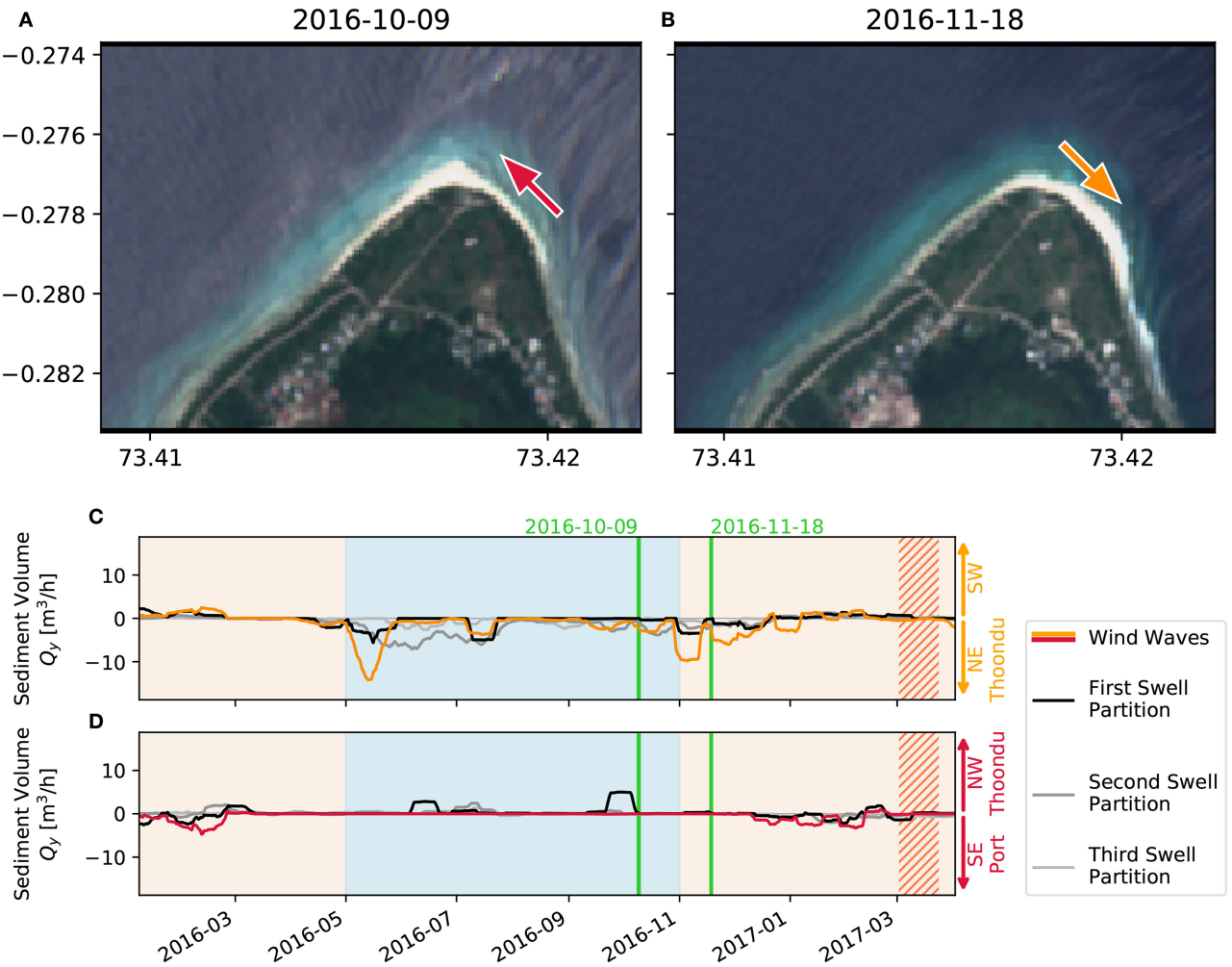

FIGURE 9 | Sentinel satellite images of northern Fuvahmulah on October 9, 2016 **(A)** and November 28, 2016 **(B)** and longshore sediment transport on Thoondu **(C)** and Geiymiskih Fannu beach **(D)** at the associated time of the satellite images (green line). **(C,D)** Show zoomed data from the longshore sediment transport rates $q_{y,wp}$ (**Figures 7**, **8**). The orange hatched area shows the time of the first field campaign for this study. The satellite images contain Copernicus Sentinel data, accessed through EO Browser (true color, red green blue).

and longitudinal direction and hourly temporal resolution (C3S, 2017). The hourly resolution of the current, publicly available model ERA5 improves the computation of significant wave heights and successfully reduces errors—especially in extreme events (Wiese et al., 2018). These factors—the good spatio-temporal data availability and trustworthy reconstruction of the wave climate—facilitate event based hind- and forecasting in the CERC formulation. On the other hand, the sheer amount of wave data results in a challenging number of feasible and reasonable numerical simulations. To tackle this challenge, this study combines the empirical CERC-formulation with information of a numerical model, calculating wave-induced currents approaching Fuvahmulah from the dominant wave directions:

The CERC-formulation is a common tool to estimate longshore sediment transport on sandy beaches (CERC, 1984; Schoonees and Theron, 1995) and works best for site-specific adaptation of the empirical coefficient K (Smith et al., 2009). It is able to process the high resolution data of the ERA5 data set. But application of the CERC-formulation for calcareous sediments and on coral reef islands has been rare (for example in Shope and Storlazzi, 2019). Its simplicity omit more complex sediment transport processes (van Rijn, 2005; Shope and Storlazzi, 2019) having an impact on each component of the CERC-equation $q_y = P_y \cdot I_y$:

The sediment transport rate q_y itself focuses on longshore sediment distribution but gives no information on cross-shore beach response (Atkinson et al., 2018) or cross-shore transport components. Therefore, the CERC-approach cannot estimate sediment transport toward the island and thus, for example, the role of the southern Fuvahmulah reef as sediment source.

The wave energy flux P_y captures the wave energy component of coastal longshore transport. Albeit the CERC-equation always includes at least one parameter at the breaker line, waves

transform differently when propagating over milder sloping sandy beaches compared to typical reef bathymetries with steep reef fronts followed by near horizontal reef flats. Furthermore, the wave energy flux P_y is based on the significant wave height H_s, but does not consider water level undulations on sub- and intratidal timescales (Pomeroy et al., 2018), sediment transport mechanisms by low-frequency waves and reef flat resonances (Roeber and Bricker, 2015; Cheriton et al., 2016; Gawehn et al., 2016), or other hydrodynamic effects on smaller scales, such as atoll lagoon flushing by wave pumping and gravity draining (Gourlay and Colleter, 2005; Callaghan et al., 2006).

Applying the sediment component I_y of the CERC equation for complex reef bathymetries requires an improved understanding over sandy or rocky bottoms. However, as of today, sediment transport over reef bottoms is still subject to current research (Pomeroy et al., 2015; Ryan et al., 2019). Moreover, while sediment mobility under waves is well-described for sandy marine aggregates (Turner and Masselink, 1998; Nielsen et al., 2001), wave-induced transport processes differ for coarser sediments (van Rijn, 2005; Austin and Masselink, 2006). The present study advances the application of the CERC-formulation on reef islands by combining measured data with insights of numerically modeled hydrodynamics, but further research is required to achieve a more sensible estimation of the empirical coefficient K for calcareous sediment volumes on coral reef islands—for example with measured sediment data on the scale of several single wave events. As sediment volumes from the CERC-equation are sensible to K, the results presented in this study (**Figures 7–9** and **Table 3**) must be interpreted as approximations of wave-induced morphodynamic processes rather than providing exact real-world sediment volumes (which is in accordance with the procedure of Shope and Storlazzi, 2019). For example: when considering the measured volumes in dry season 2017 instead of 2019, estimations of K—and thus calculated volumes—would vary by a factor of about $\pm \sim 3$.
Albeit each component q_y, P_y and I_y of the CERC-formulation underlies limitations, the equation is able to calculate longshore energy flux and corresponding sediment transport on different time scales. The results show that with highly resolved, multi-directional wave input, it can capture both the seasonal Thoondu spit formation as well as the beach formation initiated by an IOD-event in late wet season 2019 (see **Figure 9**).

When comparing the empirical with a numerical approach, the numerical approach can deliver more details on the hydrodynamic background of sediment transport: The depth-averaged hydrodynamic model indicates a more complex effect of the wave-induced current pattern near the beaches than given by the CERC method (**Figure 5**). In general, the numerical model confirms the directional components calculated with the CERC formulation (**Figure 5**). However, in the CERC formulation, waves from $\theta_p = 135^\circ$ (**Figure 5B**) would have a high influence ($\theta_\perp \sim \pm 45^\circ$) on the southern beaches, but a low influence on the east side ($\theta_\perp \sim +9^\circ$). On the contrary, the numerical model shows that wave-induced current velocities on the east and south side are in the same order of magnitude (about 1–2 m s^{-1}). A similar discrepancy can be seen on the west side for swell wave components with $\theta_p = 157^\circ$ (**Figure 5C**), inducing high currents in the numerical model, but having lower significance in the CERC-method ($\theta_\perp \sim 17^\circ$). But the $\theta_p = 202^\circ$ component shows the most significant difference: while the CERC-method calculates an upward directed sediment rate ($\theta_\perp \sim 45^\circ$) in front of the airport at the southwest side of Fuvahmulah, the current pattern of the numerical model depict a southeast ward directed current (**Figure 5D**). The numerical models also disclose an influence of south to southeastern swells on the lee-side of the island, but these are outside the northern beaches' incident wave direction range $\theta_\perp$ of −90–90° and thus remain unconsidered in the CERC-equation.

Even though numerical approaches are able to capture the hydrodynamics in reef environments (Roeber and Bricker, 2015; Masselink et al., 2019), implementation of morphodynamic changes into phase-resolving wave models is challenging (McCall et al., 2014). Here, the numerical model only shows depth-integrated flow velocities on the reef and not the altered velocity profile by the reef structure. Further research is required on the interaction of calcareous sediment and reef-island hydrodynamics in numerical models to extract more reliable and robust sediment transport rates and volumes. In the frame of this work, numerical models can only indicate sediment transport potential via wave-induced current velocity. While the results from this study illustrate that sediment transport on reef scale can be well-explained with ocean wave forcing, other studies on beach scale found further factors influencing sediment distribution—for example the complexity and roughness of reef structures and their role for hydrodynamic flow (Callaghan et al., 2006) and sediment transport (Pomeroy et al., 2015; Shope and Storlazzi, 2019) or wind-stresses and varying water levels due to sea-level rise or tides (Pomeroy et al., 2017, 2018; Atkinson et al., 2018). In the case of Fuvahmulah however, with a maximum tidal range of 1.1 m, currents from tides and ocean circulation are of minor importance, as they are about an order of magnitude below wave-induced currents (David et al., 2019). The insights from the numerical model complement the findings of the CERC-method and put the measured morphological changes into an hydrodynamic context.

The transported sediment is visible in form of sediment on the coastline of the island. In this study, UAVs recorded sediment volumes, being reconstructed by means of structure from motion (SfM). The first two campaigns were referred to the DEMs of the third campaign via vGCPs of unique natural or structural features. This approach still yields reasonably good results, but contains higher errors in the photogrammetric process than recording unique GCPs for each flight in each campaign (see **Supplementary Material**). Therefore, it should only be applied if no individual GCPs for each campaign are available—as in this case. Especially areas with deteriorated visibility can make vGCP identification and point cloud reconstruction challenging. An example are vegetated areas or areas submerged by water or sand. The results of this study however encourage the use of UAV-borne data recorded even in subpar field conditions, as they remain valuable data with useful information. In this study, errors of the DEMs aligned with vGCPs are still within the upper range of expectable errors in UAV-based photogrammetry (Casella et al., 2020).

The overview of the resulting sediment budget (**Figure 3**) is presented in volume over dry beach area. Some challenges remain by measuring volumetric sediment changes by means of UAV-borne photogrammetry, such as beach access and underwater areas. This study uses the volume over dry beach method consistently for the overview, but defines interpolation nodes on the submerged reef between the last dry point of the reef in one season and the associated dry beach point in the other season for the northern beaches Geiymiskih and Thoondu northwest. Otherwise, large volumes of the northern beaches would remain unspecified. The error of defining the coordinates of the interpolation nodes is within the error range of the photogrammetric process. The interpolation of wet season beaches at Thoondu north depends on estimated reef depths derived from orthophotos and reef depths of adjacent beaches and can contain errors in decimeter scale. The interpolation between two nodes on the reef neglects the bottom roughness of the beach and thus introduces further inaccuracies to the volumes. With sediment volumes in the order of $\mathcal{O}(4-5)$ cubic meters, the total influence of these simplifications is however minor. Also, erosion due to coastal infrastructure is in the order of (cubic-) decimeters and rather affects the consolidated material of the coast of Fuvahmulah (David et al., 2019) than the bulk sediment evaluated with the volume over dry beach method. Thus, erosion must be studied on a different scale.

Sediment supply depends on the location of corals on the reef (Ryan et al., 2019) and coral type (Hamylton et al., 2017). Gross and net production as well as bio-erosion of calcium carbonate are site specific and depend on different environmental factors. In general, reef island formation is based on the fact that the coral reef produces calcium carbonate, which erodes and is transported over the reef (Mandlier and Kench, 2012). Insufficient sediment supply can have several impacts: coasts retreat depending on their orientation toward the dominant incident wave direction, reef island positions on an atoll varies (Shope and Storlazzi, 2019), or islands disappear as net sediment accretion cannot keep up with sea level rise (Albert et al., 2016). With sufficient sediment supply and without artificial interference, the coastline of reef islands is meant to be stable (Kench, 2012). This study does not provide a specific sediment production budget for Fuvahmulah, but uses the bio-erosion estimates of $3.4 \pm 0.4\,\mathrm{kg\,CaCO_3\,m^{-2}\,yr^{-1}}$ from an island on the neighboring atoll (Ryan et al., 2019). Here, *"the upper reef* [platform] *surface act*[s] *as the carbonate factory for islands"* (Ryan et al., 2019). Despite the regional proximity and similarities of both reefs, total carbonate production rate of the reef depends on several factors, such as the eco-geomorphological zones on the reef platform (Hamylton et al., 2017; Ryan et al., 2019), having an influence on the bio-erosion rate and thus on the calculations in this study.

While the west side of Fuvahmulah is stable, the port construction blocks the sediment transport and leads to sand accumulation in the south of the island in front of the port, as well as slow, but substantial erosion on the port's lee side in the southeast of the island. This erosion becomes visible in examinations on smaller scales and epitomizes a disturbance of natural systems by anthropogenic interventions (the port's impact on the southcoast of Fuvahmulah was analyzed in David et al., 2019). On the other hand, the sediment budgets verify sediment produced on the reef migrates around the island to the lee-side of Fuvahmulah. Then, the final destination of the sediment is are the northern beaches Thoondu and Geiymiskih. Here, a sediment volume deficit from wet to dry season indicates sediment moving off the reef plateau, especially since volume changes at adjacent beaches are low. The positive sediment budget between dry season 2017 and 2019 support the thesis of reef recovery in the region after the 2016 reef bleaching event (Ryan et al., 2019).

5. CONCLUSION

Ocean climate pressures influence sediment production and distribution pathways on the reef. The dynamic reef island morphology is a natural response to changing impacts. Within reef island environments however, sustainable, low-regret coastal development requires an understanding of the underlying processes of island morphology.

The present study deals with the fringing reef island Fuvahmulah on the Maldives. Based on three field campaigns, UAV-based photogrammetry revealed intra- and interannual changes of sediment volumes and coastlines. The coastline of the island was separated into morphological cells showing that the lateral coastlines on the west and east of the elliptical island are mostly stable. Only on the southeastern coast above the seaport, Fuvahmulah experiences erosion, which becomes measurable at a lower scale (David et al., 2019). In contrast, the lee-side in the north of Fuvahmulah has a highly active morphology, where beach face and location change even within the seasons. The general morphological pattern on the northern headland is characterized by typical seasonal sediment depots on Geiymiskih and Thoondu beach in the dry season. In the wet season the sediment moves to the northern tip of Fuvahmulah, where the Thoondu spit is formed. This natural feature makes the beach very popular and is highly valued by the community and considered a landmark of the island (Ratter et al., 2019).

Morphological changes on the reef are triggered by hydrodynamic forcing. Therefore, this study exploits hourly climate reanalysis model wave data to quantify longshore sediment distribution around the island with the CERC method. Dominant south to southeasterly swells are characteristic for the regional Maldivian hydrodynamic regime (Kench and Brander, 2006; Kench and Mann, 2017). These swells induce a constant sediment supply from the southeastern reef plateau. The sediment stream goes around the lateral sides of Fuvahmulah to the northern headland, where the Thoondu spit forms in the wet season. Local wind-wave and subordinate swell events shape the northern beaches within the seasons.

By adapting and validating the empirical coefficient K with the measurements from the field campaigns, the CERC formulation is capable of capturing morphodynamic changes after hydrodynamic events. This method facilitates processing the high resolution wave data from the climate data models for quantitative hind- and forecast of longshore sediment

transport. Numerical methods give supplementary insights beyond the empirical CERC approach and hence a more holistic view on the complex hydrodynamic background of the reef for certain combinations of dominant wave parameters or single events. However, further advances in numerical models are required to directly couple hydrodynamic drivers and morphodynamic response on reef islands and calcareous sediment.

This study shows that seasonal wave climate and associated, wave-induced currents can explain the formation of local characteristic beach phenomena like the Thoondu spit. On annual timescales the seasonally dynamic morphology stabilizes the island's shoreline analogous to beach nourishment on sandy beaches. This study presented coastal engineering methods to exploit publicly available climate reanalysis data in high-resolution to assess the site-specific influence of hydrodynamic drivers on reef island morphology. Even though erosion on Fuvahmulah has to be studied on a different scale (David et al., 2019), sediment trajectories reveal locations with increased erosion potential on the lee-side of disturbances in the natural sediment stream. Because anthropogenic interventions into the natural dynamics disturb the natural ability to respond to ocean climate pressures the design of coastal infrastructure on low-lying reef islands must include an assessment of reef islands' natural beach nourishment potential to avoid interference before taking action. With this, reef island communities can reduce shoreline erosion, improve their resilience and decrease their risk to suffer from sea level rise and associated impacts.

DATA AVAILABILITY STATEMENT

The field data supporting the findings of this study are available from the corresponding author upon reasonable request. Wave climate data is available from the Copernicus Climate Change Service (C3S, 2017). Satellite images from Copernicus Sentinel data were accessed through the EO Browser.

AUTHOR CONTRIBUTIONS

CD conducted the field campaign, research, analysis, and wrote the manuscript with input from TS. TS (co-)designed the research project, provided guidance, edited, and contributed to the final manuscript. All authors contributed to the article and approved the submitted version.

FUNDING

This study took place in the project Dealing with change in SIDS: societal action and political reaction in sea level change adaptation in Small Island Developing States (DICES), grant no. SCHL 503/17-1. The project was framed within the priority program (SPP 1889) 'Regional Sea Level Change and Society' (SeaLevel, see www.spp-sealevel.de) of the German Research Foundation (Deutsche Forschungsgemeinschaft, DFG). The publication of this article was funded by the Open Access fund of Leibniz Universität Hannover.

ACKNOWLEDGMENTS

The authors would like to thank Ali Ahmed, Pablo Ballesteros, Tatiana Ivanova, René Klein, Nina Kohl, Manò Schütt, Ibrahim Shiyan (Panda), Zahid as well as Marion, and Uwe Zander for their help in the field campaigns. On the Maldives, the authors were supported by the Maldives Meteorological Service (MMS), Fuvahmulah Island Council, and Fuvahmulah DIVE School.

The authors further appreciate the involvement of the working group of Maike Paul for reviewing the manuscript. We further acknowledge the working group of Jan Visscher, Rik Gijsman, as well as our project members in DICES Susann Adloff, Arne Henning, Beate Ratter, and Katrin Rehdanz for their professional input.

Additionally the authors thank Volker Roeber and Jannek Gundlach for their feedback concerning numerical models as well as Jean Bidlot, Mark Hemer, and Todd Spindler for their help in accessing climate reanalysis data. Also, Elisa Casella and Alessio Rovere gave valuable insights and feedback to UAV-based photogrammetry, while Tobias Kersten helped with geodetic questions before the third field campaign and while post-processing.

SUPPLEMENTARY MATERIAL

The Supplementary Material for this article can be found online at: https://www.frontiersin.org/articles/10.3389/fmars.2020.538675/full#supplementary-material

REFERENCES

Albert, S., Leon, J. X., Grinham, A. R., Church, J. A., Gibbes, B. R., and Woodroffe, C. D. (2016). Interactions between sea-level rise and wave exposure on reef island dynamics in the Solomon Islands. *Environ. Res. Lett.* 11:054011. doi: 10.1088/1748-9326/11/5/054011

Andersson, A. (2015). A fundamental paradigm for coral reef carbonate sediment dissolution. *Front. Mar. Sci.* 2:52. doi: 10.3389/fmars.2015.00052

Atkinson, A. L., Baldock, T. E., Birrien, F., Callaghan, D. P., Nielsen, P., Beuzen, T., et al. (2018). Laboratory investigation of the bruun rule and beach response to sea level rise. *Coast. Eng.* 136, 183–202. doi: 10.1016/j.coastaleng.2018.03.003

Austin, M. J., and Masselink, G. (2006). Swash–groundwater interaction on a steep gravel beach. *Cont. Shelf Res.* 26, 2503–2519. doi: 10.1016/j.csr.2006.07.031

Bidlot, J.-R. (2016). *Ocean Wave Model Output Parameters*. Reading: European Centre for Medium-RangeWeather Forecasts (ECMWF).

Bosboom, J., and Stive, M. J. F. (2015). *Coastal Dynamics I, Volume 0.5*. Delft: Delft Academic Press.

Burcharth, H. F., Hawkins, S. J., Zanuttigh, B., and Lamberti, A. (2007). "Design tools related to engineering," in *Environmental Design Guidelines for Low Crested Coastal Structures, Chapter 13*, eds H. F. Burcharth, S. J. Hawkins, B. Zanuttigh, and A. Lamberti (Oxford: Elsevier Science Ltd), 203–333. doi: 10.1016/B978-008044951-7/50033-6

C3S (2017). *ERA5, Fifth Generation of ECMWF Atmospheric Reanalyses of the Global Climate by the Copernicus Climate Change Service (C3S)*. Copernicus Climate Change Service Climate Data Store (CDS). Available online at: https://cds.climate.copernicus.eu/cdsapp#!/home (accessed December 6, 2019).

Cai, W., Santoso, A., Wang, G., Weller, E., Wu, L., Ashok, K., et al. (2014). Increased frequency of extreme Indian Ocean Dipole events due to greenhouse warming. *Nature* 510, 254–258. doi: 10.1038/nature13327

Caldwell, P. C., Merrifield, M. A., and Thompson, P. R. (2015). *Sea level Measured by Tide Gauges From Global Oceans-The Joint Archive for Sea Level Holdings (NCEI Accession 0019568). Dataset. Version 5.5*. NOAA National Centers for Environmental Information.

Callaghan, D. P., Nielsen, P., Cartwright, N., Gourlay, M. R., and Baldock, T. E. (2006). Atoll lagoon flushing forced by waves. *Coast. Eng.* 53, 691–704. doi: 10.1016/j.coastaleng.2006.02.006

Casella, E., Collin, A., Harris, D., Ferse, S., Bejarano, S., Parravicini, V., et al. (2016). Mapping coral reefs using consumer-grade drones and structure from motion photogrammetry techniques. *Coral Reefs* 36, 269–275. doi: 10.1007/s00338-016-1522-0

Casella, E., Drechsel, J., Winter, C., Benninghoff, M., and Rovere, A. (2020). Accuracy of sand beach topography surveying by drones and photogrammetry. *Geomar. Lett.* 40, 255–268. doi: 10.1007/s00367-020-00638-8

CERC (1984). *Shore Protection Manual, Vol. 1*. Vicksburg, MS: Coastal Engineering Research Center (CERC), Department of the U.S. Army,Waterways Experiment Station, Corps of Engineers, Coastal Engineering Research Center.

Chave, K. E., Smith, S. V., and Roy, K. J. (1972). Carbonate production by coral reefs. *Mar. Geol.* 12, 123–140. doi: 10.1016/0025-3227(72)90024-2

Cheriton, O. M., Storlazzi, C. D., and Rosenberger, K. J. (2016). Observations of wave transformation over a fringing coral reef and the importance of low-frequency waves and offshore water levels to runup, overwash, and coastal flooding. *J. Geophys. Res. Oceans* 121, 3121–3140. doi: 10.1002/2015JC011231

Collins, M., Sutherland, M., Bouwer, L., Cheong, S.-M., Frlicher, T., Combes, H. J. D., et al. (in press). "Extremes, abrupt changes and managing risk," in *IPCC Special Report on the Ocean and Cryosphere in a Changing Climate*, eds H. O. Pörtner, D. Roberts, V. Masson-Delmotte, P. Zhai, M. Tignor, E. Poloczanska, et al., 589–655.

Dangendorf, S., Hay, C., Calafat, F. M., Marcos, M., Piecuch, C. G., Berk, K., et al. (2019). Persistent acceleration in global sea-level rise since the 1960s. *Nat. Clim. Change* 9, 705–710. doi: 10.1038/s41558-019-0531-8

David, C. G., Roeber, V., Goseberg, N., and Schlurmann, T. (2017). Generation and propagation of ship-borne waves–solutions from a Boussinesq-type model. *Coast. Eng.* 127, 170–187. doi: 10.1016/j.coastaleng.2017.07.001

David, C. G., Schlurmann, T., and Roeber, V. (2019). "Coastal Infrastructure on Reef Islands–the Port of Fuvahmulah, the Maldives as example of maladaptation to sea-level rise?" in *Coastal Structures 2019*, eds N. Goseberg and T. Schlurmann (Hannover: Bundesanstalt fr Wasserbau), 874–885.

David, C. G., Schulz, N., and Schlurmann, T. (2016). "Assessing the application potential of selected ecosystem-based, low-regret coastal protection measures," in *Ecosystem-Based Disaster Risk Reduction and Adaptation in Practice*, eds F. G. Renaud, K. Sudmeier-Rieux, M. Estrella, and U. Nehren (Cham: Springer International Publishing), 457–482. doi: 10.1007/978-3-319-43633-3_20

Duvat, V. K. E., and Magnan, A. K. (2019). Rapid human-driven undermining of atoll island capacity to adjust to ocean climate-related pressures. *Sci. Rep.* 9:15129. doi: 10.1038/s41598-019-51468-3

East, H. K., Perry, C. T., Kench, P. S., Liang, Y., and Gulliver, P. (2018). Coral reef island initiation and development under higher than present sea levels. *Geophys. Res. Lett.* 45, 11265–11274. doi: 10.1029/2018GL079589

Emanuel, K. (1988). The maximum intensity of hurricanes. *J. Atmos. Sci.* 45, 1143–1155. doi: 10.1175/1520-0469(1988)045<1143:TMIOH>2.0.CO;2

Ferrario, F., Beck, M. W., Storlazzi, C. D., Micheli, F., Shepard, C. C., and Airoldi, L. (2014). The effectiveness of coral reefs for coastal hazard risk reduction and adaptation. *Nat. Commun.* 5:3794. doi: 10.1038/ncomms4794

Gawehn, M., van Dongeren, A., van Rooijen, A., Storlazzi, C. D., Cheriton, O. M., and Reniers, A. (2016). Identification and classification of very low frequency waves on a coral reef flat. *J. Geophys. Res. Oceans* 121, 7560–7574. doi: 10.1002/2016JC011834

Gourlay, M. R., and Colleter, G. (2005). Wave-generated flow on coral reefs—an analysis for two-dimensional horizontal reef-tops with steep faces. *Coast. Eng.* 52, 353–387. doi: 10.1016/j.coastaleng.2004.11.007

Hamylton, S. M., Duce, S., Vila-Concejo, A., Roelfsema, C. M., Phinn, S. R., Carvalho, R. C., et al. (2017). Estimating regional coral reef calcium carbonate production from remotely sensed seafloor maps. *Rem. Sens. Environ.* 201, 88–98. doi: 10.1016/j.rse.2017.08.034

Hanson, J. L., and Phillips, O. M. (2001). Automated analysis of ocean surface directional wave spectra. *J. Atmos. Ocean. Technol.* 18, 277–293. doi: 10.1175/1520-0426(2001)018<0277:AAOOSD>2.0.CO;2

Harris, D. L., Rovere, A., Casella, E., Power, H., Canavesio, R., Collin, A., et al. (2018). Coral reef structural complexity provides important coastal protection from waves under rising sea levels. *Sci. Adv.* 4:eaao4350. doi: 10.1126/sciadv.aao4350

Hermes, J. C., Masumoto, Y., Beal, L. M., Roxy, M. K., Vialard, J., Andres, M., et al. (2019). A sustained ocean observing system in the Indian Ocean for climate related scientific knowledge and societal needs. *Front. Mar. Sci.* 6:355. doi: 10.3389/fmars.2019.00355

Hildebrandt, A., Schmidt, B., and Marx, S. (2019). Wind-wave misalignment and a combination method for direction-dependent extreme incidents. *Ocean Eng.* 180, 10–22. doi: 10.1016/j.oceaneng.2019.03.034

Horrillo, J., Grilli, S. T., Nicolsky, D., Roeber, V., and Zhang, J. (2014). Performance benchmarking tsunami models for NTHMP's inundation mapping activities. *Pure Appl. Geophys.* 172, 869–884. doi: 10.1007/s00024-014-0891-y

IPCC (2012). "Managing the risks of extreme events and disasters to advance climate change adaptation," in *A Special Report of Working Groups I and II of the Intergovernmental Panel on Climate Change (IPCC)*, eds C. B. Field, V. Barros, T. F. Stocker, Q. Dahe, D. J. Dokken, K. L. Ebi, et al. (Cambridge; New York, NY: Cambridge University Press), 582.

Kench, P. S. (2012). "Compromising Reef Island shoreline dynamics: legacies of the engineering paradigm in the Maldives," in *Pitfalls of Shoreline Stabilization: Selected Case Studies*, eds J. A. G. Cooper and O. H. Pilkey (Dordrecht: Springer Netherlands), 165–186. doi: 10.1007/978-94-007-4123-2_11

Kench, P. S., and Brander, R. W. (2006). Response of reef island shorelines to seasonal climate oscillations: South Maalhosmadulu atoll, Maldives. *J. Geophys. Res. Earth Surf.* 111. doi: 10.1029/2005JF000323

Kench, P. S., and Mann, T. (2017). Reef Island evolution and dynamics: insights from the Indian and Pacific Oceans and perspectives for the Spermonde Archipelago. *Front. Mar. Sci.* 4:145. doi: 10.3389/fmars.2017.00145

Kumar, P., Kaur, S., Weller, E., and Min, S.-K. (2019). Influence of natural climate variability on the extreme ocean surface wave heights over the Indian Ocean. *J. Geophys. Res. Oceans* 124, 6176–6199. doi: 10.1029/2019JC015391

Longuet-Higgins, M. S. (1970). Longshore currents generated by obliquely incident sea waves: 2. *J. Geophys. Res.* 75, 6790–6801. doi: 10.1029/JC075i033p06790

Lynett, P. J., Gately, K., Wilson, R., Montoya, L., Arcas, D., Aytore, B., et al. (2017). Inter-model analysis of tsunami-induced coastal currents. *Ocean Modell.* 114, 14–32. doi: 10.1016/j.ocemod.2017.04.003

Magnan, A., Garschagen, M., Gattuso, J. P., Hay, J. E., Hilmi, N., Holland, E., et al. (in press). "Integrative cross-chapter box on low-lying islands and coasts," in *Special Report on Ocean and Cryosphere in a Changing Climate*, eds H. O. Pörtner, D. Roberts, V. Masson-Delmotte, P. Zhai, M. Tignor, E. Poloczanska, et al., 657–674.

Mandlier, P. G., and Kench, P. S. (2012). Analytical modelling of wave refraction and convergence on coral reef platforms: implications for island formation and stability. *Geomorphology* 159–160, 84–92. doi: 10.1016/j.geomorph.2012.03.007

Masselink, G., Tuck, M., McCall, R., van Dongeren, A., Ford, M., and Kench, P. (2019). Physical and numerical modeling of infragravity wave generation and transformation on coral reef platforms. *J. Geophys. Res. Oceans* 124, 1410–1433. doi: 10.1029/2018JC014411

McCall, R., Masselink, G., Poate, T., Roelvink, J., Almeida, L., Davidson, M., et al. (2014). Modelling storm hydrodynamics on gravel beaches with XBeach-G. *Coast. Eng.* 91, 231–250. doi: 10.1016/j.coastaleng.2014.06.007

McLean, R., and Kench, P. (2015). Destruction or persistence of coral atoll islands in the face of 20th and 21st century sea-level rise? *Wiley Interdiscipl. Rev. Clim. Change* 6, 445–463. doi: 10.1002/wcc.350

MEE (2014). *Environment & Social Assessment & Management Framework–Climate Change Adaptation Project*. Technical report, Ministry of Environment and Energy. Available online at: http://documents.worldbank.org/curated/en/939971468329099370/pdf/E47010SAR0EA0P1533010Box385392B00PUBLIC0.pdf (accessed December 27, 2019).

Möller, I., Kudella, M., Rupprecht, F., Spencer, T., Paul, M., van Wesenbeeck, B. K., et al. (2014). Wave attenuation over coastal salt marshes under storm surge conditions. *Nat. Geosci.* 7, 727–731. doi: 10.1038/ngeo2251

Naeem, H. (2006). *Foahmulaku Beach Erosion Survey & Coastal Protection Report*. Technical Report. Malé: Ministry of Environment, Energy and Water.

Narayan, S., Beck, M. W., Reguero, B. G., Losada, I. J., van Wesenbeeck, B., Pontee, N., et al. (2016). The effectiveness, costs and coastal protection benefits of natural and nature-based defences. *PLoS ONE* 11:e154735. doi: 10.1371/journal.pone.0154735

Nielsen, P., Robert, S., Mller-Christiansen, B., and Oliva, P. (2001). Infiltration effects on sediment mobility under waves. *Coast. Eng.* 42, 105–114. doi: 10.1016/S0378-3839(00)00051-X

Nurse, L. A., McLean, R. F., Agard, J., Briguglio, L. P., Duvat-Magnan, V., Pelesikoti, N., et al. (2014). "Small islands," in *Climate Change 2014, Impacts, Adaptation, and Vulnerability. Part B: Regional Aspects. Contribution of Working Group II to the Fifth Assessment Report of the Intergovernmental Panel of Climate Change*, eds V. R. Barros, C. B. Field, D. J. Dokken, M. D. Mastrandrea, K. J. Mach, T. E. Bilir, et al. (Cambridge; New York, NY: Cambridge University Press), 1613–1654.

Oppenheimer, M., Glavovic, B., Hinkel, J., van de Wal, R., Magnan, A. K., Abd-Elgawad, A., et al. (in press). "Sea Level rise and implications for low lying islands, coasts and communities," in *IPCC Special Report on the Ocean and Cryosphere in a Changing Climate*, eds H. O. Portner, D. Roberts, V. Masson-Delmotte, P. Zhai, M. Tignor, E. Poloczanska, et al., 702.

Paul, M., and Gillis, L. (2015). Let it flow: how does an underlying current affect wave propagation over a natural seagrass meadow? *Mar. Ecol. Prog. Ser.* 523, 57–70. doi: 10.3354/meps11162

Perry, C. T., Alvarez-Filip, L., Graham, N. A. J., Mumby, P. J., Wilson, S. K., Kench, P. S., et al. (2018). Loss of coral reef growth capacity to track future increases in sea level. *Nature* 558, 396–400. doi: 10.1038/s41586-018-0194-z

Perry, C. T., Kench, P. S., Smithers, S. G., Riegl, B., Yamano, H., and Leary, M. J. O. (2011). Implications of reef ecosystem change for the stability and maintenance of coral reef islands. *Glob. Change Biol.* 17, 3679–3696. doi: 10.1111/j.1365-2486.2011.02523.x

Pisapia, C., Burn, D., and Pratchett, M. S. (2019). Changes in the population and community structure of corals during recent disturbances (February 2016–October 2017) on Maldivian coral reefs. *Sci. Rep.* 9:8402. doi: 10.1038/s41598-019-44809-9

Pomeroy, A. W., Lowe, R. J., Dongeren, A. R. V., Ghisalberti, M., Bodde, W., and Roelvink, D. (2015). Spectral wave-driven sediment transport across a fringing reef. *Coast. Eng.* 98, 78–94. doi: 10.1016/j.coastaleng.2015.01.005

Pomeroy, A. W. M., Lowe, R. J., Ghisalberti, M., Storlazzi, C., Symonds, G., and Roelvink, D. (2017). Sediment transport in the presence of large reef bottom roughness. *J. Geophys. Res. Oceans* 122, 1347–1368. doi: 10.1002/2016JC011755

Pomeroy, A. W. M., Lowe, R. J., Ghisalberti, M., Winter, G., Storlazzi, C., and Cuttler, M. (2018). Spatial variability of sediment transport processes over intratidal and subtidal timescales within a fringing coral reef system. *J. Geophys. Res. Earth Surf.* 123, 1013–1034. doi: 10.1002/2017JF004468

Ratter, B., Hennig, A., and Zahid (2019). Challenges for shared responsibility–political and social framing of coastal protection transformation in the Maldives. *Die Erde J. Geograph. Soc. Berlin* 150, 169–183. doi: 10.12854/erde-2019-426

Roeber, V., and Bricker, J. D. (2015). Destructive tsunami-like wave generated by surf beat over a coral reef during Typhoon Haiyan. *Nat. Commun.* 6:7854. doi: 10.1038/ncomms8854

Roeber, V., and Cheung, K. F. (2012). Boussinesq-type model for energetic breaking waves in fringing reef environments. *Coast. Eng.* 70, 1–20. doi: 10.1016/j.coastaleng.2012.06.001

Roeber, V., Cheung, K. F., and Kobayashi, M. H. (2010). Shock-capturing Boussinesq-type model for nearshore wave processes. *Coast. Eng.* 57, 407–423. doi: 10.1016/j.coastaleng.2009.11.007

Rutten, J., Ruessink, B. G., and Price, T. D. (2017). Observations on sandbar behaviour along a man-made curved coast. *Earth Surf. Process. Landf.* 43, 134–149. doi: 10.1002/esp.4158

Ryan, E. J., Hanmer, K., and Kench, P. S. (2019). Massive corals maintain a positive carbonate budget of a Maldivian upper reef platform despite major bleaching event. *Sci. Rep.* 9:6515. doi: 10.1038/s41598-019-42985-2

Saji, N., and Yamagata, T. (2003). Possible impacts of Indian Ocean Dipole mode events on global climate. *Clim. Res.* 25, 151–169. doi: 10.3354/cr025151

Saji, N. H., Goswami, B. N., Vinayachandran, P. N., and Yamagata, T. (1999). A dipole mode in the tropical Indian Ocean. *Nature* 401, 360–363. doi: 10.1038/43854

Schoonees, J. S., and Theron, A. K. (1995). *Accuracy and Applicability of the SPM Longshore Transport Formula, Chapter 188*. Kobe: American Society of Civil Engineers.

Schoonees, T., Mancheño, A. G., Scheres, B., Bouma, T. J., Silva, R., Schlurmann, T., et al. (2019). Hard structures for coastal protection, towards greener designs. *Estuar. Coasts* 42, 1709–1729. doi: 10.1007/s12237-019-00551-z

Shope, J. B., and Storlazzi, C. D. (2019). Assessing morphologic controls on Atoll Island alongshore sediment transport gradients due to future sea-level rise. *Front. Mar. Sci.* 6:245. doi: 10.3389/fmars.2019.00245

Skirving, W. J., Heron, S. F., Marsh, B. L., Liu, G., De La Cour, J. L., Geiger, E. F., et al. (2019). The relentless march of mass coral bleaching: a global perspective of changing heat stress. *Coral Reefs* 38, 547–557. doi: 10.1007/s00338-019-01799-4

Smith, E. R., Wang, P., Ebersole, B. A., and Zhang, J. (2009). Dependence of total longshore sediment transport rates on incident wave parameters and breaker type. *J. Coast. Res.* 2009, 675–683. doi: 10.2112/07-0919.1

Stive, M. J., de Schipper, M. A., Luijendijk, A. P., Aarninkhof, S. G., van Gelder-Maas, C., van Thiel de Vries, J. S., et al. (2013). A new alternative to saving our beaches from sea-level rise: the sand engine. *J. Coast. Res.* 2013, 1001–1008. doi: 10.2112/JCOASTRES-D-13-00070.1

Storlazzi, C. D., Elias, E. P., and Berkowitz, P. (2015). Many Atolls may be uninhabitable within decades due to climate change. *Sci. Rep.* 5:14546. doi: 10.1038/srep14546

Storlazzi, C. D., Gingerich, S. B., van Dongeren, A., Cheriton, O. M., Swarzenski, P. W., Quataert, E., et al. (2018). Most atolls will be uninhabitable by the mid-21st century because of sea-level rise exacerbating wave-driven flooding. *Sci. Adv.* 4:eaap9741. doi: 10.1126/sciadv.aap9741

Temmerman, S., Meire, P., Bouma, T. J., Herman, P. M. J., Ysebaert, T., and Vriend, H. J. D. (2013). Ecosystem-based coastal defence in the face of global change. *Nature* 504, 79–83. doi: 10.1038/nature12859

Tessler, Z. D., Vörösmarty, C. J., Grossberg, M., Gladkova, I., Aizenman, H., Syvitski, J. P. M., et al. (2015). Profiling risk and sustainability in coastal deltas of the world. *Science* 349, 638–643. doi: 10.1126/science.aab3574

Tory, K. J., and Frank, W. M. (2010). "Tropical cyclone formation," in *Global Perspectives on Tropical Cyclones* (San Jose, CA: World Scientific Publishing), 55–91. doi: 10.1142/7597

Turner, I. L., and Masselink, G. (1998). Swash infiltration-exfiltration and sediment transport. *J. Geophys. Res. Oceans* 103, 30813–30824. doi: 10.1029/98JC02606

van Rijn, L. C. (2005). *Principles of Sedimentation and Erosion Engineering in Rivers, Estuaries and Coastal Seas*. Amsterdam: Aqua Publications.

Wessel, P., and Luis, J. F. (2017). The GMT/MATLAB toolbox. *Geochem. Geophys. Geosyst.* 18, 811–823. doi: 10.1002/2016GC006723

Wiese, A., Staneva, J., Schulz-Stellenfleth, J., Behrens, A., Fenoglio-Marc, L., and Bidlot, J.-R. (2018). Synergy of wind wave model simulations and satellite observations during extreme events. *Ocean Sci.* 14, 1503–1521. doi: 10.5194/os-14-1503-2018

Wing, M. G., Eklund, A., and Kellogg, L. D. (2005). Consumer-grade global positioning system (GPS) accuracy and reliability. *J. Forestry* 103, 169–173. doi: 10.1093/jof/103.4.169

Woodroffe, C., McLean, R., Smithers, S., and Lawson, E. (1999). Atoll reef-island formation and response to sea-level change: West Island, Cocos (Keeling) Islands. *Mar. Geol.* 160, 85–104. doi: 10.1016/S0025-3227(99)00009-2

Conflict of Interest: The authors declare that the research was conducted in the absence of any commercial or financial relationships that could be construed as a potential conflict of interest.

Copyright © 2020 David and Schlurmann. This is an open-access article distributed under the terms of the Creative Commons Attribution License (CC BY). The use, distribution or reproduction in other forums is permitted, provided the original author(s) and the copyright owner(s) are credited and that the original publication in this journal is cited, in accordance with accepted academic practice. No use, distribution or reproduction is permitted which does not comply with these terms.

frontiers in Marine Science

ORIGINAL RESEARCH
published: 22 January 2021
doi: 10.3389/fmars.2020.539646

Severe Flooding in the Atoll Nations of Tuvalu and Kiribati Triggered by a Distant Tropical Cyclone Pam

Ron K. Hoeke[1], Herve Damlamian[2], Jérome Aucan[3] and Moritz Wandres[2]*

[1] Climate Science Centre, Commonwealth Science and Industrial Research Organisation (CSIRO), Aspendale, VIC, Australia, [2] Geoscience, Energy and Maritime Division, Pacific Community (SPC), Suva, Fiji, [3] Laboratoire d'Ecologie Marine Tropicale des Océans Pacifique et Indien (ENTROPIE), Institut de Recherche pour le Développement (IRD), Nouméa, New Caledonia

Tropical cyclone (TC) Pam formed in the central south Pacific in early March 2015. It reached a category 5 severity and made landfall or otherwise directly impacted several islands in Vanuatu, causing widespread damage and loss of life. It then moved along a southerly track between Fiji and New Caledonia, generating wind-waves of up to approximately 15 m, before exiting the region around March 15th. The resulting swell propagated throughout the central Pacific, causing flooding and damage to communities in Tuvalu, Kiribati and Wallis and Futuna, all over 1,000 km from TC Pam's track. The severity of these remote impacts was not anticipated and poorly forecasted. In this study, we use a total water level (TWL) approach to estimate the climatological conditions and factors contributing to recorded impacts at islands in Tuvalu and Kiribati. At many of the islands, the estimated TWL associated with Pam was the largest within the ∼40-year period of available data, although not necessarily the largest in terms of estimated wave setup and runup; elevated regional sea-level also contributed to the TWL. The westerly wave direction likely contributed to the severity, as did the locally exceptional storm-swell event's long duration; the overall timing and duration of the event was modulated by astronomical tides. The findings of this study give impetus to the development, implementation and/or improvement of early warning systems capable of predicting such reef-island flooding. They also have direct implications for more accurate regional flood hazard analyses in the context of a changing climate, which is crucial for informing adaptation policies for the atolls of the central Pacific.

Keywords: tropical cyclones, flooding, sea level, wave climate analysis, coastal hazards, atolls

OPEN ACCESS

Edited by:
Robert Timothy McCall, Deltares, Netherlands

Reviewed by:
Christian M. Appendini, National Autonomous University of Mexico, Mexico
Rui Caldeira, Agência Regional para o Desenvolvimento da Investigação Tecnologia e Inovação (ARDITI), Portugal

****Correspondence:***
Ron K. Hoeke
ron.hoeke@csiro.au

Specialty section:
This article was submitted to Coastal Ocean Processes, a section of the journal Frontiers in Marine Science

Received: *02 March 2020*
Accepted: *27 October 2020*
Published: *22 January 2021*

Citation:
Hoeke RK, Damlamian H, Aucan J and Wandres M (2021) Severe Flooding in the Atoll Nations of Tuvalu and Kiribati Triggered by a Distant Tropical Cyclone Pam. Front. Mar. Sci. 7:539646. doi: 10.3389/fmars.2020.539646

INTRODUCTION

Coastal areas are perceived to be at risk of increasingly frequent and severe flooding and erosion impacts associated with sea level rise (SLR). This has led to concern that island nations are especially vulnerable to coastal flooding (Nicholls et al., 2007; Seneviratne et al., 2012), particularly the atoll nations of Kiribati, Tuvalu, Marshall Islands and Maldives (Barnett and Adger, 2003; Nicholls et al., 2011). There has been some debate on the nature and timing of these impacts, however. Several studies have presented evidence that, despite sea level rise on the order of 20 cm over the

last century, atoll islands have not (yet) experienced net erosion and that many may have some capacity to keep up with future SLR (e.g., Webb and Kench, 2010; Beetham et al., 2017; Tuck et al., 2019) through the deposition of reef-derived materials during storm over wash events (e.g., Maragos et al., 1973; Smithers and Hoeke, 2014). Other studies have suggested that rates of SLR will outstrip reefs accretion rates (Perry et al., 2018), and that in any case, the increased frequency and severity of inundation will make most atoll islands uninhabitable within a few decades (e.g., Storlazzi et al., 2018). Regardless, there is widespread agreement that overall vulnerability to SLR will be heterogeneous due to differences in reef/island morphology and exposure to extreme sea level drivers (viz sea level variability, storm waves, storm surges, and astronomic tides), and that more detailed event-based case studies are needed to understand the role of background sea level (and SLR) compared to these drivers (Woodroffe, 2008; Beetham and Kench, 2018; Idier et al., 2019). Such case studies can also better inform the development of early warning forecast systems, which are essential in the face of likely increased flooding and erosion events (Storlazzi, 2018), by identifying the relative importance of the extreme sea level processes and indications of local vulnerability.

In this study, we investigate extensive flooding and erosion impacts which occurred in Tuvalu and the Gilbert Islands of Kiribati during March 2015. Unlike the case studies of Hoeke et al. (2013), Wadey et al. (2017), Ford et al. (2018), and Wandres et al. (2020), all of which focused at least primarily on events triggered by distance-source swell waves generated by mid-latitude (temperate) cyclones in the western Pacific (primarily the Federated States of Micronesia, Papua New Guinea, and Solomon Islands), the Maldives, Majuro Atoll (Marshall Islands) and Fiji, respectively, the events in Tuvalu and Kiribati described here are associated with the passage of tropical cyclone (TC) Pam. TC Pam formed in the central south Pacific in early March 2015. It reached a category five severity and made landfall or otherwise directly impacted several islands in Vanuatu, causing widespread damage and loss of life (Gov. of Vanuatu, 2015). It then moved along a southerly track between Fiji and New Caledonia, exiting the region around March 15th. The resulting swell propagated throughout the central Pacific, causing flooding and damage to communities in Tuvalu, Kiribati, and Wallis and Futuna, all over 1,000 km from TC Pam's track (Damlamian et al., 2017; **Figure 1**).

Here, we focus on the remote impacts to Tuvalu and Kiribati, which were poorly forecast or otherwise anticipated (Taupo and Noy, 2017). Multiple reports were collated (**Table 1**) and then a combination of astronomical tidal predictions and numerical wind-wave and sea level hindcasts, spanning from 1979 to the present, were combined using a total water level (TWL) approach (e.g., similar to Dodet et al., 2019), to estimate the climatological conditions and factors contributing to recorded impacts. The accuracy of these TWL components were independently assessed using tide gauge and satellite altimetry observations; it also includes an empirical wave runup estimate. This resulting proxy for flooding severity was compared to the recorded flooding and erosion impacts; the relative contribution of waves, tides and background sea level to TWL were assessed, as was event duration and wave direction.

MATERIALS AND METHODS

Summary of Impacts to Islands and Atolls

Information on which island and atolls within Tuvalu and Kiribati were impacted (or were not), and types of impacts were collated from a number of sources, primarily disaster relief agencies. These are summarized in **Table 1**; these locations are also plotted in **Figure 2**. Note that (hand drawn) "inundation" and "erosion" maps, and notes provided by the Tuvalu Public Works Department to the authors are provided in this article's **"Supplementary Material"** section.

Geophysical Data

To assess the timing and location of regional TCs, particularly TC Pam, the IBTrACS (Knapp et al., 2010) database (version 04r0)[1] was interrogated for TCs tracks; any portion of which occurred between longitudes 155°E and 170°W and latitudes of 30°S and 10°N and between the years 1979–2019 (the time period of the wave hindcast used in this study, see next section) were retained and defined as "regional" TCs. TC Pam's track is given in **Figure 1**.

To assess impacts, three different categories of sea level information were used in this analysis: wind-waves, astronomical tides, and non-tidal sea-level. These are detailed in following sub-sections.

Wind-Waves

Hourly significant wave height (H_s), integrated wave energy flux (C_gE), peak wave period (T_p) and peak wave direction (D_p) for years 1979–2019 were extracted from the CAWCR Wave Hindcast, a validated global wind-wave hindcast with increased (approximately 7 km) spatial resolution around the Pacific island nations (Durrant et al., 2014)[2] and related collections. Previous global and regional comparisons with satellite altimetry and wave buoy data have found the overall hindcast H_s bias and overall root-mean-square (RMS) difference to be on the order of −5% and < 10%, respectively, in the central Pacific (Durrant et al., 2014; Hemer et al., 2016). However, in this study, a further verification of the hindcast's ability to estimate the extreme waves associated specifically with TC Pam was performed by comparing hindcast H_s to calibrated H_s measured by multiple satellite altimeters, provided via the Ribal and Young (2019) dataset (sourced from Australia's Integrated Marine Observing System)[3]. While overall correlation coefficients (R) and errors between hindcast H_s and that estimated by various altimeters/bands indicate good agreement ($R > 0.9$, std.err. < 0.004 m) for the area and time period indicated in **Figure 1**, the hindcast overestimated the most extreme waves ($H_s > 12$) near TC Pam's eye wall compared to the altimeter data by up to several meters (**Supplementary Figure 1**). This divergence is at least partially attributable to (1) the known tendency of the WaveWatch III model to overestimate energy of waves traveling in the oblique

[1] https://www.ncdc.noaa.gov/ibtracs/

[2] https://data.csiro.au/collections/collection/CIcsiro:6616v8

[3] http://imos.org.au/

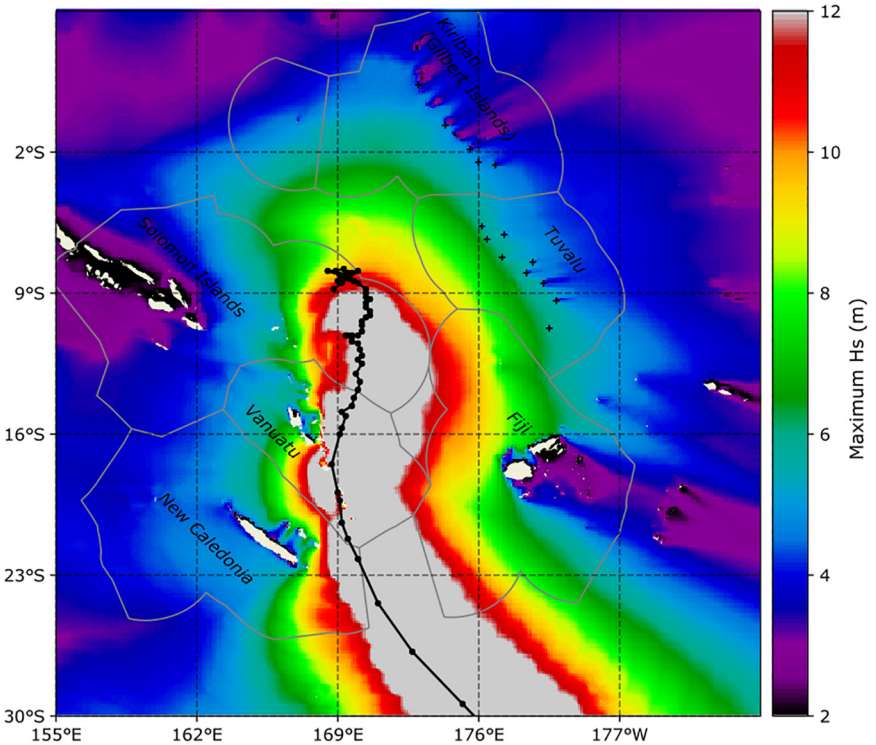

FIGURE 1 | Tropical Cyclone (TC) Pam's track (black line), with maximum hindcast significant wave height (Hs) during the TC's passage (March 6–17, 2015) indicated in color shading. Island nations/archipelagos in the area are labeled and their exclusive economic zones (Flanders Marine Institute, 2019), indicated with gray lines. The locations in **Table 1** are indicated with black +'s.

and opposing winds (as would occur in a tight-radius TC, including with the "ST4" physics package used in the hindcast) and; (2) uncertainty in the radar altimeters estimation of H_s in such extreme conditions: Ribal and Young (2019) limit their calibrations to values of $H_s < 9.0$ m. This overestimation (or divergence between hindcast and altimetry observations) of H_s does not occur at all for the same time period in the area indicated by **Figure 2** (which corresponds to the area of flooding and erosion impacts researched in this paper), and statistics in this area are modestly improved ($R > 0.92$, std.err. < 0.002 m, **Supplementary Figure 2**). For further information on the details and discussion of this hindcast/satellite altimeter comparison, please refer to **Supplementary Material**, however, the authors have confidence that the CAWCR wave hindcast represented the propagation of the wave field associated with TC Pam, and its representation within the overall extreme value statistics of the hindcast, throughout the Gilbert Islands and Tuvalu sufficiently to support the paper's conclusions.

Astronomical Tides

Hourly astronomic tidal predictions (η_{tide}) were calculated for a time period corresponding to that of the wave hindcast (years 1979–2019) from TPXO tidal constituents (version 9.1, Egbert and Erofeeva, 2002) at all locations in **Table 1**. To assess the skill of TPXO-based tidal predictions used in this study, they were compared to tidal predictions based on hourly tide gauge observations from Tarawa and Funafuti (years 1988–2018 and 1979–2017, respectively) sourced from the University of Hawaii Sea Level Center ([4]Caldwell et al., 2015). Root-mean-square-differences (RMSD) between tide gauge and TPXO predictions at Funafuti and Tarawa were 0.01 and 0.02 m, respectively. More importantly for this analysis, 99.5th quantiles differences between tide gauge and TPXO predictions at Funafuti and Tarawa were 0.021 and 0.025 m, respectively. The tidal software UTide (Codiga, 2011) was used both to estimate constituents from tide gauge observations and to calculate predictions for both the TPXO and tide gauge constituents.

Non-tidal Sea-Level

The computation of TWLs and associated extreme value analysis (see next) requires an uninterrupted time span of non-tidal sea-level data that corresponds to the wave hindcast (years 1979–2019) and the astronomical tides calculated in section "Astronomical Tides". This precludes using sea surface heights measured by satellite altimetry, which only start around 1992. We evaluated three global gridded sea level products, all available from publicly accessible data repositories, which meet this time span requirement:

1. NCEP Climate Forecast System Reanalysis Reforecast (CFSR) 6-hourly sea surface height (Saha et al., 2013);

[4]https://uhslc.soest.hawaii.edu/

TABLE 1 | Documented remote impacts in Tuvalu and Kiribati.

Island/ Atoll	Morphology notes	Summarized hazard and impacts*	TWL		Hb	
			(m)	AEP (years)	(m)	AEP (years)
Tarawa (KI)	Atoll/lagoon on western side, main settlements on southern side	**Severe:** "widespread coastal flooding"; "damage to major throughway bridge"[1,2]	2.30	40(620)	4.93	40 (162)
Nonouti (KI)	Atoll/lagoon on western side, some western-exposed villages	**Severe/moderate**: unclear from reporting[1]	2.39	40 (6397)	5.04	40 (141)
Onotoa (KI)	Atoll/lagoon on western side, some western-exposed villages	**Severe/moderate**: unclear from reporting[1]	2.36	40(425)	5.27	40 (169)
Tamana (KI)	Reef island/no lagoon, village(s) on west side;	**Severe:** "worst hit" "80 per cent of wells were badly affected" "65 homes completely destroyed, 42 damaged," "inundations"[1,2]	2.44	40(196)	5.55	40 (53)
Arorae (KI)	Reef island/no lagoon, some village(s) on west side;	**Severe/moderate**: "inundations"; unclear from reporting[1,2]	2.40	40(65)	5.45	41 (51)
Nanumea (TV)	Atoll, but village on western side	**Severe/Moderate**: 60% households affected, although some discrepancy in reporting[1,2,3,4] Severe erosion on the western side, beach receded by 6–8 meters[5].	2.73	40(158)	6.75	20(17)
Niutao (TV)	Reef island/no lagoon, village(s) on west side;	**Moderate:** 32% households affected[1,2,3,4] erosion of about 10 m on the western side[5].	2.55	13(29)	6.25	14 (15)
Nanmanga (TV)	Reef island/no lagoon, village(s) on west side;	**Moderate:** 15% households affected[1,2,3,4]	2.80	40(91)	6.96	20 (20)
Nui (TV)	Atoll; village on western side	**Severe:** 98 % households affected.[1,2,3,4] All of settlement flooded with inundation coming from both ocean and lagoon side. Aggregate deposition on the south eastern side of the atoll. Shipping channel damaged[5].	2.69	40(35)	6.72	14 (21)
Vaitupu (TV)	Atoll (very small lagoon) village(s) on west side;	**Moderate:** although some discrepancy in reporting[1,2,3,4]. First row of houses near the ocean shoreline were destroyed. Inundation extend about 50 m from ocean coastline. Erosion: beach on western side receded by 15–20 metres[5].	2.32	04(06)	5.96	10 (15)
Nukufetau (TV)	Atoll; village on western side, but behind another seaward island	**Minor:** Damaged seawall, with boulders deposited in the main shipping channel—Inundation on ocean and lagoon side shoreline[5].	2.36	05(13)	6.04	10 (17)
Funafuti (TV)	Atoll, settlements on eastern side	None reported.	2.10	03(02)	5.58	08 (12)
Nukulaelae (TV)	Atoll; village on western side	**Severe:** 66% households affected[1,2,3,4]	2.34	05(05)	6.62	10 (16)
Niulakita (TV)	Reef island/no lagoon, village on west side	None reported	2.48	10(10)	7.17	20 (20)

*The Island/Atoll column is sorted according to latitude from north to south; country is indicated in parentheses, KI for Kiribati and TV for Tuvalu. The maximum value for total water level (TWL) and breaking wave height (Hb) during the passage of TC Pam is given in meters, the following columns indicate the empirical annual exceedance probabilities (AEP) of the TWL and Hb at each location, with fitted AEPs indicated in parentheses (see section Materials and Methods" for how these quantities are calculated). *Summarized Impacts are from the following sources: [1]ICRC, 2018; [2]USAID, 2015; [3]OCHA, 2015; [4]Taupo and Noy, 2017; [5]inundation/erosion maps from the Tuvalu Public Works Department (see **Supplementary Material**). Note that for Tuvalu, "households affected" percentages are "of households reported that surges from the TC Pam entered their homes" from Taupo and Noy, 2017.*

2. CSIRO monthly sea-level reconstruction (Church and White, 2011); and
3. ORAS5 Ocean ReAnalysis System 5 (ORAS5) monthly sea surface height[5].

These sea level products were assessed for best representing background non-tidal sea levels (η_{SL}) by comparing them to the 30-days median low-pass filtered tide gauge residual sea level at Tarawa and Funafuti (see section "Astronomical Tides"). All sea levels, (including tide gauge residuals) where adjusted such that mean sea level = 0 between 1999 and 2009 prior to comparison. Correlation coefficients (R) and RMSD calculated against the low-pass filtered tide gauge residuals are shown in **Table 2**.

ORAS5 clearly outperforms the other two sea surface height products in comparison to the (observed) Tarawa and Funafuti tide gauge residuals. ORAS5 monthly values are linearly interpolated to the (hourly) times of the wave hindcast (years 1979–2019) to represent non-tidal sea levels (η_{SL}); throughout the remainder of this article, η_{SL} refers to that derived from ORAS5 sea surface height values. It should be noted that thus η_{SL} omits high-frequency (timescales < 1 month) sea level variability. However, the variance of the 30-days median low-pass filtered (observed) residuals is 0.005 m at Tarawa and 0.010 m at Funafuti. The high-frequency (remainder) residual variance at both sites is 0.001 m, i.e., 5–10 times less than that of the monthly variance; which is fairly typical of low-latitude Pacific locations where sea level variability is dominated by seasonal and interannual (e.g., ENSO) dynamics (Merrifield et al., 1999;

[5]https://www.ecmwf.int/en/research/climate-reanalysis/ocean-reanalysis

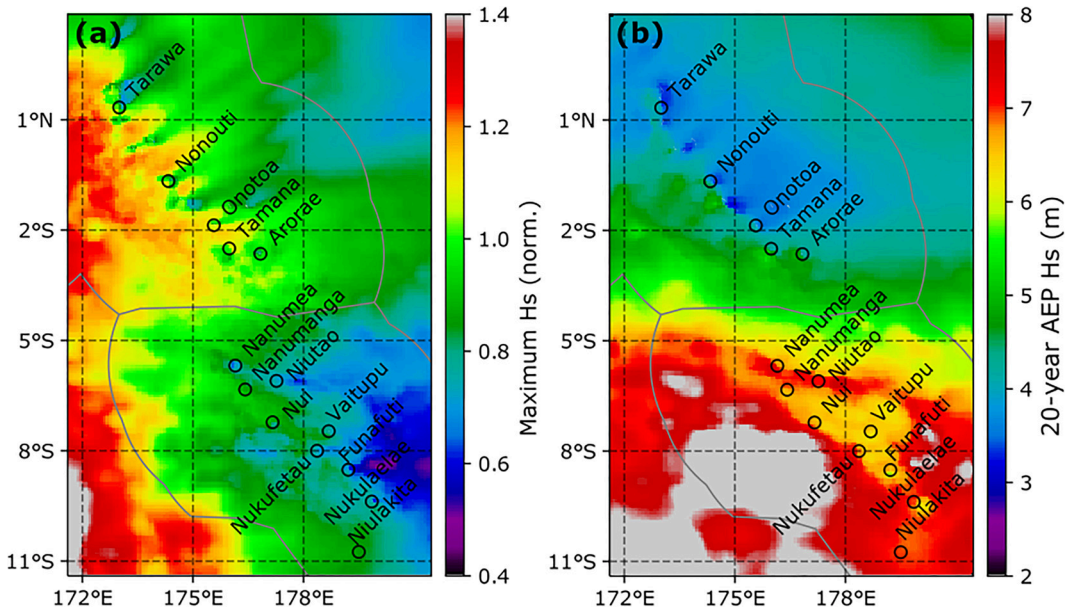

FIGURE 2 | Region and locations indicated in **Table 1**. The maximum hindcast significant wave height (H_x) during TC Pam's passage (March 6–17, 2015) is shown in subplot **(a)**, which is normalized by the local 1-in-20 year annual exceedance probability (AEP) shown in subplot **(b)**. Note H_s, rather breaking wave height (H_b) or total water level (*TWL*) as these latter quantities follow wave shoaling and breaking across shallow fringing reef, respectively, and the area of **Figure 2** (apart from the scattered islands and reefs) contains abyssal ocean depths.

TABLE 2 | Comparison of CFSR, CSIRO and ORAS5 sea surface height values with monthly-median low-pass filtered non-tidal (residual) tide gauge observations.

	CFSR		CSIRO		ORAS5	
Tide Gauge	**R**	**RMSD**	**R**	**RMSD**	**R**	**RMSD**
Tarawa	0.70	0.045 m	0.89	0.027 m	0.93	0.024 m
Funafuti	0.76	0.055 m	0.85	0.041 m	0.94	0.030 m

Church et al., 2006; Zhang and Church, 2012). Thus, the lack of inclusion of higher-frequency sea level fluctuations is assumed to introduce a relatively small error into this analysis. Future studies may evaluate introducing inverse barometer estimates, based on global sea level products to further ameliorate this error.

Extreme Value Analysis and Total Water Level (TWL)

To reduce complexity of the extreme value (statistical) analysis, we focus on four of the previously defined variables: C_gE (wave energy flux), D_p (peak wave direction), η_{tide}, and η_{SL} as well as event duration, which arises from the analysis. C_gE, rather than H_s, is chosen as a primary diagnostic variable for the analysis, since (as a measure of power, rather than energy), it tends to scale more linearly with nearshore processes such as wave runup and setup.

Extreme events are identified for each site in **Table 1** by choosing a threshold and identifying exceedances of C_gE above it; an event begins when the C_gE exceeds the threshold, and a new event is assumed only when C_gE remains below the threshold for more than 12 h (i.e., "declustering" events). The threshold for this analysis is the 99.5% quantile.

Event duration is then calculated as the amount of time that each declustered C_gE event remains above the threshold. The D_p (peak wave direction) associated with the event is taken as that occurring at the time of the peak (maximum) C_gE. The η_{SL} and η_{tide} associated with the event are the respective maxima of each occurring during the storm duration, i.e., not necessarily the water level at the time of maximum C_gE. To further aid in interpretation, empirical annual exceedance probability (AEP), also commonly called return periods or return levels, were empirically calculated from the declustered storm event maximum C_gE values at both locations.

In order to better understand how these variables (C_gE, D_p, η_{SL}, and η_{tide}) combine to create extreme sea level events, we follow a "total water level" (TWL) approach (Dodet et al., 2019), and calculate a further variable (η_2), defined as the 2% exceedance water level at the shoreline above the "still" water level, as a function of wave setup and variable swash ("runup") due to both wind-waves and infra-gravity/longwave dynamics associated with shoaling and breaking of wave groups at the reef edge. The TWL is simply calculated as:

$$\mathrm{TWL} = \eta_{SL} + \eta_{tide} + \eta_2 \quad (1)$$

To calculate η_2, we follow the simpler of the two approaches described by Merrifield et al. (2014), viz:

$$\eta_2 = b_1 H_b + b_0 \quad (2)$$

Where H_b is "breaking wave height," calculated using a simplified relation to account for wave refraction and shoaling to breaking

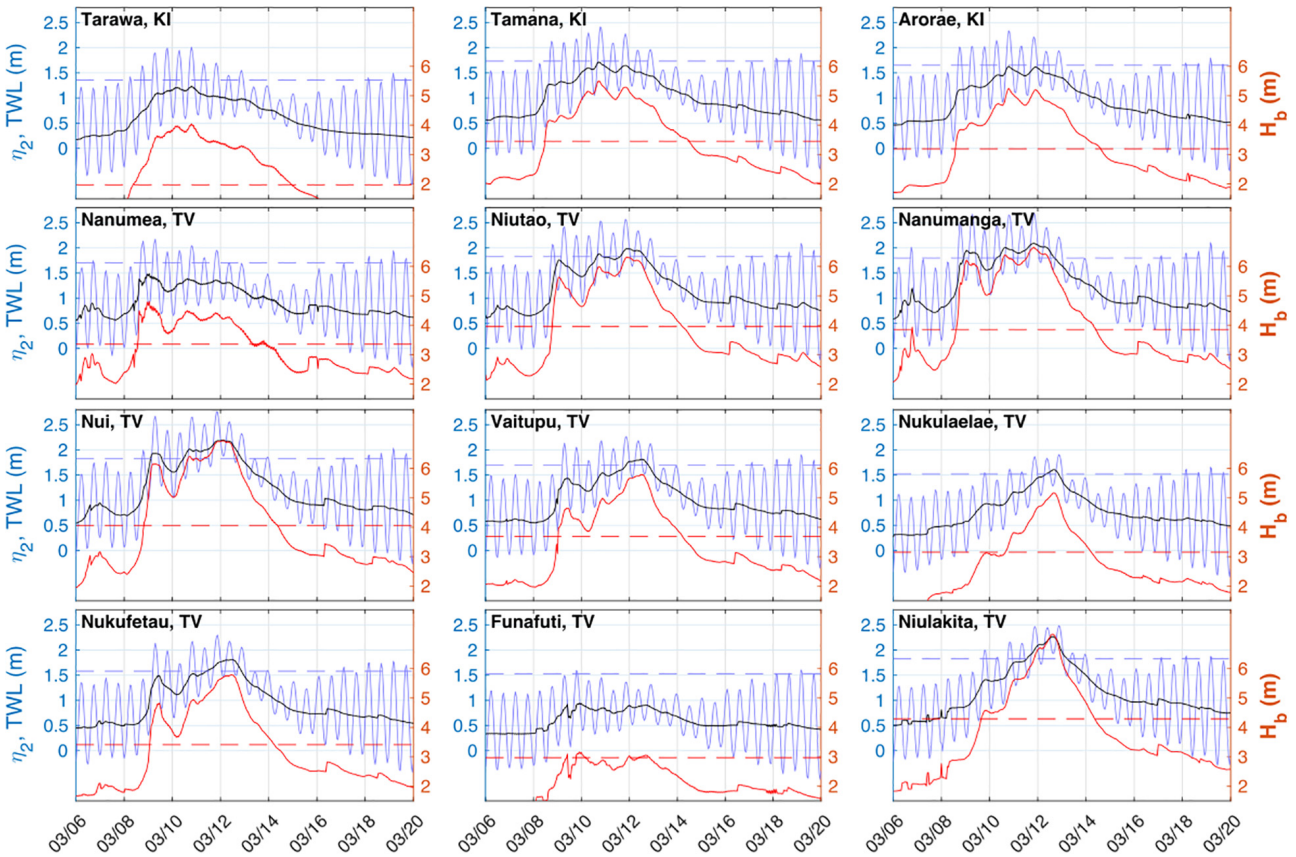

FIGURE 3 | Time series plot of estimated breaking wave height (H_b, *red*), wave setup/runup (η_2, *black*) and total water level (*TWL*, blue) for selected islands listed in **Table 1**, from March 6—March 20, 2015. The 99.5th quantiles (percentiles) for the entire hindcast timeseries (1980–2019) are shown as dashed red and blue lines for H_b and *TWL*, respectively.

depth from the (deep water) H_s provided by the wave hindcasts:

$$H_b = [H_s^2 T_p (4\pi)^{-1} - \cos(D_p - D_N)\sqrt{\gamma g}]^{2/5} \quad (3)$$

In Equation 2, the two empirical coefficients b_1 and b_0 are assumed a value of 0.3 and –0.1, both near the mean value and within the 95% confidence limits for the two study sites examined in Merrifield et al. (2014). While these sites were both in the Marshall Islands, it is arguable that the Tuvalu and Kiribati sites in this study share similar atoll/narrow fringing reef morphology to the Marshall Islands sites, although morphological effects are discussed in more detail in the following sections. In Equation 3, γ is the ratio of breaking H_b to breaking water depth and D_n is the local shore-normal angle.

RESULTS

Time series of total water level (*TWL*) and breaking wave height (H_b) centered on a 2-week period of the peak of H_b during the time period of TC Pam's passage, is presented in **Figure 3**. From these plots, it is clear that most impacted locations experienced a sustained period of 5 or more days of H_b above the 99.5th quantile threshold (based on the entire 40-year timeseries); *TWL* was similarly elevated during successive high tides during the same period. These highly elevated values (above the threshold) are noticeably absent for Funafuti, where no impacts were reported during the period; however, Nukufetau and Niulakita also did not report impacts, but experienced highly elevated *TWL* and H_b, similar to highly impacted neighboring Tuvaluan islands/atolls (**Table 1** and **Figure 3**). Potential reasons for this discrepancy are discussed later.

As previously mentioned, the timing of high tides in relation to the timing of maximum H_b (and C_gE) appear to have modulated the timing of impacts at the different islands. However, astronomical tides were not abnormally high (mostly roughly between spring and neap, **Figure 3**) during the event at any of the impacted islands. This tidal modulation could explain the lesser impacts reported in the southern islands of Tuvalu (except Nukulaelae) where the peak of H_b (and C_gE) was of shorter duration and occurred predominantly during neap tides.

To better examine the relative contribution of C_gE, tides (η_{tide}), background sea level (η_{SL}), other multivariate aspects of this event and its relation to other *TWL* extreme events, **Figures 4**, **5** present "scatterplot matrix" diagrams for Tamana and Nui, which were selected as representative of impacted locations within Kiribati and Tuvalu, respectively. These

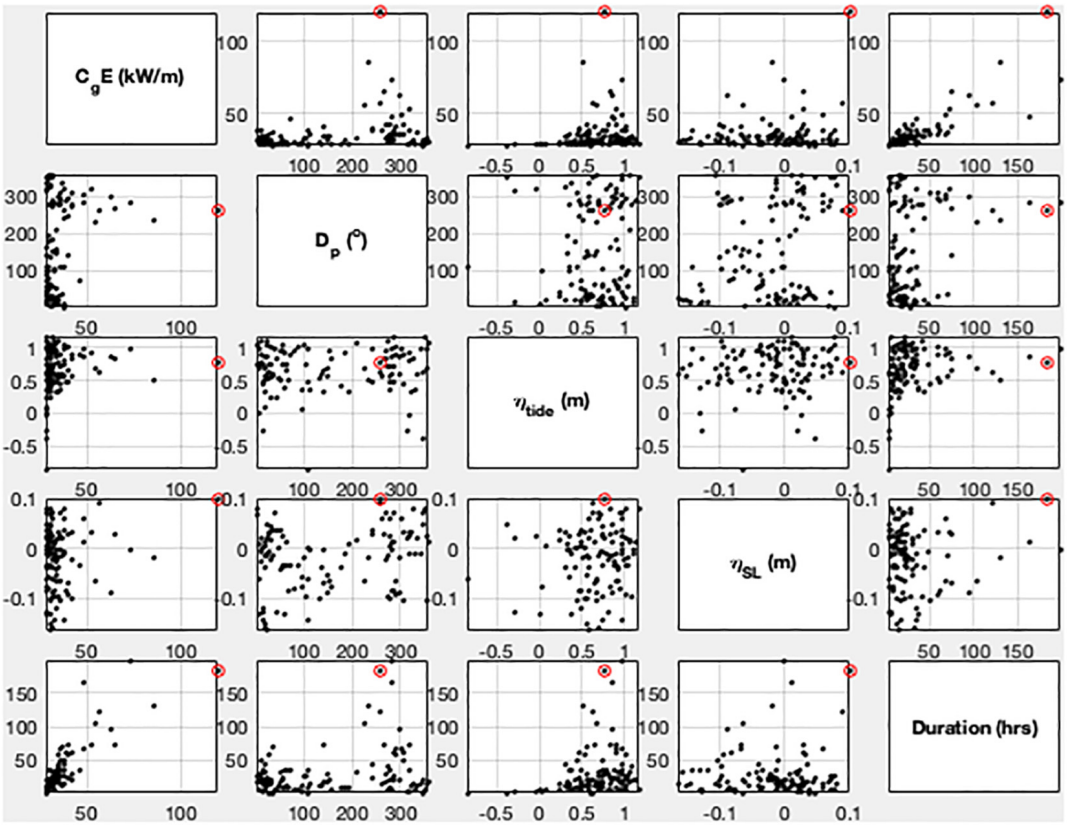

FIGURE 4 | Scatterplot matrix of Tamana (Kiribati) event-based data identified by declustering extreme sea level events with integrated wave energy flux (C_gE) above the 99.5 percentile threshold. The variables are: within-event maximum C_gE, peak wave direction (D_p) during the hour of maximum C_gE, within-event maximum astronomic tide maximum (η_{tide}), background sea level (η_{SL}), and event duration (hours). Within each subplot the event closest to March 15, 2015 (i.e., associated with TC Pam) is highlighted with a red circle.

scatterplot matrices allow the visualization of the co-occurrence C_gE, η_{tide}, and η_{SL}, as well as wave direction (D_p) and event duration for all events above the (99.5th quantile) *TWL* threshold within the hindcast record, particularly when combined with annual exceedance probability (AEP) plot of all locations (**Figure 6**).

At Tamana (Kiribati), maximum C_gE (and thus estimated wave setup/runup) was by far the highest in the entire hindcast record, on the order of 40% higher than the next highest event in terms of C_gE (**Figure 4**). The event also had the longest or second longest duration at the impacted islands. This probably contributed to the noted erosion at Tarawa, in addition to recorded severity of inundation at the impacted islands in Kiribati. At Nui (Tuvalu), maximum C_gE was not the highest in the entire hindcast record, it was third highest (**Figure 5**). However, when combined with η_{SL} and η_{tide} it created the highest *TWL* in the record (**Figure 5**). Event duration at Nui (**Figure 5**) was also among the top three events, and likely contributed to the extensive erosion recorded at many of the locations in Tuvalu, as in Kiribati.

Overall, *TWL and* H_b were the highest in the hindcast period, with a calculated empirical AEP of 40 years (the highest possible for the time duration of the hindcasts used in this study) for all islands in Kiribati with recorded impacts (**Table 1** and **Figure 6**). These results are more varied in Tuvalu: H_b empirical *AEPs* generally ranged between 10 and 20 years, in the northern islands, elevated η_{tide} and particularly η_{SL} increase *TWL* empirical AEP values above those of H_b. In the southern islands, the aforementioned later onset of elevated H_b, closer to neap tides, lead to lower *TWL* empirical AEP values relative to that of H_b. Never the less, all islands in Tuvalu which recorded severe impacts experienced greater than a 10-year AEP *TWL*, excepting Nukulaelae (**Table 1** and **Figure 6**).

In addition to the *TWL* and H_b event AEP levels of indicated in **Figure 6**, wave direction (D_p) associated with each event is also indicated by an arrow indicating the direction waves are traveling at the time of peak H_b. This indicates that all large events (AEP $>$ 10 years) are from the west in Kiribati, but not in Tuvalu. At some (but not all) Tuvalu locations, TC Pam was the largest westerly event. To further investigate the drivers the storm wave events, all regional TCs with maximum sustained winds greater than 48 knots (the lower threshold for category 2 TCs according to the southern hemisphere intensity scale) were queried. H_b and *TWL* events which occurred during or up to 5 days after TCs which occurred within $\pm$ 5 days of empirical AEP events are labeled as such in **Figure 6** and these TCs tracks are

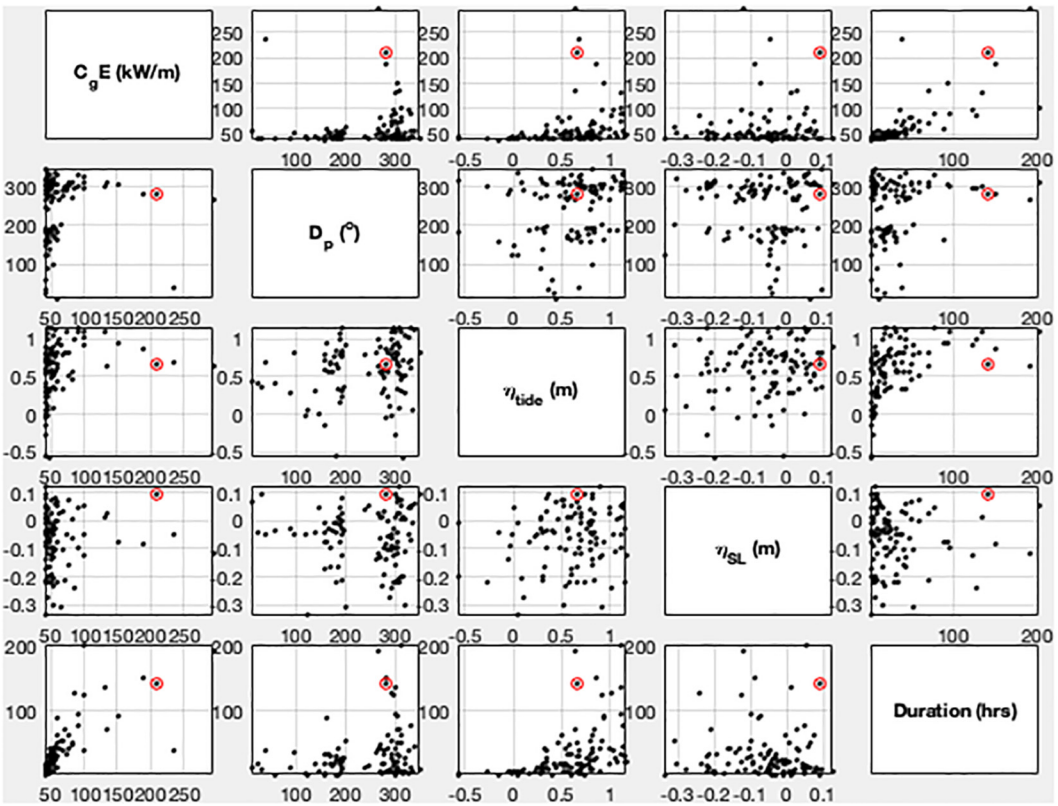

FIGURE 5 | Scatterplot matrix of Nui (Tuvalu) event-based data identified by declustering extreme sea level events with wave energy flux (C_gE), above the 99.5 percentile threshold. The variables are the same as in **Figure 4**. Within each subplot the event closest to March 15, 2015 (i.e., associated with TC Pam) is highlighted with a red circle.

plotted in **Figure 7**. This illustrates that despite TC tracks never crossing the Gilbert Islands and only very rarely crossing the Tuvalu islands within the 40-year hindcast period, all H_b events (and most *TWL* events) greater than the 10-year AEP value at all locations excepting Tarawa (the northernmost of the study site), are associated with TCs. All of the associated TCs' tracks lay primarily well to the south and west (or north and west in one case) of the Gilbert Islands and Tuvalu, and most, though not all, attained at least a TC category 4 maximum sustained wind intensity. Of note is TC Kina which occurred in early January, 1993. It is associated with the largest H_b and *TWL* at many of the southern Tuvalu islands in our analysis; severe flooding and destruction of homes were reported on Nanumea, Nanumaga, Niutao, Nui, and Vaitupu[6].

Finally, it should be reiterated that at all locations, background sea levels (η_{SL}) were the highest or among the highest on record (+0.1 m) during the TC Pam events. This definitely contributed to the overall severity of the event, particularly in Tuvalu. What portion of that is attributable to sea level rise (SLR) vs. seasonal and/or inter-annual (e.g., ENSO) sea level variability is beyond the scope of this paper, since higher order techniques (such as multivariate regression or empirical function analyses) are needed to separate these two components (Zhang and Church, 2012; Albrecht et al., 2019). This will be addressed in future studies.

DISCUSSION AND CONCLUSION

In this study, we link a widespread series flooding, island overwash and erosion events in 2015 in the atoll nations of Tuvalu and Kiribati to locally extreme values of total water level (*TWL*), composed of regional sea-level, astronomic tide and wind-wave components. Similar to other studies (e.g., Hoeke et al., 2013; Wadey et al., 2017; Ford et al., 2018; Wandres et al., 2020), extreme wind-waves associated with a distant storm (swell) was the proximate cause, or trigger, of the flooding and erosion reported here. In contrast to (or perhaps complimenting) these other studies, the swell triggering this event was generated not by distant mid-latitude storms, but by a distant tropical cyclone (TC Pam). Like these other studies, however, local TWL extremes (and impacts) were highly modulated by the timing of swell arrival relative to local tidal phase (**Table 1** and **Figure 3**) and by regional sea level anomalies. Other than the swell generated by it, meteorological phenomena directly associated with TC Pam, e.g., local wind setup and inverse barometer effect, appear to have played little, if any, role.

[6]https://reliefweb.int/report/tuvalu/tuvalu-cyclone-nina-jan-1993-dha-undro-situation-report-1

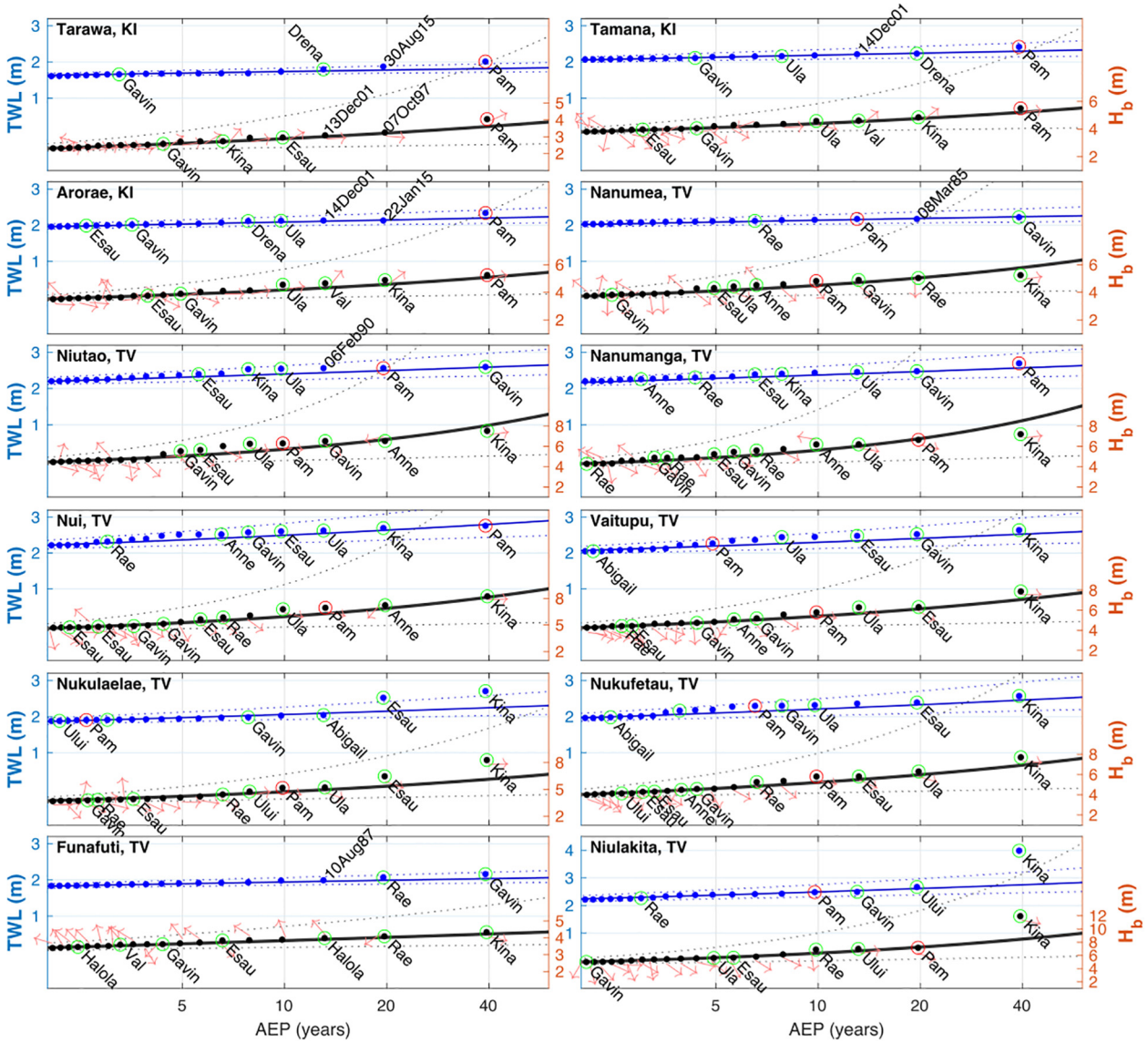

FIGURE 6 | Annual exceedance probability (AEP) plots for selected islands listed in **Table 1**. Black and blue dots indicate empirical AEPs for estimated breaking wave height (H_b), wave runup (η_2) and total water level (*TWL*), respectively; black and blue lines indicate a maximum likelihood estimate curve using a generalized Pareto tail model for the same variables, respectively. 95% confidence limits are indicated with dotted lines. Peak wave direction (D_p) for each event is indicated by red arrow on the H_b AEPs, respectively. Where *TWL* or H_b empirical AEP events have occurred during or up to 5 days after the occurrence of a TC in the region (see **Figure 6**) are highlighted with green circles and labeled with the TC name; the event associated with TC Pam is highlighted with a red circle. For events with RI > 10 years not matched with a TC are labeled with their date.

The relative severity of the flooding and erosion impacts amongst the islands and atolls included does not appear to be simply linked to the local values of *TWL* or breaking wave heights (H_b): e.g., maximum *TWLs* and H_b heights were significantly smaller (approximately 1.5 m and 30 cm smaller, respectively) in the southern Gilbert Islands (Kiribati) than in Tuvalu (**Table 1** and **Figure 6**), but reported impacts in the affected Gilbert Islands appear to be nearly as bad, perhaps worse in some cases. Local annual exceedance probabilities (AEPs), however, align much better with the reported impacts; e.g., significant wave heights (H_s), *TWL* and H_b AEPs in the southern Gilberts were almost universally higher (despite scalar height values being lower) compared to those in Tuvalu (**Figures 2**, **6** and **Table 1**). The exceptional duration of the event (greater again in the Gilberts than in Tuvalu, **Figures 4**, **5**) undoubtedly also played a role. In other words, when extreme water levels associated with TC Pam are taken into local historical context (through extreme value analysis), they align better with the reported impacts. This makes sense from a geomorphology perspective, since local storm ridges and other reef island features are highly dependent on local wave climate (e.g., Woodroffe, 2008; Vila-Concejo and Kench, 2017).

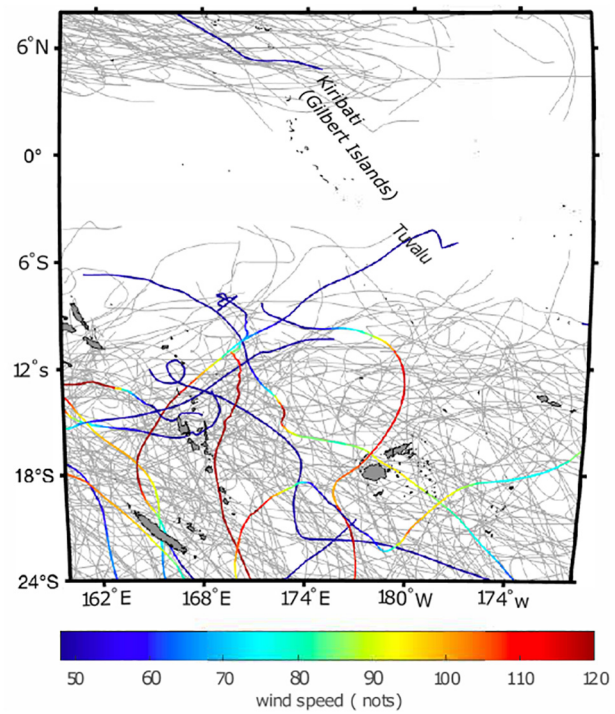

FIGURE 7 | TC tracks in region of the Gilbert Islands (Kiribati) and Tuvalu (1979–2019). TCs which were matched with *TWL* and/or H_b events above the 99.5th quantile threshold (i.e., those plotted in **Figures 4**, **5**) are plotted in color, indicating along-track maximum sustained winds; other cyclones are plotted in gray.

It also makes sense from a coastal engineering perspective (coastal defenses are typically designed using wave and/or water level exceedance probabilities); and also with respect to traditional island settlement patterns, although inconsistent coastal management and contemporary changes in settlement patterns may cloud this picture somewhat (Duvat, 2013; Kench et al., 2018).

There is also further reason to use such an approach, i.e., to describe (or predict) an island flooding and/or erosion event in the context of an extreme value analysis (EVA) of historical baseline data. In many cases, the EVA can establish a proxy or threshold for anticipated impacts, viz rather than simply predicting flood levels of so-and-so many meters, they can be predicted in terms of a known historical event or (e.g.) the 1-in-50 year level. For example: we predict the flooding impacts of TC Pam will be similar to/less than/greater than (depending on island) TC Kina in 1993 (which did indeed cause similar impacts in many of the southern Tuvalu islands, see "Results" section). This offers an opportunity to timely, easily understood information toward an increased efficiency of post disaster emergency efforts, and also provide a pathway for the development of a simple regional coastal inundation forecasting (or warning) system for locations where heights and datums of local coastal defenses may not be well know, and with computational need tailored to the current local resources.

Both applications would require further investigation to determine the reliability of existing global or regional wave forecast products to adequately predict TC- or mid-latitude storm generated waves and their subsequent propagation thousands of kilometers away: the wave hindcast used (and verified for TC Pam) in this study is approximately an order of magnitude higher spatial resolution than wave products available from the major numerical weather prediction centers for the region of this study. Ongoing efforts by regional organizations to provide downscaling of these global wave forecast products for Kiribati and Tuvalu could significantly contribute to the generation of island community scale actionable warning information; however, bias correction between forecast products and hindcast/historical products is necessary, and better overall skill assessment of both are needed. To this end, an increase in *in situ* wave observations and monitoring is required, perhaps to at least the level currently provided for sea level monitoring via the tide gauge network. Also required is improved consistency and detail in the reporting of flooding and erosion impacts; despite gathering reports from multiple sources in this study, local impacts at many islands is unclear because of inconsistencies in reporting (**Table 1**). Establishment and widespread adaptation of reef island flooding reporting guidelines would be extremely helpful in this regard.

While this *TWL* extreme value analysis approach appears to have been largely successful at describing the severity of this event at island scale, a number of issues are evident. For example, severe flooding was at Nukulaelae (Tuvalu), while TWL empirical AEP level was amongst the lowest of the impacted sites; conversely Niulakita (Tuvalu) which recorded no impacts had a (much higher) event TWL AEP of ∼10 years. Such discrepancies may of course be attributable to inaccuracies associated with the wave and/or sea level hindcasts. More likely, however, it is due to the highly simplistic approach taken in estimating wave runup and setup (η_2), which neglects any details of local reef morphology, as well as (other) natural or man-made coastal defenses or shoreline orientation (although the method is capable of the latter). It thus neglects any approximations of local wave transformations required to predict sub-island scale extreme water levels and subsequent flooding. A number of researchers are developing meta-modeling methods (e.g., Pearson et al., 2017; Beetham and Kench, 2018; Rueda et al., 2019) capable of including local details of reef morphology; a number of statistical/analytic methods based purely on a limited number of nearshore observations (Merrifield et al., 2014; Wandres et al., 2020) are also under development. Both of these approaches show promise for much more accurate estimation of local wave transformations over reefs (as relevant to island flooding) compared to the extremely simple approach taken in this study. They all also come with a low enough computational cost to be widely applied to the approach presented in this paper, e.g., by using the kind of long-term hindcast data presented here as boundary condition to establish much more locally relevant extreme value analysis-thresholding. However, these meta-model and statistical nearshore wave transformation models require detailed spatial data on reef morphology (reef flat widths, shoreline orientations, and slopes, etc.) and/or local *in situ* observations of water levels and waves, which are currently available only in very

few locations. Also, further research into how to incorporate reef passes and lagoons into such hybrid (statistical-dynamical) approaches is needed.

In summary, the type of TWL event-driven extreme value analysis presented in this paper shows promise to be a valuable tool toward improved understanding and prediction of inundation and erosion events, at both weather forecasting and for longer term future climate timescales. Improved understanding through development of such tools is generally seen as imperative to understand the continued habitability of atoll islands in the face of sea level rise (Kench et al., 2018; Storlazzi, 2018). Although it is beyond the scope of this paper to quantitatively attribute what role sea level rise may have played in the events reported here, it does implicate positive sea level anomaly, and forms a basis to examine attribution of sea level rise in reef island flooding events in future studies.

DATA AVAILABILITY STATEMENT

The datasets used in this study can be found in online repositories. The names of the repository/repositories and accession number(s) can be found in the article/ **Supplementary Material**.

AUTHOR CONTRIBUTIONS

RKH conceived the study and preformed most of the analysis and writing. HD, JA, and MW contributed data and other information, as well as assisting with writing and analysis. All authors contributed to the article and approved the submitted version.

FUNDING

RKH was supported in this research by the CSIRO Climate Science Centre and by the Earth Systems and Climate Change (ESCC) Hub, funded through the Australian Government's National Environmental Science Program.

ACKNOWLEDGMENTS

Many thanks to following: Alec Stephenson (CSIRO) who originated pieces of code used in the statistical analysis; Claire Trenham (CSIRO) who assisted in data identification and management; Kathy McInnes and Julian O'Grady (CSIRO) who provided comments on early versions of this manuscript; Xuebin Zhang (CSIRO) for recommending use of ORAS5 sea surface heigh; and Tom Durrant (Oceanum) for discussion of performance of WaveWatchIII under tropical cyclone conditions.

SUPPLEMENTARY MATERIAL

The Supplementary Material for this article can be found online at: https://www.frontiersin.org/articles/10.3389/fmars.2020.539646/full#supplementary-material

REFERENCES

Albrecht, F., Pizarro, O., Montecinos, A., and Zhang, X. (2019). Understanding sea level change in the south pacific during the late 20th century and early 21st century. *J. Geophys. Res. Oceans* 124, 3849–3858. doi: 10.1029/2018JC014828

Barnett, J., and Adger, W. N. (2003). Climate dangers and atoll countries. *Clim. Change* 61, 321–337. doi: 10.1023/B:CLIM.0000004559.08755.88

Beetham, E., and Kench, P. S. (2018). Predicting wave overtopping thresholds on coral reef-island shorelines with future sea-level rise. *Nat. Commun.* 9, 1–8. doi: 10.1038/s41467-018-06550-1

Beetham, E., Kench, P. S., and Popinet, S. (2017). Future reef growth can mitigate physical impacts of sea-level rise on atoll islands. *Earths Future* 5, 1002–1014. doi: 10.1002/2017EF000589

Caldwell, P. C., Merrfield, M. A., and Thompson, P. R. (2015). *Sea Level Measured by Tide Gauges from Global Oceans — the Joint Archive for Sea Level Holdings, Version 5.5*. NOAA National Centers for Environmental Information, Dataset. doi: 10.7289/V5V40S7W

Church, J. A., White, N., and Hunter, J. (2006). Sea-level rise at tropical pacific and Indian ocean islands. *Glob. Planet. Change* 53, 155–168. doi: 10.1016/j.gloplacha.2006.04.001

Church, J. A., and White, N. J. (2011). Sea-level rise from the late 19th to the early 21st century. *Surv. Geophys.* 32, 585–602. doi: 10.1007/s10712-011-9119-1

Codiga, D. L. (2011). *Unified Tidal Analysis and Prediction Using the UTide Matlab Functions. Technical Report 2011-01*. Narragansett, RI: University of Rhode Island.

Damlamian, H., Bosserelle, C., Raj, A., Begg, Z., Katterborn, T., Ketewai, M., et al. (2017). *Tropical Cyclone Pam: A Report on the Coastal Inundation Assessment Undertaken in Vanuatu Using an Unmanned Aerial Vehicle (UAV)*. Suva: Pacific Community (SPC).

Dodet, G., Melet, A., Ardhuin, F., Bertin, X., Idier, D., and Almar, R. (2019). The contribution of wind-generated waves to coastal sea-level changes. *Surv. Geophys.* 40, 1563–1601. doi: 10.1007/s10712-019-09557-5

Durrant, T., Greenslade, D., Hemer, M., and Trenham, C. (2014). A global wave hindcast focussed on the central and south pacific. *CAWCR Tech. Rep.* 70, 1–54. doi: 10.1016/j.coastaleng.2017.03.005

Duvat, V. (2013). Coastal protection structures in Tarawa atoll, Republic of Kiribati. *Sustain. Sci.* 8, 363–379. doi: 10.1007/s11625-013-0205-9

Egbert, G. D., and Erofeeva, S. Y. (2002). Efficient inverse modeling of barotropic ocean tides. *J. Atmos. Ocean. Technol.* 19, 183–204. doi: 10.1175/1520-04262002019<0183:EIMOBO<2.0.CO;2

Flanders Marine Institute (2019). *Maritime Boundaries Geodatabase: Maritime Boundaries and Exclusive Economic Zones (200NM), Version 11*. doi: 10.14284/386 Available online at: https://www.marineregions.org/

Ford, M., Merrifield, M. A., and Becker, J. M. (2018). Inundation of a low-lying Urban atoll island: Majuro, Marshall Islands. *Nat. Hazards* 91, 1273–1297. doi: 10.1007/s11069-018-3183-5

Hemer, M. A., Zieger, S., Durrant, T., O'Grady, J., Hoeke, R. K., McInnes, K. L., et al. (2016). A revised assessment of Australia's national wave energy resource. *Renew. Energy* 114, 85–107. doi: 10.1016/j.renene.2016.08.039

Hoeke, R. K., Mcinnes, K. L., Kruger, J. C., Mcnaught, R. J., Hunter, J. R., and Smithers, S. G. (2013). Widespread inundation of pacific islands triggered by distant-source wind-waves. *Glob. Planet. Change* 108, 128–138. doi: 10.1016/j.gloplacha.2013.06.006

ICRC (2018). *Emergency Plan of Action Final Report Pacific Region: Tropical Cyclone Pam*. Geneva: ICRC.

Idier, D., Bertin, X., Thompson, P., and Pickering, M. D. (2019). Interactions between mean sea level, tide, surge, waves and flooding: mechanisms and contributions to sea level variations at the coast. *Surv. Geophys.* 40, 1603–1630. doi: 10.1007/s10712-019-09549-5

Kench, P. S., Ford, M. R., and Owen, S. D. (2018). Patterns of island change and persistence offer alternate adaptation pathways for atoll nations. *Nat. Commun.* 9, 1–7.

Knapp, K. R., Kruk, M. C., Levinson, D. H., Diamond, H. J., Neumann, C. J., Knapp, K. R., et al. (2010). The international best track archive for climate stewardship (IBTrACS). *Bull. Am. Meteorol. Soc.* 91, 363–376. doi: 10.1175/2009BAMS2755.1

Maragos, J., Baines, G., and Beveridge, P. (1973). Tropical cyclone creates a new land formation on Funafuti atoll. *Science* 181, 1161–1164. doi: 10.1126/science.181.4105.1161

Merrifield, M. A., Becker, J. M., Ford, M., and Yao, Y. (2014). Observations and estimates of wave-driven water level extremes at the marshall islands. *Geophys. Res. Lett.* 41, 7245–7253. doi: 10.1002/2014GL061005

Merrifield, M. A., Kilonsky, B., and Nakahara, S. (1999). Interannual sea level changes in the tropical pacific associated with ENSO. *Geophys. Res. Lett.* 26, 3317–3320. doi: 10.1029/1999GL010485

Nicholls, R. J., Marinova, N., Lowe, J. A., Brown, S., Vellinga, P., de Gusmão, D., et al. (2011). Sea-level rise and its possible impacts given a 'beyond 4°C World' in the Twenty-First Century. *Philos. Trans. R. Soc. A Math. Phys. Eng. Sci.* 369, 161–181. doi: 10.1098/rsta.2010.0291

Nicholls, R. J., Wong, P. P., Burkett, V. R., Codignotto, J., Hay, J. E., McLean, R. F., et al. (2007). "Coastal systems and low-lying areas," in *Climate Change 2007: Impacts, Adaptation and Vulnerability*, eds M. L. Parry, O. F. Canziani, J. P. Palutikof, P. J. van der Linden, and C. E. Hanson (Cambridge: Cambridge University Press).

OCHA (2015). *Tuvalu: Tropical Cyclone Pam Situation Report No. 2*. New York, NY: OCHA.

Pearson, S. G., Storlazzi, C. D., van Dongeren, A. R., Tissier, M. F. S., and Reniers, A. J. H. M. (2017). A Bayesian-based system to assess wave-driven flooding hazards on coral reef-lined coasts. *J. Geophys. Res. Oceans* 122, 10099–10117. doi: 10.1002/2017JC013204

Perry, C. T., Alvarez-Filip, L., Graham, N. A. J., Mumby, P. J., Wilson, S. K., Kench, P. S., et al. (2018). Loss of coral reef growth capacity to track future increases in sea level. *Nature* 558, 396–400. doi: 10.1038/s41586-018-0194-z

Ribal, A., and Young, I. R. (2019). 33 years of globally calibrated wave height and wind speed data based on altimeter observations. *Sci. Data* 6:77. doi: 10.1038/s41597-019-0083-9

Rueda, A., Cagigal, L., Pearson, S., Antolínez, J. A. A., Storlazzi, C., van Dongeren, A., et al. (2019). HyCReWW: a hybrid coral reef wave and water level metamodel. *Comput. Geosci.* 127, 85–90. doi: 10.1016/j.cageo.2019.03.004

Saha, S., Moorthi, S., Wu, X., Wang, J., Nadiga, S., Tripp, P., et al. (2013). The NCEP climate forecast system version 2. *J. Clim.* 27, 2185–2208. doi: 10.1175/JCLI-D-12-00823.1

Seneviratne, S. I., Nicholls, N., Easterling, D., Goodess, C. M., Kanae, S., Kossin, J., et al. (2012). *Changes in Climate Extremes and Their Impacts on the Natural Physical Environment: An Overview of the IPCC SREX Report." EGU General Assembly 2012*. Geneva: IPCC.

Smithers, S. G., and Hoeke, R. K. (2014). Geomorphological impacts of high-latitude storm waves on low-latitude reef islands – observations of the december 2008 event on Nukutoa, Takuu, Papua New Guinea. *Geomorphology* 222, 106–121. doi: 10.1016/j.geomorph.2014.03.042

Storlazzi, C. D. (2018). *Challenges of Forecasting Flooding on Coral Reef–Lined Coasts." Eos 99. J. Geophys. Res. Ocean* doi: 10.1029/2018eo098517

Storlazzi, C. D., Gingerich, S. B., Van Dongeren, A., Cheriton, O. M., Swarzenski, P. W., Quataert, E., et al. (2018). Most atolls will be uninhabitable by the Mid-21st century because of sea-level rise exacerbating wave-driven flooding. *Sci. Adv.* 4:eaa9741. doi: 10.1126/sciadv.aap9741

Taupo, T., and Noy, I. (2017). At the very edge of a storm: the impact of a distant cyclone on atoll islands. *Econ. Disast. Clim. Change* 1, 143–166. doi: 10.1007/s41885-017-0011-4

Tuck, M. E., Kench, P. S., Ford, M. R., and Masselink, G. (2019). Physical modelling of the response of reef islands to sea-level rise. *Geology* 47, 803–806. doi: 10.1130/G46362.1

USAID (2015). *South Pacific – Tropical Cyclone Pam, Fact Sheet #3*. Washington, DC: USAID.

Vanuatu, G. (2015). *Tropical Cyclone Pam—Humanitarian Action Plan*. Available online at: https://reliefweb.int/sites/reliefweb.int/files/resources/vanuatu_tc_pam_hap.pdf (accessed January 15, 2020).

Vila-Concejo, A., and Kench, P. (2017). *"Storms in Coral Reefs." Coast. Storms Process. Ciavola, P and Coco, G, 127–49*. Hoboken, NJ: John Wiley and Sons.

Wadey, M., Brown, S., Nicholls, R. J., and Haigh, I. (2017). Coastal flooding in the maldives: an assessment of historic events and their implications. *Nat. Hazards* 89, 131–159. doi: 10.1007/s11069-017-2957-5

Wandres, M., Aucan, J., Espejo, A., Jackson, N., De Ramon N'Yeurt, A., and Damlamian, H. (2020). Distant-source swells cause coastal inundation on Fiji's coral coast. *Front. Mar. Sci.* 7:546. doi: 10.3389/fmars.2020.00546

Webb, A., and Kench, P. (2010). The dynamic response of reef islands to sea-level rise: evidence from multi-decadal analysis of island change in the central pacific. *Glob. Planet. Change* 72, 234–246. doi: 10.1016/j.gloplacha.2010.05.003

Woodroffe, C. D. (2008). Reef-island topography and the vulnerability of atolls to sea-level rise. *Glob. Planet. Change* 62, 77–96. doi: 10.1016/j.gloplacha.2007.11.001

Zhang, X., and Church, J. A. (2012). Sea level trends, interannual and decadal variability in the pacific ocean. *Geophys. Res. Lett.* 39:21701. doi: 10.1029/2012GL053240

Conflict of Interest: The authors declare that the research was conducted in the absence of any commercial or financial relationships that could be construed as a potential conflict of interest.

The handling editor declared a past co-authorship with several of the authors RKH, JA, and MW.

Copyright © 2021 Hoeke, Damlamian, Aucan and Wandres. This is an open-access article distributed under the terms of the Creative Commons Attribution License (CC BY). The use, distribution or reproduction in other forums is permitted, provided the original author(s) and the copyright owner(s) are credited and that the original publication in this journal is cited, in accordance with accepted academic practice. No use, distribution or reproduction is permitted which does not comply with these terms.

Advantages of publishing in Frontiers

OPEN ACCESS
Articles are free to read for greatest visibility and readership

FAST PUBLICATION
Around 90 days from submission to decision

HIGH QUALITY PEER-REVIEW
Rigorous, collaborative, and constructive peer-review

TRANSPARENT PEER-REVIEW
Editors and reviewers acknowledged by name on published articles

Frontiers
Avenue du Tribunal-Fédéral 34
1005 Lausanne | Switzerland

Visit us: www.frontiersin.org
Contact us: frontiersin.org/about/contact

REPRODUCIBILITY OF RESEARCH
Support open data and methods to enhance research reproducibility

DIGITAL PUBLISHING
Articles designed for optimal readership across devices

FOLLOW US
@frontiersin

IMPACT METRICS
Advanced article metrics track visibility across digital media

EXTENSIVE PROMOTION
Marketing and promotion of impactful research

LOOP RESEARCH NETWORK
Our network increases your article's readership